University of Strathclyde

Department of Naval Architecture, Ocean & Marine Engineering

Structural Health Monitoring of Marine Structures by using Inverse Finite Element Method

By

Adnan Kefal

A thesis presented in fulfilment of the requirements for the degree of

Doctor of Philosophy

Glasgow, UK

January, 2017

Author Statement

This thesis is the result of the author’s original research. It has been composed by the author and has not been previously submitted for examination which has led to the award of a degree.

Signed: Adnan Kefal *Date:* 23 January 2017

Dedicated to

My endless love, beautiful wife, Meltem İnci Kefal,
to whom I dedicate not only my thesis, but also my entire life
and
My son, Çınar Kefal

Acknowledgements

First of all, I would like to express my greatest and deepest gratitude to my supervisor, Dr. Erkan Oterkus, who taught me how to be an effective researcher and showed me how to succeed. I am very thankful to him not only for guiding me throughout my PhD research with passion, humbleness, and kindness, but also for supporting me to make meaningful decisions on my personal issues. Therefore, I am deeply indebted to him for many good things I have in my life today. In addition to being an inspiring supervisor, he has always taken care of me, as I was located in a foreign country, far from family and friends. I consider myself most fortunate for having met Dr. Erkan Oterkus at such a critical moment in my career.

I would like to specially thank Prof. Osman Turan for introducing me to Dr. Erkan Oterkus and inviting me to Glasgow. In addition, I am very grateful to Prof. Atilla Incecik for always being available to me during my PhD studies and serving on my PhD committee. Further, I am truly thankful for the financial support given to me by the University of Strathclyde.

I am very grateful to NASA Langley Research Center in Hampton, VA, USA for hosting me for three months during the final stages of my PhD program. In particular, I would like to express my gratitude to Dr. Alexander Tessler, who is the father of the inverse finite element method (iFEM) that is the state-of-the-art methodology adopted in this PhD thesis. I am very thankful for his support, kindness, and encouragement and for sharing with me his deep knowledge and experience of the iFEM methodology. I will never forget the moments we sat together, deriving iFEM equations on sheets of paper and discussing iFEM in depth. In addition, I will never forget the following words he spoke: "*iFEM integrates and smoothes the strain data.*" Those words made me realize the true meaning of iFEM. I also would like to thank Ms. Jan Spangler for her useful discussions and suggestions regarding the implementation of a user element subroutine in ABAQUS software.

Lastly, I am very grateful to my mother, Nurcan Kefal, and my father, Yavuz Kefal, for their strong belief in my success and their endless love.

Abstract

Structural health monitoring (SHM) is a process aimed at providing accurate and real-time information concerning structural condition and performance. SHM is a very important discipline in the areas of civil, aerospace, and marine engineering because the utilization of SHM allows us to increase both human and environmental safety in conjunction with reduction in direct economic losses. A key component of the SHM process is real-time reconstruction of a structure's three-dimensional displacement and stress fields using a network of in situ strain sensors and measured strains, which is commonly referred to as "shape and stress sensing". The inverse finite element method (iFEM) is a revolutionary shape- and stress-sensing methodology shown to be fast, accurate, and robust for usage as a part of SHM systems. In the present thesis, the general framework of iFEM, i.e., least-squares variational principle, is adopted to develop unconventional and more effective shape- and stress-sensing techniques, with focus on general engineering structures and marine structures in particular. Firstly, the original iFEM formulation for plate and shell structures, developed on the basis of first-order shear deformation theory, is summarized. Then, this formulation is utilized to develop a new four-node quadrilateral inverse-shell element, iQS4, which further extends the practical utility of iFEM for shape sensing of large-scale structures including marine structures. Various numerical examples are presented and it is demonstrated that the iQS4 formulation is robust with respect to the membrane- and shear-locking phenomena. Moreover, the iFEM/iQS4 methodology is applied to various types of marine structures including a stiffened plate, a chemical tanker, and a container ship. To simulate experimentally measured strains and to establish reference displacements, a coupled hydrodynamic and high-fidelity finite element analyses are performed. Utilizing the simulated strain-sensor strains, iFEM analysis of each marine structure is performed. As a result, the optimum locations of the on-board strain sensors are determined for each marine structure. Furthermore, a novel isogeometric Kirchhoff–Love inverse-shell element (iKLS) for more accurate shape-sensing analysis of curved/complex shell structures is presented. The new formulation employs the iFEM as a general framework and the non-uniform rational B-splines (NURBS) as the discretization technology for both structural geometry and displacement domain. Therefore, this new formulation couples the concept of isogeometric analysis with iFEM methodology and creates an innovative "isogeometric iFEM formulation". The superior shape-sensing capability of the isogeometric iFEM formulation (i.e., iKLS) is demonstrated for curved shell structures when using low-fidelity discretizations with few strain sensors. Finally, an improved iFEM formulation for dealing with shape and stress sensing of multilayered composite and sandwich plate/shell structures is described. The present iFEM formulation is based upon the minimization of a weighted-least-squares functional that uses the complete set of strain measures of refined zigzag theory (RZT). A new three-node inverse-shell element, i3-RZT, is developed based on the enhanced iFEM formulation. Various validation and demonstration problems are solved to examine the precision of the iFEM/i3-RZT methodology. The numerical results demonstrate the superior accuracy and robustness of the i3-RZT element for performing accurate shape and stress sensing of complex composite structures. In conclusion, all proposed iFEM frameworks are computationally efficient, accurate, and powerful, hence they can be helpful for shape sensing and SHM of general engineering structures, especially of marine structures.

Contents

List of Figures

List of Tables

Chapter 1

General Introduction

1.1 Introduction

The main aim of this chapter is to describe the background, motivation, and objectives of the research contained in this PhD thesis. The remainder of the chapter is divided into four sections. In the first part (Section 1.2), some basic information about structural health monitoring (SHM) is given. Then, the need of SHM systems for marine structures is discussed in detail. Next, the available methods that can be used as part of SHM systems are briefly described, the limitations of these techniques are highlighted, and the need for further research on SHM systems is explained. Finally, the inverse finite element method (iFEM), which was originally introduced by Tessler and Spangler (2003, 2005) at the National Aeronautics and Space Administration (NASA) Langley Research Center, is described, with the main benefits of using the iFEM methodology emphasized regarding the motivation of the research. In the second part (Section 1.3), the main objectives of this PhD research study are highlighted, while in the third part (Section 1.4), the structure of the thesis is presented. In the last part (Section 1.5), concluding remarks on the information contained in this chapter are given.

1.2 Background and Motivation

Structural health monitoring (SHM) is an interdisciplinary procedure that (1) integrates sensing systems into a structure, (2) processes the data collected from the sensing systems in real time, and (3) provides decisive real-time information from the structure about its global and/or local structural state. The main objective of SHM is to detect unusual structural behaviors to pinpoint failures or an unhealthy structural condition. The exercise of SHM serves to increase human and environmental safety as well as reduce maintenance costs. As a consequence, the installation of an SHM system to an engineering structure is essential for detailed structural management of a structure, including inspection, maintenance, and repair plans (Glisic and Inaudi, 2007).

A catastrophic failure or sinking of ships can result in crucial financial losses, human life losses, and pollution of marine environment. A harsh marine environment together with strong weather conditions is very likely to cause structural damages on ship structures because ships are exposed to long-term cyclic loadings from continuous sea waves as well as short-term extreme loadings such as rogue waves, rainstorms, strong gales, and seaquakes. Moreover, contact between sea water and the material of ships (high-strength steel, in most cases) causes fast corrosion, erosion, and hence thickness reduction. This phenomenon triggers the initiation of damage growth and increases the size of existing damage. Hence, a catastrophic failure of ships might be unavoidable without an appropriate on-site assessment of structural integrity. Furthermore, the number of new vessels is increasing day to day such that new structural designs, construction techniques, and materials are progressively being used in the shipbuilding industry. As a result, it is necessary to increase knowledge about the on-site structural performance not only of traditionally designed ships but also newly designed ships. SHM systems can be a potential solution to prevent the aforementioned serious damage cases; achieve detailed structural management, including inspection and maintenance plans; and allow the marine industry to increase both human and environmental safety as well as reduce maintenance costs.

A key technology of the SHM process is real-time reconstruction of a structure's three-dimensional displacement and stress fields using a network of in situ strain sensors and measured strains, which is commonly referred to as "shape and stress sensing" or "displacement and stress monitoring". A well-suited algorithm for performing shape and stress sensing of a structure should have the following characteristics: (1) it should be general enough to take complex structural topologies and boundary conditions into account; (2) robust, stable, and accurate under a wide range of loading conditions, material systems, and inherent errors in the strain measurements; and finally, (3) sufficiently fast for real-time applications (Gherlone et al., 2012).

Tikhonov and Arsenin (1977) introduced a regularization term that guarantees a confident smoothness degree to solve this inverse problem (shape sensing), and most inverse methods use some type of Tikhonov regularization. For instance, Maniatty et al. (1989) and Maniatty and Zabaras (1989) utilized regularization techniques to solve inverse elastic and elastoviscoplastic problems, respectively. Moreover, Schnur and Zabaras (1990) calculated surface tractions on a body from internal displacements measured at discrete sensor locations. To solve this inverse problem, they minimized the difference between the calculated and measured displacements by employing spatial regularization, which stabilizes the minimization process. Maniatty and Zabaras (1994) also applied the spatial regularization technique in collaboration with a statistical approach discussed by Tarantola (1987). The authors utilized Tarantola's statistical theory to estimate the errors in the solution of an inverse problem. However, this methodology requires iterations and may therefore lead to convergence difficulties and high computational costs, especially for complex three-dimensional structures. Apart from the inverse methods that use some type of Tikhonov regularization, a variety of shape-sensing algorithms have been proposed to solve real-time reconstruction of displacements in beam and/or plate structures subjected to bending loads (e.g., Pisoni et al., 1995; Liu and Lin, 1996; Davis et al., 1996; Jones et al., 1998; Bogert et al., 2003; Kim and Cho, 2004; Ko et al., 2009; Nishio et al., 2010; Chierichetti, 2014). Besides, plenty of researchers have considered hull structural monitoring as an important case study and have thus proposed different types of SHM systems for marine structures (e.g., Kageyama et al., 1998; Wang et al., 2001; Torkildsen et al., 2005; Van der Cammen, 2008; Murawski et al., 2012; Phelps and Morris, 2013). For more information, see Chapter 2.

Most of the inverse methods or SHM systems (i.e., used for marine structures) mentioned in the previous paragraph do not take the complexity of boundary conditions and structural topology into account. They also require satisfactorily precise loading information that is difficult to obtain in real-time conditions outside the laboratory environment. Moreover, some of these methods require material information about the structure. Furthermore, many of these methods are restricted to static loads and linear displacements and cannot be adapted to dynamic loads and nonlinear displacements, as a consequence of their inherent assumptions. Finally, most of these inverse methods are not fast enough for real-time applications of a viable SHM system due to their time-consuming analysis. Hence, they are not generally suited for use in on-board SHM algorithms.

In addition, none of the existing hull structural monitoring systems recommended by class societies and researchers (vid. Chapter 2) can be used to monitor three-dimensional full-field displacements and stresses of a marine vessel. In fact, these current SHM systems only monitor several points on the structure such as two points on the weather deck amidships. The questions which remain unanswered are how much reliable information these SHM systems provide to the master/operator of the ship, in terms of the ships' global structural health, and if any alternative solutions exist. These questions can be answered as follows: (1) as a result of the complex structural topology of marine structures and the dynamic loads of waves and winds, due to the complexity and statistical features of oceanographic phenomena, global structural health monitoring of a marine structure may be far more challenging than the monitoring offered by the existing hull structural monitoring systems, and (2) the possible solution to this challenge may be achieved by an SHM algorithm that can provide real-time monitoring of the three-dimensional full-field displacements and stresses of a marine structure.

The inverse finite element method (iFEM) is a state-of-the-art methodology originally introduced by Tessler and Spangler (2003, 2005) for real-time reconstruction of three-dimensional full-field structural displacements, strains, and stresses of structures that are instrumented by strain sensors. The general mathematical concept of the iFEM methodology uses a least-squares variational principle that minimizes the sum of squared errors between the analytical and experimental values of strain measures. It is worth noting that this variational formulation allows the entire structural geometry to be discretized by suitable inverse finite elements (e.g., beam, frame, plate, shell and solid elements) in which measured strains can be adapted to element strains in the least-squares sense.

Tessler and Spangler (2003, 2005) developed the mathematical concept mentioned above for shape sensing of plate and shell structures. The formulation was based on minimization of a least-squares functional that uses the complete set of strain measures of first-order shear deformation theory (FSDT), including the membrane strain measures, bending curvatures, and transverse-shear strain measures. Remarkably, the minimization process results in a system of linear algebraic equations which can be solved to determine unknown displacements at any real time. Once the structural deformed shape is reconstructed, the full-field strains can be calculated by utilizing the displacements. Then, the three-dimensional stress state of the structure can be evaluated from the structure's full-field strains and material properties. Finally, the three-dimensional stresses can be adapted to an equivalent stress by means of an appropriate failure criterion (e.g., von Mises yield criterion), which can enable real-time damage predictions.

Unlike the other inverse methods, the iFEM methodology possesses the aforementioned characteristics (i.e., described in the third paragraph) required for a powerful SHM algorithm. For example, the main advantage of the iFEM algorithm is that the static and dynamic behavior of any structure can be obtained without prior knowledge of its loading or material, since only the strain-displacement relationship is used in the formulation (Gherlone et al., 2012). Moreover, the iFEM methodology has general applicability to any type of structural topology and boundary condition because using inverse beam, frame, plate, shell, and solid finite elements can enable an effective discretization of the physical domain. Furthermore, Gherlone et al. (2014) demonstrated that the iFEM framework is precise, powerful, and sufficiently fast for real-time applications. Recently, a U.S. patent (US 8,515,675 B2) was obtained for a system that performs shape sensing of a downhole structure using the iFEM methodology (Stoesz, 2013). All of these beneficial aspects of the iFEM methodology motivate this research study, with the aim to broaden the horizons of the iFEM technology for SHM of general engineering structures and marine structures in particular.

1.3 Objectives of the Research

The research described in this thesis has four main objectives:

1. Development of a novel four-node quadrilateral inverse-shell element (iQS4) based on iFEM methodology that uses a weighted-least-squares functional. This new element is developed using the kinematic assumptions of FSDT; thus, its application ranges from thin to moderately thick shell structures. Moreover, the iQS4 element possesses six degrees of freedom (DOF) at each node, including a hierarchical drilling rotation DOF such that shape-sensing analysis of large-scale structures (i.e., marine structures) can be performed simply based on the iFEM/iQS4 methodology. To the best of the author's knowledge, there is currently no study available in the literature concerning a four-node inverse-shell element that provides a detailed investigation and description of the mathematical formulation. This goal is achieved in Kefal, Oterkus, et al. (2016) as part of the research described in this thesis (Chapter 3).
2. Creation of iQS4 models to investigate displacement and stress monitoring of marine structures based on iFEM methodology. As explained in the previous objective, the iQS4 element is practically useful for large-scale structures; therefore, this framework is used as starting point for the application of iFEM to marine structures described in Chapter 4. To the best of the author's knowledge, this is the first attempt to apply iFEM methodology to shape and stress sensing of marine structures. The results of this study have been published in Kefal and Oterkus (2015, 2016a, 2016b).
3. Development of an isogeometric Kirchhoff–Love inverse-shell element (iKLS) for shape-sensing analysis of curved/complex shell structures (Chapter 5). The iKLS element formulation is based on a weighted-least-squares functional that is discretized using high-order continuous $(C^p, p > 0)$ non-uniform rational B-splines (NURBS); thus, the formulation couples the concept of isogeometric analysis (Hughes et al., 2005) with iFEM methodology and creates an innovative "isogeometric iFEM formulation". The overall strategy presented in Chapter 5 is

an extended and improved version of the study published in Kefal and Oterkus (2017), and to the best of the author's knowledge, this is the first time that an isogeometric iFEM formulation has become available in the literature.

4. Development of (1) an enhanced iFEM formulation and (2) a three-node inverse-shell element dealing with shape and stress sensing of multilayered composite and sandwich plate/shell structures possessing a high degree of anisotropy and heterogeneity (Chapter 6). The improved iFEM formulation is based upon a weighted-least-squares functional that uses a complete set of strain measures of refined zigzag theory or RZT (Tessler et al., 2009, 2010). These strain measures includes membrane, bending, zigzag, and full transverse-shear strain measures. To the best of the author's knowledge, no iFEM formulation takes into account all strain measures of the RZT and implements an inverse-shell element (i.e., i3-RZT) for shape and stress sensing of composite shell structures. These goals are accomplished in Kefal, Tessler, et al. (2016) as part of the research described in this thesis (Chapter 6).

In conclusion, the ultimate goal of this research is to produce unconventional and more effective iFEM frameworks that can be helpful in SHM of general engineering structures and marine structures in particular.

1.4 Structure of the Thesis

This thesis is constituted by the following seven chapters:

- Chapter 1. This chapter provides basic information about SHM, its impact on marine structures, the current approaches (e.g., inverse methods, hull structural monitoring systems) used by researchers to perform shape sensing analysis as a part of SHM systems, and the limitations of the approaches which justify the need for further research in this field. In this manner, the benefits of iFEM methodology (i.e., the state-of-the-art methodology used in this thesis) are highlighted, and then the objectives of research and the organization of this thesis are described.
- Chapter 2. This chapter provides a historical overview and the advantages and limitations of the most popular numerical techniques used up to now to solve the shape-sensing problem of beam and plate structures. Moreover, detailed background information (including class societies' recommendations) about the

current hull structural monitoring systems used on-board ship structures are investigated in this chapter. Furthermore, the limitations of these techniques are used to justify the iFEM methodology. Finally, numerical and experimental studies performed using the iFEM methodology are discussed in detail and the current research is put into perspective.

- Chapter 3. This chapter presents the novel iQS4/iFEM methodology, which is an inverse-shell element formulation suitable for shape and stress sensing of thin and moderately thick plate/shell structures. As a final remark in this chapter, the practical applicability of the iQS4/iFEM methodology for more complex structures is demonstrated by performing various case studies, including a study in which the strain measurements involve up to ten percent random noise.
- Chapter 4. This chapter describes the feasibility and applicability of the iFEM methodology for displacement and stress monitoring of marine structures by performing various iFEM analyses of typical marine structures that are modelled with the iQS4 element (presented in Chapter 3). As a result of the iFEM analysis of these structures, the optimum locations of the on-board strain sensors are determined and clearly demonstrated using various iQS4 models.
- Chapter 5. This chapter presents a novel isogeometric iFEM methodology which couples the NURBS-based isogeometric analysis with the iFEM methodology. For this purpose, the mathematical formulation of the iKLS element, which is a rotation-free inverse-shell element suitable for shape sensing of complex/curved thin shell structures, is developed and presented in this chapter. As a final remark in this chapter, the superior capabilities of the iKLS element are demonstrated by various curved shell problems, including a Scordelis–Lo roof, a pinched hemisphere, and a partly clamped hyperbolic paraboloid.
- Chapter 6. This chapter describes an improved RZT-based iFEM formulation for performing accurate shape and stress sensing analysis of multilayered composite and sandwich plates or flat shells. Additionally, this chapter presents the mathematical formulation of the new i3-RZT element, which is applicable to thin and moderately thick composite/sandwich shell structures and developed based on the presented iFEM methodology. As a concluding remark of this chapter, the theoretical foundation of the current formulation is quantitatively assessed, and the

predictive capabilities of the i3-RZT element are demonstrated by analyzing two benchmark problems: (1) laminates with different laminate stacking sequences (i.e., uniaxial, cross-ply, and angle-ply) and (2) a wedge structure with a hole near one of the clamped ends.

- Chapter 7. This chapter reviews the research objectives, summarizes the major findings, highlights the novelty and contribution of this research study to the field, discusses the gaps and the recommended future work, and closes with final remarks.

1.5 Conclusion

Vessels are operated under challenging conditions because the marine environment can cause structural failure due to extreme or cyclic loadings, corrosion, and erosion. Structural failure may lead to major accidents that may result in crew or passenger life loses, pollution of the marine environment, and very expensive maintenance/repair costs. Structural health monitoring (SHM) is a multidisciplinary technology area that addresses these problems through providing reliable real-time information from a structure about its global or local structural condition by integrating sensing systems into the structure. A fundamental technology for the SHM procedure is dynamic tracking of a structure's three-dimensional displacement and stress fields utilizing a network of in situ strain sensors and measured strains, generally known as shape and stress sensing. Many different inverse algorithms have been proposed for shape and stress sensing, and researchers and industry have developed various types of hull structural monitoring systems. However, SHM of marine structures is more complicated than the capabilities proposed by those inverse algorithms and monitoring systems can account for, as a result of their inherent limitations; further research in this field is therefore needed. The inverse finite element method (iFEM) is a revolutionary technology that possesses all necessary features required for a robust shape and stress sensing algorithm and can be utilized as a part of SHM systems. In this research study, the iFEM methodology is therefore used to overcome the major shortcomings of the currently available approaches and systems. This thesis is constituted of seven chapters. The four objectives of this research study are (1) the development of a robust four-node inverse-shell element for shape sensing of large-scale structures, (2) application of the iFEM methodology to SHM of marine structures, (3) creation of a novel isogeometric inverse-shell element for shape sensing of complex/curved shell structures, and (4) development of an RZT-based inverse-shell element for shape sensing of multilayered composite and sandwich plates/shells. The ultimate goal is to produce original and superior iFEM frameworks that can be used as guidelines for SHM of general engineering structures and marine structures in particular.

Chapter 2

Literature Review

2.1 Introduction

The scope of this chapter is to summarize the literature review undertaken to realize this work. As mentioned earlier in Chapter 1, the main focus of this research study is to introduce novel iFEM frameworks that can be useful for SHM of marine structures. The main motivations of this work are threefold: (1) the limitations of the currently available numerical methods used for shape sensing, (2) the shortcomings of the available SHM systems for marine structures, and (3) the beneficial aspects of the iFEM methodology, which make the iFEM a robust shape-sensing algorithm. Therefore, in the remainder of this chapter, (1) an extensive historical overview of the most popular numerical methods (inverse algorithms) proposed for shape sensing is provided in Section 2.2, (2) the literature concerning SHM systems of marine structures is reviewed in Section 2.3, and (3) all of the numerical and experimental studies developed based on the iFEM methodology are historically investigated in Section 2.4. In particular, the advantages and disadvantages of each study being reviewed are highlighted. Moreover, the historical connections among these studies are established and emphasized in the following sections. Finally, the concluding remarks of this chapter are provided in Section 2.5.

2.2 Numerical Methods for Shape Sensing

Shape and stress sensing is the fundamental technology of the SHM process. Many shape-sensing studies have been performed to solve the bending problem of a beam. To begin, Pisoni et al. (1995) developed a modal approach for the real-time reconstruction of the structurally deformed shape of a vibrating body. They used vibration mode shapes of the body and experimental strain measurements (e.g., strain gauge readings) to construct the displacement-strain relationship. In other words, the displacement field was expressed in terms of displacement and strain mode shapes as well as experimental strain signals. They verified the effectiveness of the proposed modal methodology for a clamped end beam using just two strain gauges. Similar modal-based approaches were employed for shape sensing of beam structures in a series of works conducted by Li and Ulsoy (1999), Kang et al. (2007), and Kim et al. (2011).

In particular, Li and Ulsoy (1999) analytically calculated the mode shapes of a cantilever beam and subsequently used them together with strain gauge measurements to obtain high-precision vibration measurements of the beam. Besides, Kang et al. (2007) reconstructed the response of a clamped end beam, which was subjected to dynamic excitation, from strain signals obtained from FBG strain sensors. Similarly, Kim et al. (2011) presented shape estimation of rotating beam structures, e.g., helicopter rotors and wind turbines, using the modal approach and FBG sensors. Both Kang et al. (2007) and Kim et al. (2011) performed a priori FEM analysis to establish the displacement and strain mode shapes for constructing a displacement-strain transformation matrix. The main disadvantage of using these modal approaches is that the number of estimated mode shapes is only restricted to the number of strain sensors placed on the beam, requiring more sensors to estimate the vibration or deformed shapes at higher frequency excitation (Kang et al., 2007).

In addition, Liu and Lin (1996) reconstructed the flexural rigidity of a beam by minimizing the error norm of equilibrium equations derived from a finite element formulation of the beam. They expressed the equilibrium equations in terms of the longitudinal strains of the beam elements; consequently, the element strains measured in the structural tests simply identified the element properties. However, their approach requires cumbersome modifications in the final equations to avoid singular solutions, showing that the complex boundary conditions may create an ill-posed problem.

Moreover, Davis et al. (1996) regenerated a simple static-beam response from a set of discrete strain data obtained from a fiber Bragg grating (FBG) strain sensor. For this purpose, they used optimized trial functions that satisfy the essential boundary conditions of the beam, i.e., zero rotation and displacement at the clamped end. Moreover, they employed weighting factors for each of the trial strain functions, which permit a linear combination of weighted trial functions to match the measured strain. However, their approach requires many trial functions and strain sensors when more complicated deformations are predicted.

Besides, Todd and Vohra (1999) fitted experimentally measured strains into an a priori set of global and piece-wise continuous basis functions and proper weights. Then, they evaluated the displacement field of the beam by utilizing strain-displacement relationships. In contrast to Davis et al. (1996), who used classical beam theory, they showed how shear effects can be incorporated with the reconstruction of transverse displacements without requiring an independent measure of the shear strain.

Furthermore, based on classical beam theory, Kim and Cho (2004) and Ko et al. (2009) integrated discretely measured strains to calculate the continuous beam deflection. Kim and Cho (2004) performed regression analysis on experimental strain data to obtain a continuous strain curvature function that leads to an evaluation of a beam’s deformed shape. Ko et al. (2009) computed the deflection and cross-section twist of an aircraft wing using a load-independent method that approximates the beam curvature with piece-wise polynomials. Kim and Cho (2004) used FBG strain sensors to collect the experimental/actual strain data, whereas Ko et al. (2009) performed high-fidelity FEM analysis of the wing to simulate strain sensors. Then, Derkevorkian et al. (2013) experimentally investigated the accuracy of the shape-estimation methodology proposed by Ko et al. (2009) through an experimental setup with an aluminum wing-like swept-plate model. The authors also presented a comparison study between Ko et al.’s methodology and the classical modal-based estimation approach that uses the structure’s mode shapes structure to transform the measured strains into displacements. The advantages and disadvantages of each method were discussed well in this comparison study.

Recently, Glaser et al. (2012) performed shape sensing of a beam using a method based upon a spline technique in which spline coefficients are estimated using continuity conditions, boundary conditions, and measured curvature estimates. They defined the kinematics of the beam model based on Euler–Bernoulli beam hypotheses and estimated the measured curvatures from strain readings of strain gauges. However, the applicability of their method was only shown for a simply supported beam setup.

More recently, Chierichetti (2014) developed an iterative approach named the load confluence algorithm (LCA) to reconstruct the load and response of a complete structure based on modal decomposition of the structure's finite element model. For this purpose, the algorithm is capable of utilizing different types of experimental measurements such as strains, displacements, velocities, and accelerations in the formulation. Based on the LCA algorithm, the author reconstructed the dynamic response of two beams connected with a nonlinear spring using the experimental measurements obtained from several locations. However, the LCA method requires a numerical estimation of a loading case that corresponds to equivalent external loads applied to the system before the regeneration of the displacement field.

In addition to the studies concerning the shape sensing of beam-type structures, several authors have considered the real-time monitoring of plate structures. For instance, apart from Pisoni et al. (1995), Foss and Haugse (1995) also studied a modal method which employs the deformation and strain mode shapes of a plate together with the measured surface strains to regenerate the deformed shape of the plate. Foss and Haugse (1995) experimentally calculated the mode shapes of the plate using strain gauges and accelerometers. Although this computation may be time consuming, it has the advantage of not requiring any knowledge of material properties. Moreover, Bogert et al. (2003) and Rapp et al. (2009) adopted a modal-based inverse algorithm for shape sensing of a cantilever plate. Bogert et al. (2003) used strain rosettes to obtain the measured surface strains, whereas Rapp et al. (2009) used a plate specimen instrumented with FBG sensors. Both authors generated vibration mode shapes of the plate through high-fidelity FEM analysis. Although the numerically and experimentally obtained results of their plate specimens agree well, this approach requires the use of a large number of natural vibration modes. Therefore, a computationally expensive eigenvalue analysis must be performed, especially if the method is implemented using a high-fidelity mesh.

Additionally, Jones et al. (1998) used a least-squares formulation to solve the shape-sensing problem of a cantilever honeycomb plate under arbitrary loading conditions. According to Kirchhoff plate hypotheses, the FBG-measured strains were fitted with a cubic polynomial and integrated with the use of approximate boundary conditions at the clamped end. They compared the least-squares estimates of displacement magnitudes with those of FEM analysis. Additionally, they experimentally verified the accuracy of the proposed formulation in single-point loading tests. However, their formulation is not general enough for complex geometries due to the inherent assumptions made for a simple cantilever plate.

Also, Shkarayev et al. (2001, 2002) proposed a two-step solution procedure for shape sensing of aerospace structures. The first step involves finite element analysis of the structure to calculate strains for possible load cases. Then, an inverse interpolation algorithm is applied that constructs a parametric approximation (i.e., using spatial distribution functions) of the loading through least-squares minimization of calculated and measured strains. Once the load approximation is accurately defined, the methodology leads to the solution of the displacements. The main drawback of the proposed formulation is that it requires the recovery of the applied loading, which may have a non-trivial physical topology in real environment.

Furthermore, Nishio et al. (2010) proposed a shape-reconstruction algorithm using an FEM model of a target structure. The algorithm enforces the compatibility between the analytical and measured bending curvatures of the Kirchhoff plate theory in a weighted-least-squares sense. Using the proposed algorithm, the authors reconstructed the deflection of a composite cantilever plate specimen in which Brillouin-scattering-based optical fiber sensors were embedded. However, it is difficult to generalize their approach, since the weighting coefficients in the least-square terms are computed to resolve inherent errors in the strain-sensor data by considering the given data-acquisition tool, the load condition, and the test specimen. Besides, their method can only be applied to thin plates, since it uses classical bending assumptions to define the strain-displacement relationships.

2.3 SHM Systems for Marine Structures

Different monitoring schemes have been used on different types of marine vessels for many years. In 1994, the International Maritime Organization (IMO) originally recommended the utilization of hull stress monitoring systems to facilitate the safe operation of ships. The requirements for a typical hull structural monitoring system are regulated by class societies including the American Bureau of Shipping (1995, 2015), Det Norske Veritas (1997, 2011), and Lloyds Register (2004). These regulations provide a general guide that discusses the need for fitting of hull condition monitoring systems (e.g., motion monitoring, stress monitoring, and voyage data recording) on all types and sizes of merchant vessels. Moreover, they clearly specify the critical elements of these monitoring systems, i.e., the configuration and types of sensors to be used as well as measurement accuracy, data storage, and data analysis. However, these guidelines only provide a global outline on how data processing should take place, and there has been little change in this basic configuration ever since the IMO originally introduced its requirements in 1994.

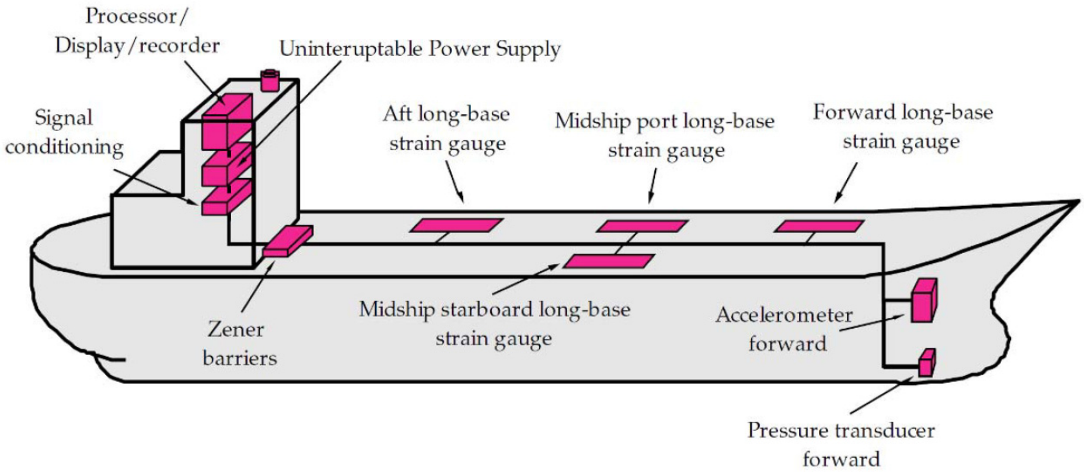

Figure 2.1 Typical hull structure monitoring system configuration for bulk carrier or tanker (Lloyds Register, 2004).

To monitor global longitudinal stresses amidships, Det Norske Veritas (1997, 2011) requires that the hull condition monitoring system of any merchant ship consist of at least two strain gauges amidships (one port, one starboard on deck), a data processor, and a graphical user interface on the bridge. For bulk carriers or tankers, Lloyds Register (2004) proposed a more typical configuration with four long-base strain gauges as depicted in Figure 2.1. These long-base strain gauges are installed on top of the main deck amidships (port and starboard) and at the quarter lengths of vessels to monitor hull girder stress (one side only). The American Bureau of Shipping (1995, 2015) also recommended a hull structural monitoring system similar to this configuration for tankers, bulk carriers, and general cargo ships. Assuming that the hull girder is a simple beam and using Hooke's Law, these strain measurements can be converted to vertical and horizontal bending and torsional stresses of the hull girder for a given sea state. Then, this information can be utilized to infer the fatigue life of the ship.

Apart from the regulations of class societies and the IMO, many researchers consider hull structural monitoring an important area of study. Kageyama et al. (1998) developed a fiber-optic laser-Doppler velocimeter (LDV) as a displacement sensor to measure the global deformations of marine structures. They conducted two laboratory tests to demonstrate that the LDV sensor has potential advantages, such as unlimited gage length, applicability to dynamic measurement, and lessened effects of temperature. To estimate the fatigue life and residual strength of the ship's structure, they proposed installing the LDV sensor together with an optical time-domain reflectometer in primary members or highly stressed regions of the structure. Torkildsen et al. (2005) provided an outline of a ship hull health monitoring system installed on the Royal Norwegian Navy (i.e., a navy vessel). Its existing SHM system consists of a network of fiber-optic sensors to measure strain and temperature, X-band wave radar to estimate wave height and direction measurements, and a microwave altimeter mounted to the bow to measure oncoming wave profiles. The authors utilized FEM analysis of the ship hull to identify optimum locations for the fiber-optic sensors. Once their SHM system is installed on-board, it provides real-time information on both the global wave load on the hull and the local load at a number of selected critical areas.

Wang et al. (2001) used FBG sensors to increase the precision of obtained strain data during the SHM process of marine structures. They utilized beneficial features of FBG sensors for ship hull monitoring, e.g., their small size and weight, extended stability, reliability, high resistance to corrosion, and insensitivity to the outside environment such as to electromagnetic fields and noise interference. Moreover, Murawski et al. (2012) performed a damage-detection experiment an on offshore platform leg model using FBG sensors and investigated the mechanical strain changes due to dynamic loadings. In this study, the scheme of a SHM system with five FBG sensors was also demonstrated on sailing ships. Dynamic characterizations of the mast were investigated for different states of sailing conditions by utilizing the measurements obtained from FBG sensors. Similarly, Majewska et al. (2014) presented an experimental approach for SHM of sailing ships by using FBG sensors. They installed an FBG sensor grid to the foremast of a sailing ship to determine the strain/stress level of the foremast during different ship operations.

Andersson et al. (2011) proposed a hull condition monitoring system for damage monitoring of ships made of fiber-reinforced plastics. Their technique uses acoustic vibrations that exist in the hull structure and on-board sensor data as input. When a sensor is close to a damaged part of the hull, specific indications will be detected by the damage indication algorithm. In addition, Sielski (2012) experimentally monitored fatigue crack initiation and the propagation of aluminum ship structures using a ship structural reliability program that included a SHM tool. Their global method requires modal analysis, and the local method is dependent on the relation between lamb wave propagation and sensor diagnostics. In this study, the authors proposed that SHM could be improved by (1) developing more accurate fatigue and fracture models, (2) improving the model in terms of corrosion detection, and (3) installing sensors to continuously detect damage.

Van der Cammen (2008) developed a model to calculate the fatigue life of structural members in the side-shell, deck, and bottom of a floating production storage and offloading unit (FPSO). The proposed model derives load accumulation data from specified locations of the structure using recorded sensor data and data processing techniques, i.e., time-domain methods, wave spectrum methods, and statistical response evaluation. The model was validated against full-scale experimental measurements and can assist practical SHM systems in assessing motions and extreme events such as slamming stress and fatigue. Similarly, Hageman et al. (2013)

developed a hull fatigue monitoring system for FPSO vessels. They developed their fatigue prediction technique based on Bayesian statistics. Their system predicts the fatigue consumption from environmental conditions and experimentally measured strains, and then compares the predicted fatigue consumption with the design fatigue consumption to make conclusions on the hull structure's performance. On the other hand, Zhu and Frangopol (2013) used SHM data obtained from sensors to improve the accuracy and redundancy of reliability assessments of a ship's cross-sections. Prior load effects are updated according to SHM data related to the wave-induced load using the Bayesian updating method. The authors concluded that integration of SHM data can considerably decrease the uncertainty in a distribution parameter, and hence, updated performance indicators come closer to the correct values.

Phelps and Morris (2013) provided an extensive review of the technical and commercial aspects of available hull structural monitoring systems along with consideration of the differences between installations on navy ships as compared to on merchant ships. Moreover, Van der Horst et al. (2013) proposed a recent technique based on wireless monitoring as an application of SHM for marine structures. Van der Horst and co-workers indicated that implementing networks of wireless sensors can effectively enable the detection of fatigue cracks in a structure, although it has some disadvantages, such as a lack of robust connectivity and inadequate data rates. They concluded that the conventional methods for detecting cracks and recent techniques for monitoring crack propagation can be combined together to increase the sensitivity and efficiency of the SHM process. Furthermore, Nichols et al. (2014) described the structured decision making (SDM) process for using available information (loading data, model output, etc.) and producing a plan of action for maintaining the structure. Their example shows that SDM minimizes both transit time and the probability of failure through a user-defined cost function. However, developing this approach requires models that describe the loading data, predict the structural response to the load, and forecast the accumulated damage.

2.4 Historical Overview of Inverse Finite Element Method

Unlike the other inverse methods, the iFEM methodology possesses the following beneficial features that justify the iFEM as a superior shape-sensing algorithm:

- The iFEM methodology does not require any loading and/or material information to reconstruct the three-dimensional displacement field of the structure.
- The iFEM formulation does not require the entire structure to be installed with strain sensors to monitor the entire structural displacements. Only few locations need to be instrumented with any type of strain sensors such as strain rosettes, strain gauges, fiber optic cables.
- The iFEM methodology is free from complex structural geometry and/or boundary conditions.
- The iFEM algorithm can provide robust, stable, and accurate displacement results even with the strain measurements have inherent errors (e.g., noise).
- The iFEM framework is sufficiently fast for real-time monitoring applications.

Since the first publication of the iFEM algorithm (Tessler and Spangler, 2003, 2005), many different numerical and experimental studies have been devoted to expanding the horizons of the iFEM methodology in the literature. Tessler and Spangler (2004) developed a three-node inverse shell element (iMIN3) utilizing lowest-order anisoparametric C^0 continuous shape functions and adopting the kinematic assumptions of FSDT plate theory. Tessler and Spangler (2004) initially assessed the predictive capability of the iMIN3 element on numerically generated strain data. Then, Quach et al. (2005) and Vazquez et al. (2005) demonstrated the robustness of the iMIN3 element by conducting laboratory tests using experimentally measured real-time strain data. Apart from iMIN3, to the best of the author's knowledge, no inverse-shell element currently exists for the shape sensing of plate and shell structures. The first four-node quadrilateral inverse-shell element, iQS4, was published by Kefal, Oterkus, et al. (2016) as part of the research described in this thesis (vid. Chapter 3).

Moreover, Paczkowski and Riggs (2007) utilized iFEM methodology to deal with large displacements and nonlinear strains. They used a similar least-squares error functional as the one used in the original iFEM formulation by Tessler and Spangler (2003, 2005) but replaced linear strains with Green–Lagrange strains and adopted a "total Lagrangian" formulation. Based on the proposed nonlinear iFEM formulation, two inverse elements were developed: (1) a two-node inverse-beam element using exact shape functions of Euler–Bernoulli beam theory and (2) a six-node inverse-plane element using isoparametric shape functions. The performance of these elements was tested for a cantilever beam subjected to large displacement, and the results indicated that the inverse-plane element was more encouraging than the inverse-beam element for practical applications.

Furthermore, Cerracchio et al. (2010) and Gherlone et al. (2012) formulated a robust inverse-frame element that uses the kinematic assumptions of Timoshenko beam theory, including stretching, bending, transverse-shear, and torsion-deformation modes. Their iFEM applications are tailored toward one-dimensional structures such as trusses, beams, and frames. In a series of works presented by Gherlone et al. (2011a, 2011b, 2012, 2014), the superior capability of the authors' inverse-frame element was validated using both numerically generated and experimentally measured strain data, with several shape-sensing analyses performed of three-dimensional frame structures undergoing static and/or damped harmonic excitations.

In addition, Tessler et al. (2011, 2012) revised the least-squares functional of the original iFEM formulation by introducing weighting coefficients for individual section strains of the iMIN3 element. These weighting constants enable an iMIN3 discretization to have very sparse measured strain data, such that only few structural components need to be instrumented with FBG sensors providing either single-core (axial) or rosette (tri-axial) strain measurements. In particular, Tessler et al. (2012) performed linear and nonlinear shape- and stress-sensing analyses of an aluminum stiffened flap with two rectangular cut-outs using an iMIN3 discretization with different networks of strain sensors. To predict the nonlinear deformations in real time, the iMIN3 mesh was updated using the deformations calculated at each small strain increment. This study demonstrated the superior capability and practical usefulness of the iMIN3 element for shape and stress sensing of plate and shell structures undergoing small and/or large displacements.

De Mooij et al. (2016) utilized the mathematical concepts of the iFEM methodology to formulate a new inverse algorithm for shape sensing of structures that are instrumented with strain and/or displacement sensors. Their formulations incorporate the Tikhonov regularization terms to obtain smoother results. The proposed inverse algorithm was tested and validated using two cantilever plate problems that were analyzed earlier by Kefal, Oterkus, et al. (2016). The numerical results of these examples demonstrated that their inverse algorithm was capable of predicting accurate displacements even when using fewer displacement/strain sensors.

In a series of works (Tessle, 2007; Tessler et al., 2011, 2012), the possible applications of the iFEM methodology were discussed for SHM of future aerospace vehicles. Likewise, Cerracchio et al. (2015a) presented another application of the iFEM algorithm in aerospace structures by performing real-time displacement monitoring of a typical stiffened composite panel subjected to mechanical and thermal loads. However, none of the aforementioned iFEM frameworks have been applied to shape and stress sensing of marine structures. Kefal and Oterkus (2015, 2016a, 2016b) achieved this goal for the first time in the literature, as part of the research described in this thesis (vid. Chapter 4).

To numerically solve a number of engineering problems, Hughes et al. (2005) introduced isogeometric analysis (IGA), which employs the same functions, i.e., non-uniform rational B-splines (NURBS), used to describe the geometry of the computational domain in the analysis framework. Since then, IGA has received a great deal of attention from both academia and industry as a result of its beneficial features: (1) exact representation of computational geometry, (2) simplified mesh refinement, (3) smooth (high order continuity) basis functions, and finally (4) integration of design and analysis in only one computational geometry. To the best of the author’s knowledge, none of the iFEM formulations offer these kinds of beneficial aspects, which can be very important for shape-sensing analysis of engineering structures, especially for curved shell structures. In order to utilize the aforementioned features of IGA in shape-sensing analysis, Kefal and Oterkus (2017) coupled the concept of IGA with iFEM methodology to introduce the first isogeometric iFEM formulation, which is the fundamental part of the research described in Chapter 5.

For structural analysis of composite and sandwich structures, Tessler et al. (2009, 2010) developed the refined zigzag theory (RZT) that allows more accurate predictions of displacement, strain, and stress variations at anywhere in the structure, especially through-the-thickness direction of the structure. Recently, Cerracchio et al. (2013, 2015b) improved the original iFEM formulation (Tessler and Spangler, 2003, 2005) by including the zigzag kinematics of the RZT. This recent formulation was intended for SHM applications dealing with multilayered composite and sandwich structures possessing a high degree of anisotropy and heterogeneity. However, their formulation lacks precise definition of transverse-shear strain measures in the variational principle. Moreover, to the best of the author's knowledge, no inverse-shell element has been implemented based on the RZT. To overcome these limitations, Kefal, Tessler, et al. (2016) improved the RZT-based iFEM formulation and then developed the first three-node triangular inverse-shell element, i3-RZT, based on RZT, which are the main parts of the study described in Chapter 6.

2.5 Conclusion

In this chapter, a detailed literature review, which enables historical interpretation of the subjects undertaken in this PhD research study, was provided. Firstly, the advantages and limitations of the most popular numerical techniques used up to now to investigate the shape sensing of beams and plates were examined. After that, the details of the SHM monitoring systems proposed for marine structures were studied. The use of the current approach (i.e., iFEM methodology) was justified in light of its superior capabilities concerning shape-sensing analysis. In order to put the current research into perspective, finally, a historical outline of the shape-sensing algorithms that utilize the iFEM methodology was provided. The following list summarizes the findings that are most relevant to this research. To the best of the author's knowledge, (1) none of the iFEM formulations has been implemented using a four-node inverse-shell element with drilling degrees of freedom (DOF), (2) none of the iFEM formulations have been applied to marine structures, (3) none of the iFEM formulations have served the beneficial features of IGA for shape-sensing analysis, and (4) no inverse-shell element has been implemented based on an iFEM formulation that utilizes the complete set of strain measures consistent with RZT.

Chapter 3

Quadrilateral Inverse-Shell Element with Drilling DOF

3.1 Introduction

As explained earlier in Section 2.3, various types of iFEM formulations and inverse elements have been developed on the basis of different beam, plate, and shell theories. The main and novel aim of this chapter is to introduce the reader to the iFEM formulation for plate and flat shell structures, and develop a new four-node quadrilateral inverse-shell element, iQS4, which expands the library of existing iFEM-based inverse elements. This new element includes hierarchical drilling rotation DOF and further extends the practical usefulness of iFEM methodology for shape and stress sensing analysis of large-scale structures, e.g., marine structures. In this chapter, the iFEM/iQS4 formulation is derived from a weighted-least-squares functional that uses FSDT as its kinematic framework. Therefore, iFEM/iQS4 methodology is applicable for the analysis of thin and moderately thick plate and shell structures. This chapter is organized as follows: the iFEM formulation for plate and flat shell structures are given in Section 3.2. Mathematical structure of the iQS4 element is described in Section 3.3. In Section 3.4, two validation problems are solved and discussed in detail. In addition, the practical applicability of the iQS4 element to more complex structures is examined by performing various case studies including a study where strain measurements involve up to ten percent random noise. Finally, concluding remarks of this chapter can be found in Section 3.5. The overall study described in this chapter can be found in Kefal, Oterkus, et al. (2016), and to the best of the authors' knowledge, this is first time that the iFEM formulation is implemented using a four-node inverse-shell element. As previously mentioned, the practical capability of the iQS4 element is very promising, therefore the iQS4/iFEM framework presented in this chapter is used as a foundation for shape and stress sensing analysis of large-scale marine structures that are described in the next chapter.

3.2 The iFEM Formulation for Plate and Flat Shell Structures

Reissner (1945) and Mindlin (1951) developed the first-order shear deformation theory, which introduces an additional kinematic variable (i.e., the bending rotation) to account for transverse-shear deformation in an average sense while retaining the non-deformable normal assumption. The main benefits of the FSDT are that (1) it is applicable for the analysis of thin and moderately thick plate and shell structures, and (2) its kinematics have variational index of 1, thus require only C^0-continuous displacement interpolations that can be readily established with conventional Lagrange shape functions. As a result of these beneficial aspects, the FSDT have been widely used in structural analysis of homogeneous and composite plate- and shell-type structures. In fact, the original iFEM formulation (Tessler and Spangler, 2003, 2005) also used the kinematics of the FSDT, which is adopted to develop the iQS4 element and revisited in the remainder of this section. Firstly, the inverse problem of the plate is described in Section 3.2.1. Secondly, the kinematics relations of FSDT are briefly reviewed and the strain field is properly rewritten in order to define the strain measures to be used in the iFEM formulation (Section 3.2.2). Thirdly, the computation of the experimental section strains is extensively studied in Section 3.2.3. Finally, the weighted-least-squares functional of the iFEM formulation is discussed in Section 3.2.4.

3.2.1 The inverse problem

Consider an arbitrary plate of uniform thickness $2h$ as depicted in Figure 3.1. The material points of the plate are located by the orthogonal Cartesian coordinates (x_1, x_2, z). The symbol $z \in [-h, +h]$ defines the thickness coordinate of the plate, the plane located at $z = 0$ referred to as the mid-plane of the plate, and the in-plane coordinates are identified by $(x_1, x_2) \in A$ where A represents the area of the mid-plane. The plate is restrained against rigid body motion and also subjected to external forces that may include the in-plane and out-of-plane components, T and q, as shown in Figure 3.1.

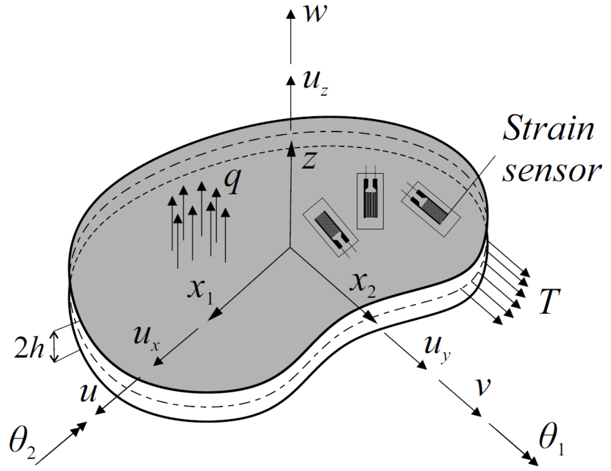

Figure 3.1 Notation for the plate or flat shell body.

Strain sensors are mounted on the surface of plate as depicted in Figure 3.1, which provides real-time information about the state of strain in the plate. The inverse problem herein is the reconstruction of the three-dimensional deformations of the plate using only the experimentally measured discrete surface strains and boundary constraints. The precise solution of this inverse problem will be established using iFEM methodology.

3.2.2 Kinematic relations

The orthogonal components of the displacement vector, corresponding to any material point within the plate shown in Figure 3.1, can be described in accordance with the FSDT as

$$u_1(x_1, x_2, z) \equiv u(x_1, x_2) + z\,\theta_1(x_1, x_2) \tag{3.1}$$

$$u_2(x_1, x_2, z) \equiv v(x_1, x_2) + z\,\theta_2(x_1, x_2) \tag{3.2}$$

$$u_z(x_1, x_2, z) \equiv w(x_1, x_2) \tag{3.3}$$

where $u_\alpha \equiv u_\alpha(x_1, x_2, z)$ $(\alpha = 1, 2)$ are the in-plane displacements and $u_z \equiv u_z(x_1, x_2, z)$ is the transverse displacement (deflection) across the uniform shell thickness. In Equations (3.1-2), the functions $u \equiv u(x_1, x_2)$ and $v \equiv v(x_1, x_2)$ represent the mid-plane displacements (translations) along x_1 and x_2 directions, respectively. Moreover, the functions $\theta_1 \equiv \theta_1(x_1, x_2)$ and $\theta_2 \equiv \theta_2(x_1, x_2)$ represent average bending rotations of the transverse normal around the positive x_2 and negative x_1 directions, respectively. Furthermore, the function $w \equiv w(x_1, x_2)$ is the transverse deflection in Equation (3.3). These functions, i.e., kinematic variables of the FSDT, can be written in a compact vector form as

$$\mathbf{u} = \begin{bmatrix} u & v & w & \theta_1 & \theta_2 \end{bmatrix}^T \tag{3.4}$$

Calculating the relevant partial derivatives of Equations (3.1-2), the linear strain-displacement relations give rise to the in-plane strains

$$\varepsilon_{11} = u_{1,1} = e_1 + z\,\kappa_4 \tag{3.5}$$

$$\varepsilon_{22} = u_{2,2} = e_2 + z\,\kappa_5 \tag{3.6}$$

$$\gamma_{12} = u_{1,2} + u_{2,1} = e_3 + z\,\kappa_6 \tag{3.7}$$

where, henceforward, $(\bullet)_{,\alpha} \equiv \frac{\partial(\bullet)}{\partial x_\alpha}$ denotes a partial derivative with respect to in-plane coordinate x_α $(\alpha = 1, 2)$. In Equations (3.5-7), the symbols e_α $(\alpha = 1, 2, 3)$ and κ_α $(\alpha = 4, 5, 6)$ denote the membrane strain measures and bending curvatures, respectively. The explicit forms of these terms can be defined in terms of the compact form of kinematic variables $\mathbf{u}$ as

$$\mathbf{e}(\mathbf{u}) \equiv \begin{Bmatrix} e_1 \\ e_2 \\ e_3 \end{Bmatrix} = \begin{Bmatrix} u_{,1} \\ v_{,2} \\ u_{,2} + v_{,1} \end{Bmatrix} \tag{3.8}$$

$$\boldsymbol{\kappa}(\mathbf{u}) \equiv \begin{Bmatrix} \kappa_4 \\ \kappa_5 \\ \kappa_6 \end{Bmatrix} = \begin{Bmatrix} \theta_{1,1} \\ \theta_{2,2} \\ \theta_{1,2} + \theta_{2,1} \end{Bmatrix} \tag{3.9}$$

Taking the corresponding partial derivatives of Equations (3.1-3) in accordance with linear strain-displacement relations, the transverse shear strain measures can also be defined as

$$\boldsymbol{\gamma}(\mathbf{u}) \equiv \begin{Bmatrix} \gamma_7 \\ \gamma_8 \end{Bmatrix} = \begin{Bmatrix} u_{1,z} + u_{z,1} \\ u_{2,z} + u_{z,2} \end{Bmatrix} = \begin{Bmatrix} w_{,1} + \theta_1 \\ w_{,2} + \theta_2 \end{Bmatrix} \tag{3.10}$$

where $(\bullet)_{,z} \equiv \frac{\partial(\bullet)}{\partial z}$ denotes a partial derivative with respect to thickness coordinate z. It is worth to note that the plane-stress assumption $\sigma_{zz} = 0$ within the theory implies that the transverse-normal strain ε_{zz} does not contribute to the strain energy.

3.2.3 Computation of experimental section strains

Discrete in situ surface strain measurements (readings) that are obtained from on-board sensors are crucial according to the iFEM formulation. With today's technology, conventional strain rosettes or embedded fibre-optic sensor networks (e.g., FBG sensors) can be used to collect a large amount of on-board strain data. Using these discrete strain readings, experimental section strains can be computed at n discrete locations, $\mathbf{x}_i \equiv (x_1, x_2)_i$ $(i = 1 - n)$ located in the mid-plane of the plate. As depicted in Figure 3.2, at least two different strain rosettes $(\boldsymbol{\varepsilon}_i^+, \boldsymbol{\varepsilon}_i^-)$ must be placed along the thickness direction of each particular location $\mathbf{x}_i$. For the sake of clarity, the exact locations of these sensors and their strain readings can be identified as

$$\boldsymbol{\varepsilon}_i^+(\mathbf{x}_i, z_i = +h) = [\varepsilon_{11}^+ \quad \varepsilon_{22}^+ \quad \gamma_{12}^+]_i \tag{3.11}$$

$$\boldsymbol{\varepsilon}_i^-(\mathbf{x}_i, z_i = -h) = [\varepsilon_{11}^- \quad \varepsilon_{22}^- \quad \gamma_{12}^-]_i \tag{3.12}$$

where the in situ surface strain measures with the superscripts '+' and '–' pertain to the strain rosettes located on the top and bottom surfaces of the plate, respectively. In Equations (3.11-12), the subscripts (11) and (22) denote the normal strain measurement along the directions x_1 and x_2, whereas the front subscript (12) denotes the shear strain measurement in the x_1x_2 plane.

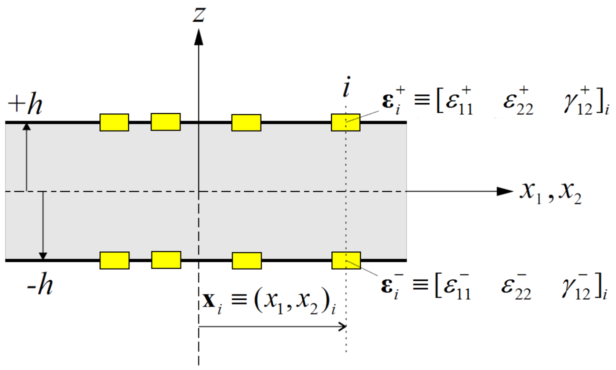

Figure 3.2 Surface strains measured by strain rosettes at discrete locations $(\mathbf{x}_i, \pm h)$.

Evaluating Equations (3.5-7) at the discrete locations $(\mathbf{x}_i, \pm h)$ $(i = 1 - n)$, where the strain sensors are located, experimental membrane strain measures $\mathbf{E}_i$ and bending curvatures $\mathbf{K}_i$ can be computed at the same point $\mathbf{x}_i$ as (Tessler and Spangler, 2003, 2005)

$$\mathbf{E}_i \equiv \begin{Bmatrix} \mathrm{E}_1 \\ \mathrm{E}_2 \\ \mathrm{E}_3 \end{Bmatrix}_i = \frac{1}{2} \begin{Bmatrix} \varepsilon_{11}^+ + \varepsilon_{11}^- \\ \varepsilon_{22}^+ + \varepsilon_{22}^- \\ \gamma_{12}^+ + \gamma_{12}^- \end{Bmatrix}_i \quad (i = 1 - n) \tag{3.13}$$

$$\mathbf{K}_i \equiv \begin{Bmatrix} \mathrm{K}_4 \\ \mathrm{K}_5 \\ \mathrm{K}_6 \end{Bmatrix}_i = \frac{1}{2h} \begin{Bmatrix} \varepsilon_{11}^+ - \varepsilon_{11}^- \\ \varepsilon_{22}^+ - \varepsilon_{22}^- \\ \gamma_{12}^+ - \gamma_{12}^- \end{Bmatrix}_i \quad (i = 1 - n) \tag{3.14}$$

where in situ section strains, $\mathbf{E}_i$ and $\mathbf{K}_i$, correspond to their analytic counterparts, $\mathbf{e}(\mathbf{u})$ and $\boldsymbol{\kappa}(\mathbf{u})$, given by Equations (3.8-9), respectively. In addition, the in situ transverse-shear strain measures that correspond to their analytic counterparts, $\boldsymbol{\gamma}(\mathbf{u})$, given by Equation (3.10), can be symbolically identified by

$$\mathbf{G}_i \equiv [\Gamma_7 \quad \Gamma_8]_i^T \quad (i = 1 - n) \tag{3.15}$$

In Equations (3.13) through (3.15), the uppercase Greek letters are used to indicate the existence of experimental error in the strain measurements. Although the in situ surface strains are simply used to compute the $\mathbf{E}_i$ and $\mathbf{K}_i$ as given in Equations (3.13-

14), they cannot be directly used to calculate the $\mathbf{G}_i$. It is noted, however, that in the deformation of thin shells, the contributions of $\mathbf{G}_i$ are much smaller than that of the bending curvatures. Therefore, the $\mathbf{G}_i$ contributions can be safely omitted from the iFEM formulation for practical engineering applications modelled by using thin shells. On the other hand, in deformation of thick shells, a significant amount of the deflection is caused by transverse-shear stresses. As a consequence, it is necessary to compute the $\mathbf{G}_i$ in order to perform an accurate iFEM analysis of thick shell structures.

Experimental strain data can be processed analytically by using curve fitting or smoothing techniques (Lancaster and Salkauskas, 1986). In this manner, the six section strain measures, $\mathbf{E}_i$ and $\mathbf{K}_i$, can be represented as continuous functions that are defined everywhere in the mid-plane of the plate. The vectors containing the smoothed experimental strain measures will henceforth be denoted as $\mathbf{E}$ and $\mathbf{K}$, where the 'i' subscript is removed to differentiate these continuous quantities from the discrete ones. A smoothing procedure, developed by Tessler et al. (1998, 1999), called Smoothing Element Analysis (SEA), can be used to obtain $\mathbf{E}$ and $\mathbf{K}$ that are represented by piecewise, nearly C^1-continuous polynomial functions with C^0-continuous first-order derivatives. As a result of the SEA analysis, the first-order derivatives of $\mathbf{K}$ can be accurately computed and subsequently used to obtain the $\mathbf{G}$ or $\mathbf{G}_i$ through the equilibrium equations of the FSDT. This calculation will be crucial for shape sensing of thick plate and shell structures. Hence, the mathematical details of obtaining the $\mathbf{G}_i$ via FSDT equilibrium equations is established for an isotropic material of the plate, which has an elastic modulus of E and Poisson's ratio of ν. Using the smoothed experimental strain measures, the constitutive relations can be defined based on the plane-stress assumption $(\sigma_{zz} = 0)$ as

$$\begin{Bmatrix} \sigma_{11} \\ \sigma_{22} \\ \tau_{12} \end{Bmatrix} = \frac{E}{1-\nu^2} \begin{bmatrix} 1 & \nu & 0 \\ \nu & 1 & 0 \\ 0 & 0 & (1-\nu)/2 \end{bmatrix} \left(\begin{Bmatrix} \mathrm{E}_1 \\ \mathrm{E}_2 \\ \mathrm{E}_3 \end{Bmatrix} + z \begin{Bmatrix} \mathrm{K}_4 \\ \mathrm{K}_5 \\ \mathrm{K}_6 \end{Bmatrix} \right) \tag{3.16}$$

$$\begin{Bmatrix} \tau_{1z} \\ \tau_{2z} \end{Bmatrix} = \frac{E}{2(1+\nu)} \begin{bmatrix} 1 & 0 \\ 0 & 1 \end{bmatrix} \begin{Bmatrix} \Gamma_7 \\ \Gamma_8 \end{Bmatrix} \tag{3.17}$$

where $(\sigma_{11}, \sigma_{22}, \tau_{12})$ and (τ_{1z}, τ_{2z}) are in-plane and transverse-shear stress components, respectively. The equilibrium equations of the FSDT defines shear resultants in terms of first-order derivatives of moment resultants as

$$Q_{1z} = M_{11,1} + M_{12,2} \tag{3.18}$$

$$Q_{2z} = M_{12,1} + M_{22,2} \tag{3.19}$$

where (M_{11}, M_{22}, M_{12}) and (Q_{1z}, Q_{2z}) represent the moment and shear resultants, respectively. These resultants can be explicitly expressed using the Equations (3.16-17) as

$$M_{11} = \int_{-h}^{+h} z\,\sigma_{11}\,dz = \frac{2Eh^3}{3(1-\nu^2)}(\mathrm{K}_4 + \nu\,\mathrm{K}_5) \tag{3.20}$$

$$M_{22} = \int_{-h}^{+h} z\,\sigma_{22}\,dz = \frac{2Eh^3}{3(1-\nu^2)}(\nu\,\mathrm{K}_4 + \mathrm{K}_5) \tag{3.21}$$

$$M_{12} = \int_{-h}^{+h} z\,\tau_{12}\,dz = \frac{Eh^3}{3(1+\nu)}\mathrm{K}_6 \tag{3.22}$$

$$Q_{1z} = \kappa \int_{-h}^{+h} \tau_{1z}\,dz = \frac{\kappa Eh}{1+\nu}\Gamma_7 \tag{3.23}$$

$$Q_{2z} = \kappa \int_{-h}^{+h} \tau_{2z}\,dz = \frac{\kappa Eh}{1+\nu}\Gamma_8 \tag{3.24}$$

where κ is shear correction factor that is commonly taken as $\kappa = 5/6$ for plate and shells. In addition, FSDT has three membrane stress resultants given by

$$N_{11} = \int_{-h}^{+h} \sigma_{11}\,dz = \frac{2Eh}{1-\nu^2}(\mathrm{E}_1 + \nu\,\mathrm{E}_2) \tag{3.25}$$

$$N_{22} = \int_{-h}^{+h} \sigma_{22}\,dz = \frac{2Eh}{1-\nu^2}(\nu\,\mathrm{E}_1 + \mathrm{E}_2) \tag{3.26}$$

$$N_{12} = \int_{-h}^{+h} \tau_{12}\,dz = \frac{Eh}{1+\nu}\mathrm{E}_3 \tag{3.27}$$

Inserting the Equations (3.20-24) into (3.18-19) and subsequently cancelling the synonyms, the in situ transverse-shear strain measures can be explicitly expressed as

$$\mathbf{G} \equiv \begin{Bmatrix} \Gamma_7 \\ \Gamma_8 \end{Bmatrix} = \frac{h^2}{3\kappa}\left(\frac{2}{1-\nu} \begin{Bmatrix} \mathrm{K}_{4,1} + \nu \mathrm{K}_{5,1} \\ \nu \mathrm{K}_{4,2} + \mathrm{K}_{5,2} \end{Bmatrix} + \begin{Bmatrix} \mathrm{K}_{6,2} \\ \mathrm{K}_{6,1} \end{Bmatrix} \right) \tag{3.28}$$

where Γ_α $(\alpha = 7,8)$ are defined everywhere in the mid-plane of the plate, thus they can be sampled at any particular location $\mathbf{x}_i$ to obtain $\mathbf{G}_i$. Note that the overall outcome of this computational procedure will also provide the continuous form of all experimental section strains, e.g., $\boldsymbol{\varepsilon} = [\mathbf{E} \quad \mathbf{K} \quad \mathbf{G}]$.

3.2.4 The weighted-least-squares functional

Following the original iFEM methodology (Tessler and Spangler, 2003, 2005) as a general framework, utilizing the weighting coefficients introduced in (Tessler et al., 2011), and accounting for the membrane, bending, and transverse-shear deformations of the FSDT, a weighted-least-squares functional, $\Phi(\mathbf{u})$, can be expressed as

$$\Phi(\mathbf{u}) = \sum_{\alpha=1}^{8} w_\alpha \, \varphi_\alpha \tag{3.29}$$

where w_α $(\alpha = 1-8)$ are positive valued weighting coefficients associated with the individual section strains and the functional φ_α $(\alpha = 1-8)$ is the least-squares functional of experimental section strains ($\boldsymbol{\varepsilon}$ or $\boldsymbol{\varepsilon}_i$) and kinematic variables $\mathbf{u}$. If the discrete experimental strain measures are directly used in iFEM analysis, the least-squares functional becomes $\varphi_\alpha = \varphi_\alpha(\mathbf{u}, \boldsymbol{\varepsilon}_i)$ $(\alpha = 1-8)$ and can be defined in the form of the normalized Euclidean norms given as

$$\varphi_\alpha \equiv \frac{1}{n} \sum_{i=1}^{n} \left[e_\alpha(\mathbf{u})_i - \mathrm{E}_{\alpha i} \right]^2 \quad (\alpha = 1,2,3) \tag{3.30}$$

$$\varphi_\alpha \equiv \frac{(2h)^2}{n} \sum_{i=1}^{n} \left[\kappa_\alpha(\mathbf{u})_i - \mathrm{K}_{\alpha i} \right]^2 \quad (\alpha = 4,5,6) \tag{3.31}$$

$$\varphi_\alpha \equiv \frac{1}{n} \sum_{i=1}^{n} \left[\gamma_\alpha(\mathbf{u})_i - \Gamma_{\alpha i} \right]^2 \quad (\alpha = 7,8) \tag{3.32}$$

If the raw strain data are smoothed a priori (i.e., using SEA analysis as described in section 3.2.3) such that the continuous experimental strain measures become available for iFEM analysis, the least-squares functional becomes $\varphi_\alpha = \varphi_\alpha(\mathbf{u},\boldsymbol{\varepsilon})$ $(\alpha = 1-8)$ and can be defined in terms of the dimensionless L_2 squared norms given as

$$\varphi_\alpha \equiv \frac{1}{A}\int_A \left[e_\alpha(\mathbf{u}) - \mathrm{E}_\alpha\right]^2 dA \quad (\alpha = 1,2,3) \tag{3.33}$$

$$\varphi_\alpha \equiv \frac{(2h)^2}{A}\int_A \left[\kappa_\alpha(\mathbf{u}) - \mathrm{K}_\alpha\right]^2 dA \quad (\alpha = 4,5,6) \tag{3.34}$$

$$\varphi_\alpha \equiv \frac{1}{A}\int_A \left[\gamma_\alpha(\mathbf{u}) - \Gamma_\alpha\right]^2 dA \quad (\alpha = 7,8) \tag{3.35}$$

The weighting constants w_α $(\alpha = 1-8)$ in Equation (3.29) control the complete coherence between the analytic section strains and their experimentally measured values. Their proper usage is especially critical for those problems involving relatively few locations of strain gages. When every analytic section strain has a corresponding measured in situ value ($\boldsymbol{\varepsilon}$ or $\boldsymbol{\varepsilon}_i$), the weighting constants are set as $w_\alpha = 1$ $(\alpha = 1-8)$ for Equations (3.30-32) or (3.33-35). In the case of a missing in situ strain component, the corresponding weighting constant is set as a small number, e.g., $\lambda = 10^{-5}$, and Equations (3.30-32) or (3.33-35) take on the reduced form defined by the L_2 squared norms

$$\varphi_\alpha \equiv \frac{1}{A}\int_A \left[e_\alpha(\mathbf{u})\right]^2 dA \quad (\mathrm{w}_\alpha = \lambda),\ (\alpha = 1,2,3) \tag{3.36}$$

$$\varphi_\alpha \equiv \frac{(2h)^2}{A}\int_A \left[\kappa_\alpha(\mathbf{u})\right]^2 dA \quad (\mathrm{w}_\alpha = \lambda),\ (\alpha = 4,5,6) \tag{3.37}$$

$$\varphi_\alpha \equiv \frac{1}{A}\int_A \left[\gamma_\alpha(\mathbf{u})\right]^2 dA \quad (\mathrm{w}_\alpha = \lambda),\ (\alpha = 7,8) \tag{3.38}$$

Furthermore, the iFEM methodology also permits the use of "strain-less" inverse elements – the type of elements that do not have any in situ section strain measurements. For these strain-less elements, all squared norms in Equations (3.36-38) are multiplied by the small weighting constants $w_\alpha = \lambda = 10^{-5}$ $(\alpha = 1-8)$.

Therefore, an iFEM discretization can have very sparse measured strain data, and yet the necessary interpolation connectivity can still be maintained between the elements that have strain-sensor data.

3.3 The Four-Node Quadrilateral Inverse-Shell Element Formulation

The four-node quadrilateral inverse-shell element, labelled iQS4, is developed on the basis of the weighted-least-squares iFEM formulation, and has six displacement DOF per node (refer to Figure 3.3). The beneficial aspects of this new element are such that, due to the inclusion of drilling rotations, singular solutions can be simply avoided when modelling complex shell structures and, moreover, for membrane problems, iQS4 has less tendency toward shear locking. The generic way to obtain the element formulation, writing local membrane and bending matrices for a flat geometry and adding them together, is followed because it is a satisfactory approach in terms of iFEM methodology.

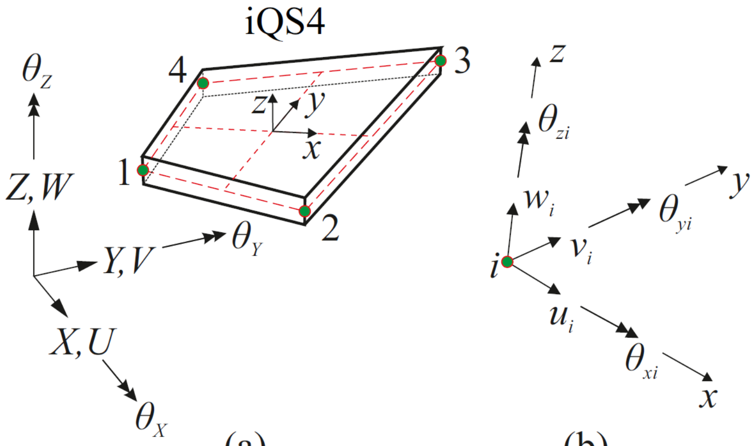

(a) (b)

Figure 3.3 (a) Four-node quadrilateral inverse-shell element, iQS4, depicted within global (*X, Y, Z*) and local (*x, y, z*) frames of reference; (b) Nodal DOF corresponding to local (element) coordinates (*x, y, z*).

The first step is to define a set of convenient coordinate frames of reference to guarantee the geometric uniqueness of the assembled shell structure. A local coordinate system (x, y, z) serves as the element frame of reference, with its origin $(0,0,0)$ located at the centroid of the mid-plane quadrilateral. In the following derivations, these local coordinates (x, y, z) are associated with the orthogonal Cartesian coordinates (x_1, x_2, z) used to define the kinematic relations of FSDT in Section 3.2.2. Hence, the coordinates $(x, y) \equiv (x_1, x_2)$ are the in-plane coordinates and $z \in [-h, +h]$ defines the thickness coordinate. To assemble element matrices into a global system of equations, suitable transformation matrices, $\mathbf{T}^e$, defining the local to global transformations can be simply established in accordance with procedures described in the following paragraph.

The coordinates of element nodes referred to the global coordinate system, (X, Y, Z), are given as

$$\mathbf{X}_i = \begin{bmatrix} X_i & Y_i & Z_i \end{bmatrix}^T (i = 1-4) \tag{3.39}$$

Each edge length d_i of the mid-plane quadrilateral and global coordinates of each edge mid-point $\mathbf{c}_i$ can be calculated as

$$\left.\begin{aligned} d_i &= \left\| \mathbf{X}_j - \mathbf{X}_i \right\| \\ \mathbf{c}_i &= \frac{\mathbf{X}_j + \mathbf{X}_i}{2} \end{aligned}\right\} (i = 1,2,3,4; j = 2,3,4,1) \tag{3.40}$$

Using Equation (3.40), global coordinates of mid-plane quadrilateral centroid can be defined as

$$\mathbf{C} = \frac{\sum_{k=1}^{4} \mathbf{c}_k d_k}{\sum_{k=1}^{4} d_k} \tag{3.41}$$

Unit normal vector to the mid-plane quadrilateral, $\mathbf{n}$, and unit vectors along local *y*- and *x*- axis, $\mathbf{p}$ and $\mathbf{l}$, can respectively be computed as

$$\mathbf{n} = \frac{\mathbf{A} \times \mathbf{B}}{\left\| \mathbf{A} \times \mathbf{B} \right\|} \tag{3.42}$$

$$\mathbf{p} = \frac{\mathbf{A} + \mathbf{B}}{\left\| \mathbf{A} + \mathbf{B} \right\|} \tag{3.43}$$

$$\mathbf{l} = \mathbf{p} \times \mathbf{n} \tag{3.44}$$

where

$$\mathbf{A} = \mathbf{X}_3 - \mathbf{X}_1 \tag{3.45}$$

$$\mathbf{B} = \mathbf{X}_4 - \mathbf{X}_2 \tag{3.46}$$

are diagonal vectors, with $\mathbf{A}$ pointing out from node-1 to node-3, whereas $\mathbf{B}$ pointing out from node-2 to node-4. Using Equations (3.39), (3.41), and (3.43-44), local coordinates of the iQS4 element nodes can be determined as

$$\left.\begin{aligned} x_i &= \left(\mathbf{X}_i - \mathbf{C}\right)\cdot\mathbf{l} \\ y_i &= \left(\mathbf{X}_i - \mathbf{C}\right)\cdot\mathbf{p} \end{aligned}\right\}\left(i = 1-4\right) \tag{3.47}$$

With the unit vectors $\mathbf{n}$, $\mathbf{p}$, and $\mathbf{l}$, given in Equations (3.42-44), the transformation matrix, $\mathbf{T}^e$, can be defined as

$$\mathbf{T}^e = \begin{bmatrix} \mathbf{T} & 0 & 0 & 0 & 0 & 0 & 0 & 0 \\ 0 & \mathbf{T} & 0 & 0 & 0 & 0 & 0 & 0 \\ 0 & 0 & \mathbf{T} & 0 & 0 & 0 & 0 & 0 \\ 0 & 0 & 0 & \mathbf{T} & 0 & 0 & 0 & 0 \\ 0 & 0 & 0 & 0 & \mathbf{T} & 0 & 0 & 0 \\ 0 & 0 & 0 & 0 & 0 & \mathbf{T} & 0 & 0 \\ 0 & 0 & 0 & 0 & 0 & 0 & \mathbf{T} & 0 \\ 0 & 0 & 0 & 0 & 0 & 0 & 0 & \mathbf{T} \end{bmatrix} \tag{3.48}$$

with

$$\mathbf{T} = \begin{bmatrix} \mathbf{l}^T & \mathbf{p}^T & \mathbf{n}^T \end{bmatrix}^T \tag{3.49}$$

where $\mathbf{T}$ is the stress transformation matrix from the local to the global coordinate system.

The (x, y) reference plane of the iQS4 quadrilateral element can be uniquely defined in terms of bilinear isoparametric shape functions $N_i(s,t)$ $(i = 1-4)$ and the element local nodal coordinates (x_i, y_i) $(i = 1-4)$, where s and t are dimensionless isoparametric coordinates (refer to Figure 3.4). These mapping functions can be expressed as

$$x(s,t) \equiv x = \sum_{i=1}^{4} N_i \, x_i \tag{3.50}$$

$$y(s,t) \equiv y = \sum_{i=1}^{4} N_i \, y_i \tag{3.51}$$

with

$$N_i = \frac{1}{4}(1+s_i \, s)(1+t_i \, t) \quad (i=1-4) \tag{3.52}$$

where $(s_i, t_i) \in [-1,+1]$ are isoparametric coordinates of the element nodes as presented in Figure 3.4.

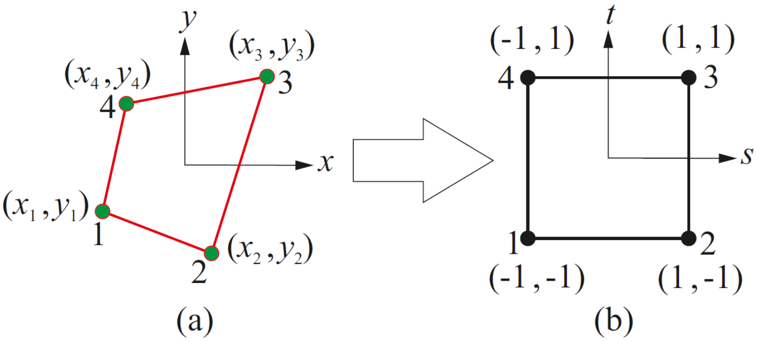

Figure 3.4 (a) Mid-plane (*x, y*)-reference surface and nodal coordinates of iQS4 element; (b) Parent element in isoparametric coordinates.

The nodal DOF, consisting of positive *x* translations u_i, positive *y* translations v_i, and positive counter clockwise drilling rotations θ_{zi}, define the u and v membrane displacements (kinematic variables) as

$$u = \sum_{i=1}^{4} (N_i \, u_i + L_i \, \theta_{zi}) \tag{3.53}$$

$$v = \sum_{i=1}^{4} (N_i \, v_i + M_i \, \theta_{zi}) \tag{3.54}$$

Moreover, transverse displacement and two bending rotations w, θ_x, and θ_y (kinematic variables) are defined by the nodal DOF of positive *z* translation w_i and positive counter clockwise rotations around the *x*- and *y*- axes, θ_{xi} and θ_{yi}, as

$$w = \sum_{i=1}^{4} (N_i \, w_i - L_i \, \theta_{xi} - M_i \, \theta_{yi}) \tag{3.55}$$

$$\theta_1 = \sum_{i=1}^{4} N_i \, \theta_{yi} \tag{3.56}$$

$$\theta_2 = -\sum_{i=1}^{4} N_i \theta_{xi} \tag{3.57}$$

In Equations (3.53-57), the functions L_i and M_i are the anisoparametric shape functions that were originally developed by Tessler and Hughes (1983) for a four-node quadrilateral plate element, MIN4 (Mindlin-type, four-nodes). These shape functions were also used by Cook (1994) to define the interaction between the hierarchical drilling rotation DOF and the membrane displacements. The explicit forms of these anisoparametric interpolation functions are given as

$$\left.\begin{aligned} M_i &= a_j \, N_{j+4} - a_i \, N_{i+4} \\ L_i &= b_j \, N_{j+4} - b_i \, N_{i+4} \end{aligned}\right\} (i = 1,2,3,4\,; j = 4,1,2,3) \tag{3.58}$$

where (a_i, b_i) $(i = 1-4)$ can be expressed in terms of local coordinates of iQS4 element as

$$\left.\begin{aligned} a_i &= x_i - x_k \\ b_i &= y_k - y_i \end{aligned}\right\} (i = 1,2,3,4\,; k = 2,3,4,1) \tag{3.59}$$

and the quadratic shape functions, N_i $(i = 5-8)$, are defined as

$$N_{i+4} = \frac{(1-s^2)(1+t_i \, t)}{16} \quad (i = 1,3) \tag{3.60}$$

$$N_{i+4} = \frac{(1+s_i \, s)(1-t^2)}{16} \quad (i = 2,4) \tag{3.61}$$

Introducing Equations (3.53-57) into (3.8-10) results in explicit definitions of analytic section strains in terms of the element nodal displacement vector, $\mathbf{u}^e$, as

$$\mathbf{e}(\mathbf{u}^e) = \begin{bmatrix} \mathbf{B}_1 \, \mathbf{u}^e & \mathbf{B}_2 \, \mathbf{u}^e & \mathbf{B}_3 \, \mathbf{u}^e \end{bmatrix}^T \tag{3.62}$$

$$\boldsymbol{\kappa}(\mathbf{u}^e) = \begin{bmatrix} \mathbf{B}_4 \, \mathbf{u}^e & \mathbf{B}_5 \, \mathbf{u}^e & \mathbf{B}_6 \, \mathbf{u}^e \end{bmatrix}^T \tag{3.63}$$

$$\boldsymbol{\gamma}(\mathbf{u}^e) = \begin{bmatrix} \mathbf{B}_7\,\mathbf{u}^e & \mathbf{B}_8\,\mathbf{u}^e \end{bmatrix}^T \tag{3.64}$$

with

$$\mathbf{u}^e = \begin{bmatrix} \mathbf{u}_1^e & \mathbf{u}_2^e & \mathbf{u}_3^e & \mathbf{u}_4^e \end{bmatrix}^T \tag{3.65}$$

$$\mathbf{u}_i^e = \begin{bmatrix} u_i & v_i & w_i & \theta_{xi} & \theta_{yi} & \theta_{zi} \end{bmatrix}^T (i = 1-4) \tag{3.66}$$

where the matrices $\mathbf{B}_\alpha$ $(\alpha = 1-8)$ contain derivatives of the shape functions and can be respectively defined as

$$\mathbf{B}_\alpha = \begin{bmatrix} \mathbf{B}_\alpha^1 & \mathbf{B}_\alpha^2 & \mathbf{B}_\alpha^3 & \mathbf{B}_\alpha^4 \end{bmatrix} \quad (\alpha = 1-8) \tag{3.67}$$

with

$$\left.\begin{aligned} \mathbf{B}_1^i &= \begin{bmatrix} N_{i,x} & 0 & 0 & 0 & 0 & L_{i,x} \end{bmatrix} \\ \mathbf{B}_2^i &= \begin{bmatrix} 0 & N_{i,y} & 0 & 0 & 0 & M_{i,y} \end{bmatrix} \\ \mathbf{B}_3^i &= \begin{bmatrix} N_{i,y} & N_{i,x} & 0 & 0 & 0 & L_{i,y} + M_{i,x} \end{bmatrix} \end{aligned}\right\} (i = 1-4) \tag{3.68}$$

$$\left.\begin{aligned} \mathbf{B}_4^i &= \begin{bmatrix} 0 & 0 & 0 & 0 & N_{i,x} & 0 \end{bmatrix} \\ \mathbf{B}_5^i &= \begin{bmatrix} 0 & 0 & 0 & -N_{i,y} & 0 & 0 \end{bmatrix} \\ \mathbf{B}_6^i &= \begin{bmatrix} 0 & 0 & 0 & -N_{i,x} & N_{i,y} & 0 \end{bmatrix} \end{aligned}\right\} (i = 1-4) \tag{3.69}$$

$$\left.\begin{aligned} \mathbf{B}_7^i &= \begin{bmatrix} 0 & 0 & N_{i,x} & -L_{i,x} & (N_i - M_{i,x}) & 0 \end{bmatrix} \\ \mathbf{B}_8^i &= \begin{bmatrix} 0 & 0 & N_{i,y} & -(L_{i,y} + N_i) & -M_{i,y} & 0 \end{bmatrix} \end{aligned}\right\} (i = 1-4) \tag{3.70}$$

where, $(\bullet)_{,x} \equiv \frac{\partial(\bullet)}{\partial x}$ and $(\bullet)_{,y} \equiv \frac{\partial(\bullet)}{\partial y}$ denote the partial derivative with respect to in-plane coordinates x and y, respectively. Since the membrane strain measures, $\mathbf{e}(\mathbf{u}^e)$, are associated with the stretching of the middle surface, the $\mathbf{B}_\alpha$ $(\alpha = 1-3)$ matrix contains the derivatives of the shape functions that are associated with the membrane behavior. Moreover, the bending curvatures and transverse-shear strain measures, $\boldsymbol{\kappa}(\mathbf{u}^e)$ and $\boldsymbol{\gamma}(\mathbf{u}^e)$, are associated with bending deformations, thus the $\mathbf{B}_\alpha$ $(\alpha = 4-8)$ matrices accordingly contain the corresponding derivatives of the shape functions that define the element bending response.

The iFEM methodology reconstructs the deformed shape of a discretized structure by minimizing a weighted-least-squares functional with respect to the nodal DOF of the entire discretization. Assuming that only discrete experimental strain measures $\boldsymbol{\varepsilon}_i$ become available, and then substituting Equation (3.62-64) into the weighted-least-squares functional, given by Equations (3.29-32), reveals this functional, $\Phi_e(\mathbf{u}^e)$, for an individual iQS4 element given as

$$\Phi_e(\mathbf{u}^e) = \sum_{\alpha=1}^{8} w_\alpha \, \varphi_\alpha(\mathbf{u}^e, \boldsymbol{\varepsilon}_i) \tag{3.71}$$

By virtue of these assumptions, all strain compatibility relations are explicitly satisfied so that Equation (3.71) can be minimized with respect to the nodal displacement DOF, $\mathbf{u}^e$, giving rise to

$$\frac{\partial \Phi_e(\mathbf{u}^e)}{\partial \mathbf{u}^e} = \boldsymbol{\Gamma}^e \mathbf{u}^e - \boldsymbol{\varepsilon}^e = 0 \tag{3.72}$$

or simply

$$\boldsymbol{\Gamma}^e \mathbf{u}^e = \boldsymbol{\varepsilon}^e \tag{3.73}$$

where $\boldsymbol{\Gamma}^e$ is the element left-hand-side matrix; $\boldsymbol{\varepsilon}^e$ is the element right-hand-side vector, which is a function of the measured strain values; and $\mathbf{u}^e$ is the nodal displacement vector of the element.

The $\boldsymbol{\Gamma}^e$ matrix combines the contribution of every analytic section strain component and its corresponding weighting constant w_α $(\alpha = 1-8)$ and is given by

$$\boldsymbol{\Gamma}^e = \sum_{\alpha=1}^{8} w_\alpha \, \mathbf{k}_\alpha^e \tag{3.74}$$

where $\mathbf{k}_\alpha^e$ $(\alpha = 1-8)$ matrices denote the contribution of each analytic section strain component and can be explicitly written in terms of the $\mathbf{B}_\alpha$ $(\alpha = 1-8)$ matrices as

$$\mathbf{k}_\alpha^e = \frac{1}{n} \sum_{i=1}^{n} \left[\left[\mathbf{B}_\alpha(\mathbf{x}_i) \right]^T \mathbf{B}_\alpha(\mathbf{x}_i) \right] \; (\alpha = 1-3,7,8) \tag{3.75}$$

$$\mathbf{k}_\alpha^e = \frac{(2h)^2}{n} \sum_{i=1}^{n} \left[\left[\mathbf{B}_\alpha(\mathbf{x}_i) \right]^T \mathbf{B}_\alpha(\mathbf{x}_i) \right] \; (\alpha = 4-6) \tag{3.76}$$

The $\boldsymbol{\varepsilon}^e$ vector is a function of the measured section-strain values (computed using strain sensors readings), and is given by

$$\boldsymbol{\varepsilon}^e = \sum_{\alpha=1}^{8} w_\alpha \, \mathbf{f}_\alpha^e \tag{3.77}$$

where $\mathbf{f}_\alpha^e$ $(\alpha = 1-8)$ vectors denote the contribution of each experimental section strain component and can be explicitly written in terms of experimental section strains as

$$\mathbf{f}_\alpha^e = \frac{1}{n} \sum_{i=1}^{n} \left[\left[\mathbf{B}_\alpha(\mathbf{x}_i) \right]^T \mathrm{E}_{\alpha i} \right] \; (\alpha = 1-3) \tag{3.78}$$

$$\mathbf{f}_\alpha^e = \frac{(2h)^2}{n} \sum_{i=1}^{n} \left[\left[\mathbf{B}_\alpha(\mathbf{x}_i) \right]^T \mathrm{K}_{\alpha i} \right] \; (\alpha = 4-6) \tag{3.79}$$

$$\mathbf{f}_\alpha^e = \frac{1}{n} \sum_{i=1}^{n} \left[\left[\mathbf{B}_\alpha(\mathbf{x}_i) \right]^T \Gamma_{\alpha i} \right] \; (\alpha = 7,8) \tag{3.80}$$

Note that, in Equations (3.75-76) and (3.78-80), the $\mathbf{x}_i \equiv (x, y)_i$ $(i = 1, n)$ represents the locations at the mid-plane of iQS4 element, where the experimental section strains are computed. Once the element (local) matrix equations are established, the element contributions to the global linear equation system of the discretized structure can be performed as

$$\mathbf{AU} = \mathbf{Q} \tag{3.81}$$

with

$$\mathbf{A} = \underset{e=1}{\overset{nel}{\Omega}} \left[(\mathbf{T}^e)^T \boldsymbol{\Gamma}^e \, \mathbf{T}^e \right] \tag{3.82}$$

$$\mathbf{U} = \underset{e=1}{\overset{nel}{\Omega}} \left[(\mathbf{T}^e)^T \mathbf{u}^e \right] \tag{3.83}$$

$$\mathbf{Q} = \underset{e=1}{\overset{nel}{\Omega}} \left[(\mathbf{T}^e)^T \boldsymbol{\varepsilon}^e \right] \tag{3.84}$$

where $\mathbf{T}^e$ is the transformation matrix of the nodal DOF of an element from the local to the global coordinate system, $\mathbf{A}$ is the global left-hand-side matrix, which is a symmetric matrix and independent of the measured strain values, $\mathbf{U}$ is the global nodal displacement vector, and $\mathbf{Q}$ is the global right-hand-side vector, which is a function of the measured strain values. In Equations (3.82-84), the parameter nel stands for the total number of inverse finite elements and the symbol $\underset{e=1}{\overset{nel}{\Omega}}$ represents assembly of the element matrices/vectors into global matrices/vectors.

The global left-hand-side matrix $\mathbf{A}$ includes the rigid body mode of the discretized structure. Therefore, it is a singular matrix. By prescribing problem-specific displacement boundary conditions, the resulting system of equations can be reduced from Equation (3.81) as

$$\mathbf{A}_R \mathbf{U}_R = \mathbf{Q}_R \tag{3.85}$$

where $\mathbf{A}_R$ is a positive definite matrix that is always non-singular and invertible. The solution of Equation (3.85) is very fast because the matrix $\mathbf{A}_R$ remains unchanged for a given distribution of strain sensors, and its inverse should be calculated only once during the real-time monitoring process. However, the right-hand-side vector $\mathbf{Q}_R$ is dependent on the discrete surface strain data obtained from in situ strain sensors. Hence, it needs to be updated at each strain-data acquisition increment. Finally, the matrix–vector multiplication $\mathbf{A}_R^{-1} \mathbf{Q}_R$ gives rise to the unknown DOF vector $\mathbf{U}_R$, which provides the deformed structural shape at any real time. To assess the global displacement and rotation response, it is convenient to compute the total displacement, U_T, as

$$U_T = \sqrt{U^2 + V^2 + W^2} \tag{3.86}$$

and the total rotation, θ_T, as

$$\theta_T = \sqrt{\left(\theta_X\right)^2 + \left(\theta_Y\right)^2 + \left(\theta_Z\right)^2} \tag{3.87}$$

where U, V, and W are the translations along the global *X*-, *Y*-, and *Z*-axes, respectively, and θ_X, θ_Y, and θ_Z are the rotations around the global *X*-, *Y*-, and *Z*-axes, respectively (refer to Figure 3.3). Moreover, the continuous strain field throughout the structure can be obtained using the evaluated displacement values. Furthermore, the constitutive relationship between stress and strain will allow determination of stress distribution. For instance, according to the local coordinate system (x, y, z) of the iQS4 element, the constitutive relationship defined by Equations (3.16-17) can be rewritten in terms of evaluated displacement values, $\mathbf{u}^e$, as

$$\begin{Bmatrix} \sigma_{xx} \\ \sigma_{yy} \\ \tau_{xy} \end{Bmatrix} = \frac{E}{1-\nu^2} \begin{bmatrix} 1 & \nu & 0 \\ \nu & 1 & 0 \\ 0 & 0 & (1-\nu)/2 \end{bmatrix} \left(\begin{Bmatrix} \mathbf{B}_1 \\ \mathbf{B}_2 \\ \mathbf{B}_3 \end{Bmatrix} + z \begin{Bmatrix} \mathbf{B}_4 \\ \mathbf{B}_5 \\ \mathbf{B}_6 \end{Bmatrix} \right) \mathbf{u}^e \tag{3.88}$$

$$\begin{Bmatrix} \tau_{xz} \\ \tau_{yz} \end{Bmatrix} = \frac{E}{2(1+\nu)} \begin{bmatrix} 1 & 0 \\ 0 & 1 \end{bmatrix} \begin{Bmatrix} \mathbf{B}_7 \\ \mathbf{B}_8 \end{Bmatrix} \mathbf{u}^e \tag{3.89}$$

Once the stress components at any point inside the iQS4 element domain are calculated using Equations (3.88-89), transformation of the stress components from the local to the global coordinate system can be performed as

$$\boldsymbol{\sigma} = (\mathbf{T})^T \boldsymbol{\sigma}^e \mathbf{T} \tag{3.90}$$

where local and global stress tensors are represented respectively as

$$\boldsymbol{\sigma}^e = \begin{bmatrix} \sigma_{xx} & \tau_{xy} & \tau_{xz} \\ \tau_{xy} & \sigma_{yy} & \tau_{yz} \\ \tau_{xz} & \tau_{yz} & \sigma_{zz} \end{bmatrix} \tag{3.91}$$

$$\boldsymbol{\sigma} = \begin{bmatrix} \sigma_{XX} & \tau_{XY} & \tau_{XZ} \\ \tau_{XY} & \sigma_{YY} & \tau_{YZ} \\ \tau_{XZ} & \tau_{YZ} & \sigma_{ZZ} \end{bmatrix} \tag{3.92}$$

and $\mathbf{T}$ is the stress transformation matrix that is defined by Equation (3.49). Then, three-dimensional global stresses can be converted to an equivalent stress using the von Mises failure criterion (i.e., a suitable failure criterion for ductile materials such as metals) as

$$\sigma_{VM} = \frac{1}{\sqrt{2}} \sqrt{(\sigma_{XX} - \sigma_{YY})^2 + (\sigma_{XX} - \sigma_{ZZ})^2 + (\sigma_{YY} - \sigma_{ZZ})^2 + 6(\tau_{XY}^2 + \tau_{XZ}^2 + \tau_{YZ}^2)} \tag{3.93}$$

Finally, the von Mises stress can be checked against the yield strength of the material for damage detection as part of the SHM process.

3.4 Numerical Examples

In this section, two validation problems, (1) a cantilevered plate under static transverse force near free tip, and (2) a short cantilever beam under shear loading, are solved and discussed in detail. Following the validation cases, the applicability of the iQS4 element to more complex structures is demonstrated by the analysis of a thin-walled cylinder. For this problem, the effects of noisy strain measurements on the accuracy of the iFEM solution are examined using strain measurements that involve five and ten percent random noise, respectively. Finally, the effect of sensor locations, number of sensors, the discretization of the geometry, and the influence of noise on the strain measurements are assessed with respect to the solution accuracy.

3.4.1 A cantilever plate under static transverse force near free tip

A rectangular cantilever plate subjected to a static transverse force applied near the free tip has a length of 0.254 m, a height of 0.0762 m, and a uniform thickness of 3.175 mm (refer to Figure 3.5). The plate is made of aluminum having an elastic modulus of 73.084 GPa and a Poisson’s ratio of 0.33. The concentrated force of $F = 25.728$ N is applied in the negative Z direction near the tip. This plate was originally analyzed and then tested in a mechanics laboratory by Bogert et al. (2003). Subsequently, Tessler and Spangler (2004) analyzed this plate configuration using the iFEM methodology. Using a relatively coarse iMIN3 discretization that has a single strain rosette within each element, the authors obtained a highly accurate reconstruction of the full-field displacement response.

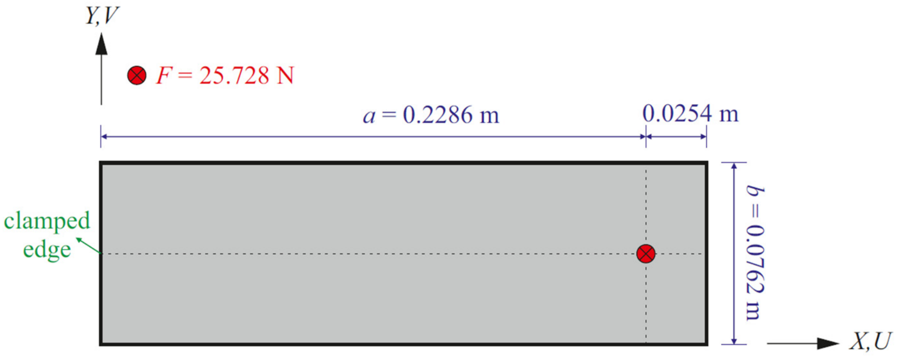

Figure 3.5 Cantilever plate under transverse force applied near free tip.

In this first example, the above stated problem is analyzed once again using the iFEM/iQS4 methodology to validate the present element bending capability. There is no need to model the part of the plate to the right of the applied force because it is free of stress. Therefore, the following iFEM and direct FEM models are defined over the domain $X \in [0, a]$ and $Y \in [0, b]$ (refer to Figures 3.5-6). To establish an accurate reference solution, a convergence study was performed using direct FEM analyses utilizing an in-house FEM code. The most refined mesh consisted of 432 uniformly distributed square elements, possessing 2886 DOF. The FEM deflections and rotations are used to compute the simulated strain-sensor strains.

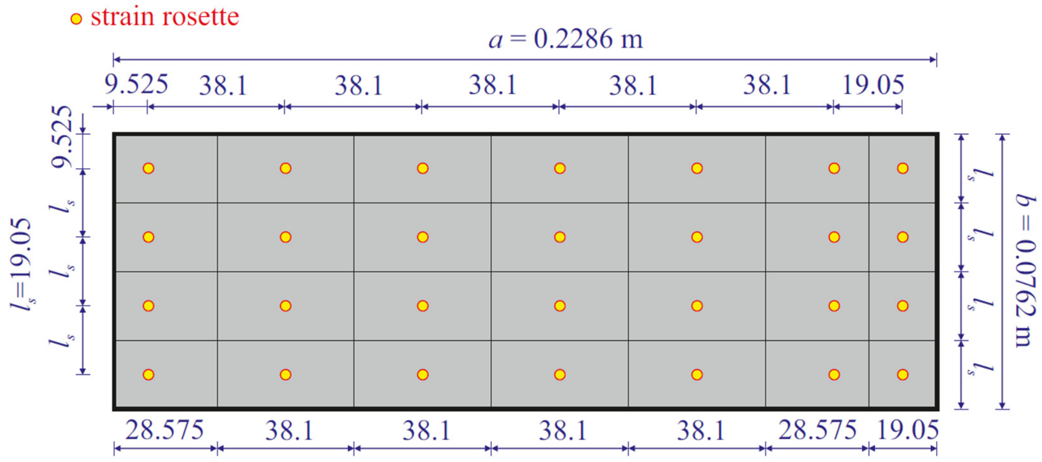

Figure 3.6 Plate discretization using 28 iQS4 elements and exact locations [mm] of strain rosettes.

To remain consistent with the work by Tessler and Spangler (2004), in the present iFEM analysis the same strain rosette locations are used. As depicted in Figure 3.6, the iQS4 model has 28 rectangular-shaped elements each having a single strain rosette. Except for eight of the strain rosettes (i.e., the first four which are near to the clamped edge and the second four which are near to the loading edge), the strain rosettes are placed at the centroids of each iQS4 element. Since the material properties of the plate are symmetric with respect to the mid-plane and the resulting deformations are due to bending only, the strain distribution is anti-symmetric with respect to the mid-plane and hence the strain rosettes need only be positioned on one of the bounding surfaces (in this case, the top surface) of the iQS4 elements.

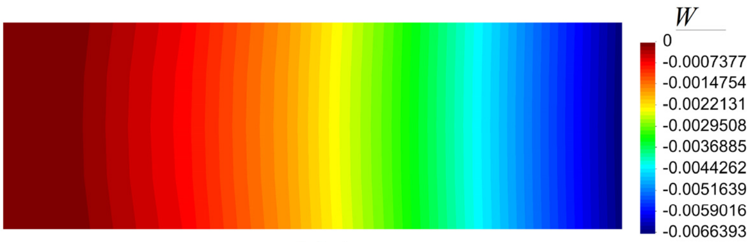

(a) iFEM

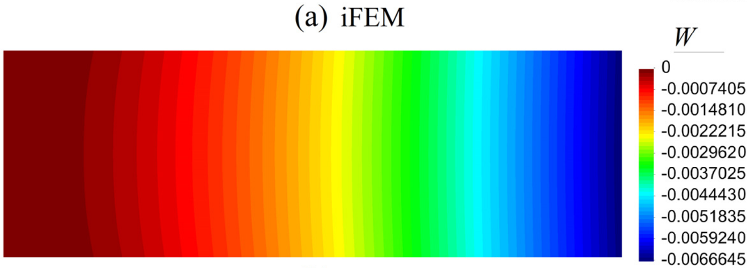

(b) FEM

Figure 3.7 Contour plots of W displacement: (a) iFEM analysis using 28 iQS4 elements and a single strain rosette per element; (b) Direct FEM analysis.

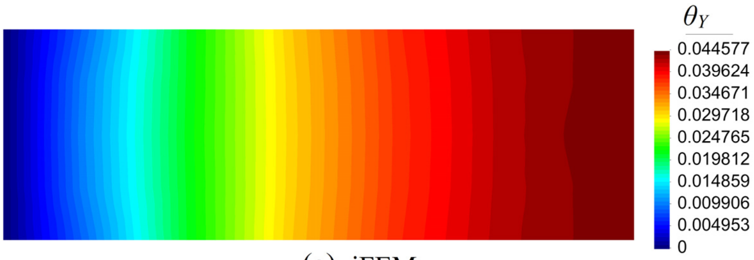

(a) iFEM

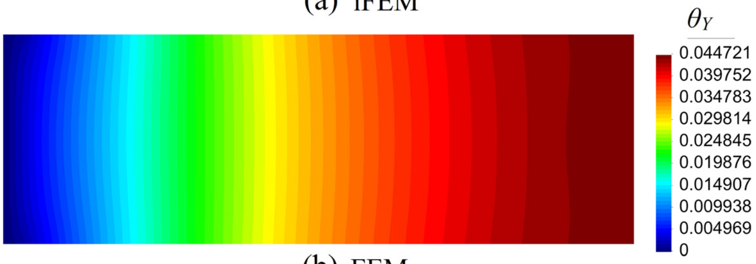

(b) FEM

Figure 3.8 Contour plots of θ_Y rotation: (a) iFEM analysis using 28 iQS4 elements and a single strain rosette per element; (b) Direct FEM analysis.

In Figures 3.7-9, contour plots for the transverse displacement and two bending rotations are compared between the iFEM and high-fidelity FEM analyses. The percent difference between the iFEM and FEM predictions for the maximum deflection is only 0.4%; this result is in close agreement with the predictions of Tessler and Spangler (2004). Similar accuracy is evidenced for the maximum bending rotations, with the percent difference of 0.3% for the *Y*-rotation, and 1.5% for the *X*-rotation. Both the iFEM and direct FEM contours are graphically indistinguishable in the figures. These results also confirm the superior bending predictions of iQS4, especially considering the low-fidelity mesh used in the iFEM analysis.

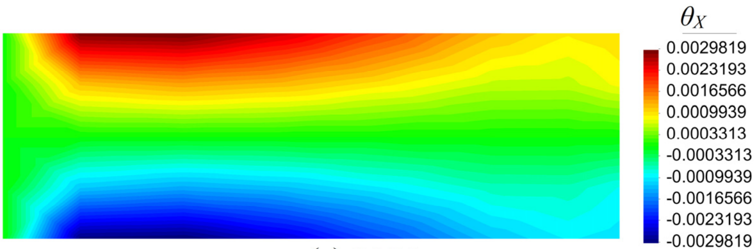

(a) iFEM

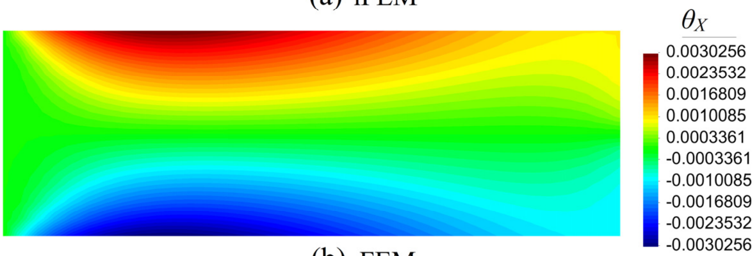

(b) FEM

Figure 3.9 Contour plots of θ_X rotation: (a) iFEM analysis using 28 iQS4 elements and a single strain rosette per element; (b) Direct FEM analysis.

3.4.2 A short cantilever beam under shear loading

The shear-loaded short cantilever beam has been used by many authors, e.g., Allman (1988), Ibrahimbegovic et al. (1990), to validate the membrane response of new elements. Herein, this problem is revisited to assess the membrane capability of iQS4. The length L, the dimensions $a \times 2h$ of the constant rectangular cross section, the elastic modulus E, and the Poisson's ratio v of the beam are given in Figure 3.10. The right edge of the beam is subjected to a shear loading P, whereas the left edge of the beam is fully clamped.

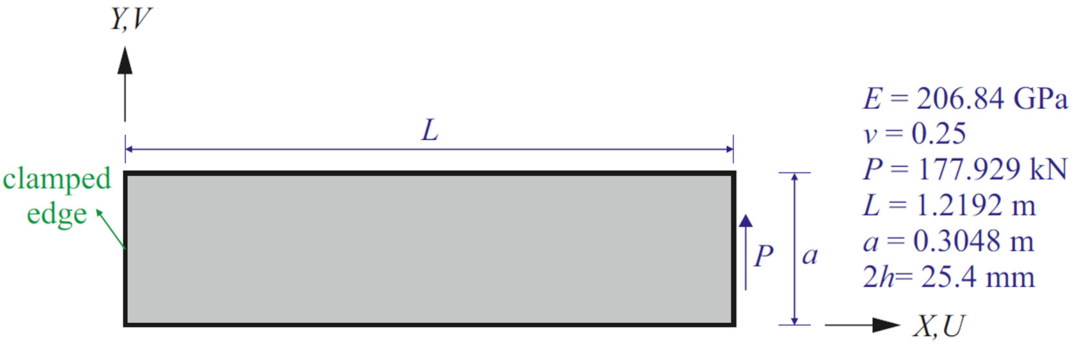

Figure 3.10 Short cantilever beam under shear loading at free edge.

According to Timoshenko and Goodier (1951), the elasticity solution of the vertical displacement of the tip, V , is

$$V = \frac{2PL^3}{Eha^3} + \frac{(4+5v)PL}{4Eah} = 9.025 \text{ mm} \tag{3.94}$$

for the properties are described in Figure 3.10. To establish an accurate reference solution, a convergence study was performed using direct FEM analysis. The highest fidelity mesh has 1,024 uniformly distributed square elements and 2,210 DOF. The maximum V displacement obtained from the direct FEM analysis is 9.042 mm which agrees well with the analytical solution. These FEM deflections are used to calculate the simulated in situ strains.

Two different iFEM beam analyses are performed using varying number of strain rosettes. Since the material properties and the resulting membrane deformations of the beam are symmetric with respect to the mid-plane, the strain rosettes can be placed on one of the bounding surfaces (in this case, the top surface). In the first example, the iQS4 model of the beam has 64 square-shaped elements each having a single rosette as depicted in Figure 3.11. To investigate the effect of drilling rotation, the iFEM beam analyses are performed by both including and excluding the drilling rotation. In Figure 3.12, contour plots for the V displacements are compared between these two cases. The iFEM and direct FEM analyses produce the maximum V displacement that differs only by 0.5% when the drilling rotation is included; it is 6.2% when the drilling rotation is excluded.

In the second example, the same problem is analyzed once again using a coarser iQS4 discretization that has only 16 square-shaped elements, each having a single-strain rosette as illustrated in Figure 3.13. To demonstrate the effect of drilling rotation on the membrane response, contour plots of the V displacement are shown in Figure 3.14, where the results correspond to the cases of including and excluding the drilling rotation. The iFEM and direct FEM predictions for the maximum deflection are identical when the drilling rotation is included in the iQS4 element formulation. By excluding the drilling rotation, the maximum V displacement is underestimated by 19.2%. These results demonstrate that iQS4 has a superior membrane-response capability when implemented with the hierarchical drilling rotation. The formulation also decreases the tendency toward membrane locking.

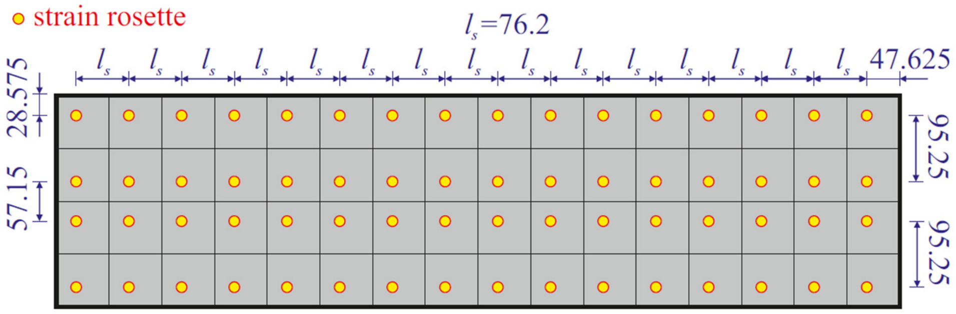

Figure 3.11 Short cantilever beam discretized using 64 iQS4 elements and exact locations [mm] of strain rosettes.

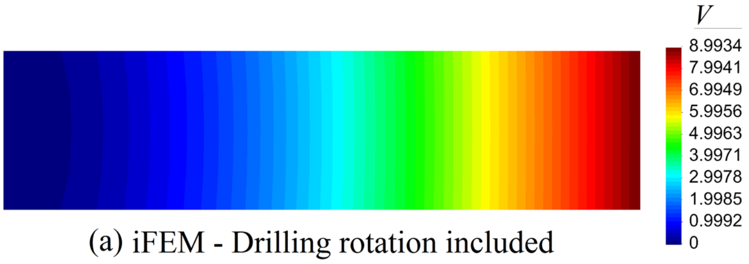

(a) iFEM - Drilling rotation included

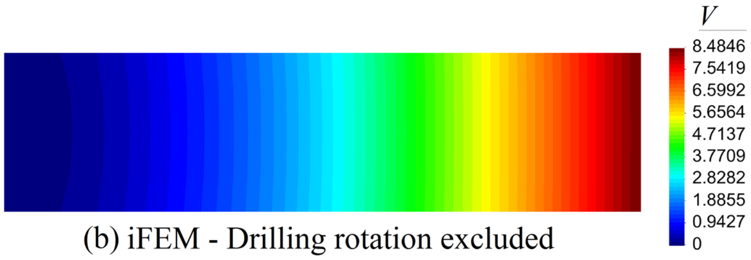

(b) iFEM - Drilling rotation excluded

Figure 3.12 Contour plots of V displacement for short cantilever beam corresponding to iFEM analysis of 64 iQS4 element model: (a) Drilling rotation included; (b) Drilling rotation excluded.

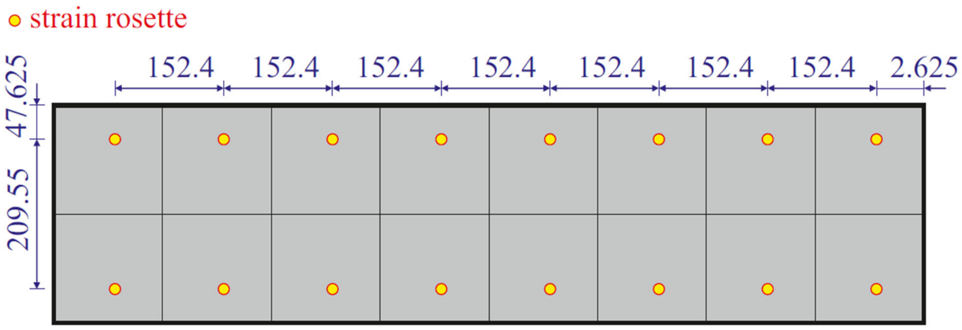

Figure 3.13 Short cantilever beam discretized using 16 iQS4 elements and exact locations [mm] of strain rosettes.

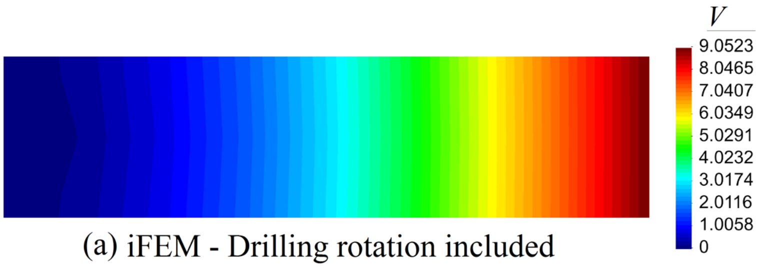

(a) iFEM - Drilling rotation included

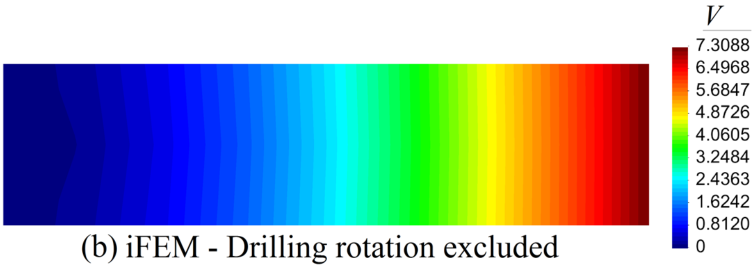

(b) iFEM - Drilling rotation excluded

Figure 3.14 Contour plots of V displacement for short cantilever beam corresponding to iFEM analysis of 16 iQS4 element model: (a) Drilling rotation included; (b) Drilling rotation excluded.

3.4.3 A thin-walled cylinder

In the previous examples described in Sections 3.4.1-2, bending and membrane capabilities of the iQS4 element have been assessed by way of simple plate and beam problems. In many practical engineering applications, however, more complicated structural topologies are common. Herein, a thin-walled cylinder having radius of 1 m, length of 5 m and uniform thickness of 20 mm is analyzed to demonstrate the robustness of the iFEM/iQS4 methodology for modelling realistic shell structures. The cylinder is made of steel having an elastic modulus of 210 GPa and the Poisson's ratio of 0.3. Both ends of the cylinder are fixed in terms of translations and rotations and a concentrated force F = 100 kN is applied at twelve different locations as illustrated in Figure 3.15.

The prescribed boundary conditions and geometry are suitable to take advantage of the symmetry planes. As shown in Figure 3.16, only one-eighth of the cylinder needs to be modelled while applying the appropriate symmetry boundary conditions. The translations along the normal axis and the rotations around the in-plane axes are constrained for each symmetry plane. For instance, the XY plane symmetry conditions are imposed constraining the translation along the Z-direction and the rotations around the X- and Y-directions.

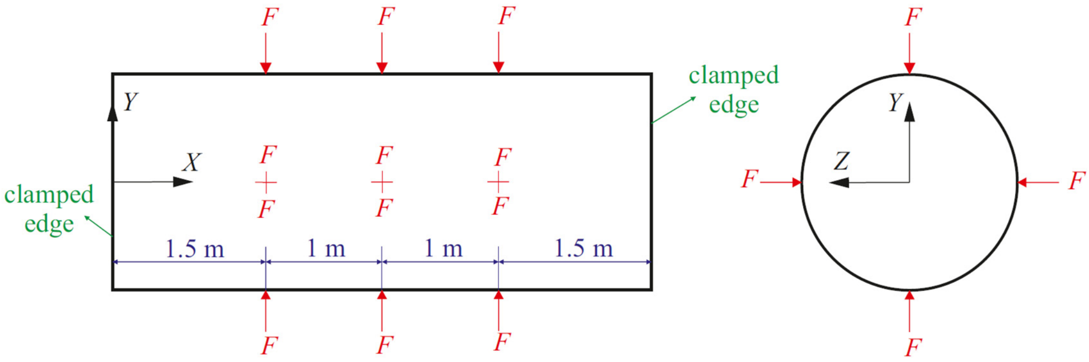

Figure 3.15 Thin-walled cylinder under concentrated forces.

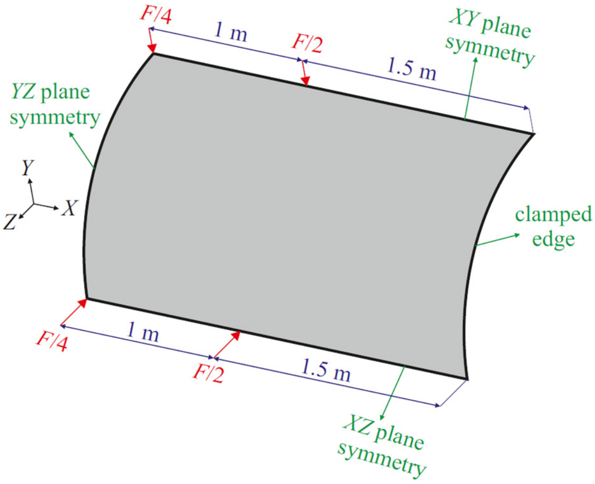

Figure 3.16 One-eighth of thin-walled cylinder with symmetric boundary conditions.

To establish an accurate reference solution for this problem, an FEM convergence study was carried out. The highest fidelity mesh has 2400 uniformly distributed rectangular elements and 15006 DOF. The FEM deflections and rotations are used to calculate the simulated strain-sensor strains. Then, three different iFEM analyses of the cylinder were performed using three different strain-rosette networks. Although the material properties of the cylinder are symmetric with respect to the mid-plane, the resulting deformations exhibit both stretching and bending response due to the complexity of the structural topology. Hence, the strain rosettes have to be placed on both the top and bottom surfaces of the cylinder. In the first case study, the iQS4 discretization is identical to the highest-fidelity mesh used in the direct FEM analysis. As presented in Figure 3.17, the iQS4 model has 2400 uniformly distributed rectangular elements each having two strain rosettes, one on the centroid of the top surface and the other one on the centroid of the bottom surface. In Figures 3.18-19, the iFEM and FEM contour plots for U_T and θ_T are presented, showing the results that are graphically indistinguishable. The percent difference between the iFEM and FEM solutions for the maximum values of U_T and θ_T are respectively 1% and 0.06%.

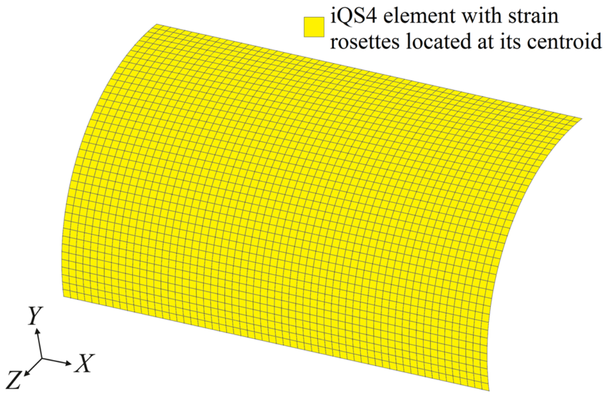

Figure 3.17 Discretization of one-eighth of thin-walled cylinder using 2400 iQS4 elements with top- and bottom-surface strain rosettes per each element.

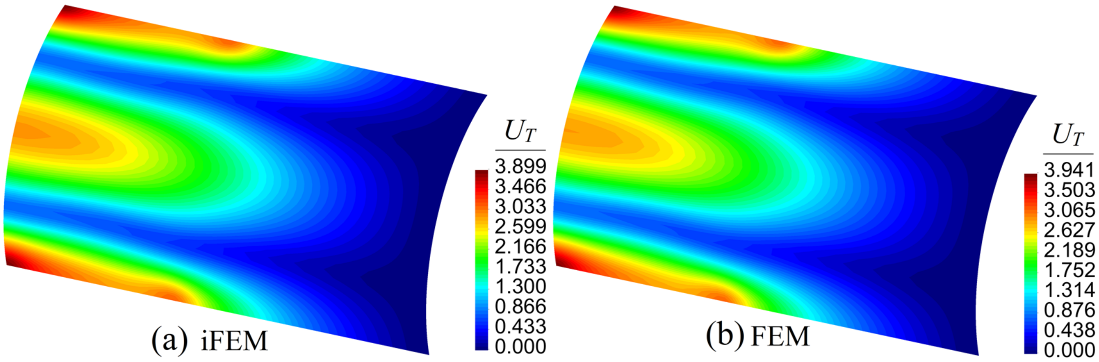

Figure 3.18 Contour plots of U_T displacement for thin-walled cylinder modelled in Figure 3.17: (a) iFEM/ iQS4 analysis; (b) Direct FEM analysis.

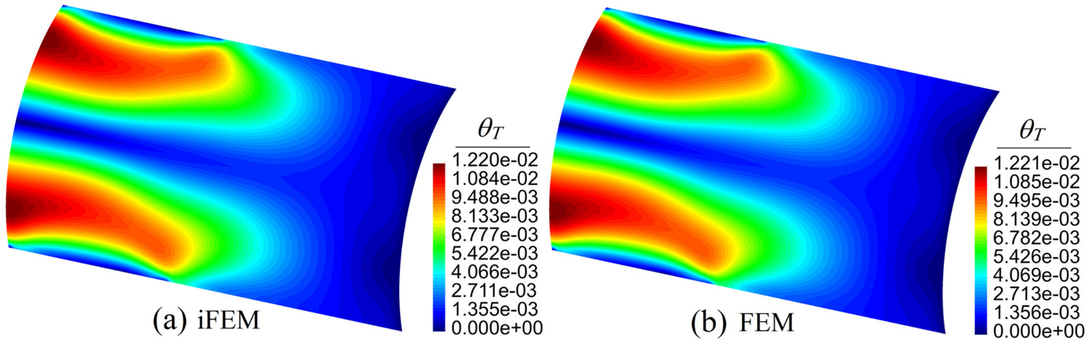

Figure 3.19 Contour plots of θ_T rotation for thin-walled cylinder modelled in Figure 3.17: (a) iFEM/ iQS4 analysis; (b) Direct FEM analysis.

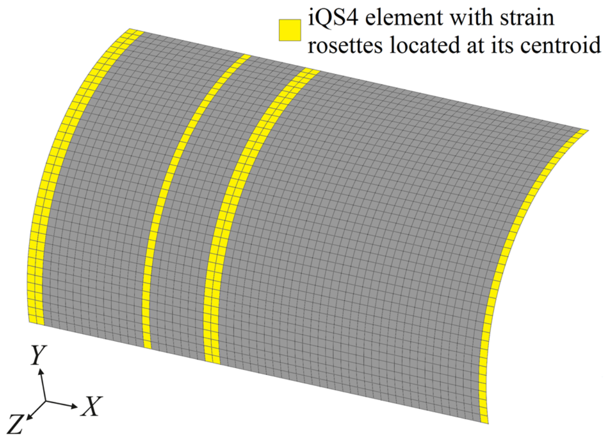

Figure 3.20 Discretization of one-eighth of thin-walled cylinder using 2400 iQS4 elements with top- and bottom-surface strain rosettes located within 240 selected elements.

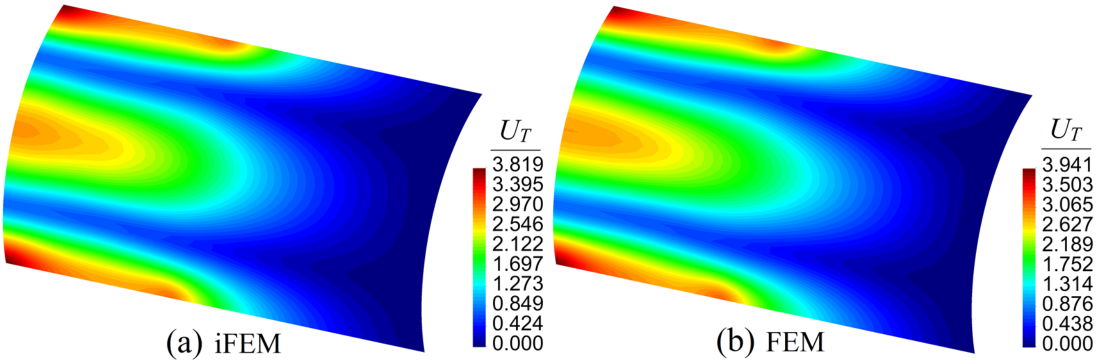
(a) iFEM
(b) FEM

Figure 3.21 Contour plots of U_T displacement for thin-walled cylinder modelled in Figure 3.20: (a) iFEM/ iQS4 analysis; (b) Direct FEM analysis.

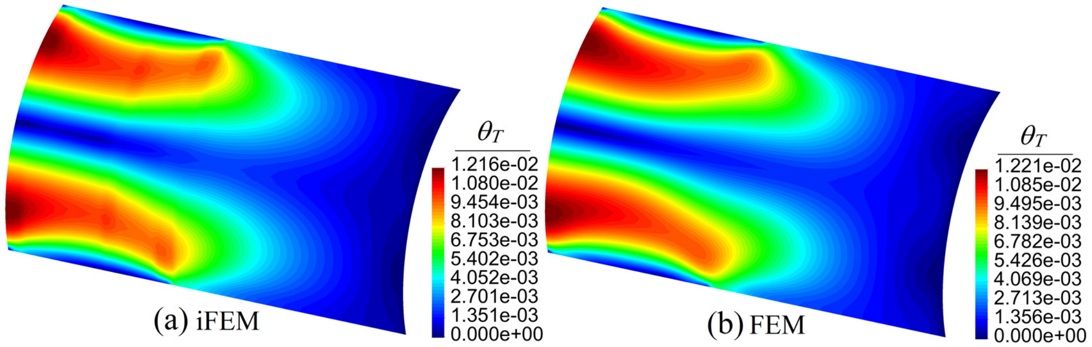
(a) iFEM
(b) FEM

Figure 3.22. Contour plots of θ_T rotation for thin-walled cylinder modelled in Figure 3.20: (a) iFEM/ iQS4 analysis; (b) Direct FEM analysis.

Although the results of first case study are satisfactory, the number of strain rosettes used may be considered too high for a practical application. In the second case study shown in Figure 3.20, the top- and bottom-surface strain rosettes are removed from 2160 iQS4 elements, with the resulting iQS4 mesh having only 240×2 strain rosettes. For an iQS4 element which has no in situ strain components, the corresponding weighting coefficients are set to 10^{-4}. In Figures 3.21-22, the contour plots for the U_T displacement and θ_T rotation are depicted for both the iFEM and high-fidelity FEM analyses. The percent difference between the iFEM and FEM predictions for the maximum U_T displacement is 3%, whereas it is only 0.5% for maximum total rotation. Remarkably, the iFEM contours are almost identical to those of FEM. The iFEM predictions remain sufficiently accurate even with the missing strain-rosette data in many elements.

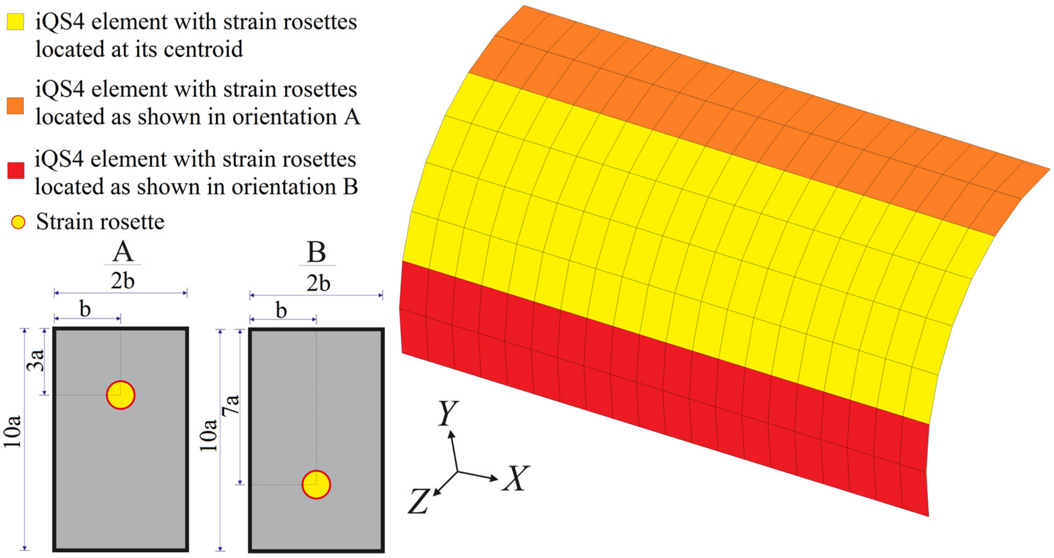

Figure 3.23 Discretization of one-eighth of thin-walled cylinder using 160 iQS4 elements with top- and bottom-surface strain rosettes located within each element.

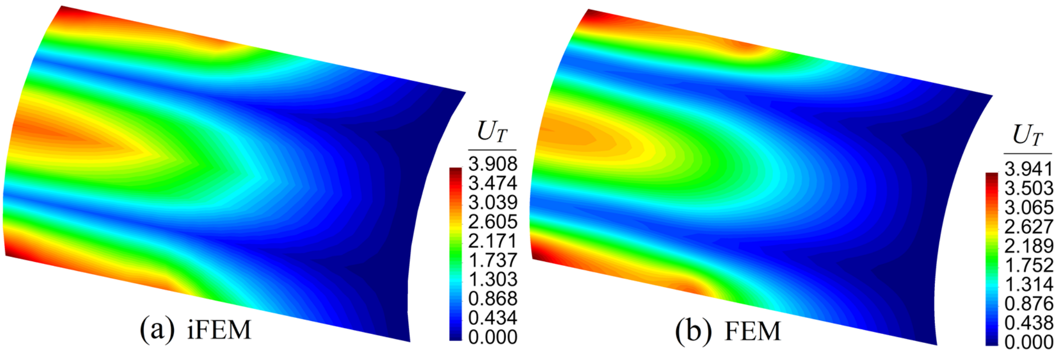

(a) iFEM (b) FEM

Figure 3.24 Contour plots of U_T displacement for thin-walled cylinder modelled in Figure 3.23: (a) iFEM/ iQS4 analysis; (b) Direct FEM analysis.

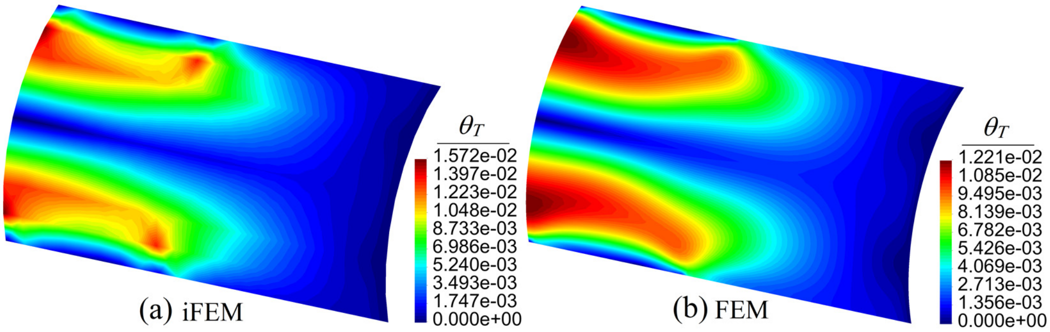

Figure 3.25 Contour plots of θ_T rotation for thin-walled cylinder modelled in Figure 3.23: (a) iFEM/ iQS4 analysis; (b) Direct FEM analysis.

In the third case study, the iQS4 model of the cylinder has 160 uniformly distributed rectangular elements each having top- and bottom-surface strain rosettes located as shown in Figure 3.23. The iFEM analysis is performed using the strain data obtained from 160×2 strain rosettes only. In Figures 3.24-25, the contour plots for the U_T displacement and θ_T rotation are presented for both the iFEM and high-fidelity FEM analyses. According to the contour plots in Figure 3.24, the percent difference between the iFEM and FEM predictions for the maximum U_T displacements is less than 1%. These results demonstrate the superior accuracy of the iFEM/iQS4 capability even when very coarse discretizations are used. Even though the percent difference between the iFEM and FEM predictions for the maximum θ_T rotation is approximately 29%, the iFEM and FEM contour plots are generally in good agreement (refer to Figure 3.25).

3.4.4 The effects of noisy strain measurements on the accuracy of the iFEM solution

The iFEM/iQS4 methodology is ultimately aimed at real engineering structures where the measured strains may be relatively noisy. Therefore, to examine iFEM/iQS4 predictive capabilities in the presence of noisy strain data, the thin-walled cylinder considered in the previous study (vid. Section 3.4.3) is revisited herein. The iFEM analyses of the cylinder are performed once again using strain data which have 5% and 10% of noise, respectively.

Signal-to-noise ratio (SNR) characterizes the relative strength of a desired signal and background noise. The SNR describes the ratio of the amplitude of the signal to the amplitude of the noise. Since SNR is a dimensionless quantity and many signals can have a wide dynamic range, SNR can be expressed on the logarithmic decibel (dB) scale as

$$SNR_{dB} = 10\log_{10}\left(\frac{P_{signal}}{P_{noise}}\right) \tag{3.95}$$

where P_{signal} and P_{noise} are respectively the average power of the signal and noise. Equation (3.95) indicates that a larger SNR typically results in a less noisy measurement, whereas a smaller SNR results in a more noisy measurement.

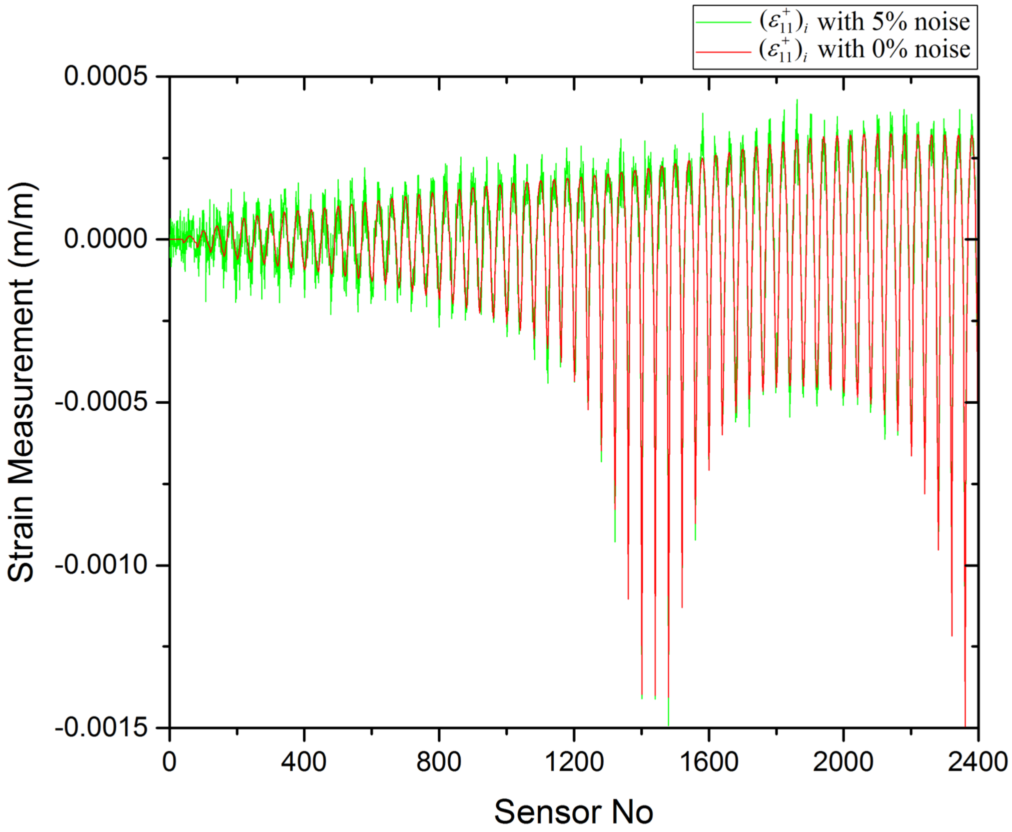

Figure 3.26 Top surface strain measurements $(\varepsilon_{11}^{+})_i$ with 0% and 5% noise.

Using Equation (3.95), SNR values corresponding to 5% noise and 10% noise can be calculated as 13.01 dB and 10 dB, respectively. The white Gaussian noise is added to the surface strain measurements for each of the specified SNR values using the built-in function *awgn()* in the Matlab/Octave toolbox. To give an example, in Figures 3.26-

27, the top surface strain measurements $(\varepsilon_{11}^{+})_i$ with 0% noise are compared to those with 5% and 10% noise. These comparisons show that the added noise levels generate significant differences in the strain measurements for each sensor.

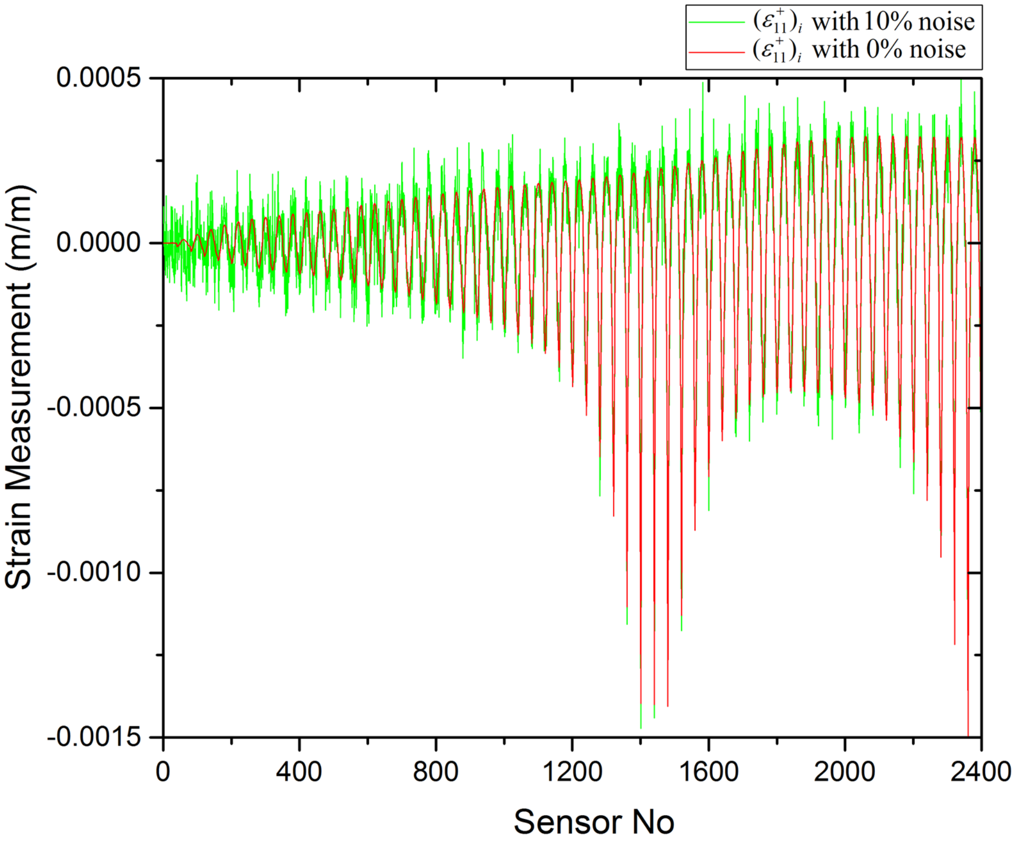

Figure 3.27 Top surface strain measurements $(\varepsilon_{11}^{+})_i$ with 0% and 10% noise.

Once the iFEM analyses of the thin-walled cylinder are performed using strain data that include 5% and 10% noise levels, percent difference between iFEM and direct FEM predictions for U_T displacement can be calculated for each node i as

$$PD\left(U_T\right) \equiv PD_i = \left| \frac{U_{T,i}^{iFEM} - U_{T,i}^{FEM}}{U_{T,\max}^{FEM}} \right| \times 100\% \tag{3.96}$$

where $U_{T,i}^{iFEM}$ is iFEM prediction for the U_T displacement at node i, $U_{T,i}^{FEM}$ is direct FEM prediction for the U_T displacement at node i, and $U_{T,\max}^{FEM}$ is direct FEM prediction of the maximum U_T displacement. In Figure 3.28, contour plots of $PD\left(U_T\right)$, corresponding to the model in Figure 3.17, are shown for the strain data with the noise levels of 0%, 5%, and 10%. The results clearly demonstrate the superior accuracy of the iFEM solutions even when the in situ strain measurements include noise up to 10%.

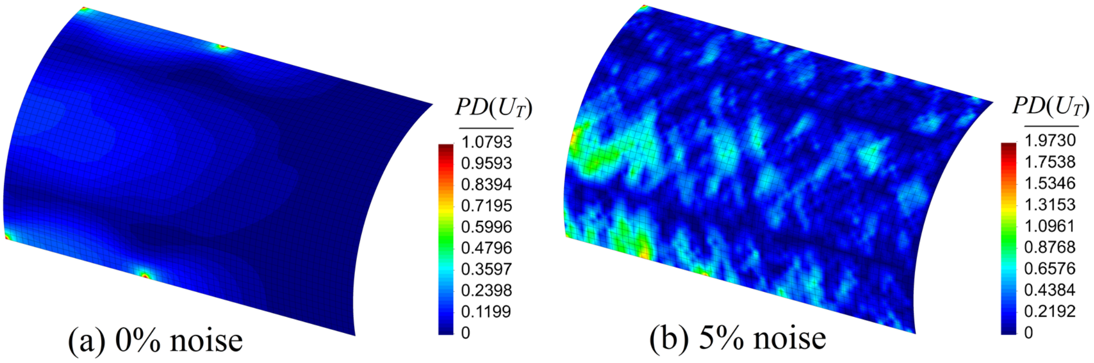

(a) 0% noise

(b) 5% noise

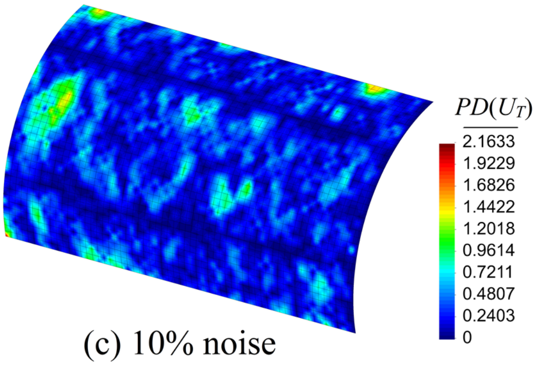

(c) 10% noise

Figure 3.28 Contour plots of $PD(U_T)$ for thin-walled cylinder modelled in Figure 3.17, with the percent noise in strain measurements: (a) 0%, (b) 5%, and (c) 10%.

Moreover, the mean-percent difference, MPD, and the root-mean-square difference, $RMSD$, comparing iFEM and FEM predictions for the U_T displacement, are calculated as

$$MPD = \frac{1}{N_n} \sum_{i=1}^{N_n} PD_i \tag{3.97}$$

and

$$RMSD = \sqrt{\frac{\sum_{i=1}^{N_n} \left(U_{T,i}^{iFEM} - U_{T,i}^{FEM} \right)^2}{N_n}} \tag{3.98}$$

where N_n is the total number of nodes.

Table 3.1 MPD for U_T displacement corresponding to iFEM/iQS4 models with noisy strain measurements.

iFEM/iQS4 Model	MPD		
	0% noise	5% noise	10% noise
1	0.0667	0.2628	0.2978
2	2.0050	2.2960	2.6680
3	0.7230	0.8771	0.9138

Table 3.2 RMSD for U_T displacement corresponding to iFEM/iQS4 models with noisy strain measurements.

iFEM/iQS4 Model	RMSD		
	0% noise	5% noise	10% noise
1	0.0040	0.0139	0.0155
2	0.0954	0.1143	0.1336
3	0.0379	0.0426	0.0493

As shown in Table 3.1-2, *MPD* and *RMSD* for the U_T displacement for each iFEM/iQS4 model are compared for the cases of 0%, 5%, and 10% noise levels for the strain measurements, respectively. The results indicate that noisy strain measurements have only insignificant effect on the accuracy of the iFEM solution.

3.5 Conclusion

In this chapter, a new four-node quadrilateral inverse-shell element (iQS4) has been developed for shape-sensing analysis of plate and shell structures which have randomly distributed strain sensors. The element formulation is based on a weighted-least-squares variational principle originally developed by Tessler and Spangler (2003, 2005). The element kinematic field accommodates quadratic interpolation functions that permit a robust drilling DOF implementation that has the advantage of avoiding singular solutions when modelling complex shell structures. The formulation is also robust with respect to the membrane and shear locking phenomena. Several numerical studies have been performed and demonstrated the computational efficiency, high accuracy and robustness of iQS4 discretizations with respect to the membrane, bending, and membrane-bending coupled structural response. The practical utility of the iFEM/iQS4 technology for application to engineering structures has been assessed using relatively low- and high-fidelity discretization strategies. The effects of sensor locations, number of sensors, and inherent errors in the measured strain data have also been explored. It has been demonstrated that even in the presence of the relatively sparse strain data that are subject to experimental noise, sufficiently accurate reconstruction of the deformed structural shapes can be achieved. Finally, the iFEM/iQS4 technology is readily implemented in any general-purpose finite element code and represents a viable computational tool for real-time structural health monitoring of general plate and shell structures.

Chapter 4

Displacement and Stress Monitoring of Marine Structures

4.1 Introduction

In Chapter 3, iQS4/iFEM formulation is developed and its application to general engineering structures is demonstrated. In fact, iQS4 element is a simple, efficient, and practically very useful to model large and complex structures such as aerospace and marine vehicles. The main focus of this chapter is to perform displacement and stress monitoring of typical marine structures based on iQS4/iFEM methodology. Hence, the feasibility and applicability of the iFEM methodology will be assessed for real-time monitoring of large scale structures, in particular marine structures. In the remainder of this chapter, three different marine structures, (1) a longitudinally and transversely stiffened plate in Section 4.2, (2) a long barge having typical chemical tanker cross-section in Section 4.3, and (3) parallel mid-body of a Panamax containership in Section 4.4, are analyzed and discussed in detail. In the iFEM analysis of these structures, experimentally measured strains are simulated by strains obtained from high-fidelity FEM solutions. Besides, utilizing an in-house hydrodynamic software, hydrodynamic loads of the long barge and Panamax containership are calculated for various frequencies of head and beam sea waves, respectively. Then, these forces are applied to FEM models of the barge and containership to compute their realistic structural responses in the sea environment. Moreover, several types of iQS4/iFEM discretization strategies including models that involve relatively few locations of strain gauges are examined. Furthermore, displacement and stress solutions of the iFEM analyses are compared to those of FEM analysis in order to determine the optimum locations of the on-board sensors. Finally, concluding remarks of this chapter is given in Section 4.5. The overall study described in this chapter has been originally published in series of works conducted by Kefal and Oterkus (2015, 2016a, 2016b), and to the best of the authors' knowledge, this is first time that the iFEM formulation is applied to different types of marine structures.

4.2 Longitudinally and Transversely Stiffened Plate

Performing shape sensing of a longitudinally and transversely stiffened plate is crucial since ship structures are generally consisted of various stiffened plates. As depicted in Figure 4.1, a square plate that represents the portion of the side of a typical longitudinally and transversely framed tanker is considered to be solved based on iQS4/iFEM formulation described in Chapter 3.

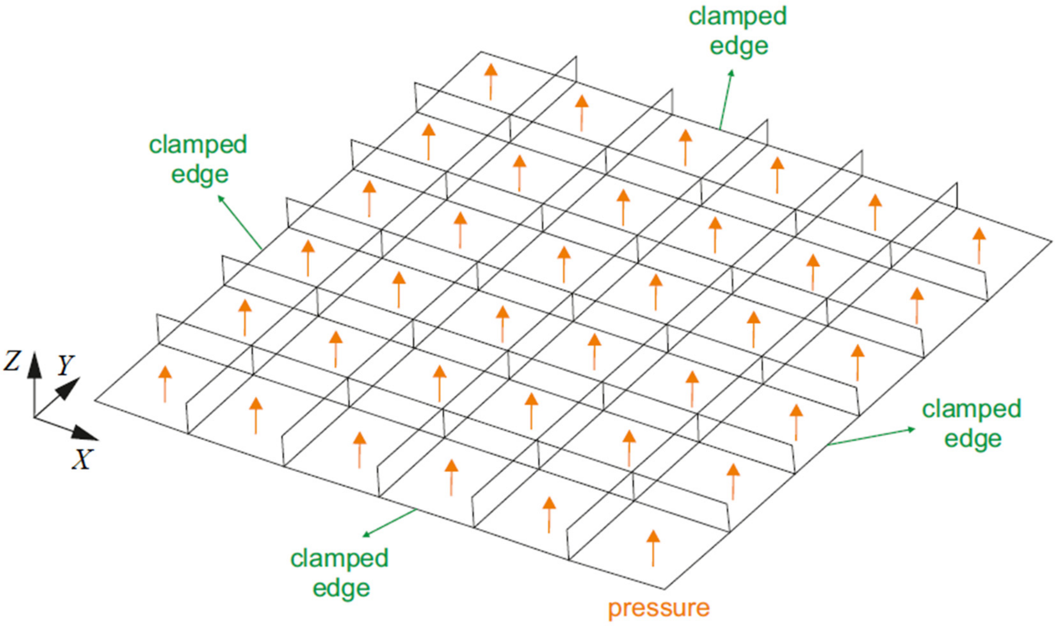

Figure 4.1 Longitudinally and transversely stiffened plate and its applied boundary conditions.

The plate has edge length of 3 m, each stiffener of the plate has a height of 150 mm, and the plate and its stiffeners have the same uniform thickness of 15 mm. The stiffened plate is made of a steel having elastic modulus of 210 GPa and Poisson's ratio of 0.3. Right, left, upper, and bottom edges of the plate including each stiffener's end edges are clamped and a static uniform transverse pressure of 40 kPa is applied to the bottom surface of the plate (refer to Figure 4.1).

To establish an accurate reference solution, a convergence study of the stiffened plate was carried out using direct FEM analysis. As presented in Figure 4.2, the highest fidelity mesh has 5400 uniformly distributed square elements and 36966 DOF. The displacements and rotations obtained from this convergence study are considered as a reference source to generate the experimental strain measurements (in situ strain data) used in following iFEM analyses.

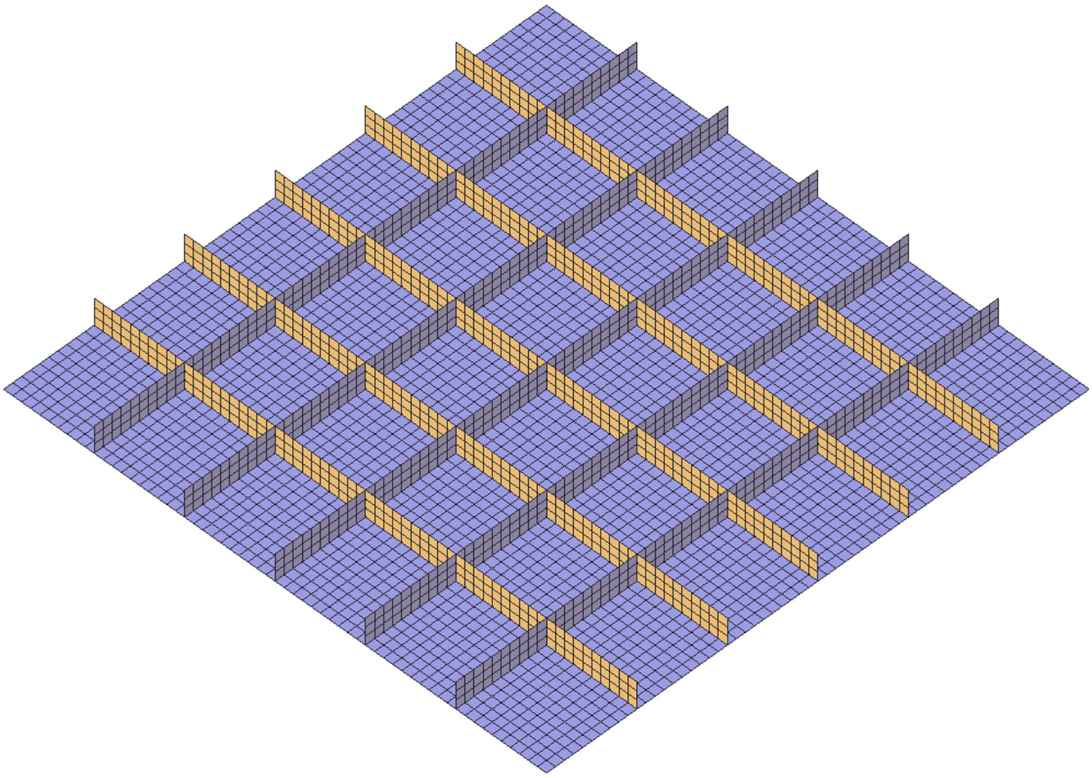

Figure 4.2 High fidelity FEM mesh of the stiffened plate.

Two different iFEM analysis of the stiffened plate are performed using varying number of strain rosettes. Although the material properties of the plate and stiffeners are symmetric with respect to the reference mid-plane, the resulting deformations exhibits both stretching and bending actions due to the complexity of the structure. Hence, the strain rosettes have to be placed on both top and bottom surfaces of structure.

In the first example, the iQS4 model of the stiffened plate consisted of 96 uniformly distributed rectangular elements each having two strain rosettes, thus total number of strain rosettes used in this case study is 96×2. As presented in Figure 4.3, strain rosettes are positioned at the center of each iQS4 element belongs to the plate, whereas each iQS4 element on each stiffener has strain rosettes placed near to reverse side of the plate.

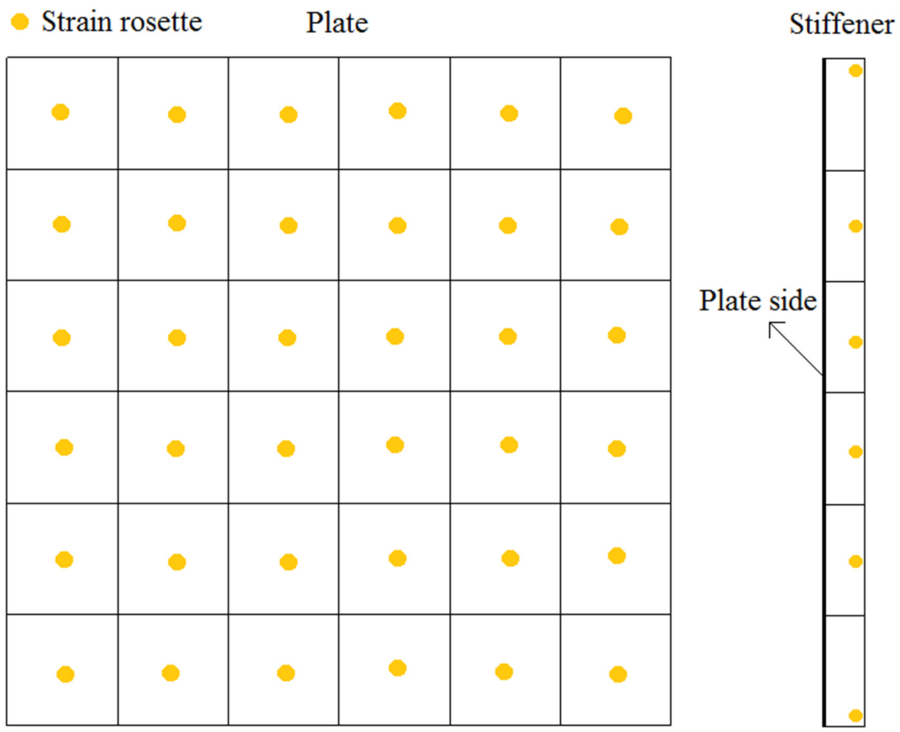

Figure 4.3 Discretization of stiffened plate using 96 iQS4 elements with top and bottom surface strain rosettes located per each element.

As depicted in Figures 4.4-5, the contour plots for U_T total displacement and θ_T total rotation are compared between iFEM and high-fidelity FEM analyses, respectively. According to the comparisons, the percent difference between iFEM and FEM predictions for the maximum displacement is 6.8% and the results are graphically agreed quite well. Even though iFEM and FEM contours for the total rotations seem slightly dissimilar from each other, the locations of maximum and minimum rotations found in iFEM and FEM analyses are in good agreement. Besides, the maximum rotation found in iFEM analysis differs only by 1.6% from those found in FEM analysis.

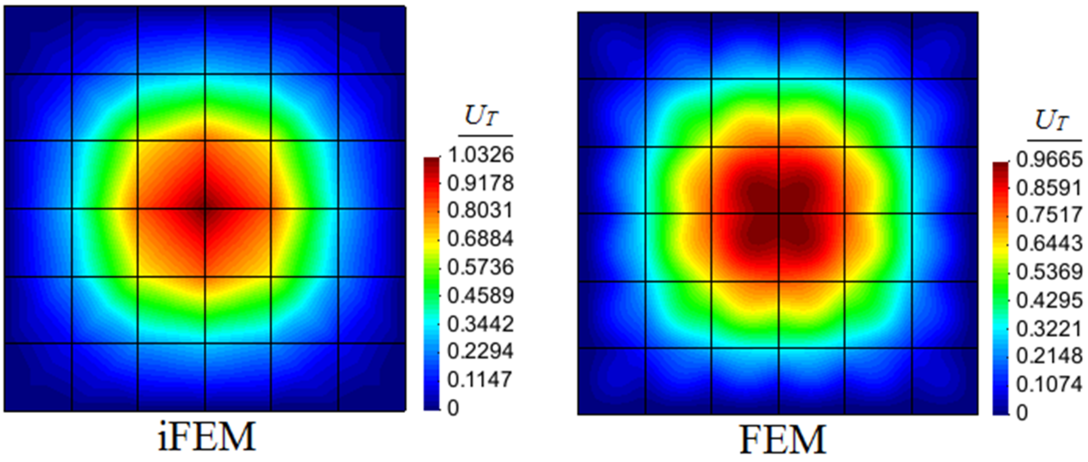

Figure 4.4 Contour plots of U_T displacement for stiffened plate modeled in Figure 4.3: iFEM/iQS4 analysis; direct FEM analysis.

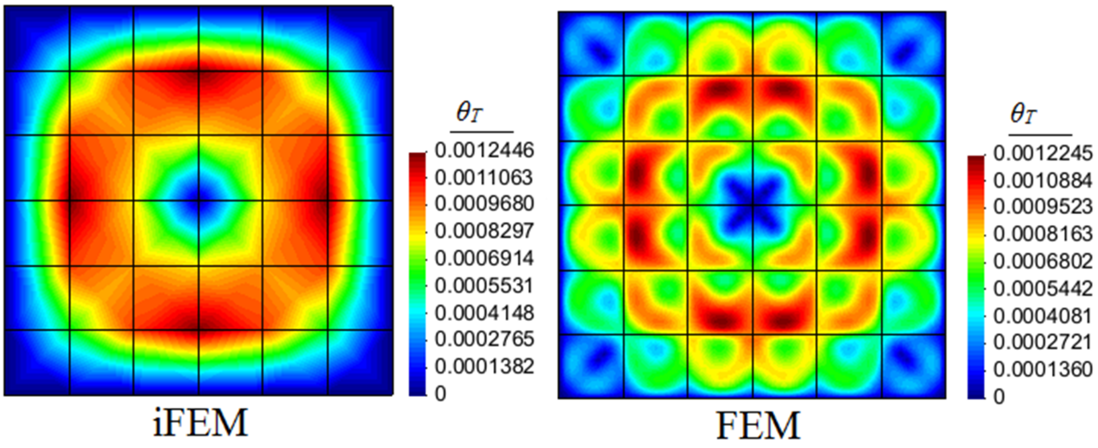

Figure 4.5 Contour plots of θ_T displacement for stiffened plate modeled in Figure 4.3: iFEM/iQS4 analysis; direct FEM analysis.

In the second example, the stiffened plate is analyzed once again using a finer iQS4 discretization that has 504 uniformly distributed rectangular elements each having two strain rosettes, one on the top surface and the other one on the bottom surface. Therefore, the iQS4 model has 504×2 strain rosettes that are located as illustrated in Figure 4.6. In Figures 4.7-8, the iFEM and FEM contour plots for U_T and θ_T are presented, showing the results that are graphically indistinguishable. The percent difference between the iFEM and FEM solutions for the maximum values of U_T and

θ_T are respectively 5.5% and 1%. These results confirms the high precision of iFEM framework when a finer iQS4 mesh including more strain rosettes is used. Moreover, these results demonstrate the superior capability of iQS4/iFEM methodology for shape sensing of the stiffened plate, i.e., primary structure of the marine structures.

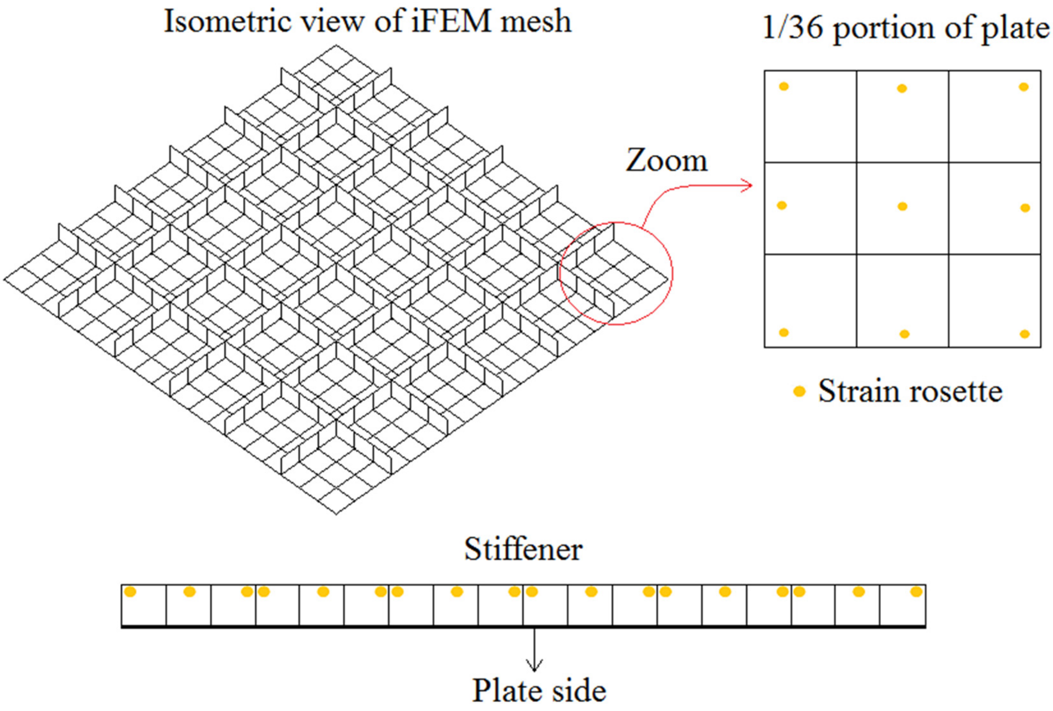

Figure 4.6 Discretization of stiffened plate using 540 iQS4 elements with top and bottom surface strain rosettes located per each element.

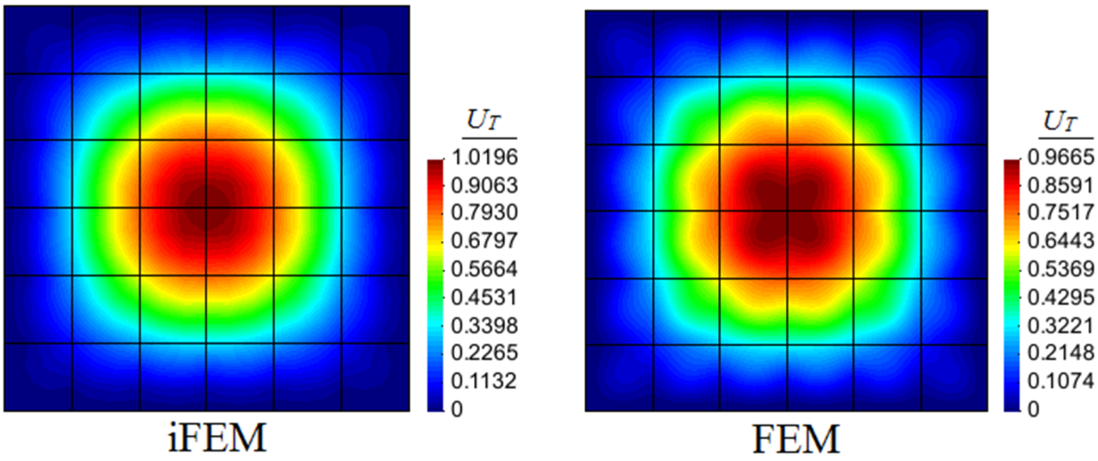

Figure 4.7 Contour plots of U_T displacement for stiffened plate modeled in Figure 4.6: iFEM/iQS4 analysis; direct FEM analysis.

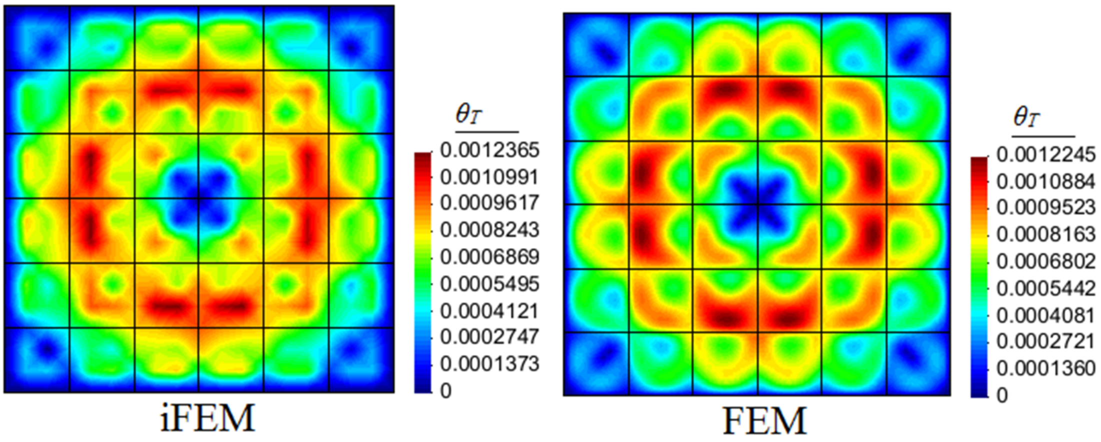

Figure 4.8 Contour plots of θ_T displacement for stiffened plate modeled in Figure 4.6: iFEM/iQS4 analysis; direct FEM analysis.

4.3 A Long Barge Floating in Head Sea Waves

In the previous section, the application of the iQS4/iFEM methodology is performed for a simple marine structure. Moreover, most of the proposed iFEM formulations (e.g., Tessler and Spangler, 2005; Tessler et al., 2011, 2012; Gherlone et al., 2012, 2014) as a numerical and experimental application on engineering structures have been limited to the SHM of aerospace vehicles (for more information, vid. Chapter 2). Hence, the main aim of this section is to apply iFEM methodology for shape and stress sensing of a chemical tanker, as a complex application to marine structures. In order to make the application more realistic and practical, a hydrodynamic analysis is performed to calculate the hydrodynamic forces. By using these forces as a loading condition, FEM analysis of the barge is performed to calculate the numerical strain data to be used as an input for the iFEM analysis. Finally, iFEM analysis of the chemical tanker is performed by utilizing the simulated strain data obtained from various locations of the structure.

4.3.1 Chemical tanker model

A typical chemical tanker cross-section as well as its structural components is presented in Figure 4.9 (Dokkum, 2003). A long barge that has a very similar cross-section to this typical chemical tanker is designed and modelled with iQS4 elements. Detailed dimensions of the barge cross-section is depicted in Figures 4.10.

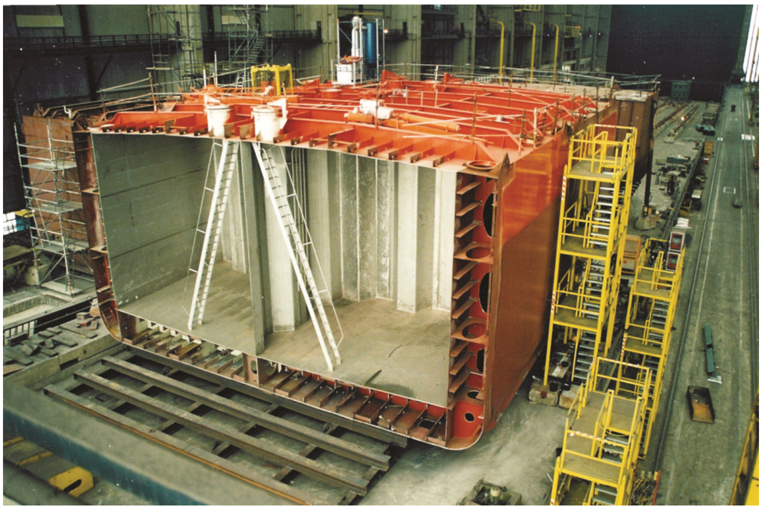

Figure 4.9 View of a tank inside a typical chemical tanker (Dokkum, 2003)

The defined global Cartesian coordinate system (X, Y, Z) has its origin ($0, 0, 0$) on the still water plane aligned vertically with the ship's center of gravity. The *XY*-plane is coincident with calm water level where *X*-axis is along the main direction of the ship, the *Y*-axis points at the port side of the ship, and *Z*-axis is positive upwards. According to the defined Cartesian coordinate system, main particulars of the barge are listed in Table 4.1.

Table 4.1 General particulars of barge

General particular	Value	Unit
Length (over all)	100	m
Breadth (moulded)	20	m
Depth (moulded)	10.5	m
Design draft (moulded)	8.25	m
Block coefficient (at design draft)	0.997	m^3/m^3
Displacement (at design draft)	16861.5	tonnes
Longitudinal center of gravity (from aft end)	50	m
Vertical center of gravity (from baseline)	5.826	m
Vertical center of buoyancy (from baseline)	4.14	m
Radius of gyration around *X*-axis	7.458	m
Radius of gyration around *Y*-axis	29.253	m
Radius of gyration around *Z*-axis	29.433	m
Radius of gyration for roll-yaw product of inertia	0	m

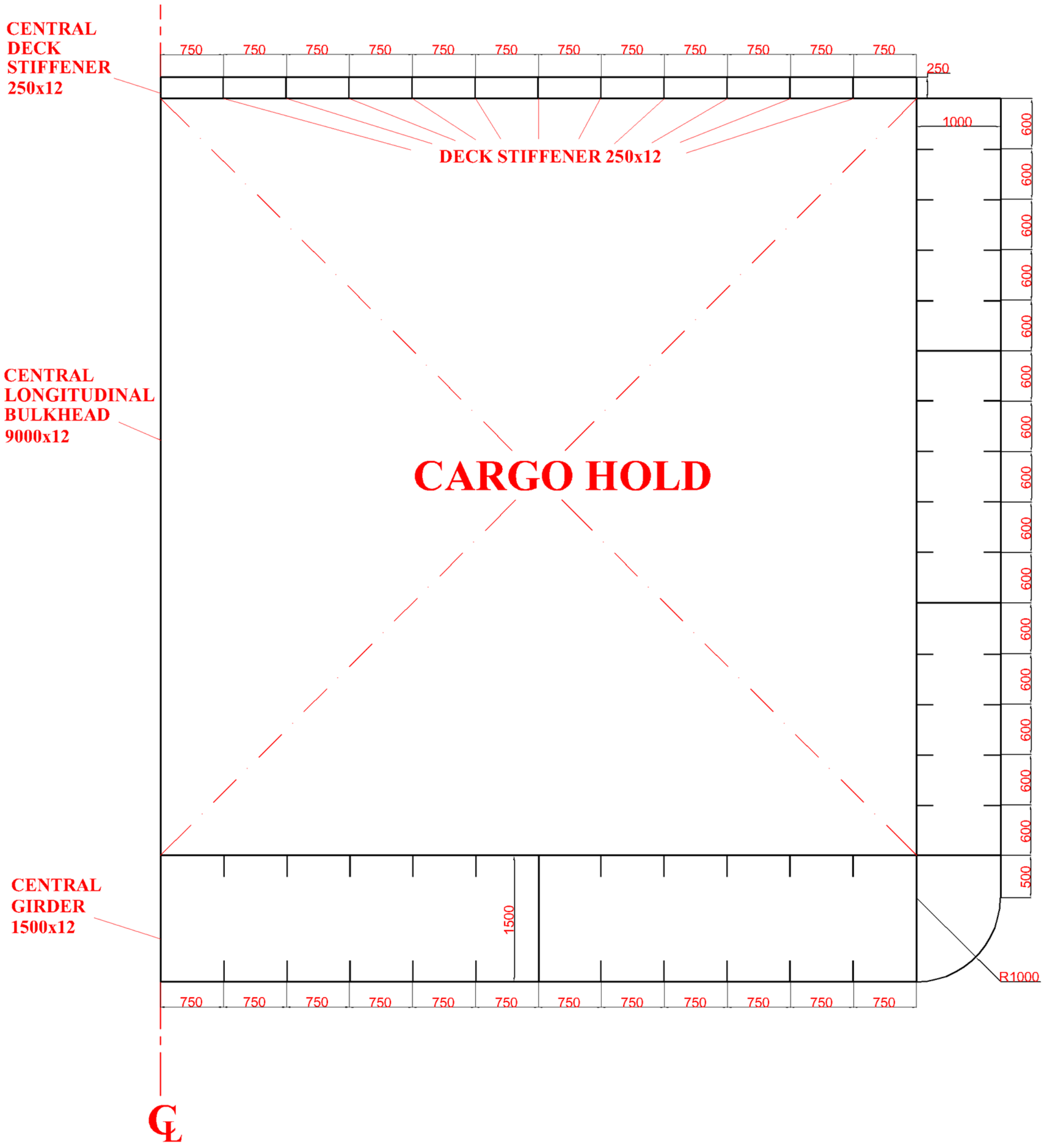

Figure 4.10 Detailed dimensions [mm] of half cross-section of the barge

It has been assumed that total number of cargo holds is eight, frame spacing between the transverse frames is 1.25 m, and all the structural components including plates, stiffeners, and bulkheads have the uniform thickness of 12 mm. All structural components of the barge are made of steel having elastic modulus of 210 GPa and Poisson's ratio of 0.3. Several isometric views of the barge structural model are illustrated in Figures 4.11 through 4.13 in order to show structural topology of the barge. Cargo tanks of the full barge model can be seen in Figure 4.11. Structural details of the quarter barge model and a detailed view of double side and bottom framing is presented in Figures 4.12 and 4.13, respectively.

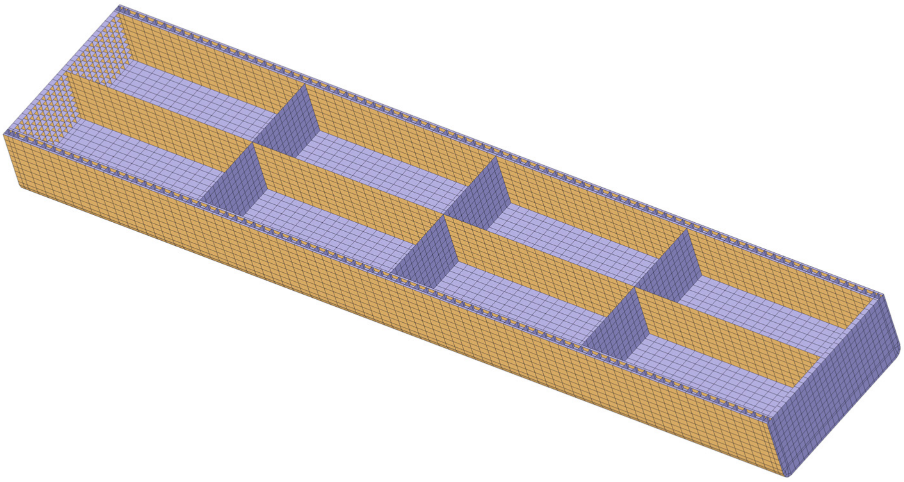

Figure 4.11 Isometric view of cargo tanks

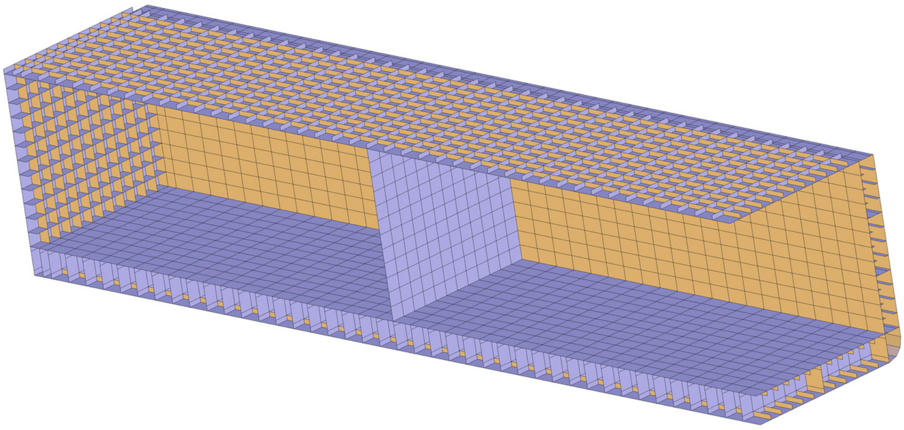

Figure 4.12 Structural details in the quarter barge model

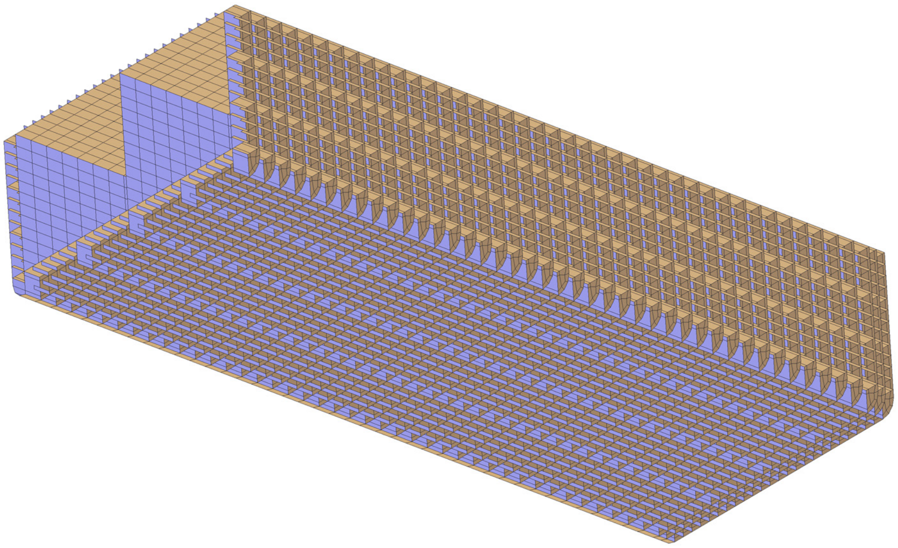

Figure 4.13 Double side and bottom framing details

4.3.2 Hydrodynamic-FEM analysis of the barge

The design of marine structures such as ships, offshore and coastal structures is significantly affected by wave-body dynamics. Therefore, hydrodynamic analysis of rigid bodies that are freely oscillating under the free water surface is extremely important. An in-house panel method code, which is a frequency-domain hydrodynamic software developed by Kefal et al. (2015), is utilized to predict the motions and wave loads of the barge. The barge is assumed to move with zero forward speed in deep water at angle $\beta = 180°$ to regular sinusoidal waves which describes the waves coming from ahead, namely head seas condition. Six DOF motions of the barge are calculated for a wave amplitude of 1 m and wave frequencies starting from 0.2 rad/s to 1.5 rad/s. Full hydrodynamic model of the barge is discretized by using 2508 flat quadrilateral panels as shown in Figure 4.14.

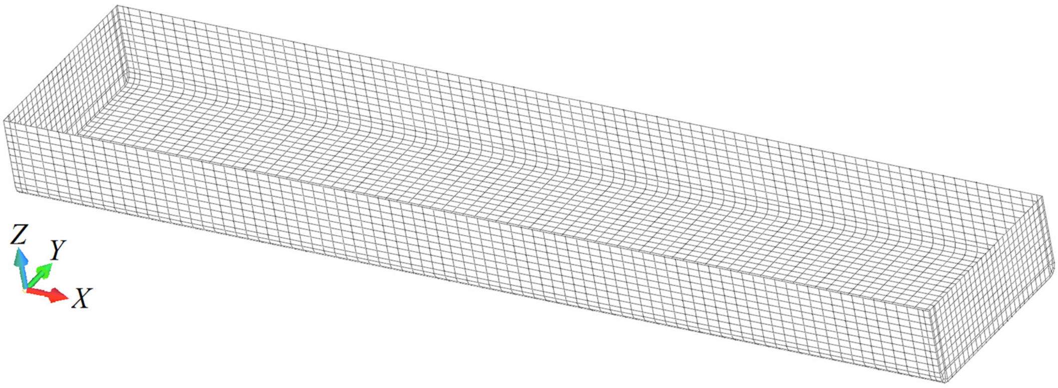

Figure 4.14 Full hydrodynamic model of the barge

The discretized body, namely coordinates of nodes used to generate the panels and nodal connectivity of these panels, is the main input for the in-house frequency-domain hydrodynamic software. The software first calculates radiation and diffraction source strengths and then velocity potentials at the centroids of the hydrodynamic panels for requested heading and frequency based on three dimensional potential flow theory and zero speed Green's function (Wehausen and Laitone, 1960; Noblesse, 1982; Newman, 1985).

Since the barge floats in head seas condition, the in-house panel method code takes into account the advantage of the lateral symmetry condition (*XZ*-plane symmetry) and generates the source strength results by using only 1254 panels. By utilizing the velocity potentials of radiated and diffracted waves, the software solves a complex form of linear and harmonic oscillatory rigid body motion equation with respect to the barge center of gravity and generates the six DOF motion results of the barge. The numerical sway, roll and yaw motion amplitudes with respect to barge center of gravity are negligibly small and in fact these results are theoretically zero because the barge is affected by head sea waves only. The motion amplitudes with respect to the barge's center of gravity for the remaining directions namely surge, heave, and pitch are illustrated in Figures 4.15.

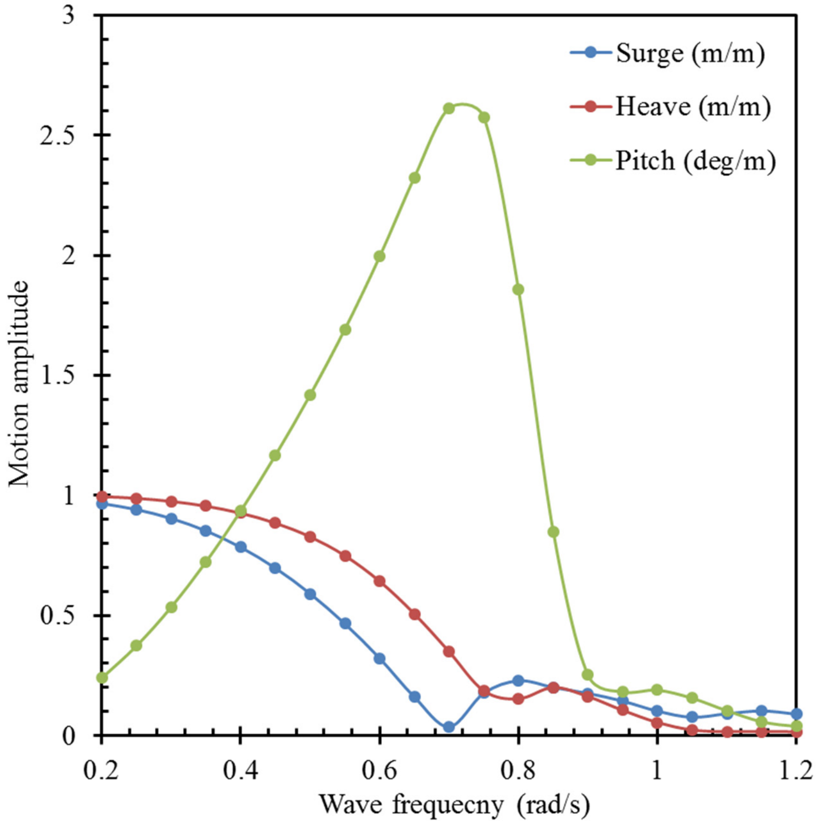

Figure 4.15 Barge's motion amplitudes with respect to wave frequencies

The change of the motion amplitudes in surge, heave and pitch directions is significant around the frequency value of 0.5 rad/s in terms of structural analysis because the oscillatory dynamic pressure calculated at this frequency causes the highest vertical bending moment distribution along the length of the barge. The hydrodynamic force variation along the barge underwater panels due to the oscillation at 0.5 rad/s is plotted in Figure 4.16.

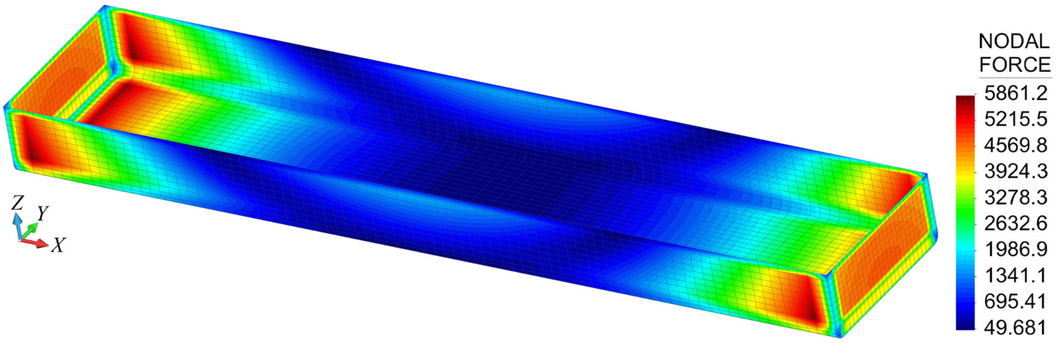

Figure 4.16 Contour plot of total hydrodynamic force [N] acting on the barge for the wave frequency value of 0.5 rad/s

For a floating structure, it is important to obtain equilibrium before performing a direct FEM analysis because an imbalanced model causes an unrealistic result. Therefore, computed hydrodynamic forces and their corresponding inertia loads are applied to the direct FEM model of the structure in order to find a realistic global structural response of the barge. Application of inertia loads is done by associating the acceleration vector to each finite element while hydrodynamic forces are applied to the nodes of each finite element below still water. Barge geometry and its constraint conditions as well as loading conditions are symmetric with respect to both *XZ* and *YZ*-plane. So, there is no need to perform direct FEM analysis of the entire structure. Hence, only one quarter of the barge is discretized by using 6908 nodes and 11065 elements (most of them are rectangular-shaped) as shown in Figure 4.17.

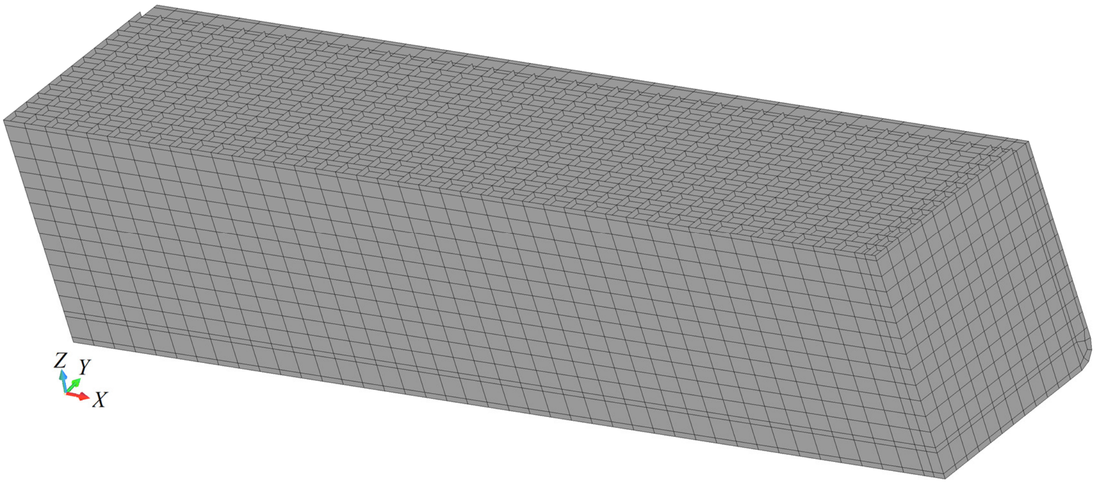

Figure 4.17 Discretization of one quarter of the barge using 11065 elements.

For the application of constraint conditions, translation along normal direction of symmetry plane and rotations around the symmetry plane axial directions are fixed for each symmetry plane. Moreover, the structural model is fixed by an artificial support along *Z*-direction in order to disable the rigid body motion. After performing the FEM analysis, the reaction force calculated at this artificial support is checked to ensure that it doesn't affect the actual equilibrium of hydrodynamic pressures and inertia loads. The loading conditions are also applied by considering the symmetry planes. As mentioned earlier, the resulting total deflection and rotation obtained from direct FEM analysis are used to produce the simulated sensor-strain data.

4.3.3 Case studies for iFEM analysis of the barge

Three different case studies of the barge are considered based on iFEM methodology by using different number of strain rosettes and their altered locations. An iFEM model, which is composed of iQS4 elements and geometrically identical to the quarter mesh model used in direct FEM analysis (Figure 4.17), is adopted in the following iFEM analysis. The strain rosettes have to be placed at the top and bottom surfaces of the iQS4 elements whose resulting deformations exhibits both stretching and bending actions due to the complexity of the barge structure. However, for the iQS4 elements whose mid-planes are superimposed on the *XZ* and *YZ* symmetry planes of the barge, the strain rosettes are only located at the top surface of these elements. Since the material properties are symmetric with respect to mid-planes of these iQS4 elements and their resulting deformations are due to stretching only, the strain distributions are symmetric with respect to their mid-planes.

In the first case, all the iQS4 elements used in discretization of iFEM model are assumed to be installed with strain sensors in order to examine the results when one-to-one mapping of the relevant strain data from direct FEM to iFEM analysis is made. Therefore, the total number of iQS4 elements that are installed with strain rosettes is 11065 from which 688 and 236 of them belongs to the *XZ* and *YZ* symmetry planes of the barge, respectively. As mentioned earlier, the strain rosettes are placed at the centroids of the top surfaces of these 924 iQS4 elements, whereas the strain rosettes are positioned on the centroids of both the top and bottom surfaces of the remaining 10141 iQS4 elements. Thus, the total number of the strain rosettes is 21206. Since the barge structure is constructed with thin shells, the weighting constants associated with the transverse shear strains are set as $w_\alpha = 10^{-4}$ $(\alpha = 7,8)$, whereas the remaining weighting constants for membrane strains and bending curvatures are respectively set as $w_\alpha = 1$ $(\alpha = 1-6)$. The total displacement results found in iFEM analysis are shown together with the reference FEM results in Figure 4.18.

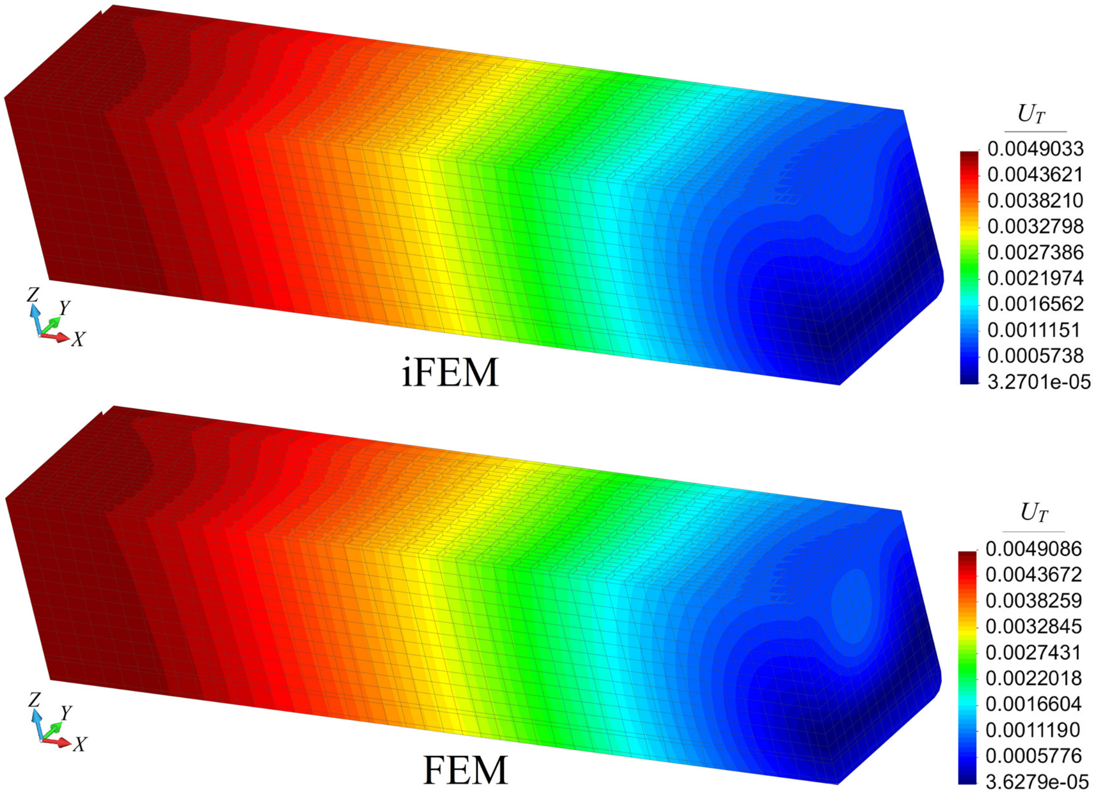

Figure 4.18 Contour plots of U_T displacement [m] for the barge: iFEM/iQS4 analysis for one-to-one strain data; direct FEM analysis.

According to the distributions, both maximum displacements are approximately 4.9 mm confirming that iFEM methodology can capture very promisingly expected results when all the structural components in one quarter of the barge are installed with strain sensors.

Once a full field deformed shape of the barge is obtained, the full field von Mises stresses on the top surfaces of the shells are calculated in iFEM analysis and compared with those found in direct FEM solution. Both von Mises stress distributions are plotted together in Figure 4.19 and contours of stress colors are identically matching each other. Moreover, the difference between the maximum von Mises results is 2.23% proving the superior accuracy of iFEM algorithm.

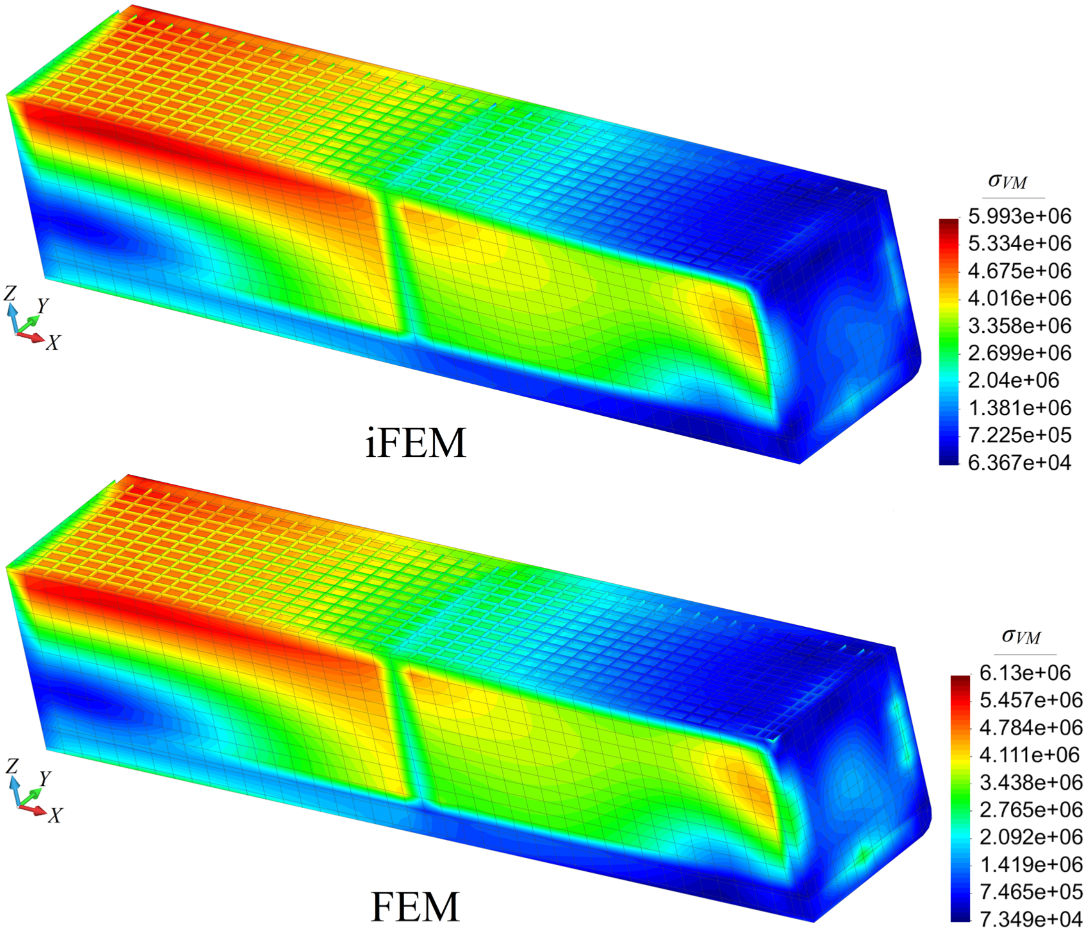

Figure 4.19 Contour plots of σ_{VM} von Mises stress [Pa] for the barge: iFEM/iQS4 analysis for one-to-one strain data; direct FEM analysis.

Secondly, iFEM analysis of the barge is performed when all strain rosettes used in the first case study are removed except the ones glued on the central deck stiffener, the central longitudinal bulkhead, and the central girder. This case study is done to assess the precision of iFEM methodology when there are missing in situ strain measurements. After removal of the strain rosettes, iFEM analysis of the barge is conducted by using the strain data collected from 688 iQS4 elements which are superimposed on the *XZ* symmetry plane of the barge. The strain rosettes are only positioned on the centroids of top surfaces of these 688 iQS4 elements. Therefore, total number of strain rosettes count as 688 for this case study. The exact locations of the strain rosettes are clearly illustrated in Figure 4.20.

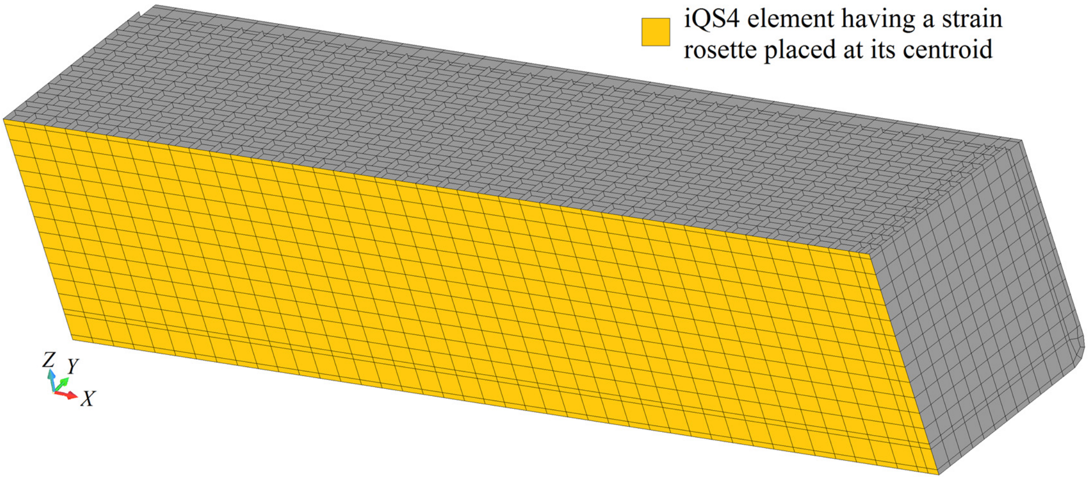

Figure 4.20 Discretization of the one quarter of the barge using 11065 iQS4 elements with top surface strain rosette located within 688 selected elements.

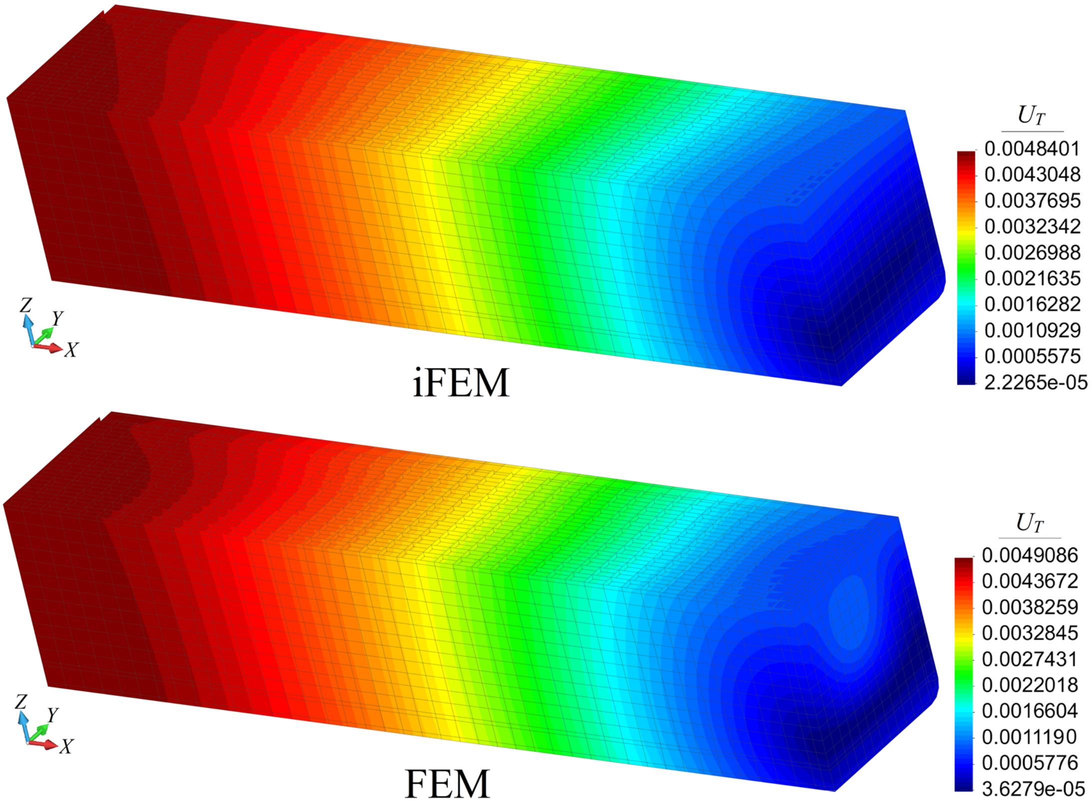

Figure 4.21 Contour plots of U_T displacement [m] for the barge modeled in Figure 4.20: iFEM/iQS4 analysis; direct FEM analysis.

For iQS4 elements on which the strain data is available, the membrane strain's weighting constants and bending curvature's weighting constants are both set as

$w_{\alpha} = 1\ (\alpha = 1-6)$, while their transverse shear strain's weighting constants are set as $w_{\alpha} = 10^{-4}\ (\alpha = 7,8)$. For iQS4 elements that do not have any sensors, namely strain-less iQS4 elements, their weighting constants are set as $w_{\alpha} = 10^{-4}\ (\alpha = 1-8)$. In both iFEM and direct FEM analysis, the von Mises stresses are evaluated according to the top surfaces of the shells. As depicted in Figure 4.21-22, the total displacements as well as the von Mises stresses obtained from iFEM analysis are respectively compared with direct FEM results.

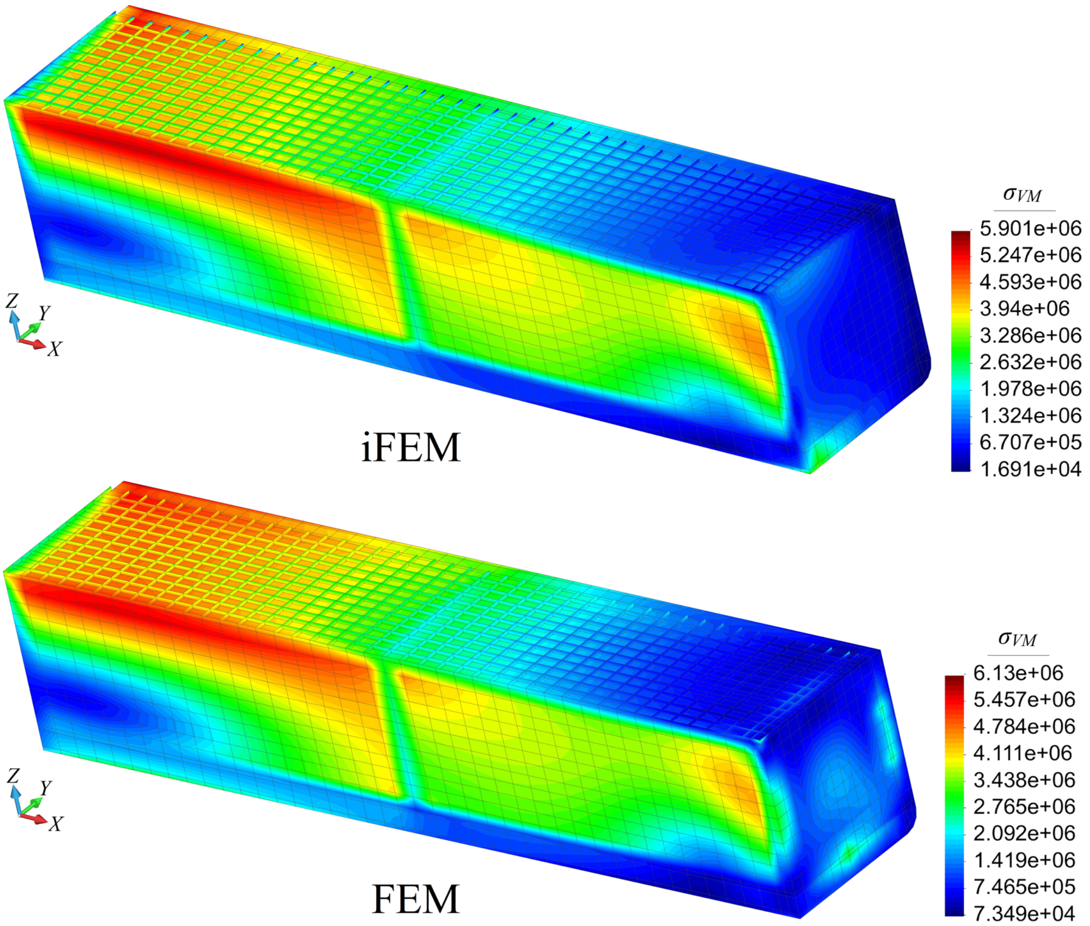

Figure 4.22 Contour plots of σ_{VM} von Mises stress [Pa] for the barge modelled in Figure 4.20: iFEM/iQS4 analysis; direct FEM analysis.

The iFEM-reconstructed displacement and von Mises stress fields fairly agree with the reference displacement and von Mises stress results. The error between the maximum displacements is 1.41%, whereas the error is 3.74% for von Mises stress comparison.

Hence, this accuracy confirms the robustness of iFEM framework even if there are missing in situ strain measurements.

Although the results obtained in the first two case studies are completely satisfactory, the proposed number of strain rosettes may be high for a practical application. Therefore, in the third case study, the iFEM analysis of the barge is performed based on the same mesh, but only using the strain data obtained from strain rosettes located at the central deck stiffener, the central girder and several critical locations on the central longitudinal bulkhead including the neutral axis of the barge, the edge near to deck, and the edges near to the transverse bulkhead. The aim of this case study is to ultimately assess the practical applicability of iFEM methodology and to examine the precision of iFEM formulation with respect to the effect of sensor locations and number of sensors. After eliminating majority of the strain sensors, the strain data collected from 196 iQS4 elements are used to perform shape- and stress-sensing of the barge. Similar to the second case study, each of these 196 iQS4 elements are installed with only one strain sensor on the centroid of the top surface because these inverse elements belong to *XZ* symmetry plane. Therefore, the total number of stain rosettes is decreased to 196 and the exact locations of these sensors are clearly presented in Figure 4.23.

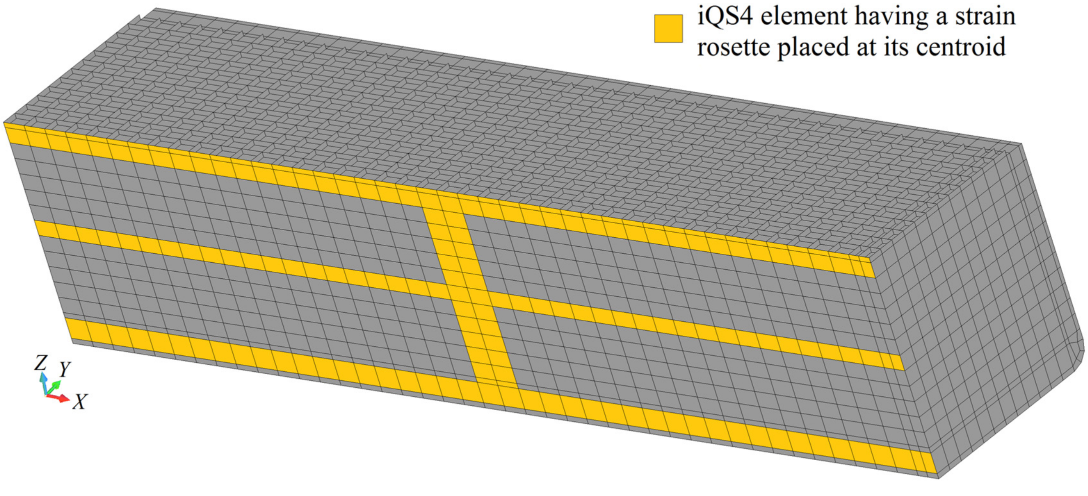

Figure 4.23 Discretization of one quarter of the barge using 11065 iQS4 elements with top surface strain rosette located within 196 selected elements.

As in the second case study, the weighting coefficients are set to $w_\alpha = 10^{-4}$ $(\alpha = 1-8)$ for each strain-less iQS4 elements, whereas they are set to $w_\alpha = 1$ $(\alpha = 1-6)$ and $w_\alpha = 10^{-4}$ $(\alpha = 7,8)$ for each iQS4 element on which the strain sensors are located. In Figure 4.24, the contour plots for total displacements are compared between iFEM and FEM analysis. Remarkably, the iFEM contours are almost identical to those of FEM.

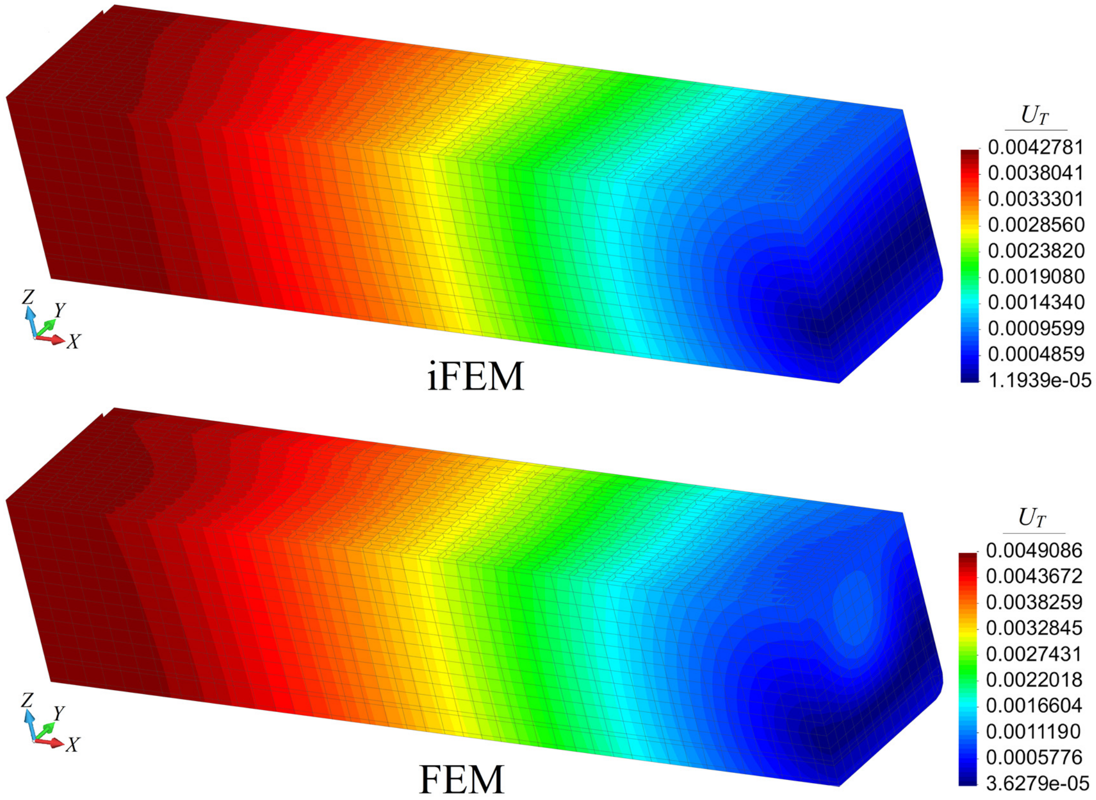

Figure 4.24 Contour plots of U_T displacement [m] for the barge modelled in Figure 4.23: iFEM/iQS4 analysis; direct FEM analysis.

The percent difference between iFEM and FEM predictions for the maximum displacement is 12.85%, confirming that a sufficiently accurate displacements can be reconstructed even if using few number of strain-sensors. In Figure 4.25, the iFEM and FEM contours for von Mises stresses computed at the top surfaces of the shells are presented, showing that the results are graphically in good agreement. The iFEM and FEM produce the maximum von Mises stress that differs by 15.56%. This numerical results verify that it is still possible to reconstruct adequately precise von Mises stress even with the missing strain-rosette data in many elements. According to results of three case studies, it can be concluded that iFEM methodology is a promising and practical technology for accomplishing accurate displacement and stress monitoring of complex marine structures.

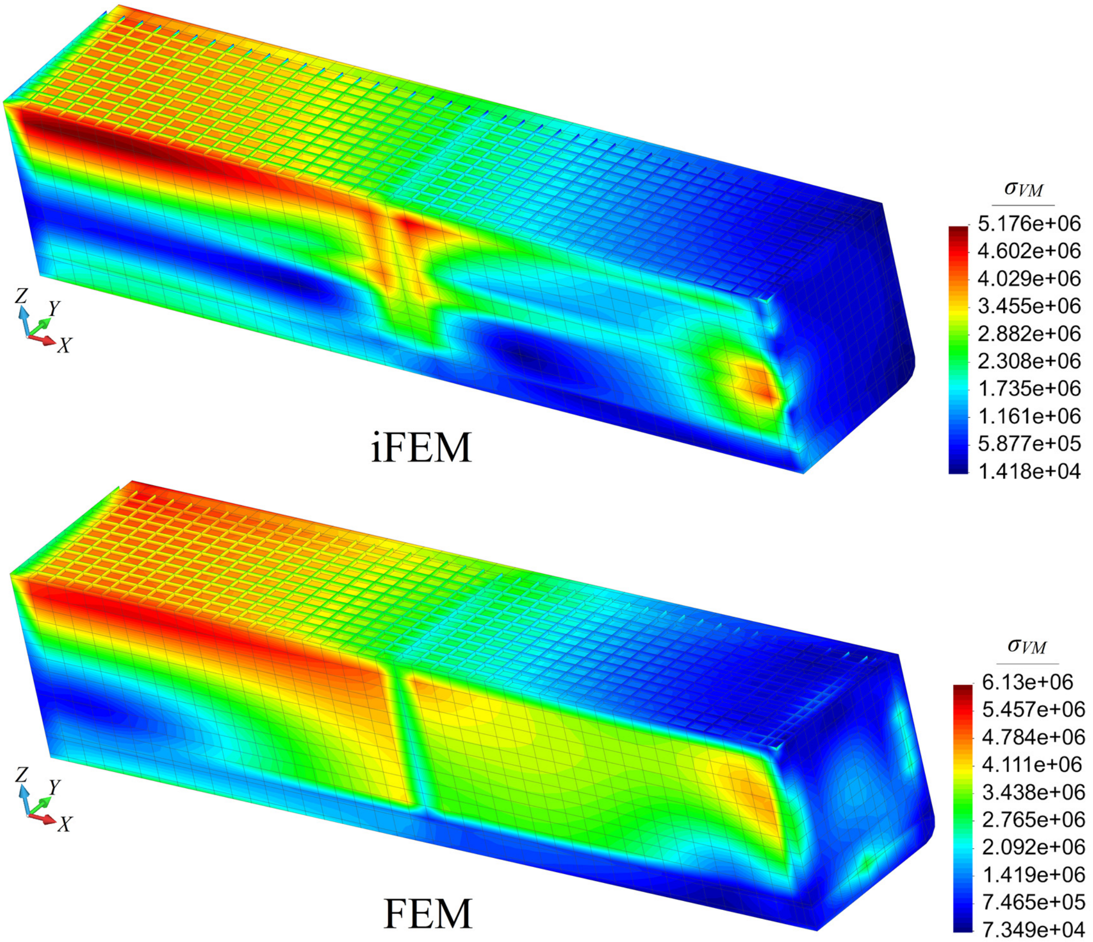

Figure 4.26 Contour plots of σ_{VM} von Mises stress [Pa] for the barge modelled in Figure 4.23: iFEM/iQS4 analysis; direct FEM analysis.

4.4 A Panamax Containership Floating in Beam Sea Waves

In the previous section, a sophisticated application of iFEM to marine structures, i.e., displacement and stress monitoring of a chemical tanker, is performed for sea state of head sea waves because this phenomenon of ship advancing in waves can be very crucial for closed-decked ships such as chemical tanker. However, for open-decked ships such as containerships, head sea wave loads may be less important than beam sea wave loads due to torsional and warping stresses induced by torsional moments. Therefore, the main focus of this section is to demonstrate the application of the iFEM methodology for monitoring multi-axial deformations and stresses of a containership floating in beam sea waves. For this purpose, the “smart methodology” proposed by Kefal et al. (2015) is followed and optimum sensor locations are determined for a parallel mid-body of a Panamax containership. Firstly, hydrodynamic analysis of the containership is performed for beam sea waves. Secondly, several direct FEM analyses of the parallel mid-body are performed using the hydrodynamic wave bending and torsion moments. Thirdly, experimentally measured strains are simulated by strains obtained from high-fidelity FEM solutions. Finally, three different iFEM analyses of the parallel mid-body are performed for three different cases; (1) pure vertical bending case, (2) pure horizontal bending case and (3) pure torsion case.

4.4.1 Panamax containership model

The body plan of S175 containership, given by Wu and Hermundstad (2002), is used as a “parent ship hull form” in order to design a Panamax containership. First of all, the hull form of the Panamax containership is obtained performing several hull form transformations of the S175 containership. These transformations are (1) linearly scaling based upon the characteristic breadth, and (2) linearly lengthening the parallel mid-body. Once the design of the hull form is completed, a typical mid-ship section is also designed for the Panamax containership.

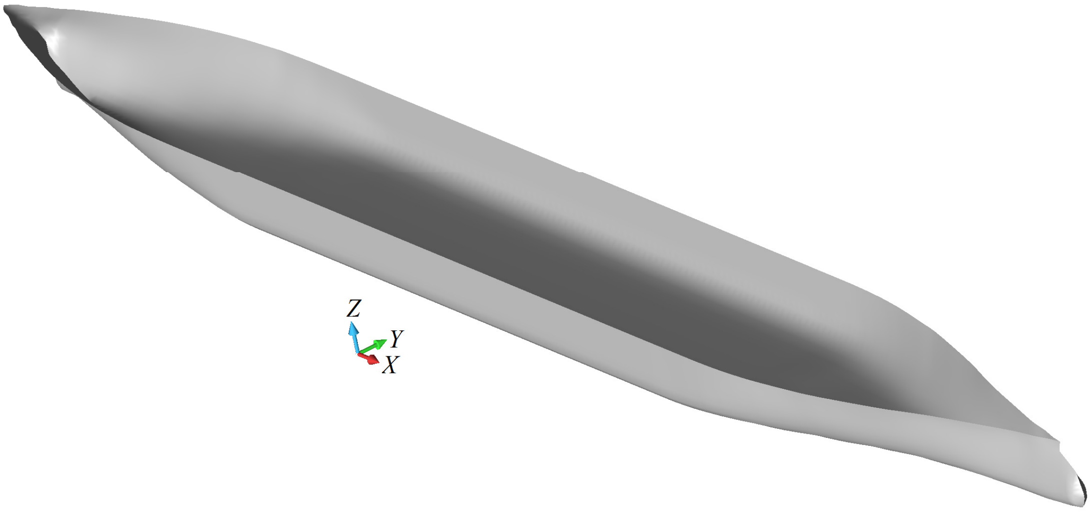

Figure 4.27 Isometric view of the hull surface below draft waterline.

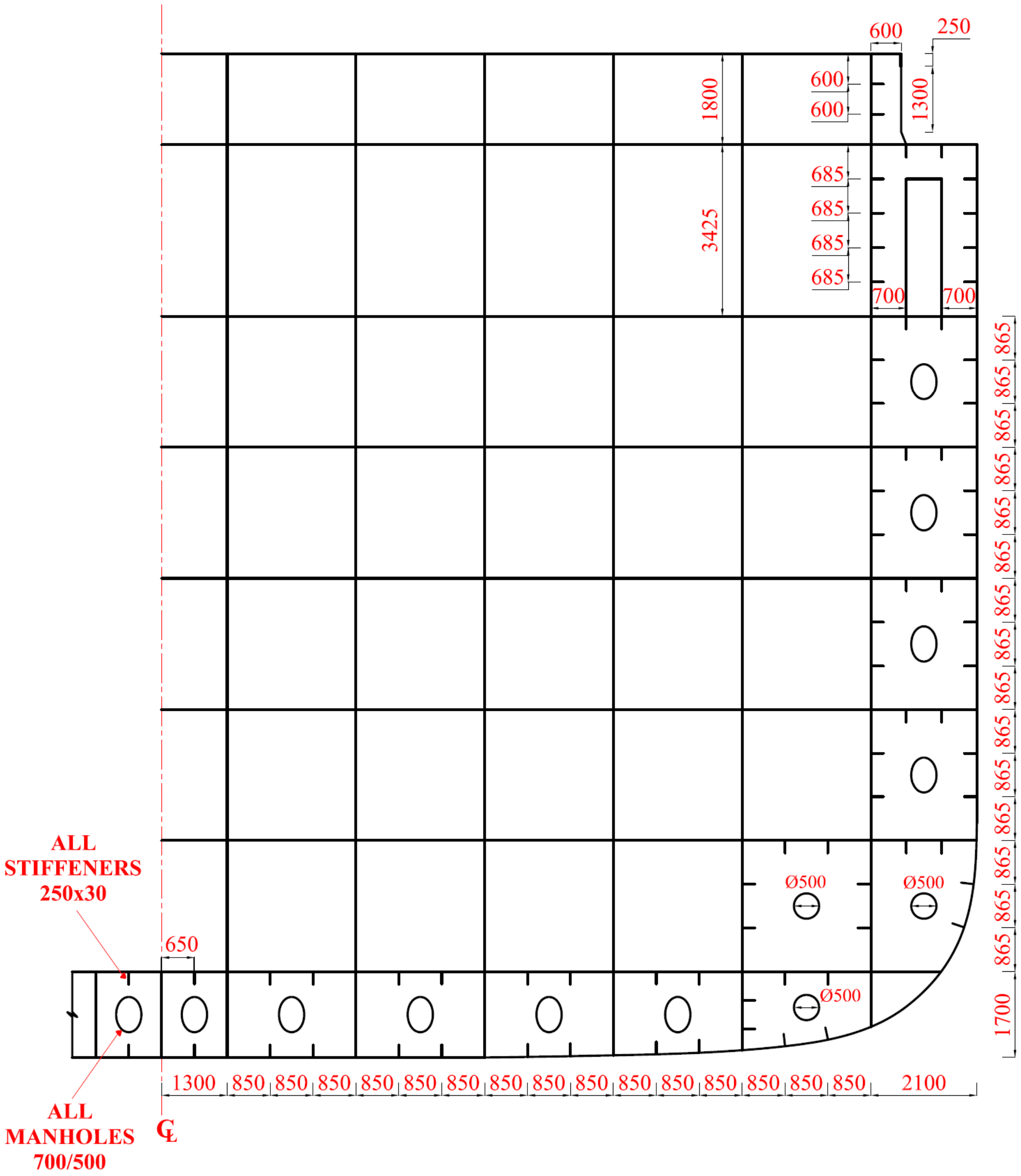

Figure 4.28. Mid-ship section of Panamax containership.

Isometric view of the hull surface below the draft waterline and mid-ship section drawings are depicted in Figures 4.27-4.28, respectively. For clarity, only one global Cartesian coordinate system (X, Y, Z) serves as containership frame of reference, with its origin $(0,0,0)$ located at the still waterline and aligned vertically with the center of gravity of the ship. The *X*-, *Y*-, and *Z*-axes point out the bow, portside, and opposite direction of the gravity, respectively. According to the global coordinate system, when the containership is loaded at its design draft, the containership has the general particulars as listed in Table 4.2.

Table 4.2 General particulars of Panamax containership.

General particular	Value	Unit
Length between perpendiculars	291	m
Breadth (moulded)	32.3	m
Depth (moulded)	19.9	m
Design draft (moulded)	12.1	m
Block coefficient (at design draft)	0.73	m^3/m^3
Displacement (at design draft)	85190.5	tonnes
Longitudinal center of gravity (from aft perpendicular)	141.2	m
Vertical center of gravity (from baseline)	12.1	m
Vertical center of buoyancy (from baseline)	6.4	m
Radius of gyration around X-axis	10.834	m
Radius of gyration around Y-axis	74.105	m
Radius of gyration around Z-axis	74.105	m
Radius of gyration for roll-yaw product of inertia	0	m

Parallel mid-body of the containership is composed of three full and two half cargo holds and is defined over the domain $X \in [-51.6 \text{ m}, +51.6 \text{ m}]$. Each ends of the cargo hold are separated with watertight bulkheads and each cargo hold is equally subdivided into two cargo compartments with a non-watertight bulkhead. Each cargo compartment has longitudinal space of 12.48 m because they are designed for stowing 2×20 foot long containers. During the design of the containership, longitudinal frame spacing methodology is adopted and each cargo compartment is supported with three transverse frames. Moreover, both watertight and non-watertight transverse bulkheads have length of 1.56 m and each bulkhead is supported with a transverse frame at both ends. For simplicity, all the structural components including plates, stiffeners, and transverse frames have been designed to have the uniform thickness of 30 mm and they are made of steel having elastic modulus of 210 GPa and Poisson’s ratio of 0.3. In order to represent the complexity of the structure more clearly, an isometric view of the parallel mid-body is illustrated in Figure 4.29.

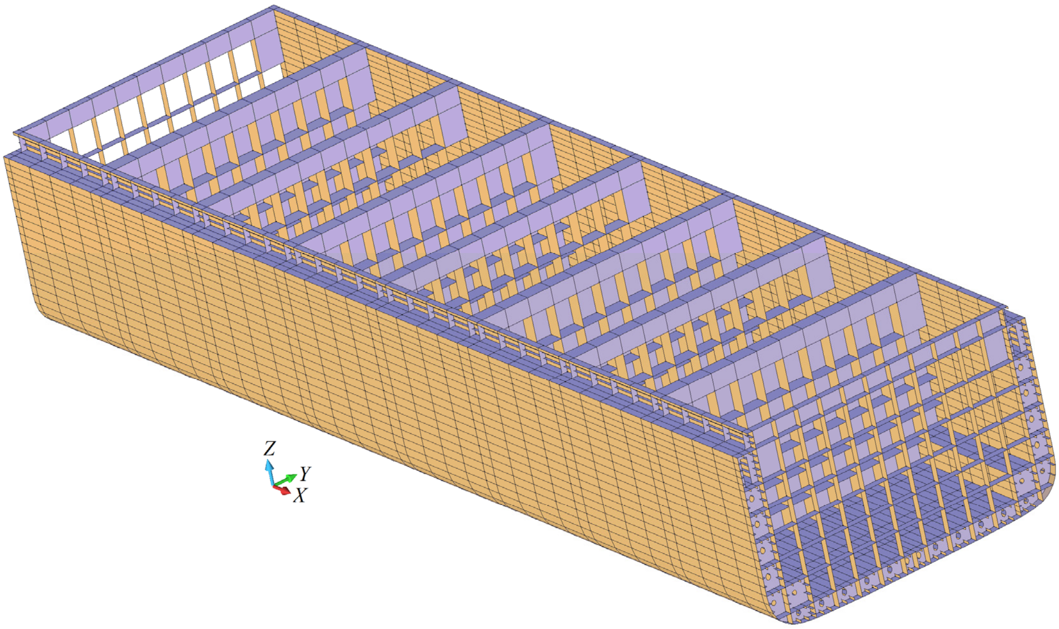

Figure 4.29 Parallel mid-body of Panamax containership.

4.4.2 Hydrodynamic-FEM analysis of the containership

In this study, the total weight of the containership is distributed along the length between perpendiculars as depicted in Figure 4.30. At this loading condition, the containership is assumed to float with zero forward speed in beam sea waves. As presented in Figure 4.31, a full hydrodynamic model consisted of 4912 flat uniformly distributed (mostly rectangular-shaped) panels is used to perform the hydrodynamic analysis.

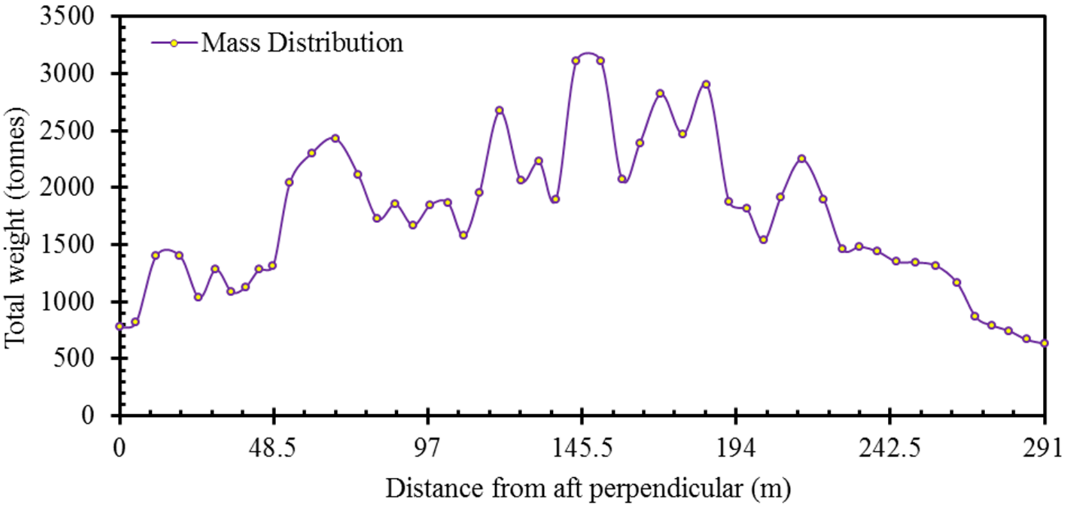

Figure 4.30 Total weight distribution of Panamax containership.

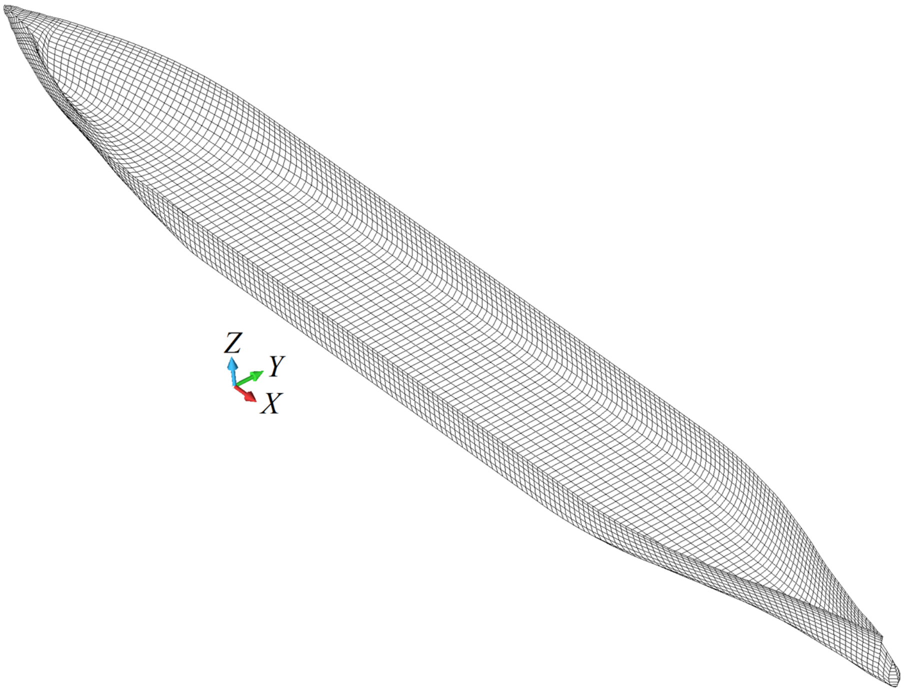

Figure 4.31 Hydrodynamic model of Panamax containership.

As a result of the hydrodynamic analysis, six DOF motions and hydrodynamic pressures of the containership are obtained for unit wave amplitude and wave frequencies ranging from 0.05 rad/s to 1.2 rad/s. The nonzero rigid body motion amplitudes, namely sway, heave, and roll motions, are plotted in Figures 4.32-33, respectively.

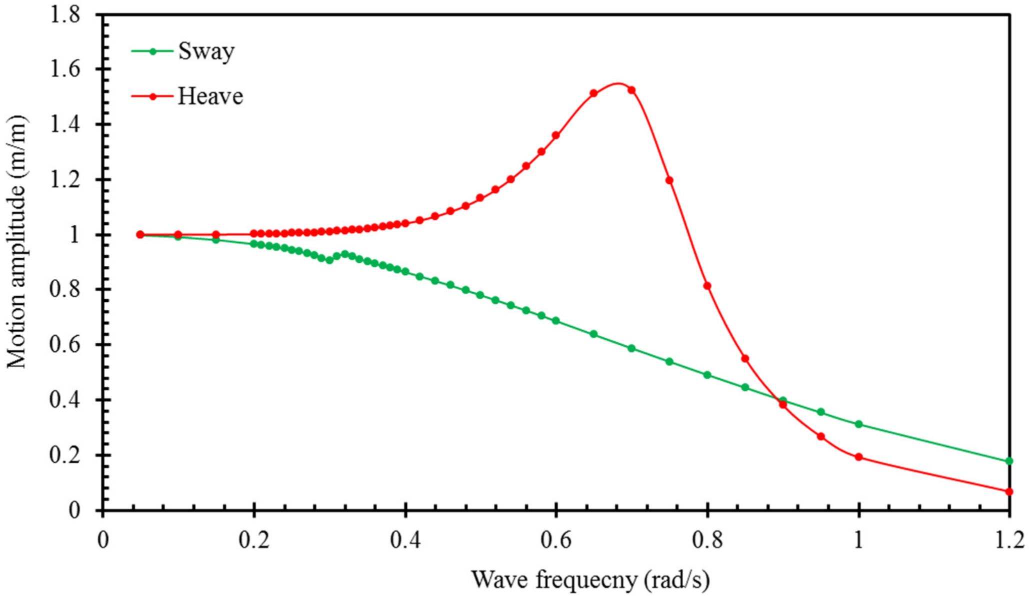

Figure 4.32 Sway and heave motion amplitudes.

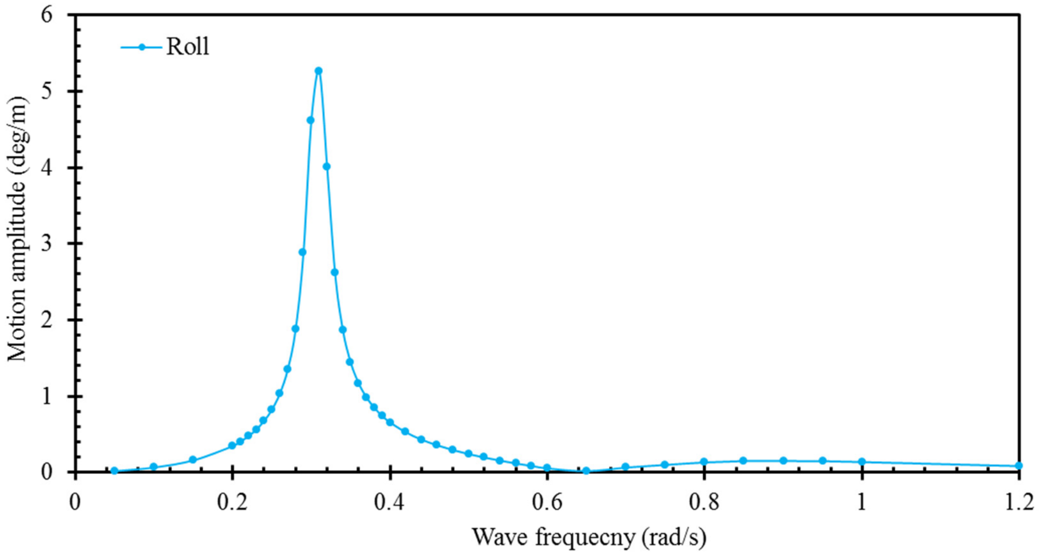

Figure 4.33 Roll motion amplitudes.

At any section along the length, hydrodynamic section forces can be calculated using the six DOF motions, the hydrodynamic pressures, and the total weight distribution. In Figure 4.33, the roll motion amplitude significantly increases between wave frequencies of 0.2 and 0.4 rad/s. Therefore, vertical and horizontal wave bending moments, M_Y and M_Z, and torsional wave moments, M_X, at section X=0 m are compared between wave frequencies of 0.2 and 0.4 rad/s as shown in Figure 4.34.

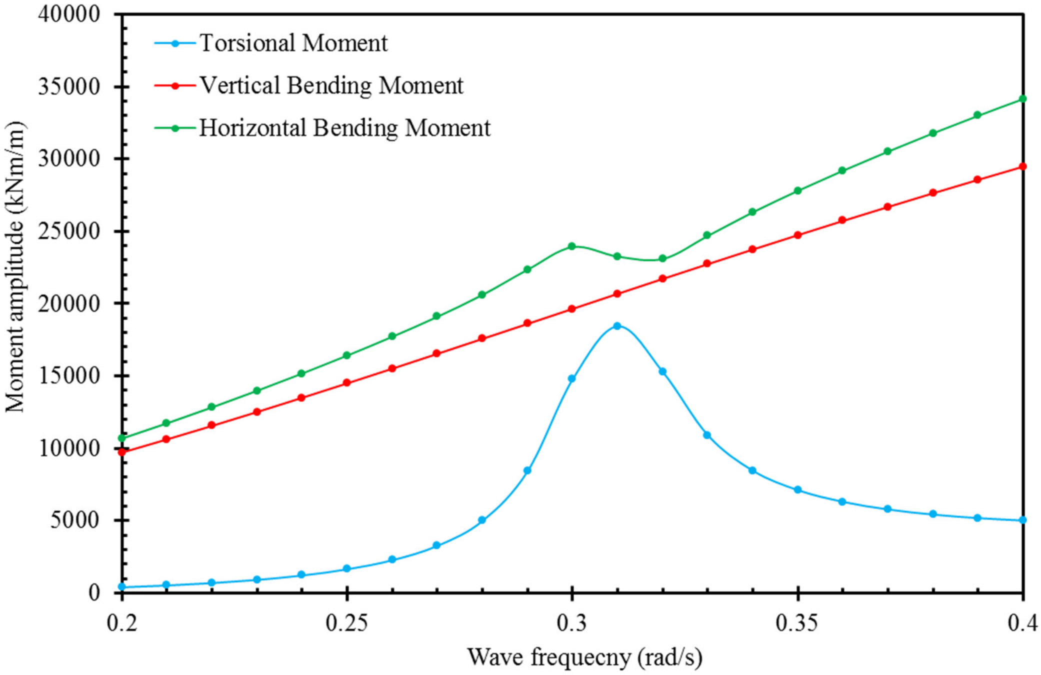

Figure 4.34 Wave vertical and horizontal bending and torsional moments.

In Figure 4.34, the most critical wave frequency is 0.31 rad/s for performing the structural analysis. Hence, the wave moments at 0.31 rad/s, M_X = 18446 kNm/m, M_Y = 20686 kNm/m, and M_Z = 23261 kNm/m, are chosen as load input for the following structural analysis. Three different FEM analyses of parallel mid-body are performed for three different loading cases; (1) pure vertical bending case, (2) pure horizontal bending case and (3) pure torsion case. The resultant deformations due to these three loading scenarios may be symmetric/antisymmetric with respect to *XZ*- and/or *YZ*-planes. Moreover, geometry of the parallel mid-body is symmetric with respect to both *XZ*- and *YZ*-planes. Therefore, only one-fourth of the mid-body is modelled to establish an accurate reference solution through high fidelity FEM analysis. As depicted in Figure 4.35, the most refined FEM mesh consists of 246,484 shell elements (mostly rectangular-shaped) and 1,428,738 DOF.

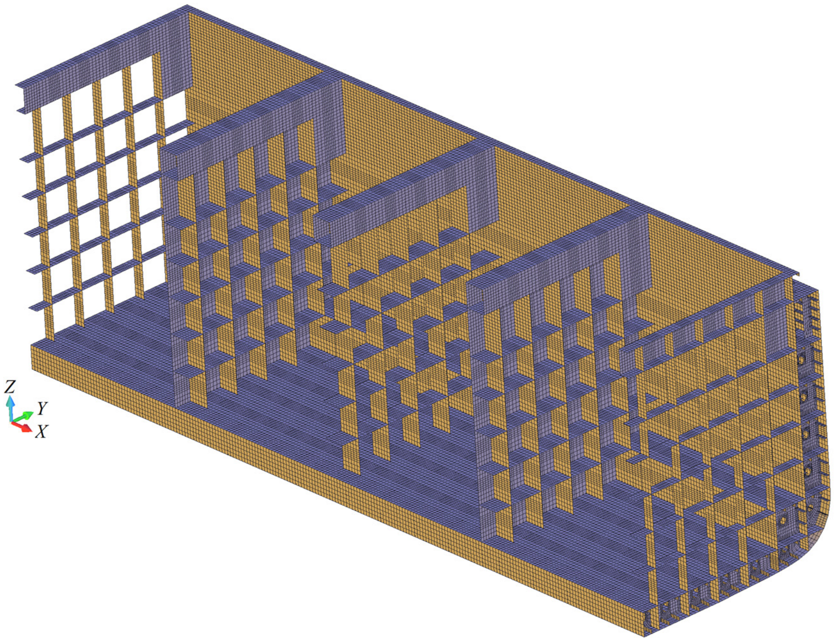

Figure 4.35 High fidelity FEM mesh of one-fourth of parallel mid-body.

The translations along the normal axis and the rotations around the in-plane axes are constrained for symmetry boundary condition, while the rotation around the normal axis and the translations along the in-plane axes are constrained for anti-symmetry boundary condition. For each loading case, the boundary conditions (BC) imposed to *XZ*- and *YZ*-planes and suitable moments applied uniformly along the length of the parallel mid-body are listed in Table 4.3.

Table 4.3 Constraint and loading boundary conditions.

Loading case	*XZ*-plane BC	*YZ*-plane BC	Moment
Pure vertical bending	Symmetry	Symmetry	M_Y
Pure horizontal bending	Anti-symmetry	Symmetry	M_Z
Pure torsion	Anti-symmetry	Anti-symmetry	M_X

Once the constraint and loading boundary conditions are applied to the high fidelity FEM model, an accurate reference solution is established. Finally, for each loading case, experimentally measured strains, $(\varepsilon_{11}^{+},\varepsilon_{22}^{+},\gamma_{12}^{+})_i$ and $(\varepsilon_{11}^{-},\varepsilon_{22}^{-},\gamma_{12}^{-})_i$, are simulated by strains obtained from the FEM analyses.

4.4.3 Case studies for iFEM analysis of the containership

Three different iFEM analyses of the parallel mid-body are performed utilizing three different strain-rosette networks for pure vertical and horizontal bending, and torsion case, respectively. To remain consistent with the above stated boundary conditions, only one-fourth of parallel mid-body is modelled with a coarse iQS4 discretization consisted of only 15318 uniformly distributed (mostly rectangular-shaped) elements and 79596 DOF as shown in Figure 4.36.

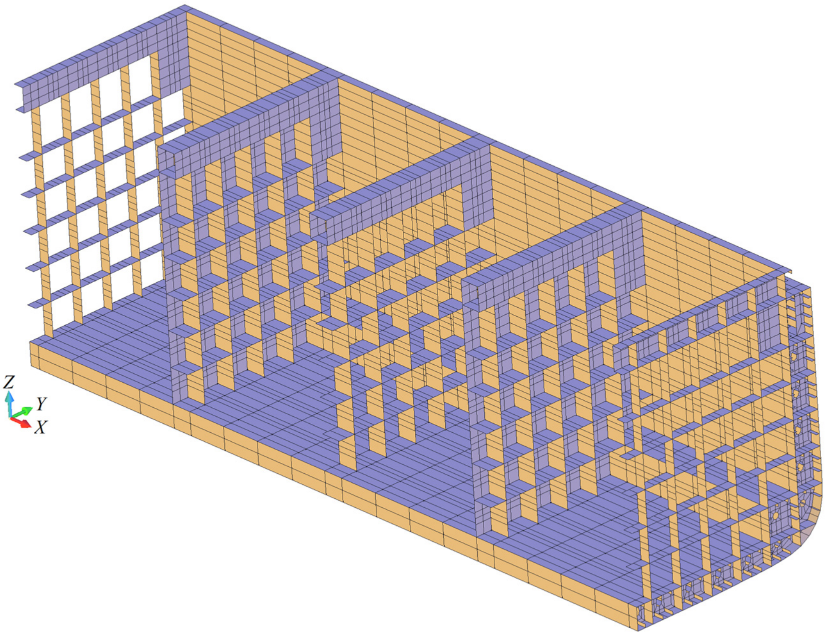

Figure 4.36 Coarse iQS4/iFEM mesh of one-fourth of parallel mid-body.

The resulting deformations of the mid-body exhibit both stretching and bending response due to the complexity of the structural topology. Hence, the strain rosettes have to be placed on both the top and bottom surfaces of the plates. Moreover, the hull structure is made up with thin shells so the weighting constants for transverse shear strains are set as $w_\alpha = 10^{-5}$ $(\alpha = 7,8)$ in the following iFEM case studies. To investigate the accuracy of iFEM predictions for the U_T displacement, $PD(U_T)$ is computed using Equation (3.96) given in Section 3.4.4. Once the structural deformed shape is obtained, von Mises stresses, σ_{VM}, are calculated on the top surfaces of the shells. Moreover, the accuracy of iFEM predictions for the σ_{VM} stress is examined by calculating the percent difference between iFEM and direct FEM predictions for σ_{VM} stress at each node i as

$$PD(\sigma_{VM}) = \left| \frac{\sigma_{VM,i}^{iFEM} - \sigma_{VM,i}^{FEM}}{\sigma_{VM,\max}^{FEM}} \right| \times 100\% \tag{4.1}$$

where $\sigma_{VM,i}^{iFEM}$ is iFEM prediction for the σ_{VM} stress at node i, $\sigma_{VM,i}^{FEM}$ is direct FEM prediction for the σ_{VM} stress at node i, and $\sigma_{VM,\max}^{FEM}$ is direct FEM prediction of the maximum σ_{VM} stress. To visualize a better deformed shape of the mid-body, contours of displacements and stresses are plotted over a visualization mesh corresponding to entire parallel mid-body. In all case studies, for an iQS4 element which has no in situ strain components, the corresponding weighting coefficients are set to 10^{-5}.

In the first case study, i.e. pure vertical bending case, the iQS4 model of the parallel mid-body has top- and bottom-surface strain rosettes located within 327 selected elements as shown in Figure 4.37. Contour plots of U_T and $PD(U_T)$ for the first iFEM analysis are depicted in Figure 4.38 where the deformed shape of the mid-body confirms the pure vertical bending of the structure. In Figure 4.38, the maximum $PD(U_T)$ is 7.248% and located at the node where the maximum U_T is occurred. In Figure 4.39, contours of σ_{VM} and $PD(\sigma_{VM})$ are presented, showing that the maximum $PD(\sigma_{VM})$ is 12.569% and its location is identical to the location of the node where the maximum σ_{VM} stress is occurred. Therefore, these results verify superior precision of the iFEM solutions for complex marine structures. These results also confirm the strain-sensor locations depicted in Figure 4.37 are the optimum locations for performing an accurate shape and stress sensing of the Panamax containership subjected to vertical wave bending moment.

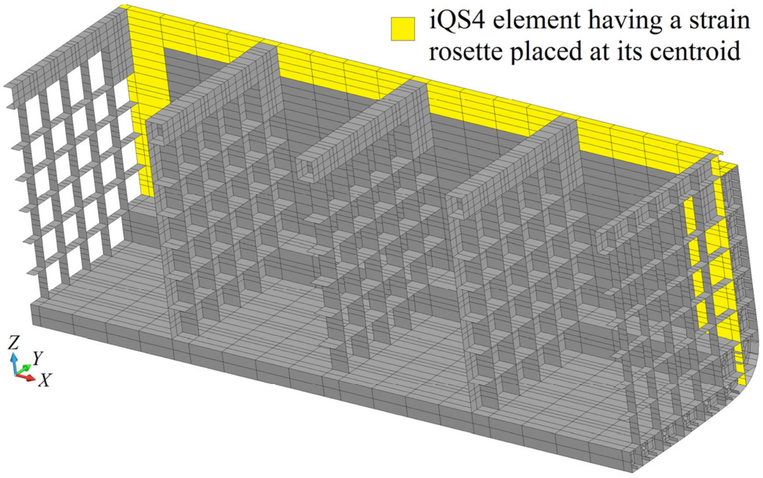

(Isometric view I)

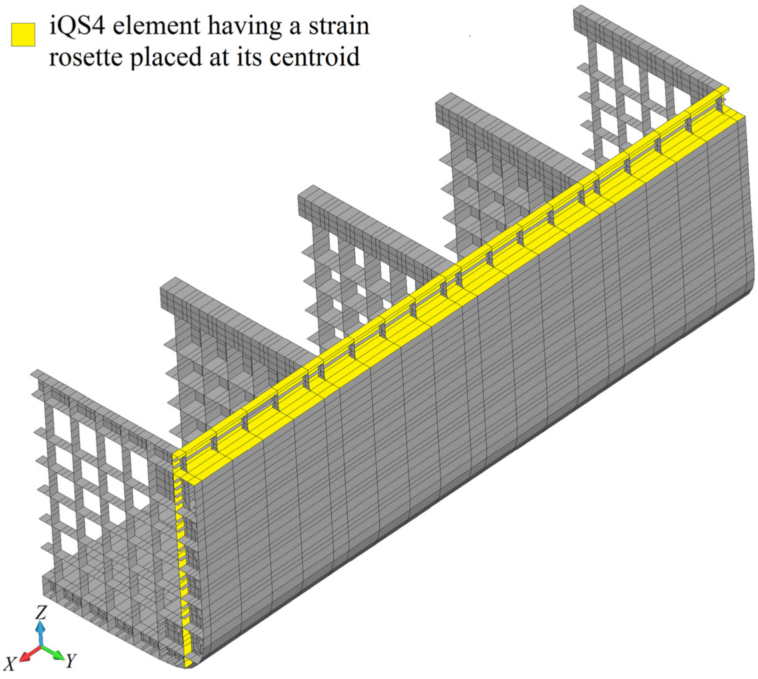

(Isometric view II)

Figure 4.37 The iQS4 model of one-fourth of parallel mid-body using top and bottom surface strain rosettes located within 327 selected elements.

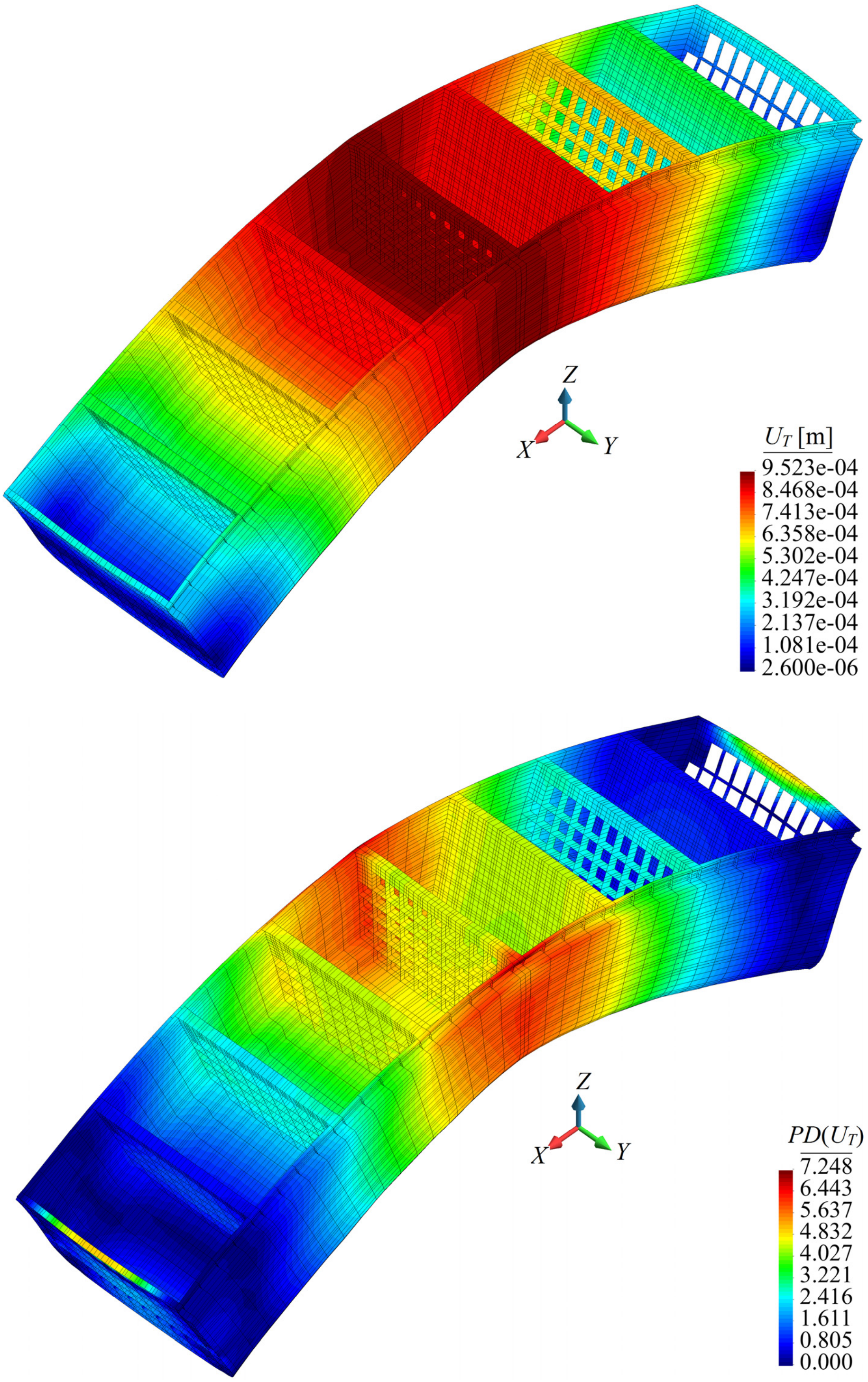

Figure 4.38 Contour plots of U_T and $PD(U_T)$ for the iQS4 model in Figure 4.37.

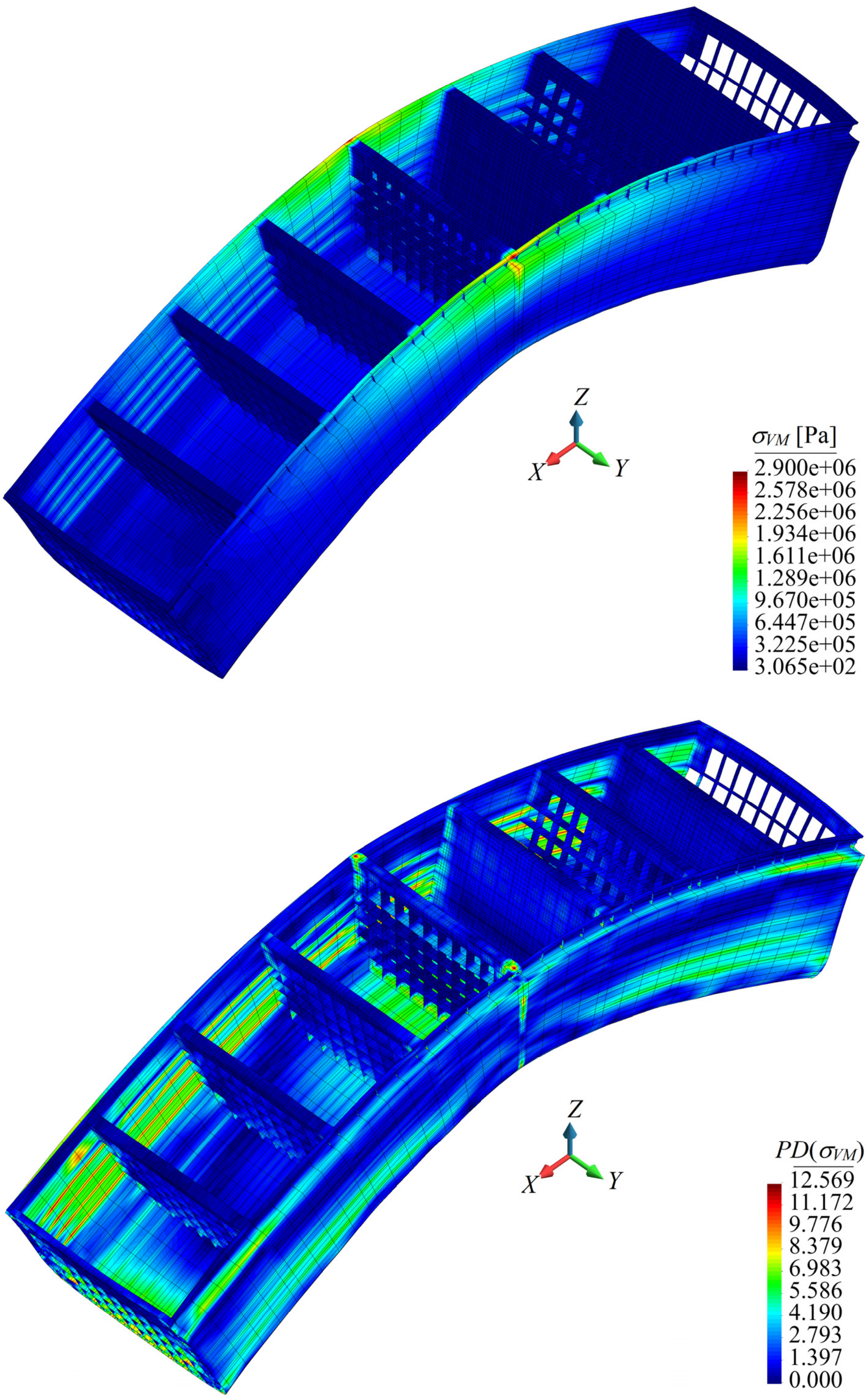

Figure 4.39 Contour plots of σ_{VM} and $PD(\sigma_{VM})$ for the iQS4 model in Figure 4.37.

In the second case study, i.e. pure horizontal bending case, the iQS4 model of the parallel mid-body has top- and bottom-surface strain rosettes located within 413 selected elements as shown in Figure 4.40. Contour plots of U_T and $PD(U_T)$ for the second iFEM analysis is demonstrated in Figure 4.41. Remarkably, the deformed shape of the mid-body is identical to the pure horizontal bending of the structure. As presented in Figure 4.41, the value of $PD(U_T)$ is approximately equal to 5.5% at the location where the maximum U_T displacement is occurred.

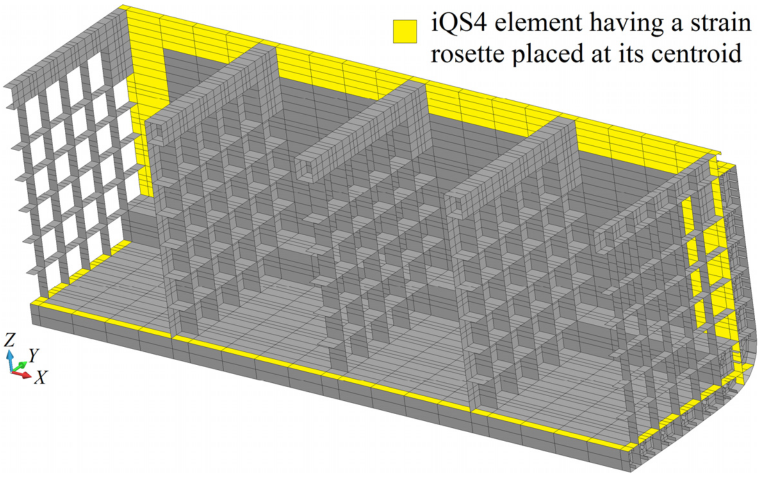

(Isometric view I)

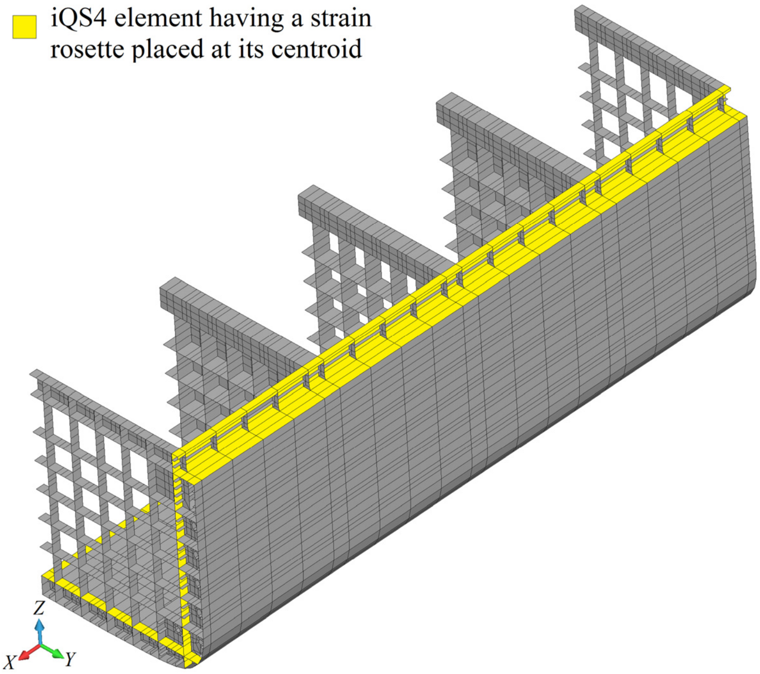

(Isometric view II)

Figure 4.40 The iQS4 model of one-fourth of parallel mid-body using top and bottom surface strain rosettes located within 413 selected elements.

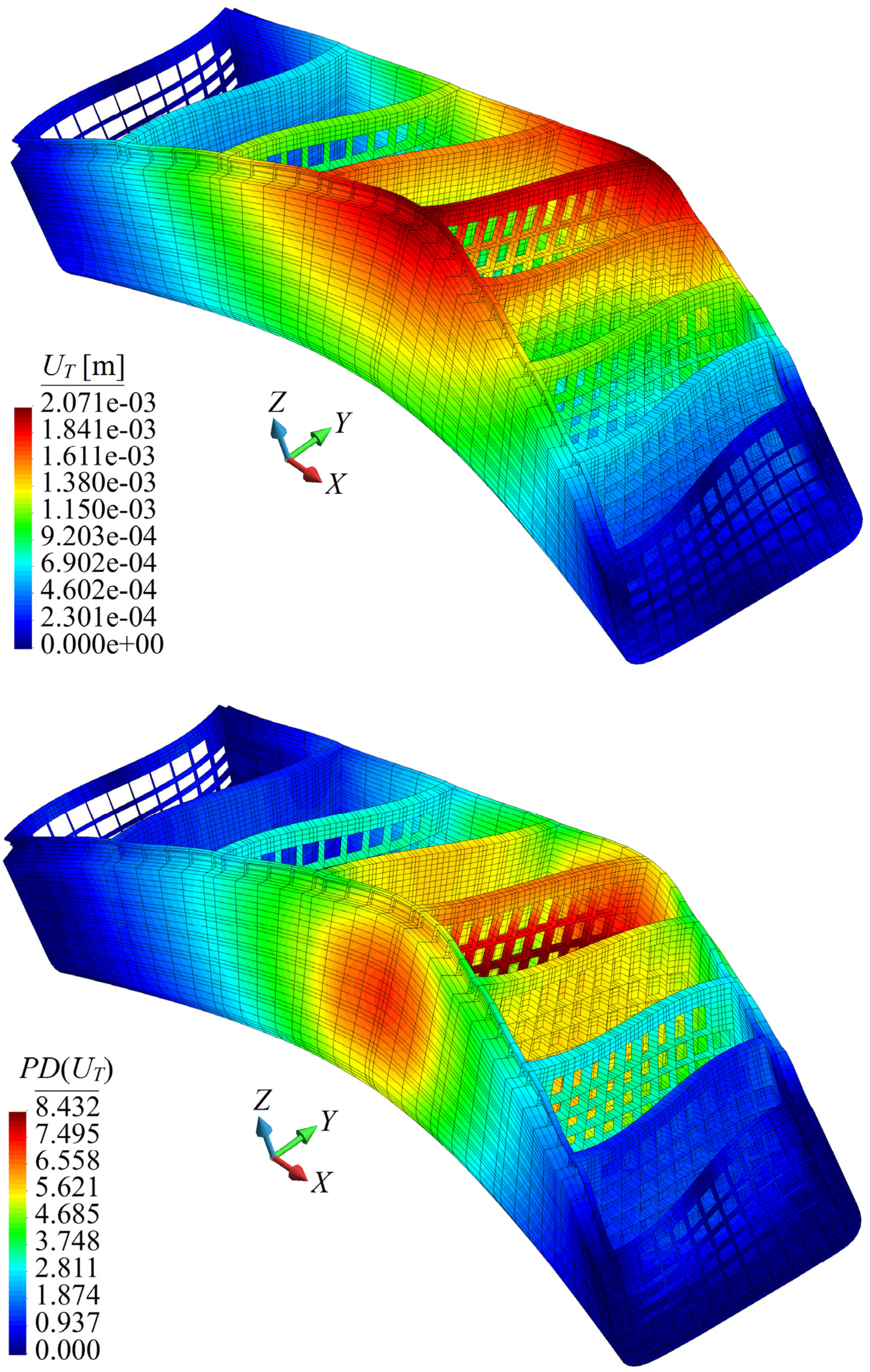

Figure 4.41 Contour plots of U_T and $PD(U_T)$ for iQS4 model in Figure 4.40.

In Figure 4.42, the contour plots of σ_{VM} and $PD(\sigma_{VM})$ is presented for the second case study. The value of $PD(\sigma_{VM})$ is around 8% at the location where the maximum σ_{VM} stress is occurred (Figure 4.42). Consequently, these results clearly demonstrate high precision of the iFEM solutions for shape and stress sensing. Furthermore, these results verify that the strain-sensor locations presented in Figure 4.41 are the optimum locations for performing a precise displacement and stress monitoring of the Panamax containership exposed to horizontal wave bending moment.

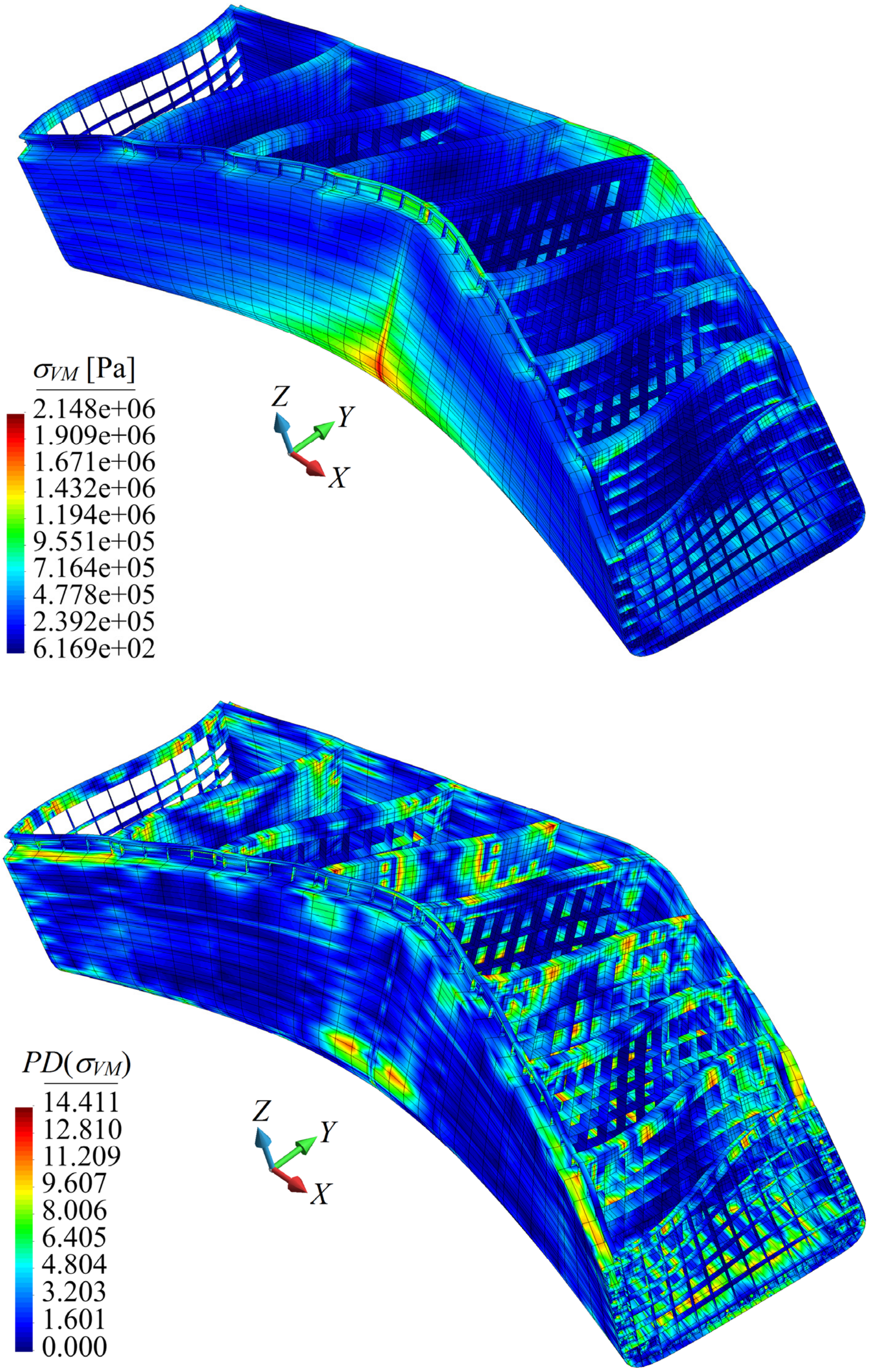

Figure 4.42 Contour plots of σ_{VM} and $PD(\sigma_{VM})$ for iQS4 model in Figure 4.40.

In the third case study, i.e. pure torsion case, the iQS4 model of the parallel mid-body has top- and bottom-surface strain rosettes located within 442 selected elements as shown in Figure 4.43. Contour plots of U_T and $PD(U_T)$ for the third iFEM analysis are depicted in Figure 4.44 where the deformed shape of the mid-body exhibits the pure torsion of the structure.

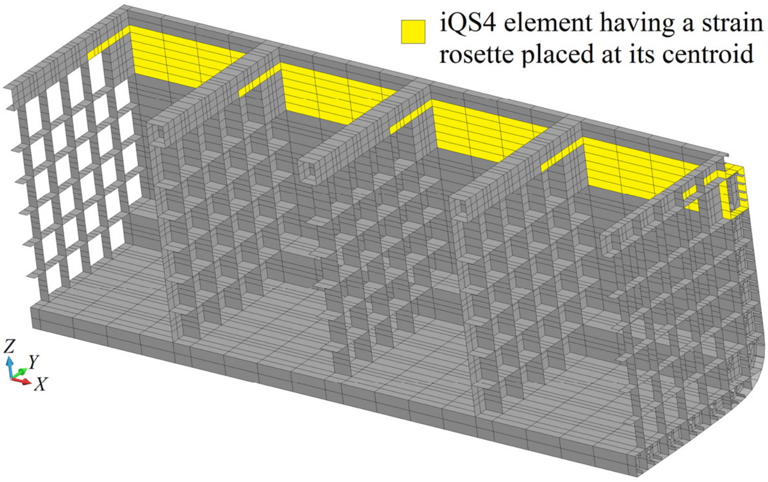

(Isometric view I)

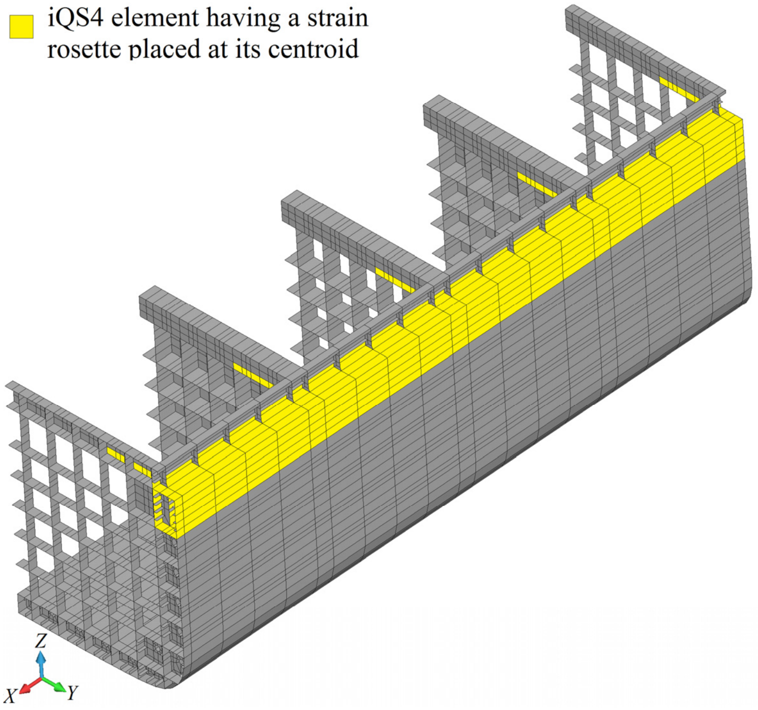

(Isometric view II)

Figure 4.43 The iQS4 model of one-fourth of parallel mid-body using top and bottom surface strain rosettes located within 442 selected elements.

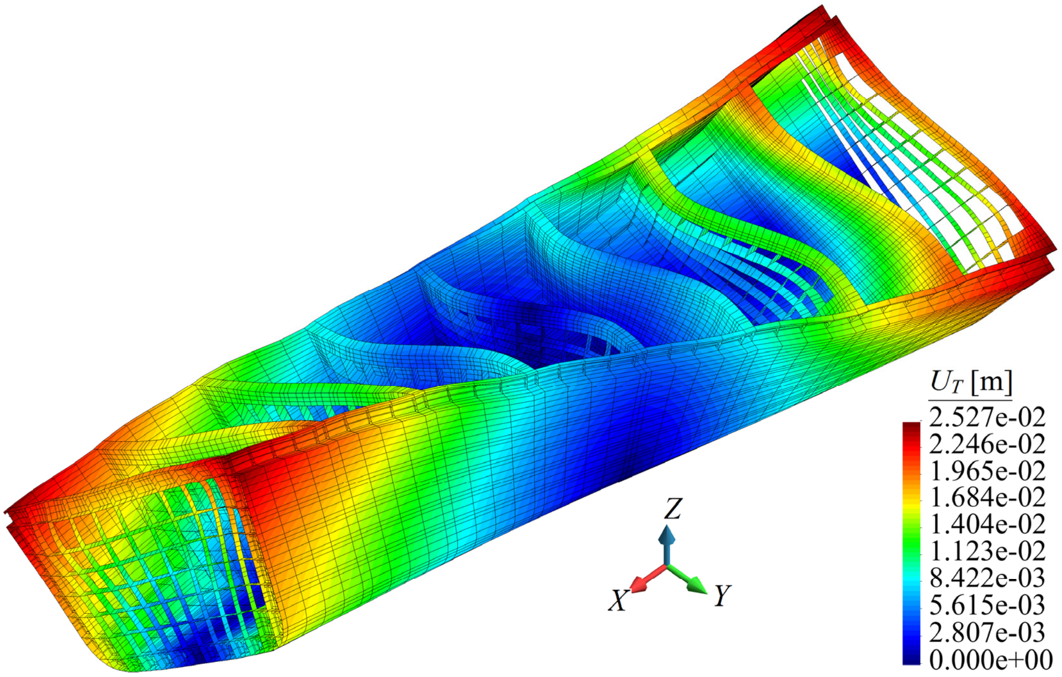

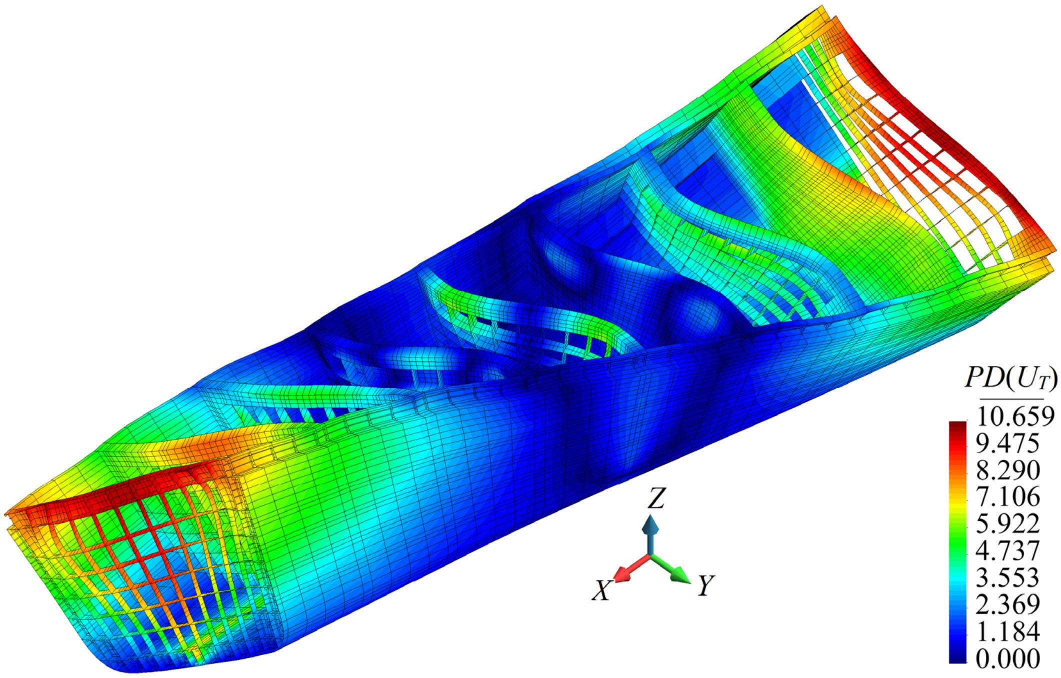

Figure 4.44 Contour plots of U_T and $PD(U_T)$ for iQS4 model in Figure 4.43.

In Figure 4.44, the value of $PD(U_T)$ is approximately equal to 7.1% at the location where the maximum U_T displacement is occurred. According to Figures 4.38, 4.41, and 4.44, the maximum U_T displacement induced due by torsional moment is much larger than the ones caused due to vertical and horizontal bending moments. This result proofs the significance of hull girder torsion loading on containerships floating in beam sea waves. In Figure 4.45, the contour plots of σ_{VM} and $PD(\sigma_{VM})$ for third iFEM analysis is presented.

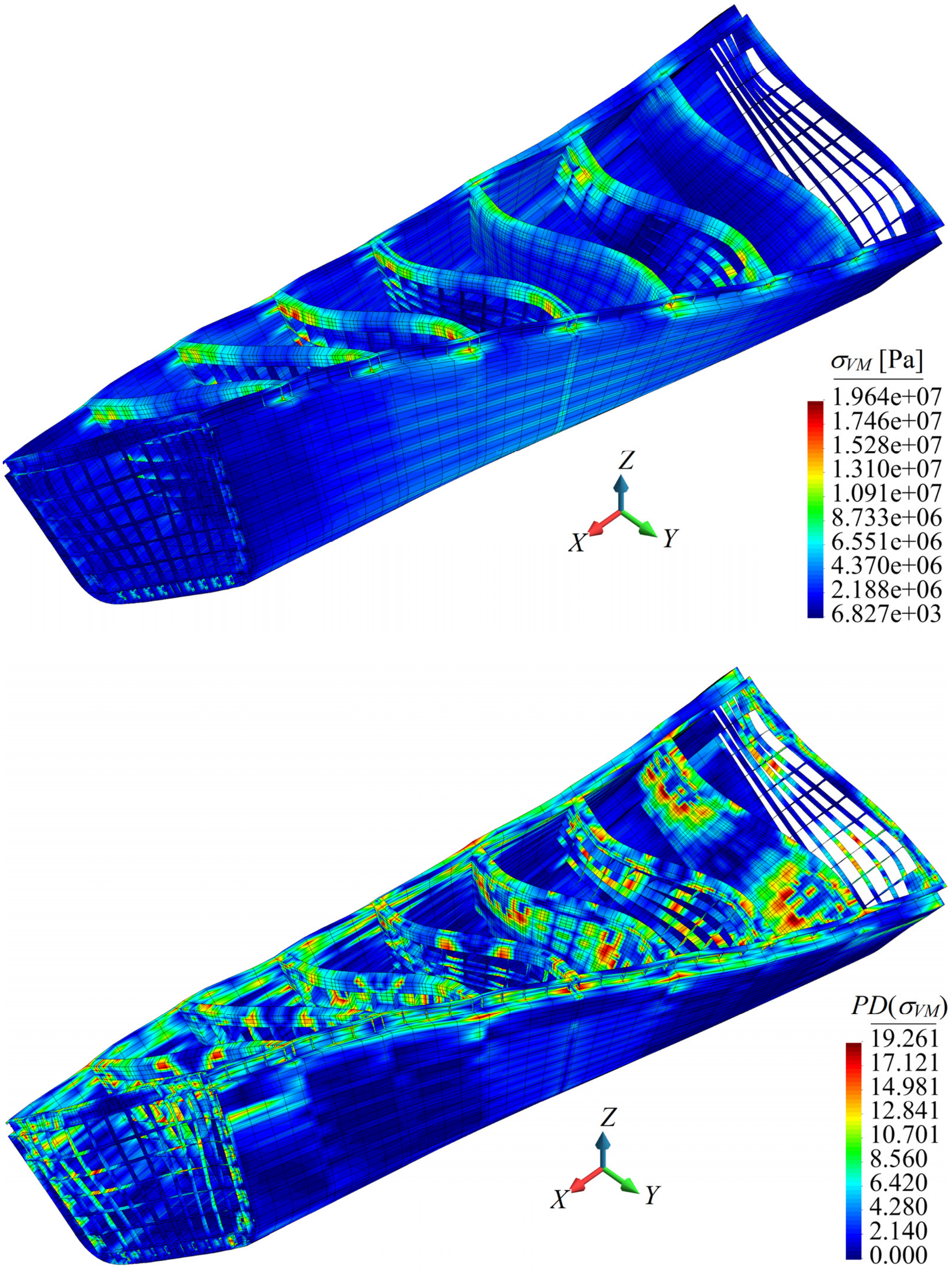

Figure 4.45 Contour plots of σ_{VM} and $PD(\sigma_{VM})$ for iQS4 model in Figure 4.43.

As depicted in Figure 4.45, the value of $PD(\sigma_{VM})$ is approximately 10.7% at the location where the maximum σ_{VM} stress is occurred. Hence, these result clearly indicates the significant precision of the iFEM solutions for displacement and stress monitoring. Moreover, these results validate that the strain-sensor locations demonstrated in Figure 4.43 are the optimum locations for performing a precise shape- and stress-sensing of the Panamax containership subjected to torsional wave moment. According to the results found in all three case studies, it can be concluded that iFEM is a superior, powerful, and innovative technology for the structural health monitoring of marine structures.

4.5 Conclusion

In this chapter, displacement and stress monitoring of three different marine structures is accomplished by using iFEM/iQS4 methodology developed in Chapter 3. These marine structures are (1) a longitudinally and transversely stiffened plate, (2) a long barge having typical chemical tanker cross-section, and (3) parallel mid-body of a Panamax containership. In order to represent floating structures (i.e., the barge and containership) in real sea environment, in-house hydrodynamic and FEM software are utilized for simulating the on-board strain-sensor strains. Then, iFEM analyses of the aforementioned marine structures are individually performed utilizing different networks of strain sensors located within the same low-fidelity iQS4 discretization of each structure. After that, the deformed shape and von Mises stresses of the stiffened plate, barge, and containership are reconstructed using in situ strain data obtained from each proposed network of strain sensors. According to the accuracy of the displacement and stress results, the optimum strain sensor locations are identified and clearly demonstrated for each iFEM case study of each marine structure. In general, the numerical results confirmed that relatively accurate deformed shapes and von Mises stresses can still be reconstructed by exploiting the weighting constants in the least-squares functional of iFEM, even though a large amount of in situ strain data is absent or only a relatively sparse strain data is collected. As a result, it can be concluded that iFEM algorithm is very promising system for performing a precise shape and stress sensing of marine structures.

Chapter 5

Isogeometric iFEM Formulation

5.1 Introduction

This chapter presents a novel isogeometric iFEM formulation, which couples the NURBS-based IGA together with the iFEM methodology for shape sensing of complex/curved thin shell structures. The primary goal is to be geometrically exact regardless of the discretization size and to obtain a smoother shape sensing even if using less number of strain sensors. For this purpose, an isogeometric Kirchhoff–Love inverse-shell element (iKLS) is developed on the basis of a weighted-least-squares functional that uses membrane and bending strain measures consistent with the Kirchhoff–Love shell theory. The novel iKLS element employs NURBS not only as a geometry discretization technology, but also as a discretization tool for displacement domain. Therefore, this development serves the following beneficial aspects of the IGA for the shape-sensing analysis based on iFEM methodology: (1) exact representation of computational geometry, (2) simplified mesh refinement, (3) smooth (high order continuity) basis functions, and finally (4) integration of design and analysis in only one computational geometry. The overall strategy presented in chapter is an extended and enhanced version of the study described in Kefal and Oterkus (2017), and to the best of the author’s knowledge, this is the first time that an isogeometric iFEM formulation become available in the literature. This chapter is organized as follows: First of all, Section 5.2 provides the background and motivation for this study. Moreover, Section 5.3 presents an iFEM formulation for thin and curved shells, which is developed utilizing the kinematics of Kirchhoff–Love shell theory in convected curvilinear coordinates. Besides, a brief summary of B-spline and NURBS basis functions is given in Section 5.4. Furthermore, the mathematical structure of the iKLS element, i.e., an example of the isogeometric iFEM formulation, is described in Section 5.5. Then, in Section 5.6, the superior capabilities of iKLS element for shape sensing of curved shells are demonstrated by various case studies including Scordelis–Lo roof, pinched hemisphere, and partly clamped hyperbolic paraboloid. Finally, the conclusions of this chapter, which indicate the advantages of the iKLS element and isogeometric iFEM methodology, is provided in Section 5.7.

5.2 Background and Motivation

Computer aided design (CAD) is applied early in the life-cycle of product manufacturing. The CAD models are moved downstream to serve as the basis for engineering and manufacturing, and even after product delivery for maintenance and support. Non-Uniform rational B-spline (NURBS) is used as a predominant technology to describe complex geometries in present CAD. This method for describing shapes is often called “isogeometry”, which easily allows a vast variety of geometries to be represented exactly same as they are in nature (refer to Figure 5.1).

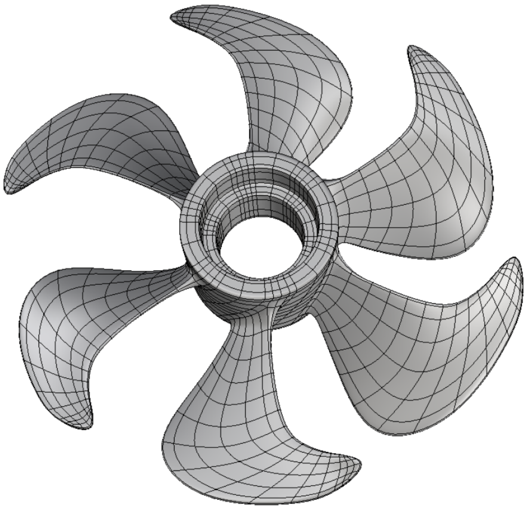

Figure 5.1 CAD model of a propeller (Taus, 2015)

There is a large collection of literature focused on NURBS basis functions and B-splines. For instance, the standard reference for NURBS is published by Piegl and Tiller (1997), and a popular introductory book is written by Rogers (2001). As a consequence of several decades of research, many efficient computer algorithms exist for fast evaluation and refinement of NURBS in today's CAD industry.

The process of generating a polygonal or polyhedral mesh that approximates a geometric domain is referred to as "mesh generation" and typically used for physical simulations such as FEM analysis, computational fluid dynamics. For example, to perform FEM analysis of a rim, the mesh of the rim is created from its CAD model as depicted in Figure 5.2. Hughes et al. (2005) claimed that this process (i.e., mesh generation from a CAD model) is a typical situation in major engineering industries and suggests a totally different geometric description for the analysis or the one that is only approximate. The authors raised the issue of mesh generation by the following statement that can be found at page 4136 in (Hughes et al., 2005): "*It is estimated that about 80% of overall analysis time is devoted to mesh generation in the automotive, aerospace, and ship building industries.*" Therefore, generation of a mesh may be costly, time consuming, and create inaccuracies.

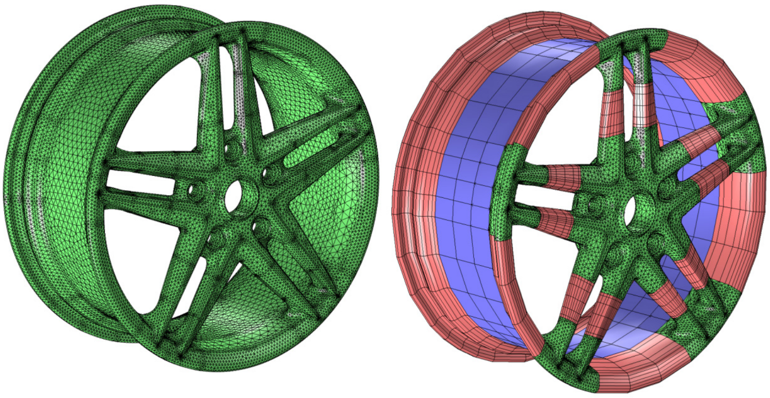

Figure 5.2 Mesh of a rim and its CAD model (Frei, 2013)

In order to bridge the gap between CAD and engineering analysis, Hughes et al. (2005) introduced isogeometric analysis (IGA) that employs NURBS to describe the geometry of the computational domain in the analysis framework. The IGA serves an exact representation of computational geometry no matter how coarse the discretization. Moreover, it simplifies the mesh refinement by eliminating the need for communication with the CAD geometry once the initial isogeometric model is constructed. Furthermore, it provides high order continuity basis functions, and finally knits the mesh generation process within CAD systems. As a result of these beneficial aspects, the IGA has received a great deal of attention in the recent years in many different fields of computational mechanics, in particular structural and fluid mechanics. To give an example, Cottrell et al. (2009) provided the definitive explanation of the IGA and its future directions. Moreover, IGA has shown advantages over traditional approaches in the context of fluid-structure interaction problems (Bazilevs et al., 2008), shell and plate problems (Benson et al., 2010), contact formulations (Temizer et al., 2011), and optimization problems (Wall et al., 2008).

Exact representation of actual structural geometry is crucial for an accurate iFEM analysis of any structure, and especially curved structures. The iFEM analysis of a smoother geometry requires more refined mesh generation for the existing flat inverse-shell elements, e.g., iQS4 (vid. Chapter 3), iMIN3 (Tessler and Spangler, 2004). A high fidelity discretization of an iFEM model may require a large number of strain sensors installed on-board structure. Therefore, performing shape sensing and SHM of a complex/curved geometry would be costly using the existing flat inverse-shell elements. Moreover, the shape functions of these flat shell elements are standard polynomial-based functions and limited to only C^0-continuity for the displacement field. However, a smoother shape sensing can be obtained, if the shape functions ensure a higher continuity $(C^p, p > 0)$ throughout the element interior and edge interface. In order to overcome the problems mentioned above and expand the horizon of the iFEM methodology further, the concept of IGA can be utilized to develop novel isogeometric inverse elements. Hence, an isogeometric iFEM formulation (i.e., iKLS element), the first of its kind, is developed in remainder of this chapter.

5.3 The iFEM Formulation for Thin Shells in Convected Curvilinear Coordinates

Kirchhoff (1850) derived the first mathematically correct theory on the structural behavior of plates which states that normals to the mid-surface in the undeformed configuration remain normal and unstretched in the deformed configuration. Based on the work of Kirchhoff for plate problems, Love (1888) derived a general theory for both curved and plane surfaces. Therefore, the term “Kirchhoff–Love” is associated with the normality hypothesis of shell structures. Kirchhoff–Love shell model is well suited for thin shell analysis because (1) it disregards both transverse shear deformations and extensibility in thickness direction and (2) the deformation behavior of elastic and homogeneous thin shells is physically dominated by membrane and bending actions. In fact, Kirchhoff–Love model is more advantageous to use in comparison to the other shell models because no shear locking occurs if the transverse shear is neglected. In the remainder of this section, the description of the inverse problem is highlighted. Then, the kinematics of 3-parameter Kirchhoff–Love shell model developed by Echter et al. (2013) are briefly revised and the strain measures to be used in the iFEM formulation are accurately defined. Lastly, the computation of the experimental section strains and weighted-least-squares functional of the iFEM formulation are briefly discussed.

5.3.1 The inverse problem

In this chapter, unless otherwise specified, Greek indices take the values of 1 and 2 while the Latin indices range from 1 to 3. Consider an arbitrary shell body, e.g., a curved shell as depicted in Figure 5.3, with a uniform thickness $2h$ that is at least one order of magnitude smaller than the characteristic dimension of the body such as the span or diameter. General convected curvilinear coordinates θ^i are used to identify a particle (material point) of the curved shell body (refer to Figure 5.3).

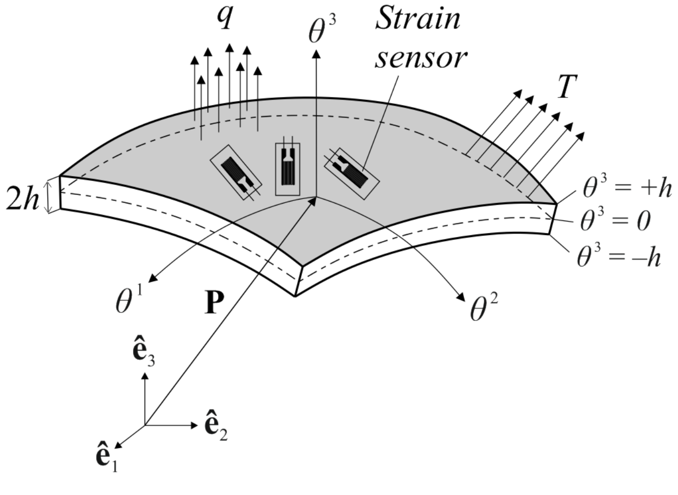

Figure 5.3 Notation for the curved shell body

The coordinate $\theta^3 \in [-h, +h]$ identifies the thickness direction of the shell and material points located at the mid-surface of the shell are described as $\theta^3 = 0$. Moreover, the in-plane coordinates are represented by $\theta^\alpha \in A$ where A denotes the area of the mid-surface. Furthermore, an orientation in three-dimensional Euclidean space $\mathbb{R}^3$ is introduced by a fixed orthogonal Cartesian coordinate system that has orthonormal basis $\hat{\mathbf{e}}_i$ pointing the direction of the coordinate axes as shown in Figure 5.3. In this regard, linear combination of the basis vectors $\hat{\mathbf{e}}_i$ and the Cartesian coordinates P_i can uniquely establish a position vector $\mathbf{P}$ of any arbitrary material point in the shell body as (refer to Figure 5.3)

$$\mathbf{P} \equiv \mathbf{P}(\theta^1, \theta^2, \theta^3) = \sum_{i=1}^{3} P_i(\theta^1, \theta^2, \theta^3)\, \hat{\mathbf{e}}_i \tag{5.1}$$

where P_i is written as a function of convective coordinates θ^i, thus defining the transformations between Cartesian and convective coordinates. It is assumed that external forces involving the in-plane and out-of-plane components, T and q, are applied to the shell body. Moreover, rigid body motion of the body is fully constrained. Furthermore, as depicted in Figure 5.3, strain sensors are attached at discrete locations on the surface of shell, providing real-time strain measurements. The inverse problem at hand is dynamic tracking of the three-dimensional displacements of the shell body utilizing only the in situ discrete surface strains and boundary restraints. The precise solution of this inverse problem will be derived based on an isogeometric iFEM methodology, which is the state of the art developed in this chapter.

5.3.2 Differential geometry and shell kinematics

The arbitrary material points in undeformed (reference) and deformed (current) configurations of the shell body can be described by position vectors $\mathbf{X}$ and $\mathbf{x}$, respectively (refer to Figure 5.4). The position vector $\mathbf{X}$ can be defined by linear function of thickness coordinate θ^3 as

$$\mathbf{X}(\theta^1, \theta^2, \theta^3) = \mathbf{F}(\theta^1, \theta^2) + \theta^3\, \mathbf{A}_3(\theta^1, \theta^2) \tag{5.2}$$

where $\mathbf{F}$ represents a position vector to a material point on the mid-surface in reference configuration and $\mathbf{A}_3$ denotes a unit-magnitude vector field (the director vector) that is perpendicular to the tangent plane of any point belongs to mid-surface in reference configuration (refer to Figure 5.4). As given in Equation (5.2), both $\mathbf{F}$ and $\mathbf{A}_3$ are only functions of the in-plane coordinates θ^α.

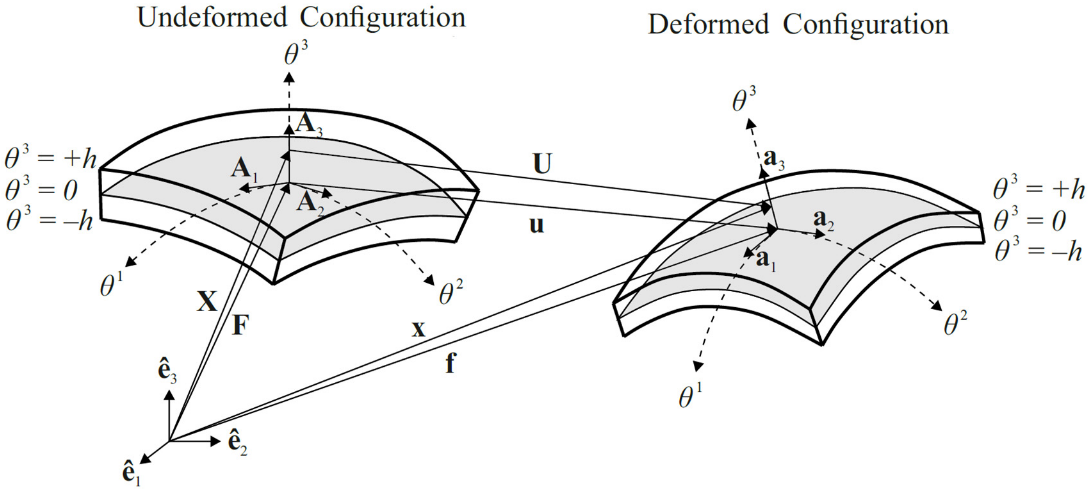

Figure 5.4 Undeformed and deformed configurations of the shell body

Taking partial derivative of $\mathbf{F}$ with respect to θ^α provides the covariant base vectors $\mathbf{A}_\alpha$ of the mid-surface in reference configuration as

$$\mathbf{A}_\alpha = \mathbf{F}_{,\alpha} \tag{5.3}$$

where, hereafter, $(\bullet)_{,\alpha} \equiv \frac{\partial(\bullet)}{\partial\theta^\alpha}$ represents a partial derivative with respect to in-plane coordinate θ^α. The director vector $\mathbf{A}_3$ can be defined by normalized cross product of these covariant base vectors $\mathbf{A}_\alpha$ as

$$\mathbf{A}_3 = \frac{\mathbf{A}_1 \times \mathbf{A}_2}{\left\|\mathbf{A}_1 \times \mathbf{A}_2\right\|} \tag{5.4}$$

Analogous to the Equation (5.2), the position vector $\mathbf{x}$ can also be defined by linear functions of thickness coordinate θ^3 as

$$\mathbf{x}(\theta^1,\theta^2,\theta^3) = \mathbf{f}(\theta^1,\theta^2) + \theta^3\,\mathbf{a}_3(\theta^1,\theta^2) \tag{5.5}$$

where $\mathbf{f}$ is a position vector to a material point on the mid-surface and $\mathbf{a}_3$ is the director vector in current configuration (refer to Figure 5.4). According to the 3-parameter Kirchhoff–Love shell model (Echter et al., 2013), the director vector $\mathbf{a}_3$ can be defined by linearized rotation of the director vector $\mathbf{A}_3$ as

$$\mathbf{a}_3 = \mathbf{A}_3 + \boldsymbol{\theta} \times \mathbf{A}_3 \tag{5.6}$$

where $\boldsymbol{\theta}$ is the rotation vector and $\boldsymbol{\theta} \times \mathbf{A}_3$ represents the difference between the directors of the reference and current configurations of the shell body as presented in Figure 5.5.

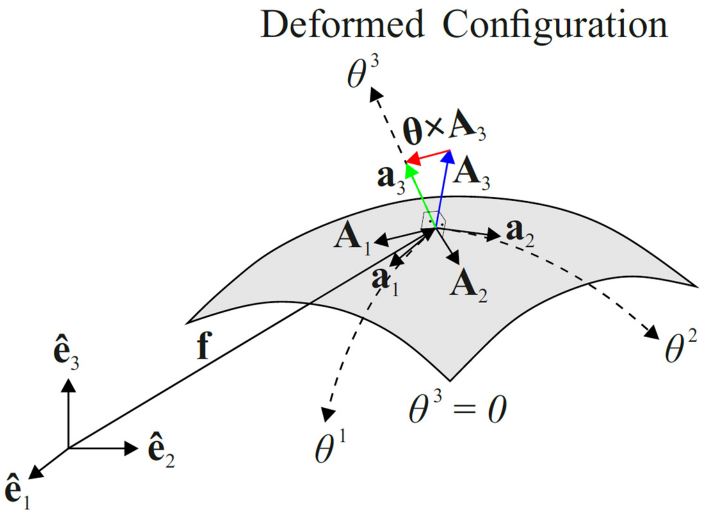

Figure 5.5 The difference vector $\boldsymbol{\theta} \times \mathbf{A}_3$ between the directors of the reference and current configurations

The displacement vector $\mathbf{U}$ of any arbitrary point in the shell body can be defined by subtracting the position vector of undeformed configuration from the position vector of deformed configuration as

$$\mathbf{U} = \mathbf{x} - \mathbf{X} = \mathbf{f} - \mathbf{F} + \theta^3 (\mathbf{a}_3 - \mathbf{A}_3) = \mathbf{u} + \theta^3 (\boldsymbol{\theta} \times \mathbf{A}_3) \tag{5.7}$$

where $\mathbf{u}$ is mid-surface displacement vector representing the translational displacements of the mid-surface of shell body from reference to current configuration as depicted in Figure 5.4. The orthogonal components of this vector can be defined as a function of in-plane coordinates θ^α; that is,

$$\mathbf{u} = [u(\theta^1,\theta^2) \quad v(\theta^1,\theta^2) \quad w(\theta^1,\theta^2)]^T \tag{5.8}$$

where the functions $u \equiv u(\theta^1,\theta^2)$, $v \equiv v(\theta^1,\theta^2)$, and $w \equiv w(\theta^1,\theta^2)$ represent translations along the covariant Cartesian base vector $\hat{\mathbf{e}}_i$, respectively. In Equations (5.6-7), the rotation vector $\boldsymbol{\theta}$ can be described in terms of in-plane covariant base vectors $\mathbf{A}_\alpha$ and related rotation angles χ_α as (Echter et al., 2013)

$$\boldsymbol{\theta} = \chi_1 \mathbf{A}_1 + \chi_2 \mathbf{A}_2 \tag{5.9}$$

with

$$\chi_1 = \frac{(\mathbf{a}_2 - \mathbf{A}_2)\cdot \mathbf{A}_3}{\|\mathbf{A}_1 \times \mathbf{A}_2\|} = \frac{\mathbf{u}_{,2} \cdot \mathbf{A}_3}{\|\mathbf{A}_1 \times \mathbf{A}_2\|} \tag{5.10}$$

$$\chi_2 = -\frac{(\mathbf{a}_1 - \mathbf{A}_1)\cdot \mathbf{A}_3}{\|\mathbf{A}_1 \times \mathbf{A}_2\|} = -\frac{\mathbf{u}_{,1} \cdot \mathbf{A}_3}{\|\mathbf{A}_1 \times \mathbf{A}_2\|} \tag{5.11}$$

where $\mathbf{u}_{,\alpha}$ denoting the partial derivatives of $\mathbf{u}$ with respect to θ^α are utilized to define rotation angles χ_α. Therefore, the rotation vector $\boldsymbol{\theta}$ is a function of $\mathbf{u}_{,\alpha}$ so that the orthogonal components of $\mathbf{u}$, namely (u, v, w), are the only unknowns, i.e., kinematic variables, to predict the displacement vector $\mathbf{U}$ in the analysis.

The partial derivatives of the displacement field $\mathbf{U}$ with respect to curvilinear convective coordinates θ^i can be evaluated as

$$\mathbf{U}_{,\alpha} = \mathbf{u}_{,\alpha} + \theta^3(\boldsymbol{\theta}_{,\alpha} \times \mathbf{A}_3 + \boldsymbol{\theta} \times \mathbf{A}_{3,\alpha}) \tag{5.12}$$

$$\mathbf{U}_{,3} = \boldsymbol{\theta} \times \mathbf{A}_3 \tag{5.13}$$

where, hereafter, $(\bullet)_{,3} \equiv \frac{\partial(\bullet)}{\partial\theta^3}$ represents a partial derivative with respect to thickness coordinate θ^3. Moreover, the covariant base vectors $\mathbf{g}_i$ of the shell body can be calculated as

$$\mathbf{g}_\alpha = \mathbf{X}_{,\alpha} = \mathbf{A}_\alpha + \theta^3 \mathbf{A}_{3,\alpha} \tag{5.14}$$

$$\mathbf{g}_3 = \mathbf{X}_{,3} = \mathbf{A}_3 \tag{5.15}$$

Using Equations (5.12) and (5.14), the linearized Green-Lagrange strain tensor defined in convected curvilinear coordinates gives rise to in-plane strains

$$\begin{Bmatrix} \varepsilon_{11} \\ \varepsilon_{22} \\ \gamma_{12} \end{Bmatrix} = \begin{Bmatrix} \mathbf{U}_{,1} \cdot \mathbf{g}_1 \\ \mathbf{U}_{,2} \cdot \mathbf{g}_2 \\ \mathbf{U}_{,1} \cdot \mathbf{g}_2 + \mathbf{U}_{,2} \cdot \mathbf{g}_1 \end{Bmatrix} = \begin{Bmatrix} e_1 \\ e_2 \\ e_3 \end{Bmatrix} + \theta^3 \begin{Bmatrix} \kappa_4 \\ \kappa_5 \\ \kappa_6 \end{Bmatrix} \equiv \mathbf{e(u)} + \theta^3\, \boldsymbol{\kappa}(\mathbf{u}) \tag{5.16}$$

where the vectors $\mathbf{e(u)}$ and $\boldsymbol{\kappa}(\mathbf{u})$ represent membrane strain measures and bending curvatures, respectively, and their components can be explicitly expressed as

$$e_1 = \mathbf{u}_{,1} \cdot \mathbf{A}_1 \tag{5.17}$$

$$e_2 = \mathbf{u}_{,2} \cdot \mathbf{A}_2 \tag{5.18}$$

$$e_3 = \mathbf{u}_{,1} \cdot \mathbf{A}_2 + \mathbf{u}_{,2} \cdot \mathbf{A}_1 \tag{5.19}$$

$$\kappa_4 = \mathbf{u}_{,1} \cdot \mathbf{A}_{3,1} + (\mathbf{A}_3 \times \mathbf{A}_1) \cdot \boldsymbol{\theta}_{,1} + \underbrace{(\boldsymbol{\theta} \times \mathbf{A}_{3,1}) \cdot \mathbf{A}_1}_{=0} \tag{5.20}$$

$$\kappa_5 = \mathbf{u}_{,2} \cdot \mathbf{A}_{3,2} + (\mathbf{A}_3 \times \mathbf{A}_2) \cdot \boldsymbol{\theta}_{,2} + \underbrace{(\boldsymbol{\theta} \times \mathbf{A}_{3,2}) \cdot \mathbf{A}_2}_{=0} \tag{5.21}$$

$$\begin{aligned} \kappa_6 = \mathbf{u}_{,1} \cdot \mathbf{A}_{3,2} + \mathbf{u}_{,2} \cdot \mathbf{A}_{3,1} + (\mathbf{A}_3 \times \mathbf{A}_2) \cdot \boldsymbol{\theta}_{,1} + (\mathbf{A}_3 \times \mathbf{A}_1) \cdot \boldsymbol{\theta}_{,2} \\ + \underbrace{(\boldsymbol{\theta} \times \mathbf{A}_{3,1}) \cdot \mathbf{A}_2}_{=0} + \underbrace{(\boldsymbol{\theta} \times \mathbf{A}_{3,2}) \cdot \mathbf{A}_1}_{=0} \end{aligned} \tag{5.22}$$

where all strain contributions of $(\boldsymbol{\theta} \times \mathbf{A}_{3,\alpha}) \cdot \mathbf{A}_\beta$ vanish identically because the vectorial quantities obtained from the cross products of $\boldsymbol{\theta}$ and $\mathbf{A}_{3,\alpha}$ are normal to the mid-surface of the shell body so that scalar multiplication of these vectorial quantities and $\mathbf{A}_\beta$ provides the final results as $(\boldsymbol{\theta} \times \mathbf{A}_{3,\alpha}) \cdot \mathbf{A}_\beta = 0$.

In addition to the in-plane strains, the linearized Green-Lagrange strain tensor defines the transverse-shear strains utilizing Equations (5.12-15) as

$$\begin{aligned} \gamma_{\alpha 3} = \mathbf{U}_{,\alpha} \cdot \mathbf{g}_3 + \mathbf{U}_{,3} \cdot \mathbf{g}_\alpha = \underbrace{\mathbf{u}_{,\alpha} \cdot \mathbf{A}_3 + (\boldsymbol{\theta} \times \mathbf{A}_3) \cdot \mathbf{A}_\alpha}_{=0} \\ + \theta^3 [\underbrace{(\boldsymbol{\theta}_{,\alpha} \times \mathbf{A}_3) \cdot \mathbf{A}_3}_{=0} + \underbrace{(\boldsymbol{\theta} \times \mathbf{A}_{3,\alpha}) \cdot \mathbf{A}_3 + (\boldsymbol{\theta} \times \mathbf{A}_3) \cdot \mathbf{A}_{3,\alpha}}_{=0}] = 0 \end{aligned} \tag{5.23}$$

Thus, Kirchhoff–Love shell model exhibits zero transverse-shear strains, $\gamma_{\alpha 3} = 0$. This indicates that the deformations of the shell body will be physically dictated by only membrane and bending actions.

5.3.3 Computation of experimental section strains

In Section 3.2.3, computation of in situ section strains that correspond to original iFEM plate formulation (Tessler and Spangler, 2003, 2005) is discussed in detail. In fact, it may be convenient to use the same relations to calculate experimental membrane and bending section strains of the presented Kirchhoff–Love shell model. Therefore, these relations are briefly revisited for consistency of the formulation. To compute the experimental section strains, the strain rosettes are located on top and bottom surface of the curved shell as depicted in Figure 5.6.

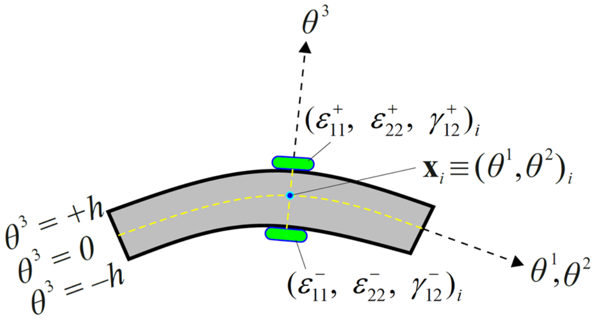

Figure 5.6 Discrete surface strains measured at $(\mathbf{x}_i, \pm h)$ $(i = 1 - n)$.

As presented in Figure 5.6, the top- and bottom-surface strains $(\varepsilon_{11}^{+}, \varepsilon_{22}^{+}, \gamma_{12}^{+})_i$ and $(\varepsilon_{11}^{-}, \varepsilon_{22}^{-}, \gamma_{12}^{-})_i$ are measured at n discrete locations $(\mathbf{x}_i, \pm h)$ $(i = 1 - n)$ where $\mathbf{x}_i = (\theta^1, \theta^2)_i$. Using these surface strain measurements, the in situ membrane strain measures and bending curvatures, $\mathbf{E}_i$ and $\mathbf{K}_i$, that correspond to their analytic counterparts $\mathbf{e}(\mathbf{u})$ and $\boldsymbol{\kappa}(\mathbf{u})$, given by Equation (5.16), can be determined at the location $\mathbf{x}_i$ on the mid-surface of the shell as follows:

$$\mathbf{E}_i \equiv \begin{Bmatrix} \mathrm{E}_1 \\ \mathrm{E}_2 \\ \mathrm{E}_3 \end{Bmatrix}_i = \frac{1}{2} \begin{Bmatrix} \varepsilon_{11}^{+} + \varepsilon_{11}^{-} \\ \varepsilon_{22}^{+} + \varepsilon_{22}^{-} \\ \gamma_{12}^{+} + \gamma_{12}^{-} \end{Bmatrix}_i \quad (i = 1 - n) \tag{5.24}$$

$$\mathbf{K}_i \equiv \begin{Bmatrix} \mathrm{K}_4 \\ \mathrm{K}_5 \\ \mathrm{K}_6 \end{Bmatrix}_i = \frac{1}{2h} \begin{Bmatrix} \varepsilon_{11}^+ - \varepsilon_{11}^- \\ \varepsilon_{22}^+ - \varepsilon_{22}^- \\ \gamma_{12}^+ - \gamma_{12}^- \end{Bmatrix}_i \quad (i = 1 - n) \tag{5.25}$$

5.3.4 The weighted-least-squares functional

Utilizing the iFEM formulation presented in (Tessler et al., 2011) as a general structure, a weighted-least-squares functional, $\Phi(\mathbf{u})$, that takes in account the membrane and bending deformations of the current Kirchhoff–Love shell model can be established as

$$\Phi(\mathbf{u}) = \sum_{\alpha=1}^{6} w_\alpha \, \varphi_\alpha \tag{5.26}$$

where w_α $(\alpha = 1-3)$ and w_α $(\alpha = 4-6)$ are positive valued weighting constants of the membrane strain measures and bending curvatures, respectively. The importance of their usage for an iFEM discretization with very sparse measured strain data was described earlier (vid. Section 3.2.4). Moreover, in Equation (5.26), the functional $\varphi_\alpha \, (\alpha = 1-6)$ is the least-squares functional associated with the individual section strains. Considering that the discrete experimental strain measures, $\mathbf{E}_i$ and $\mathbf{K}_i$, become available in the iFEM analysis, the least-squares functional can be expressed as the normalized Euclidean norms as

$$\varphi_\alpha \equiv \frac{1}{n} \sum_{i=1}^{n} \left[e_\alpha(\mathbf{u})_i - \mathrm{E}_{\alpha i} \right]^2 \quad (\alpha = 1,2,3) \tag{5.27}$$

$$\varphi_\alpha \equiv \frac{(2h)^2}{n} \sum_{i=1}^{n} \left[\kappa_\alpha(\mathbf{u})_i - \mathrm{K}_{\alpha i} \right]^2 \quad (\alpha = 4,5,6) \tag{5.28}$$

On the other hand, they can be defined in terms of the dimensionless L_2 squared norms as given in Equations (5.29-30), if raw strain data is smoothed through a priori SEA analysis (vid. Section 3.2.3) and the continuous section strains, $\mathbf{E}$ and $\mathbf{K}$, are obtained for the iFEM analysis.

$$\varphi_\alpha \equiv \frac{1}{A} \int_A \left[e_\alpha(\mathbf{u}) - \mathrm{E}_\alpha \right]^2 dA \quad (\alpha = 1,2,3) \tag{5.29}$$

$$\varphi_\alpha \equiv \frac{(2h)^2}{A}\int_A \left[\kappa_\alpha(\mathbf{u}) - \mathrm{K}_\alpha\right]^2 dA \quad (\alpha = 4,5,6) \tag{5.30}$$

Furthermore, if an experimentally measured strain component is not available in any case, the Equations (5.27-28) or (5.29-30) will be reduced to L_2 squared norms of only analytical section strains as

$$\varphi_\alpha \equiv \frac{1}{A}\int_A \left[e_\alpha(\mathbf{u})\right]^2 dA \quad (\mathrm{w}_\alpha = \lambda),\ (\alpha = 1,2,3) \tag{5.31}$$

$$\varphi_\alpha \equiv \frac{(2h)^2}{A}\int_A \left[\kappa_\alpha(\mathbf{u})\right]^2 dA \quad (\mathrm{w}_\alpha = \lambda),\ (\alpha = 4,5,6) \tag{5.32}$$

where the corresponding weighting coefficient is set to be small, e.g., $\lambda = 10^{-5}$.

5.4 Summary of B-spline and NURBS Basis Functions

Since a large group of literature have already focused on the NURBS basis functions (e.g., Piegl and Tiller, 1997; Rogers, 2001), only a very brief summary is provided here to establish the notation used in the remainder of this chapter. Three independent parameters ξ, η, and ζ that unify a parameter space (ξ, η, ζ) are utilized to describe the B-spline and NURBS basis functions. A B-spline curve can be constructed using a knot vector in one dimension and a vector of control points. A knot vector contains a non-decreasing set of coordinates in the parameter space (ξ, η, ζ). For instance, a knot vector in one dimension can be defined as $\mathbf{\Xi} = \{\xi_1, \xi_2, ..., \xi_{m+p+1}\}$ where $\xi_i \in \xi \in \mathbb{R}$ is the i^{th} knot, i is the knot index, m is the number of basis functions, and p is the polynomial order (degree). If a knot vector whose first and last knots have multiplicity $p+1$ for a B-spline of polynomial degree p, this knot vector is called as open knot vector. Each repetition of any knot in the interior of a knot vector locally decreases the degree of continuity by one. The boundaries of the elements in the parametric space are defined based on the locations of the knots. According to the Cox–De Boor recursion formula (Cox, 1972; De Boor, 1972), the set of B-spline basis functions can be defined through a recursive relation starting with piecewise constants $(p = 0)$

$$N_{i,0} = \begin{cases} 1 & \text{if } \xi_i \le \xi < \xi_{i+1}, \\ 0 & \text{otherwise,} \end{cases} \tag{5.33}$$

For $p = 1, 2, 3, \ldots,$ they are defined by

$$N_{i,p}(\xi) = \frac{\xi - \xi_i}{\xi_{i+p} - \xi_i} N_{i,p-1}(\xi) + \frac{\xi_{i+p+1} - \xi}{\xi_{i+p+1} - \xi_{i+1}} N_{i+1,p-1}(\xi) \tag{5.34}$$

where the fractions of 0/0 are defined as zero. To avoid confusion of the comma sign used in the subscripts of functions to identify the partial derivative, the degree p, henceforward, will be omitted from the subscript of any B-spline basis function. The B-spline basis functions are generally not interpolatory except at the boundaries. Also, they satisfy the partition of unity condition as

$$\sum_i N_i(\xi) = 1 \tag{5.35}$$

Moreover, they are positive valued everywhere and a basis function of degree p can span up to $p+1$ elements. Associating the control point $\mathbf{s}_i$ with the basis function $N_i(\xi)$, a B-spline curve $\mathbf{S}(\xi)$ can be defined as

$$\mathbf{S}(\xi) = \sum_{i=1}^{N_{cp}} N_i(\xi)\mathbf{s}_i \equiv \sum_i N_i(\xi)\mathbf{s}_i \tag{5.36}$$

where N_{cp} denotes the number of control points and hereafter will be omitted for conciseness of the summations including basis functions. Except the control points on the both ends of the curve, the control points are not necessarily located on the curve that they define. The Cartesian product of one-dimensional B-spline curves defines a B-spline surface as

$$\mathbf{S}(\xi,\eta) = \sum_{i,j} N_i(\xi) M_j(\eta)\mathbf{s}_{ij} \tag{5.37}$$

where $\mathbf{s}_{ij}$ is the control net. A NURBS curve $\mathbf{S}(\xi)$ can be defined as

$$\mathbf{S}(\xi) = \sum_i R_i(\xi)\mathbf{s}_i \tag{5.38}$$

where $R_i(\xi)$ is one-dimensional NURBS basis function and expressed as

$$R_i(\xi) = \frac{N_i(\xi)\, w_i}{\sum_k N_k(\xi)\, w_k} \tag{5.39}$$

and w_i is positive-valued constant and referred to as weight of i^{th} control point. Similarly, the NURBS surface $\mathbf{S}(\xi,\eta)$ can be defined as

$$\mathbf{S}(\xi,\eta) = \sum_{i,j} R_{ij}(\xi,\eta)\,\mathbf{s}_{ij} \tag{5.40}$$

where $R_{ij}(\xi,\eta)$ is the two-dimensional NURBS basis functions and expressed as

$$R_{ij}(\xi,\eta) = \frac{N_i(\xi)\, M_j(\eta)\, w_{ij}}{\sum_{k,l} N_k(\xi)\, M_l(\eta)\, w_{kl}} \tag{5.41}$$

For simplicity, the subscript ij, henceforward, is replaced by a single subscript i. Therefore, Equation (5.40) can concisely be rewritten as

$$\mathbf{S}(\xi,\eta) = \sum_{i} R_{i}(\xi,\eta)\,\mathbf{s}_{i} \tag{5.42}$$

It is important to note that, NURBS curves and surfaces have the same properties as B-spline curves and surfaces.

5.5 Isogeometric iFEM formulation for thin shells: isogeometric Kirchhoff–Love inverse-shell element

An isogeometric Kirchhoff–Love inverse-shell element, named “iKLS”, is developed on the basis of iFEM weighted-least-squares formulation. This development couples the NURBS-based IGA together with the iFEM methodology for shape-sensing analysis, thus leads a novel “isogeometric iFEM formulation”. In the following derivations, the parametric coordinates $(\xi,\ \eta,\ \zeta)$ used to define the NURBS basis functions in previous section are associated with general convected curvilinear coordinates θ^i. Hence, the coordinates $\xi = \theta^1$ and $\eta = \theta^2$ represent the in-plane coordinates and the coordinate $\zeta = \theta^3$ indicates the thickness direction of the iKLS element. The necessary position vectors $\mathbf{A}_i$ and $\mathbf{F}$ used to develop the iKLS formulation, displacement DOF (u_i, v_i, w_i) of i^{th} control point, and kinematic variables (u, v, w) are illustrated in Figure 5.7.

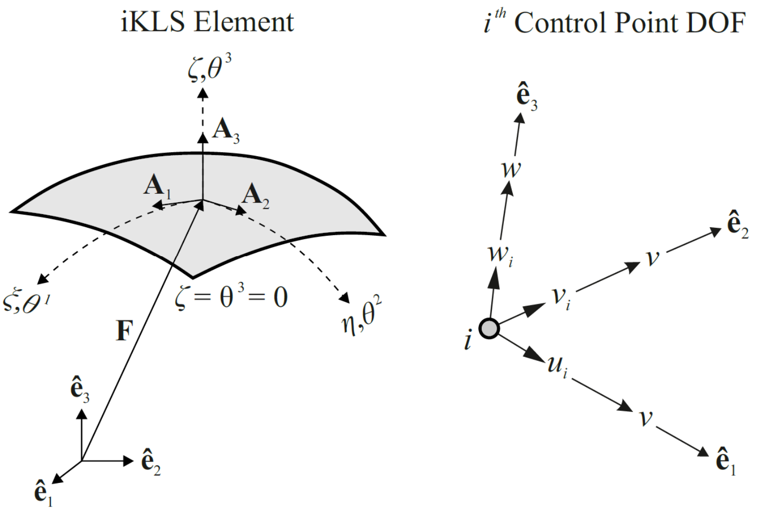

Figure 5.7 The iKLS element and displacement DOF of i^{th} control point.

To develop the iKLS element formulation, first of all, the position vector $\mathbf{F}$ to a material point on the mid-surface, which is used to define the Equation (5.2), can be described by the finite sum of two-dimensional NURBS basis functions $R_i(\xi,\eta)$ as

$$\mathbf{F} = \sum_i R_i(\xi,\eta)\,\mathbf{P}_i \equiv \sum_i R_i\,\mathbf{P}_i \tag{5.43}$$

where $\mathbf{P}_i$ are the coordinates of the control points that defines the physical geometry of the iKLS element. Secondly, taking the partial derivatives of $\mathbf{F}$ with respect to parametric coordinates ξ and η, the covariant base vectors $\mathbf{A}_\alpha$ of the mid-surface given by Equation (5.3) can be obtained as

$$\mathbf{A}_\alpha = \mathbf{F}_{,\alpha} = \sum_i R_{i,\alpha}\mathbf{P}_i \tag{5.44}$$

where the first-order derivatives of the NURBS shape function are denoted as

$$R_{i,1} = R_{i,\xi} = \partial R_i(\xi,\eta)/\partial\xi \tag{5.45}$$

$$R_{i,2} = R_{i,\eta} = \partial R_i(\xi,\eta)/\partial\eta \tag{5.46}$$

The (u, v, w) kinematic variables, i.e., orthogonal components of the mid-surface displacement vector $\mathbf{u}$ given by Equation (5.8), can be interpolated using translation

DOF (u_i, v_i, w_i) of control points and the same NURBS basis functions $R_i(\xi,\eta)$ used for the physical geometry discretization. These interpolations are explicitly given as

$$\mathbf{u} \equiv \begin{Bmatrix} u \\ v \\ w \end{Bmatrix} = \sum_i R_i(\xi,\eta) \begin{Bmatrix} u_i \\ v_i \\ w_i \end{Bmatrix} \equiv \sum_i R_i \mathbf{u}_i^e \tag{5.47}$$

Substituting Equations (5.47) into Equations (5.17-22), membrane strain measures and bending curvatures given in Equation (5.16) can be expressed in terms of displacement vector $\mathbf{u}^e$ of an iKLS element as

$$\mathbf{e}(\mathbf{u}^e) = \begin{bmatrix} \mathbf{B}_1 \mathbf{u}^e & \mathbf{B}_2 \mathbf{u}^e & \mathbf{B}_3 \mathbf{u}^e \end{bmatrix}^T \tag{5.48}$$

$$\boldsymbol{\kappa}(\mathbf{u}^e) = \begin{bmatrix} \mathbf{B}_4 \mathbf{u}^e & \mathbf{B}_5 \mathbf{u}^e & \mathbf{B}_6 \mathbf{u}^e \end{bmatrix}^T \tag{5.49}$$

with

$$\mathbf{u}^e = \begin{bmatrix} \mathbf{u}_1^e & \mathbf{u}_2^e & \cdots & \mathbf{u}_{N_{cp}}^e \end{bmatrix}^T \tag{5.50}$$

$$\mathbf{u}_i^e = \begin{bmatrix} u_i & v_i & w_i \end{bmatrix}^T \; (i = 1 - N_{cp}) \tag{5.51}$$

where the displacement vector $\mathbf{u}^e$ contains translational DOF of all the control points, and the matrices $\mathbf{B}_\alpha \equiv \mathbf{B}_\alpha(\xi,\eta)$ $(\alpha = 1 - 6)$ are functions of in-plane coordinates (ξ,η) and contain the derivatives of the NURBS basis functions. The explicit form of these matrices can be defined as

$$\mathbf{B}_\alpha = \begin{bmatrix} \mathbf{B}_\alpha^1 & \mathbf{B}_\alpha^2 & \ldots & \mathbf{B}_\alpha^{N_{cp}} \end{bmatrix} \quad (\alpha = 1 - 6) \tag{5.52}$$

with

$$\left. \begin{aligned} \mathbf{B}_1^j &= \begin{bmatrix} m_{11}^{1j} & m_{11}^{2j} & m_{11}^{3j} \end{bmatrix} \\ \mathbf{B}_2^j &= \begin{bmatrix} m_{22}^{1j} & m_{22}^{2j} & m_{22}^{3j} \end{bmatrix} \\ \mathbf{B}_3^j &= \begin{bmatrix} 2m_{12}^{1j} & 2m_{12}^{2j} & 2m_{12}^{3j} \end{bmatrix} \end{aligned} \right\} (j = 1 - N_{cp}) \tag{5.53}$$

and

$$\left.\begin{aligned}\mathbf{B}_4^j &= \left[b_{11}^{1j} \quad b_{11}^{2j} \quad b_{11}^{3j} \right] \\ \mathbf{B}_5^j &= \left[b_{22}^{1j} \quad b_{22}^{2j} \quad b_{22}^{3j} \right] \\ \mathbf{B}_6^j &= \left[2b_{12}^{1j} \quad 2b_{12}^{2j} \quad 2b_{12}^{3j} \right]\end{aligned}\right\} (j = 1 - N_{cp}) \tag{5.54}$$

In Equation (5.53), terms associated with membrane strain measures can be defined as

$$m_{\alpha\beta}^{ij} = \frac{1}{2}\left[(\mathbf{A}_\beta \cdot \hat{\mathbf{e}}_i) R_{j,\alpha} + (\mathbf{A}_\alpha \cdot \hat{\mathbf{e}}_i) R_{j,\beta} \right] \quad (j = 1 - N_{cp}) \tag{5.55}$$

In addition, terms related to bending curvatures, given in Equation (5.54), can be expressed as

$$\left.\begin{aligned} b_{\alpha\beta}^{ij} = \frac{1}{2}\left[(\mathbf{A}_{3,\beta} \cdot \hat{\mathbf{e}}_i) R_{j,\alpha} + (\mathbf{A}_{3,\alpha} \cdot \hat{\mathbf{e}}_i) R_{j,\beta} \right] & \\ + \frac{1}{2}\left[(\mathbf{A}_3 \times \mathbf{A}_\beta) \cdot \mathbf{\Theta}_\alpha^{ij} + (\mathbf{A}_3 \times \mathbf{A}_\alpha) \cdot \mathbf{\Theta}_\beta^{ij} \right] & \end{aligned}\right\} (j = 1 - N_{cp}) \tag{5.56}$$

where the terms $\mathbf{\Theta}_\alpha^{ij}$ contains second-order derivatives of the NURBS basis functions and can be explicitly defined as

$$\left.\begin{aligned} \mathbf{\Theta}_\alpha^{ij} = (\mathbf{A}_3 \cdot \hat{\mathbf{e}}_i)(\boldsymbol{\chi}_1 R_{j,\alpha 2} - \boldsymbol{\chi}_2 R_{j,1\alpha}) & \\ + (\mathbf{A}_3 \cdot \hat{\mathbf{e}}_i)(\boldsymbol{\chi}_{1,\alpha} R_{j,2} - \boldsymbol{\chi}_{2,\alpha} R_{j,1}) & \\ + (\mathbf{A}_{3,\alpha} \cdot \hat{\mathbf{e}}_i)(\boldsymbol{\chi}_1 R_{j,2} - \boldsymbol{\chi}_2 R_{j,1}) & \end{aligned}\right\} (j = 1 - N_{cp}) \tag{5.57}$$

In Equation (5.57), the second-order derivatives of the NURBS shape function are represented as

$$R_{i,11} = R_{i,\xi\xi} = \partial^2 R_i(\xi,\eta) / \partial \xi^2 \tag{5.58}$$

$$R_{i,22} = R_{i,\eta\eta} = \partial^2 R_i(\xi,\eta) / \partial \eta^2 \tag{5.59}$$

$$R_{i,12} = R_{i,\xi\eta} = \partial^2 R_i(\xi,\eta) / \partial \xi \, \partial \eta \tag{5.60}$$

The terms $\boldsymbol{\chi}_\alpha$ used in Equation (5.57) and their first-order partial derivatives with respect to parametric coordinates ξ and η can be calculated as

$$\boldsymbol{\chi}_\alpha = \frac{\mathbf{A}_\alpha}{\left\| \mathbf{A}_1 \times \mathbf{A}_2 \right\|} \tag{5.61}$$

and

$$\boldsymbol{\chi}_{\alpha,\alpha} = \frac{\mathbf{A}_{\alpha,\alpha} - \boldsymbol{\chi}_{\alpha}\left[\mathbf{A}_{1,\alpha}\cdot(\mathbf{A}_2\times\mathbf{A}_3) + \mathbf{A}_{2,\alpha}\cdot(\mathbf{A}_3\times\mathbf{A}_1)\right]}{\left\|\mathbf{A}_1\times\mathbf{A}_2\right\|} \tag{5.62}$$

Moreover, the first-order derivatives $\mathbf{A}_{3,\alpha}$ used to define Equations (5.56) and (5.57) can be computed as

$$\mathbf{A}_{3,\alpha} = \frac{\mathbf{A}_{1,\alpha}\times\mathbf{A}_2 + \mathbf{A}_1\times\mathbf{A}_{2,\alpha} - \mathbf{A}_3\left[\mathbf{A}_{1,\alpha}\cdot(\mathbf{A}_2\times\mathbf{A}_3) + \mathbf{A}_{2,\alpha}\cdot(\mathbf{A}_3\times\mathbf{A}_1)\right]}{\left\|\mathbf{A}_1\times\mathbf{A}_2\right\|} \tag{5.63}$$

Once the discrete experimental and analytical section strains are calculated using Equations (5.24-25) and (5.48-49), respectively, they can be inserted into Equations (5.26-28). As a result, the weighted-least-squares functional, $\Phi_e(\mathbf{u}^e)$, accounting for membrane and bending deformations can be expressed for an individual iKLS element as follows:

$$\Phi_e(\mathbf{u}^e) = \frac{1}{n}\sum_{i=1}^{n}\left(\sum_{\alpha=1}^{3} w_\alpha[e_\alpha(\mathbf{u}^e)_i - \mathrm{E}_{\alpha i}]^2 + (2h)^2\sum_{\alpha=4}^{6} w_\alpha[\kappa_\alpha(\mathbf{u}^e)_i - \mathrm{K}_{\alpha i}]^2\right) \tag{5.64}$$

All strain compatibility relations are explicitly satisfied based on these assumptions, therefore Equation (5.64) can be minimized with respect to displacement vector $\mathbf{u}^e$ of an iKLS element as

$$\frac{\partial\Phi_e(\mathbf{u}^e)}{\partial\mathbf{u}^e} = \frac{1}{n}\sum_{i=1}^{n}\left(\sum_{\alpha=1}^{3} w_\alpha\frac{\partial[e_\alpha(\mathbf{u}^e)_i - \mathrm{E}_{\alpha i}]^2}{\partial\mathbf{u}^e} + (2h)^2\sum_{\alpha=4}^{6} w_\alpha\frac{\partial[\kappa_\alpha(\mathbf{u}^e)_i - \mathrm{K}_{\alpha i}]^2}{\partial\mathbf{u}^e}\right) = 0 \tag{5.65}$$

where the terms associated with derivatives of section strains can be respectively expressed as

$$\frac{\partial[e_\alpha(\mathbf{u}^e)_i - \mathrm{E}_{\alpha i}]^2}{\partial\mathbf{u}^e} = 2[\mathbf{B}_\alpha(\mathbf{x}_i)\mathbf{u}^e - \mathrm{E}_{\alpha i}]^T\,\mathbf{B}_\alpha(\mathbf{x}_i)\quad(\alpha = 1-3) \tag{5.66}$$

$$\frac{\partial[\kappa_\alpha(\mathbf{u}^e)_i - \mathrm{K}_{\alpha i}]^2}{\partial\mathbf{u}^e} = 2[\mathbf{B}_\alpha(\mathbf{x}_i)\mathbf{u}^e - \mathrm{K}_{\alpha i}]^T\,\mathbf{B}_\alpha(\mathbf{x}_i)\quad(\alpha = 4-6) \tag{5.67}$$

Inserting the expressions given by Equations (5.66-67) into (5.65) gives rise to

$$\frac{\partial\Phi_e(\mathbf{u}^e)}{\partial\mathbf{u}^e} = 2\left(\boldsymbol{\Gamma}^e\mathbf{u}^e - \boldsymbol{\varepsilon}^e\right) = 0 \tag{5.68}$$

or simply

$$\mathbf{\Gamma}^e \, \mathbf{u}^e = \boldsymbol{\varepsilon}^e \tag{5.69}$$

where $\mathbf{\Gamma}^e$ is the element left-hand-side matrix; $\boldsymbol{\varepsilon}^e$ is the element right-hand-side vector, which is a function of the measured strain values; and $\mathbf{u}^e$ is the nodal displacement vector of the element.

The $\mathbf{\Gamma}^e$ matrix can be explicitly written in terms of the $\mathbf{B}_\alpha$ $(\alpha = 1-6)$ matrices and their corresponding weighting constants w_α $(\alpha = 1-6)$ as

$$\mathbf{\Gamma}^e = \frac{1}{n}\sum_{i=1}^{n}\left(\sum_{\alpha=1}^{3}\left[w_\alpha \left[\mathbf{B}_\alpha(\mathbf{x}_i)\right]^T \mathbf{B}_\alpha(\mathbf{x}_i)\right] + (2h)^2 \sum_{\alpha=4}^{6}\left[w_\alpha \left[\mathbf{B}_\alpha(\mathbf{x}_i)\right]^T \mathbf{B}_\alpha(\mathbf{x}_i)\right]\right) \tag{5.70}$$

The $\boldsymbol{\varepsilon}^e$ vector is a function of experimental section strains, and is given by

$$\boldsymbol{\varepsilon}^e = \frac{1}{n}\sum_{i=1}^{n}\left(\sum_{\alpha=1}^{3}\left[w_\alpha \left[\mathbf{B}_\alpha(\mathbf{x}_i)\right]^T \mathrm{E}_{\alpha i}\right] + (2h)^2 \sum_{\alpha=4}^{6}\left[w_\alpha \left[\mathbf{B}_\alpha(\mathbf{x}_i)\right]^T \mathrm{K}_{\alpha i}\right]\right) \tag{5.71}$$

It is important to note that the matrices $\mathbf{B}_\alpha$ $(\alpha = 1-6)$ in Equations (5.70-71) are calculated at the discrete locations $\mathbf{x}_i \equiv (\xi, \eta)_i$ $(i = 1, n)$ on the mid-surface of the iKLS element, where the corresponding top- and bottom-surface strain rosettes are located. Using the local matrix equations (i.e., Equations 5.69-71), the steps described in Section 3.3 can be revisited to obtain global linear equation system of the discretized structure: refer to Equations (3.78-81) by omitting $\mathbf{T}^e$ from these equations. Finally, the resulting system of equations (refer to Equation 3.82) can be obtained by applying problem-specific constraint boundary conditions, and then subsequently solved to acquire real-time deformed shape of the shell body.

5.6 Numerical Examples

In the following section, shape-sensing capability of the iKLS element is assessed and validated solving three different shell problems. First of all, Scordelis–Lo roof and the pinched hemisphere problems are solved as benchmark problems for validating the membrane and bending capability of the iKLS element, respectively. In fact, these problems are the first two test cases of a very well-known shell obstacle course proposed and studied by Belytschko et al. (1985) and MacNeal and Harder (1985). Moreover, hyperbolic paraboloid proposed by Bathe et al. (2000) has been widely used in the literature for evaluating the shell elements' performance because the shell structure is subjected to stress states of varying complexity. Therefore, after validating the membrane and bending capability of the iKLS element, the partly clamped hyperbolic paraboloid problem is solved to better assess the ability of the iKLS element against the locking phenomenon.

5.6.1 Scordelis–Lo Roof

A portion of a cylindrical shell whose two end sections are fixed by rigid diaphragms has a radius of $r = 25$ m, length of $L = 50$ m, and thickness of $2h = 0.25$ m as depicted in Figure 5.8. The constraint boundary conditions pertaining to rigid diaphragms can be specified as $V = W = 0$. The cylindrical shell made of an isotropic material having an elastic modulus of $E = 432$ MPa, a zero Poisson's ratio $v = 0$, and a density of $\rho = 4$ kg/m^3. A distributed loading represented as a gravitational load $g = 90$ m/s^2 is applied in negative Z direction (refer to Figure 5.8). This problem was originally solved in Scordelis and Lo (1969), then it has been extensively studied by many researchers (e.g., Mac Neal and Harder, 1985) and is so-called Scordelis–Lo roof.

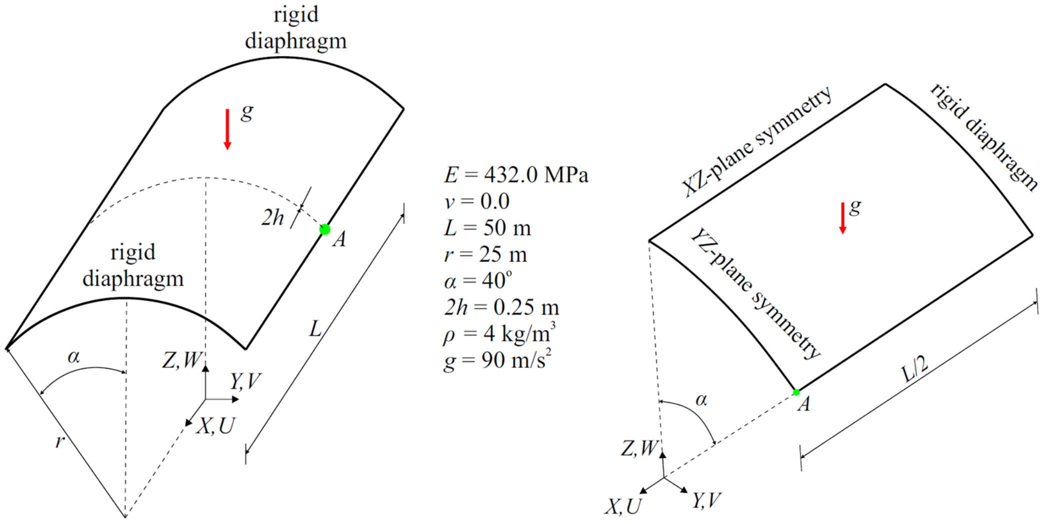

(a) (b)

Figure 5.8 (a) Scordelis–Lo roof; (b) One-fourth of Scordelis–Lo roof with symmetric boundary conditions.

In this section, Scodelis-Lo roof is analyzed once again using the isogeometric iFEM methodology to validate membrane capability of the iKLS element because a substantial part of the strain energy is exhibited by membrane strain energy during the deformation of the roof. There is no need to model whole roof because the applied boundary conditions and geometry of the roof is suitable to take the advantage of symmetry conditions. Therefore, the following iFEM and direct FEM models are defined over one fourth of the geometry and relevant symmetry constraint boundary conditions are applied (refer to Figures 5.8).

To establish an accurate reference solution, a convergence study was performed using direct FEM analyses utilizing an in-house FEM code. The most refined mesh consisted of 8100 uniformly distributed rectangular elements, possessing 49686 DOF. The vertical displacement along *Z*-direction at the midpoint of the lateral side (i.e., point A as depicted in Figure 5.8) is denoted by the symbol W_A. As a result of high-fidelity FEM analysis performed, the value of this vertical displacement is obtained as $W_A = -0.3017\text{ m}$ which aggress very well with the reference solution predicted in MacNeal and Harder (1985) as $W_A = -0.3024\text{ m}$. Thus, the FEM deflections and rotations can be safely used to compute the simulated strain-sensor strains in the following iFEM analysis.

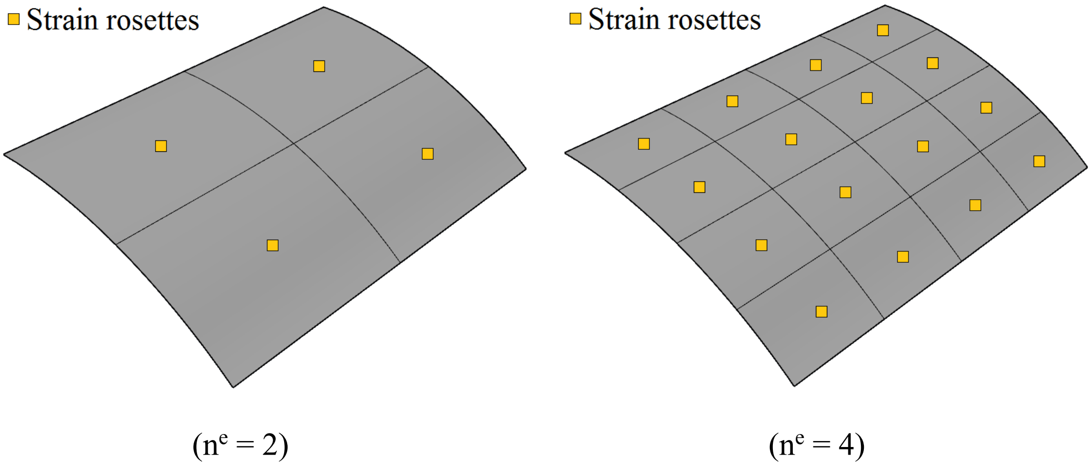

Figure 5.9 Discretization of one-fourth of Scordelis–Lo roof using iKLS elements with top- and bottom-surface strain rosettes per each element.

In the present iFEM analysis, the Scordelis–Lo roof is analyzed using seven different iKLS discretization where the edges of the roof are divided by the same number of element subdivisions ($n^e = 2,\ldots,8$). For each iKLS model, the polynomial degrees of the NURBS shape functions are fixed to $p = q = 8$ and C^1-continuity is attained across an interior element boundary. Every single iKLS element is instrumented with two strain rosettes, one on the centroid of the top surface and the other one on the centroid of the bottom surface. In Figure 5.9, examples of strain rosette configurations are shown for iKLS discretization ($n^e = 2$) and ($n^e = 4$).

To assess the accuracy of the displacement predictions, it would be convenient to use maximum values of displacements obtained from the high-fidelity FEM solutions (reference) as normalization factors. These normalizations are given as

$$\bar{\chi} = \chi / \left|\chi_{\max}^{\mathrm{FEM}}\right| \quad (\chi = U, V, W) \tag{5.72}$$

where maximum values of the reference displacements are $U_{\max}^{\mathrm{FEM}} = -0.0125\ \mathrm{m}$, $V_{\max}^{\mathrm{FEM}} = -0.1588\ \mathrm{m}$, and $W_{\max}^{\mathrm{FEM}} = -0.3017\ \mathrm{m}$. The legend "iFEM" represents the isogeometric iFEM solutions, whereas the legend "Reference" represents the high-fidelity FEM solutions (henceforward, refer to all graphs). In Figures 5.10-13, maximum values of the iFEM and FEM predictions for the $\bar{U}$, $\bar{V}$, $\bar{W}$ normalized displacements given in Equation (5.72) are plotted versus the number of element subdivisions (n^e) of the Scordelis–Lo roof, respectively.

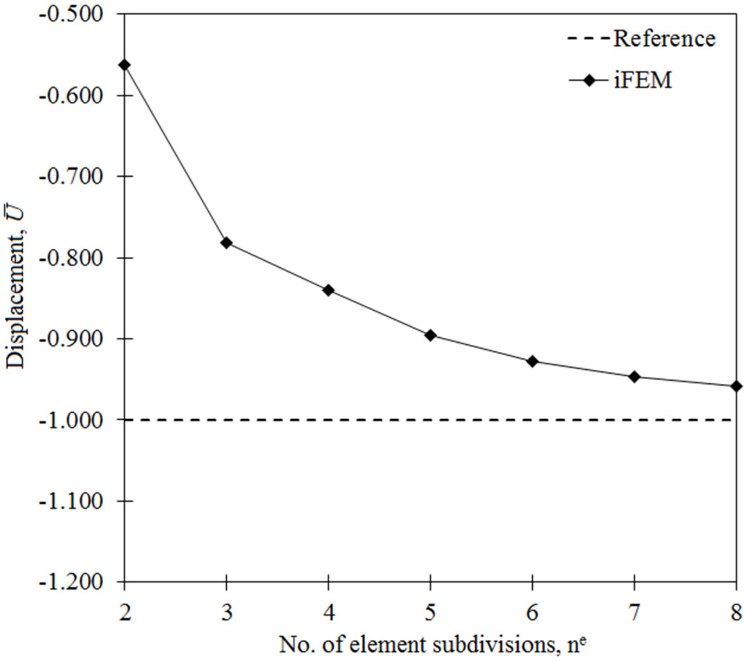

Figure 5.10 Displacement $\bar{U}$ versus number of element subdivisions n^e for Scordelis–Lo roof.

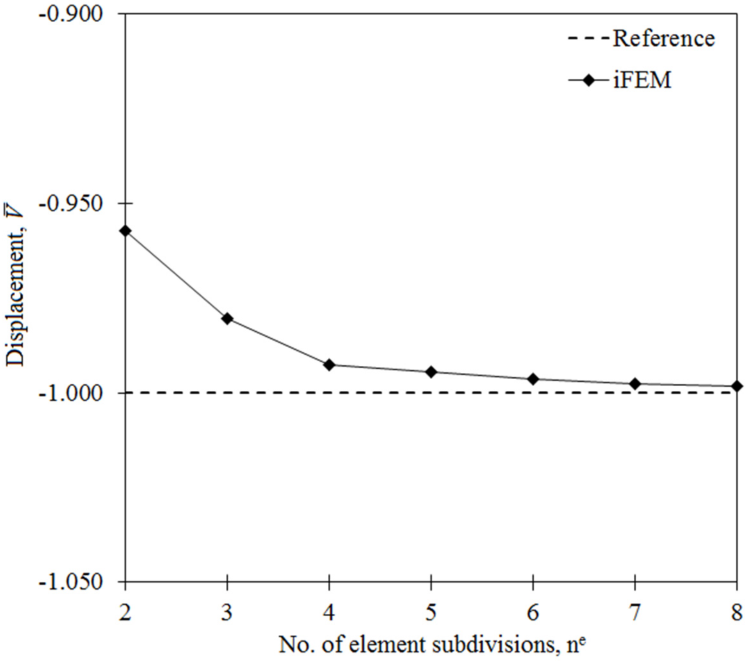

Figure 5.11 Displacement $\bar{V}$ versus number of element subdivisions n^e for Scordelis–Lo roof.

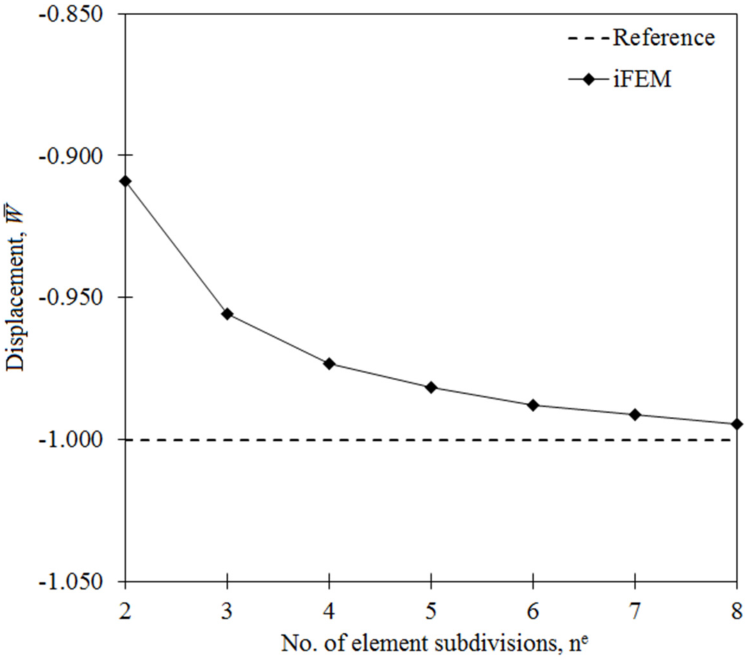

Figure 5.12 Displacement $\bar{W}$ versus number of element subdivisions n^e for Scordelis–Lo roof.

These graphs show that the iFEM predictions for the $\bar{V}$ and $\bar{W}$ displacements convergence to the reference solution much quicker than the iFEM predictions for the

$\bar{U}$ displacement. In fact, the deformed shape (total deformation) of the roof is mainly caused by the maximum reference displacement $V_{\max}^{\text{FEM}}$ and $W_{\max}^{\text{FEM}}$ because these reference displacements are at least ten times greater than the displacement $U_{\max}^{\text{FEM}}$; hence, convergence of iFEM predictions for displacement $\bar{U}$ will not play distinguished role for the real-time reconstruction of the total deformation. As a result, the results depicted in Figures 5.10-13 confirm that the isogeometric iFEM formulation of the iKLS element predicts displacements that are as accurate as those of the reference solutions.

Moreover, in Figures 5.13-15, the iFEM and FEM contour plots for $\bar{U}$, $\bar{V}$, and $\bar{W}$ are presented, showing the results that are graphically indistinguishable. In these figures, the displacement results pertaining to iFEM analysis are obtained using the iKLS discretization ($n^e = 4$) with 16×2 strain rosettes in total. The percent difference between the iFEM and FEM solutions for the maximum values of $\bar{U}$, $\bar{V}$, and $\bar{W}$ are respectively 15.9%, 0.8%, and 2.8%. Even though the percent difference for displacement $\bar{U}$ is relatively high, as explained in above paragraph, this displacement doesn't contribute much to the deformed shape. Therefore, these percent differences and contour plots clearly demonstrate the superior accuracy of the iKLS element for membrane structural responses, especially considering the low-fidelity discretization ($n^e = 4$) with few sensors used in iFEM analysis of a complex/curved geometry.

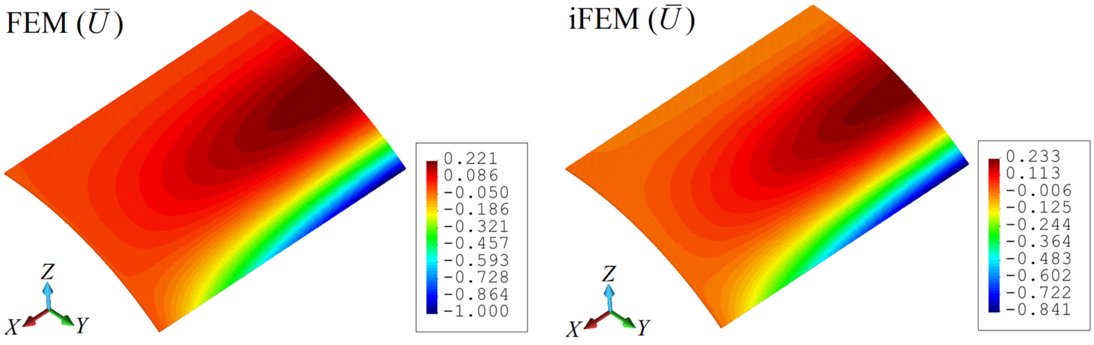

Figure 5.13 Contour plots of $\bar{U}$ displacement for Scordelis–Lo roof: Comparison between high-fidelity FEM and iFEM ($n^e = 4$) analyses.

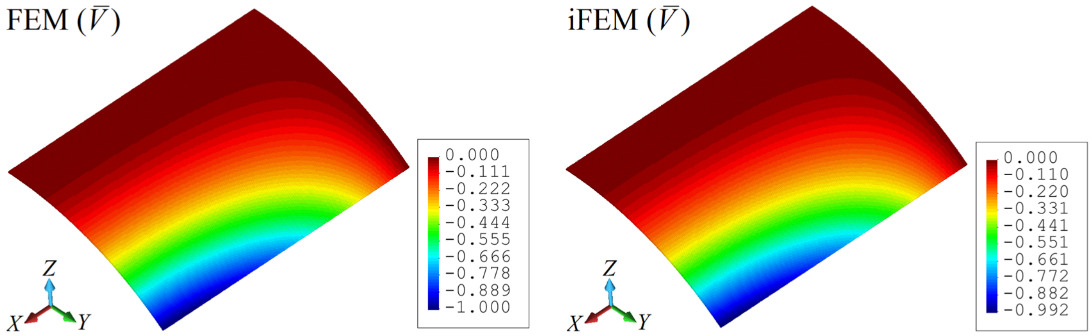

Figure 5.14 Contour plots of $\bar{V}$ displacement for Scordelis–Lo roof: Comparison between high-fidelity FEM and iFEM ($n^e = 4$) analyses.

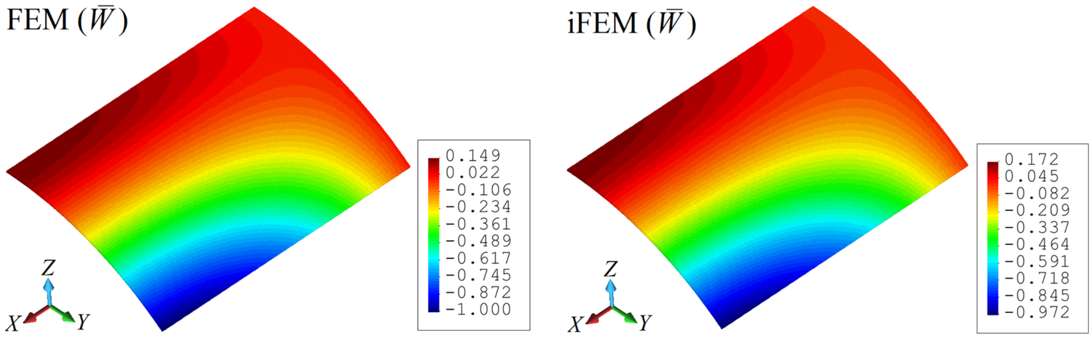

Figure 5.15 Contour plots of $\bar{W}$ displacement for Scordelis–Lo roof: Comparison between high-fidelity FEM and iFEM ($n^e = 4$) analyses.

As a summary, using iKLS element allow us to improve the accuracy of shape-sensing analysis even if a very coarse mesh (with a low number of strain sensors) is used for the analysis. This is because the polynomial degree (p,q) of the NURBS can be elevated without changing the location of knots, hence the number of elements (i.e., number of sensors) will remain unchanged. This feature of the isogeometric iFEM formulation is the notable technology that is used in this case study to obtain accurate displacements even with a low-fidelity iKLS discretization.

5.6.2 The pinched hemisphere

A hemispheric shell subjected to four different concentrated loads (with magnitude of $F = 2$ N) has a radius of $r = 10$ m and thickness of $2h = 40$ mm as shown in Figure 5.16. The prescribed boundary conditions are the minimum required to prevent rigid body motions. In other words, the apex of the hemisphere along Z-direction needs to be fixed in order to eliminate the rigid body motion. The hemisphere is made of an isotropic material properties with an elastic modulus of $E = 68.25$ MPa and a Poisson's ratio of $v = 0.3$. Morley and Morris (1978) originally solved this problem, and after that Mac Neal and Harder (1985) and Belytschko et al. (1985) studied this hemisphere problem in detail.

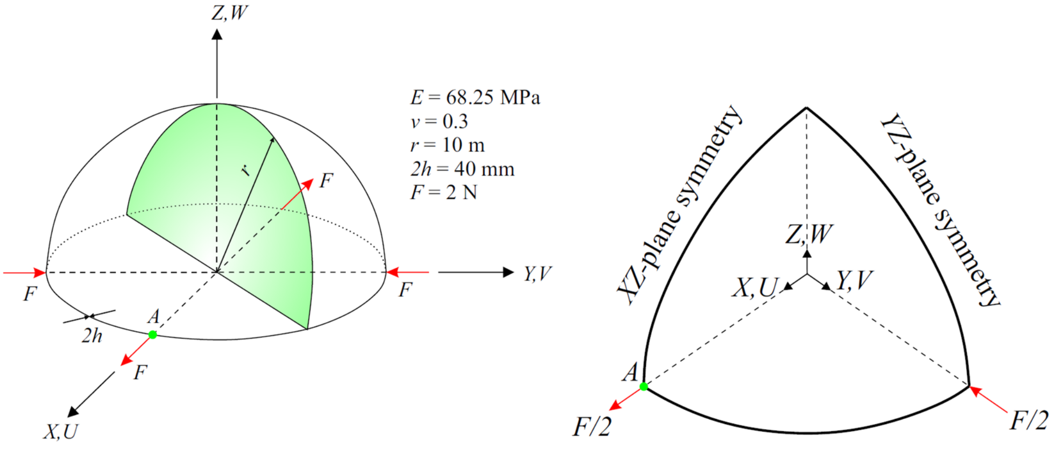

(a) (b)

Figure 5.16 (a) Pinched hemisphere; (b) One-fourth of the hemisphere with symmetric boundary conditions.

In contrast to the Scordelis–Lo roof problem solved in the previous section, this hemisphere problem is challenging in terms of demonstrating bending capability of the iKLS element because it exhibits almost none of membrane strains. Moreover, doubly curved geometry and concentrated loads make this problem highly sensitive to locking phenomena. Therefore, in this section, the pinched hemisphere is analyzed once again based on the presented isogeometric iFEM formulation. Similar to the Scordelis–Lo roof problem, it is also possible to take the advantage symmetry for this problem. Thus, the following iFEM and direct FEM models are defined over one quarter of the hemisphere and suitable symmetry constraint and loading boundary conditions are applied as shown in Figure 5.16.

First, an accurate reference solution is established through a convergence study that is performed using direct FEM analysis. The most refined mesh consisted of 7500 uniformly distributed rectangular elements, possessing 45906 DOF. To examine the accuracy of this high-fidelity FEM analysis, the quantity of interest is the displacement along the direction of the loading F at point A (refer to Figure 5.16), which is represented by the symbol U_A. The value of this displacement is found as $U_A = 0.0921\text{ m}$ from the high-fidelity FEM analysis, which is in a fairly well agreement with the reference solution, $U_A = 0.0940\text{ m}$, found by MacNeal and Harder (1985). Thus, the FEM deflections and rotations can be securely used to compute the simulated in situ surface strains in the following iFEM analysis.

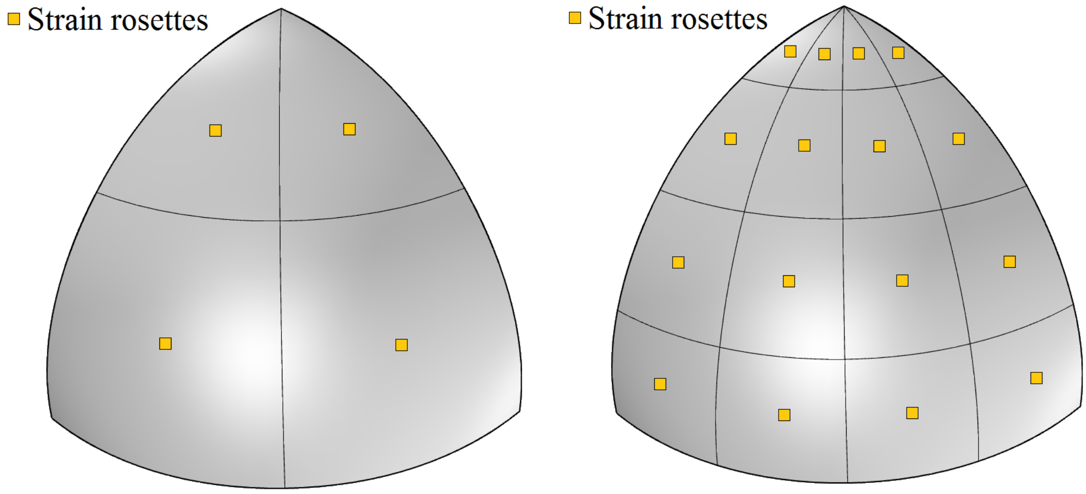

($n^e = 2$) ($n^e = 4$)

Figure 5.17 Discretization of one-fourth of the hemisphere using iKLS elements with top- and bottom-surface strain rosettes per each element.

In the current iFEM analysis, five different iKLS discretization are generated by uniformly dividing edges of one quarter of the hemisphere into 2, 4, 6, 8, and 10 segments (i.e., number of element subdivisions, n^e), respectively. Similar to iKLS discretization used for Scordelis–Lo roof, the polynomial degrees of the NURBS shape functions are fixed to $p = q = 8$ and C^1-continuity across an interior element boundary is ensured for each iKLS model. Moreover, two strain rosettes are located per each element of each iKLS model, one on the centroid of the top surface and the other one on the centroid of the bottom surface. According to this arrangement of in situ strain rosettes, examples of strain rosette configurations are illustrated for iKLS discretization ($n^e = 2$) and ($n^e = 4$) in Figure 5.17. For clear assessment of the accuracy of the displacement predictions, the normalized displacements ($\bar{U}$, $\bar{V}$, $\bar{W}$) given by Equation (5.72) are used herein with the normalization factors, $U_{\max}^{\text{FEM}} = 0.0921\text{ m}$,

$V_{\max}^{\text{FEM}} = -0.0921\text{ m}$, and $W_{\max}^{\text{FEM}} = 0.0457\text{ m}$, that are maximum values of the displacements obtained from the high-fidelity FEM analysis of the hemisphere.

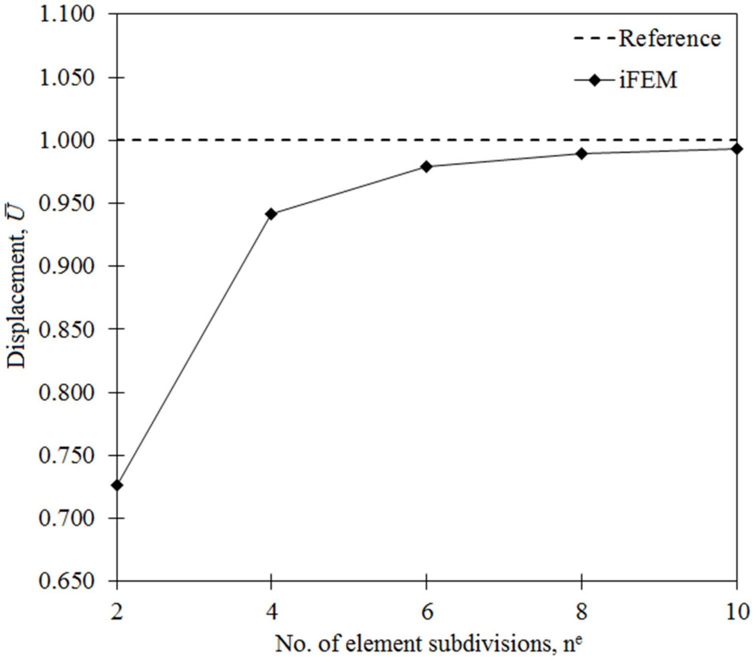

Figure 5.18 Displacement $\bar{U}$ versus number of element subdivisions n^e for hemisphere.

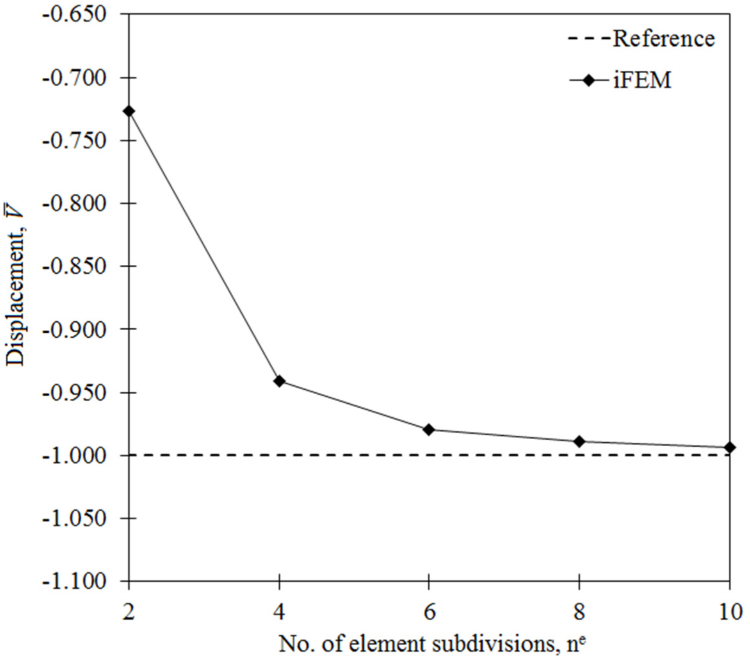

Figure 5.19 Displacement $\bar{V}$ versus number of element subdivisions n^e for hemisphere.

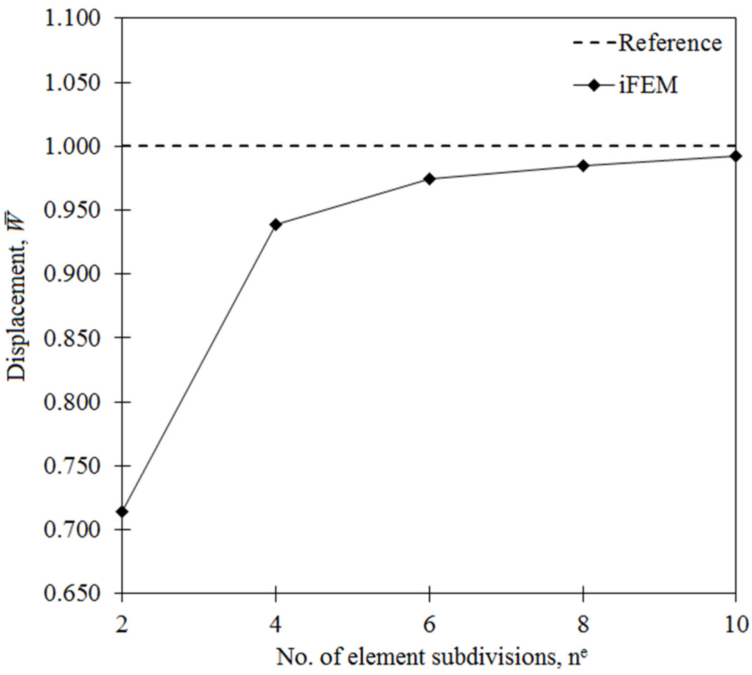

Figure 5.20 Displacement $\bar{W}$ versus number of element subdivisions n^e for hemisphere.

In Figures 5.18-20, the maximum values of displacements ($\bar{U}$, $\bar{V}$, $\bar{W}$) are compared between iFEM and reference FEM analysis for varying number of element subdivisions (n^e) of the hemisphere, respectively. These plots demonstrates the following two observations: (1) once the element subdivision become $n^e = 4$, the percent differences between iFEM and FEM solutions for all three displacements are approximately 6%, and (2) the convergence rate of the iFEM predictions to reference solutions follows a similar path for all three displacements. These observations confirm the superior bending capability of the iKLS element, even if a low-fidelity discretization ($n^e = 4$) with few number of sensors (i.e., $16 \times 2 = 32$ strain rosettes in total) is used in the shape-sensing analysis.

In addition, the contour plots for the $\bar{U}$, $\bar{V}$, and $\bar{W}$ displacements are depicted in Figures 5.21-23 where contour plots for iFEM analysis are graphically almost identical to those of FEM analysis. Note that, in these figures, the displacement results for the iFEM analysis are predicted using the iKLS discretization ($n^e = 6$) with 36×2 strain rosettes in total. As presented in Figures 5.21-23, the percent difference between the iFEM and FEM estimates for the maximum values of $\bar{U}$, $\bar{V}$, and $\bar{W}$ are about 2.1%, 2.1%, and 2.5%, respectively. Remarkably, these predictions demonstrate the high quality precision of isogeometric iFEM solutions for shape-sensing analysis of a complex/curved geometry.

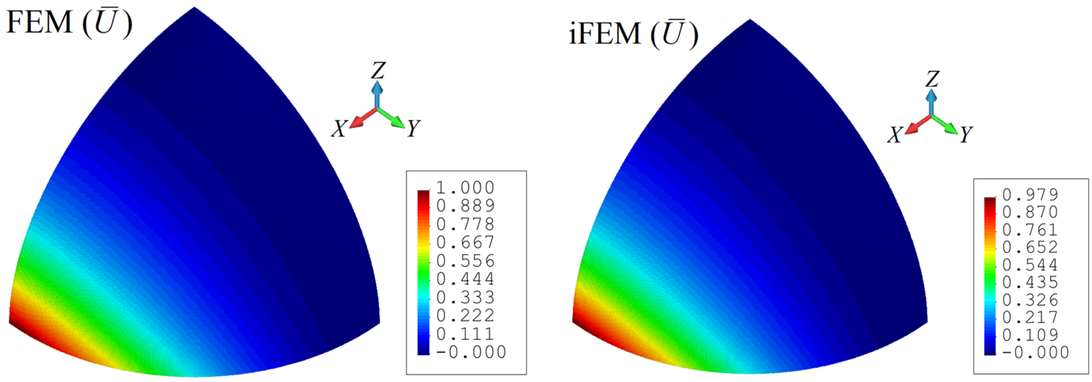

Figure 5.21 Contour plots of $\bar{U}$ displacement for hemisphere: Comparison between high-fidelity FEM and iFEM ($n^e = 6$) analyses.

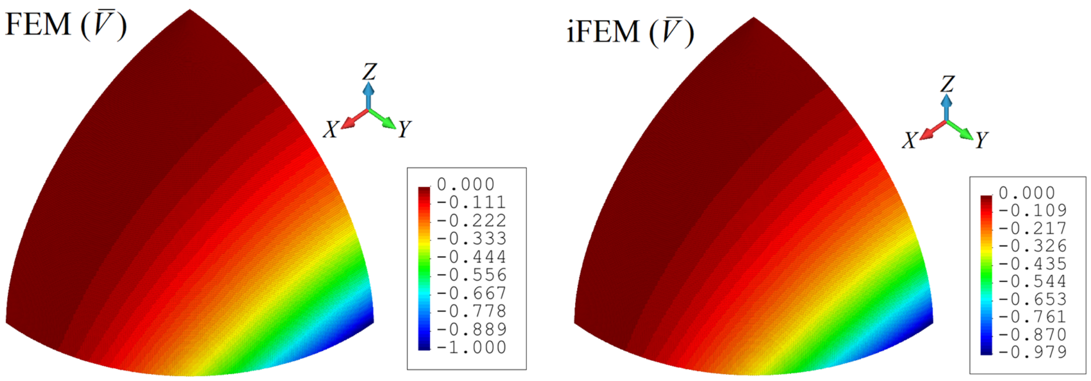

Figure 5.22 Contour plots of $\bar{V}$ displacement for hemisphere: Comparison between high-fidelity FEM and iFEM ($n^e = 6$) analyses.

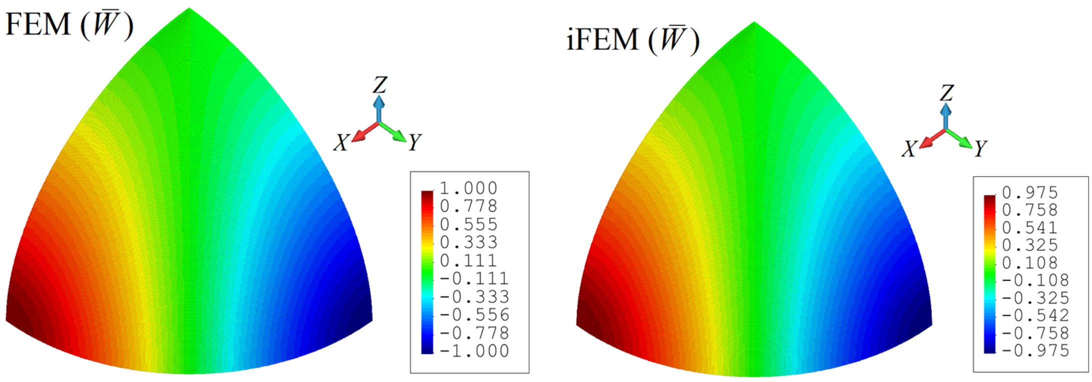

Figure 5.23 Contour plots of $\bar{W}$ displacement for hemisphere: Comparison between high-fidelity FEM and iFEM ($n^e = 6$) analyses.

5.6.3 Partly clamped hyperbolic paraboloid

A partly clamped hyperbolic paraboloid subjected to its self-weight has length of L = 1 m and uniform thickness of $2h$ = 1 mm as depicted in Figure 5.24. The mid-surface of the hyperbolic paraboloid is defined as

$$Z = X^2 - Y^2 \tag{5.73}$$

where the domain of the surface is defined over $(X,Y) \in [-L/2; L/2]$ (refer to Figure 5.24). It is worth note herein that this surface can be readily constructed using second order B-splines. The hyperbolic paraboloid is made of an isotropic material having an elastic modulus of E = 200 GPa, a Poisson's ratio ν = 0.3, and a density of ρ = 8000 kg/m^3. As presented in Figure 5.24, the mid-surface is clamped from the edge located at $X = -L/2$ and a unit gravitational load of g = 1 m/s^2 is applied to the mid-surface.

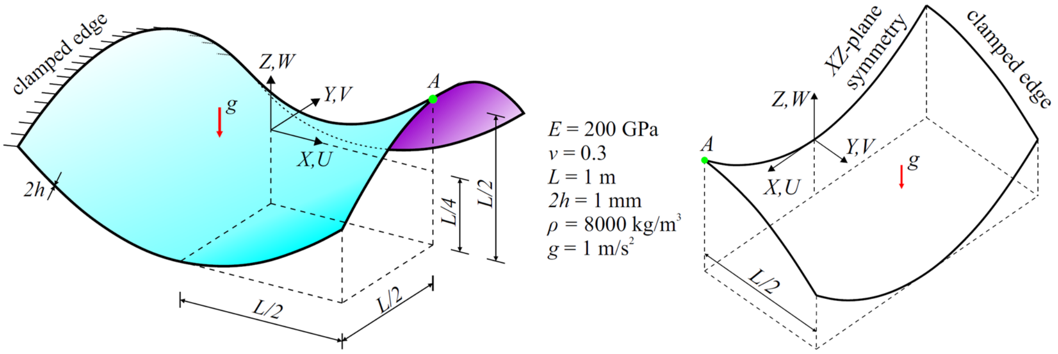

(a) (b)

Figure 5.24 (a) Hyperbolic paraboloid; (b) One half of the hyperbolic paraboloid with symmetric boundary conditions.

This problem was originally solved in Chapelle and Bathe (1998) where it was suggested as a good test for locking behavior. Then, Bathe et al. (2000) also performed FEM analysis of this problem and confirmed that it is an excellent test for locking in bending-dominated situations. Therefore, in this section, shape-sensing analysis of the presented hyperbolic paraboloid is performed based on the isogeometric iFEM methodology in order to better assess the capability of the iKLS element against the locking phenomenon. The prescribed boundary conditions and geometry are suitable to take advantage of the symmetry plane. Therefore, as shown in Figure 5.24, only half of the hyperbolic paraboloid can be modelled while applying the appropriate symmetry boundary conditions. Utilizing an in-house FEM code, an FEM convergence study was carried out to establish an accurate reference solution for this problem. The highest fidelity mesh has 22500 uniformly distributed rectangular elements and 136806 DOF. To assess the accuracy of the FEM convergence study, the quantity of reference is denoted by the symbol W_A representing the vertical displacement along Z-direction at point A, i.e., the midpoint of the edge located at $X = +L/2$ (refer to Figure 5.24). The reference solution was found as $W_A = -6.3941\text{ mm}$ in Bathe et al. (2000), whereas the high-fidelity FEM analysis predicts this vertical displacement as $W_A = -6.4061\text{ m}$ which agrees well with its associated reference solution. Hence, the FEM deflections and rotations are directly used to compute the simulated in situ strains.

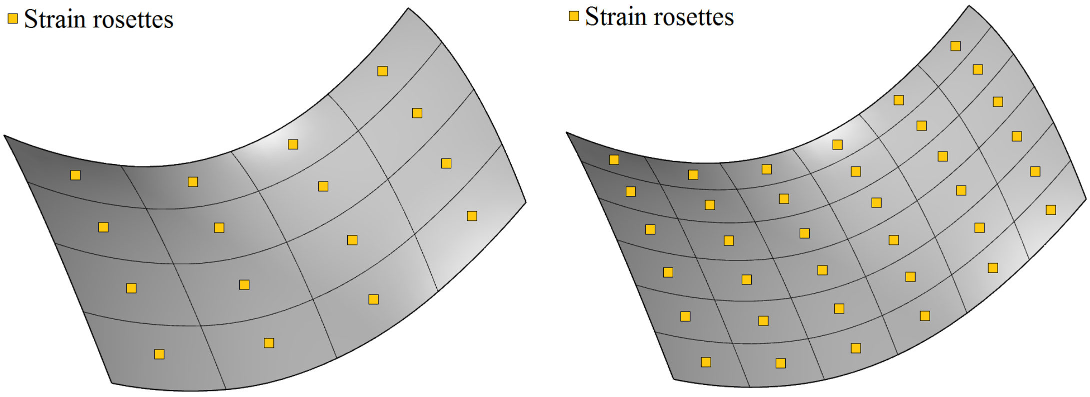

($n^e = 4$) ($n^e = 6$)

Figure 5.25 Discretization of half of the hyperbolic paraboloid using iKLS elements with top- and bottom-surface strain rosettes per each element.

In the following iFEM analysis, the hyperbolic paraboloid is analyzed using five different iKLS mesh where edges of the geometry are uniformly divided into same number of element subdivisions (n^e = 2, 4, 6, 8, 10), respectively. Similar to the previous case studies, the polynomial order is defined as $p = q = 8$ for the NURBS shape functions. However, as opposed to the previous case studies, C^2-continuous NURBS basis functions are attained across an interior element boundary by arranging multiplicity of the corresponding knot value. Therefore, this arrangement allow the exact surface given by Equation (5.73) to be encapsulated in the iKLS model. Two strain rosettes are located in each iKLS element at the following positions: (1) on the centroid of the top surface, and (2) on the centroid of the bottom surface. To give an example of strain rosette configurations, the iKLS models ($n^e = 4$) and ($n^e = 6$) are presented in Figure 5.25.

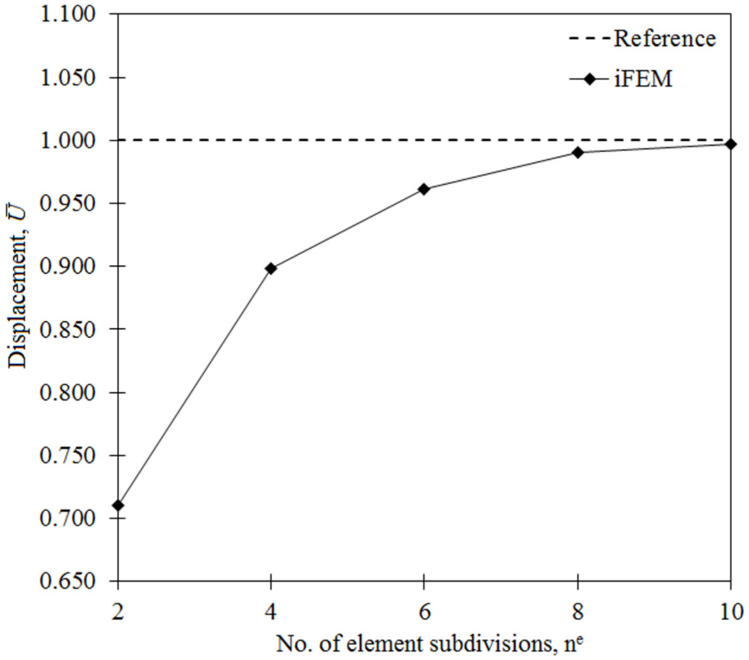

Figure 5.26 Displacement $\bar{U}$ versus number of element subdivisions n^e for hyperbolic paraboloid.

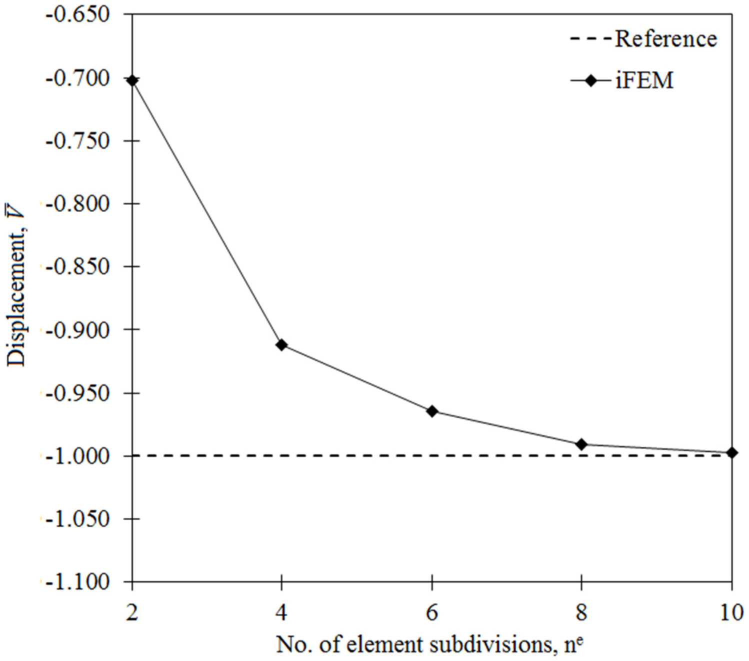

Figure 5.27 Displacement $\bar{V}$ versus number of element subdivisions n^e for hyperbolic paraboloid.

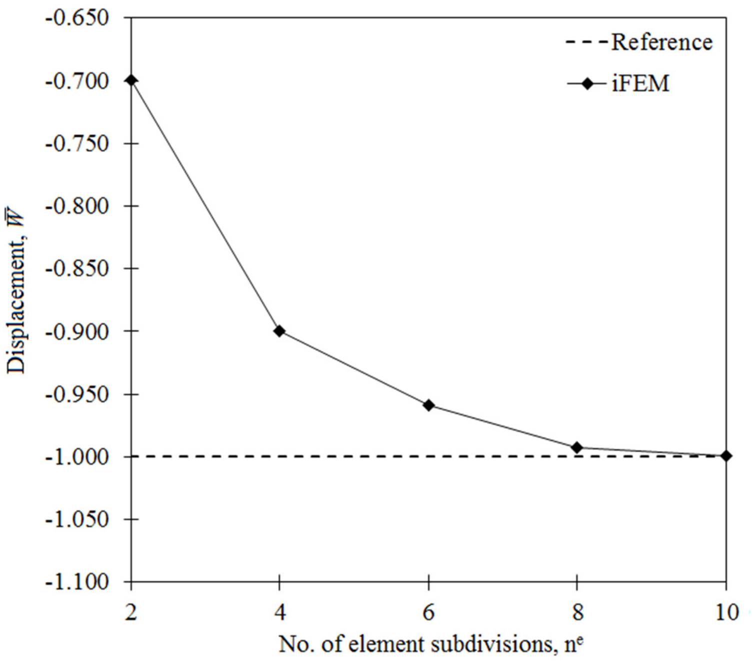

Figure 5.28 Displacement $\bar{W}$ versus number of element subdivisions n^e for hyperbolic paraboloid.

Similar to the previous case studies, the normalized displacements ($\bar{U}$, $\bar{V}$, $\bar{W}$) given by Equation (5.72) are also calculated for the hyperbolic paraboloid in order to clearly examine the precision of the displacement estimates. The following maximum values of the displacements are obtained in the high-fidelity FEM analysis of the hyperbolic paraboloid: $U_{\max}^{\text{FEM}} = 3.612 \text{ mm}$, $V_{\max}^{\text{FEM}} = 1.927 \text{ mm}$, and $W_{\max}^{\text{FEM}} = 7.372 \text{ mm}$ which are used as the normalization factors in the Equation (5.72). As depicted in Figures 5.26-28, the maximum values of $\bar{U}$, $\bar{V}$, and $\bar{W}$ are compared between iFEM and reference FEM analysis for varying number of element subdivisions (n^e), respectively. These results demonstrated that the iFEM predictions for the $\bar{U}$, $\bar{V}$, and $\bar{W}$ displacements convergence to their reference solutions by following a similar pathway. In addition, as can be from these figures, the percent differences between iFEM and FEM estimates for all three displacements are approximately 30% when iKLS discretization ($n^e = 2$) is used, whereas these percent differences are dramatically reduced to 10% for the case ($n^e = 4$). Finally, iKLS discretization ($n^e = 10$) predicts displacements that are as perfectly accurate as those of the reference solutions.

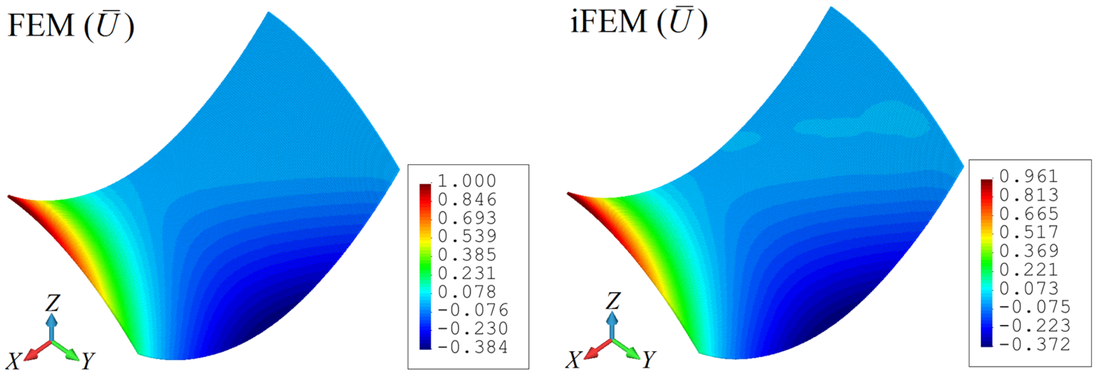

Figure 5.29 Contour plots of $\bar{U}$ displacement for hyperbolic paraboloid: Comparison between high-fidelity FEM and iFEM ($n^e = 6$) analyses.

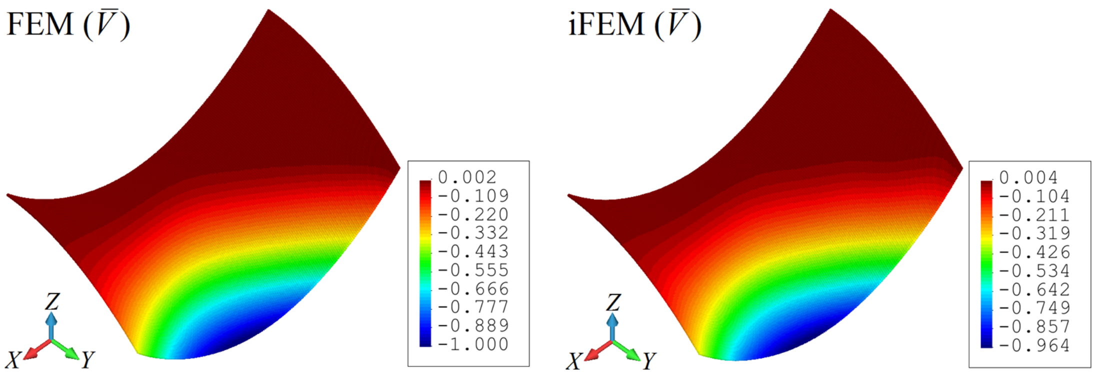

Figure 5.30 Contour plots of $\bar{V}$ displacement for hyperbolic paraboloid: Comparison between high-fidelity FEM and iFEM ($n^e = 6$) analyses.

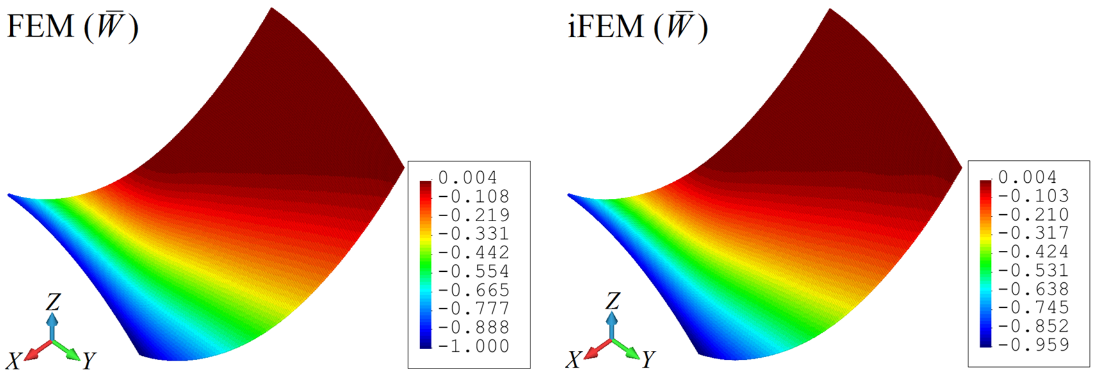

Figure 5.31 Contour plots of $\bar{W}$ displacement for hyperbolic paraboloid: Comparison between high-fidelity FEM and iFEM ($n^e = 6$) analyses.

Besides, in Figures 5.29-31, contour plots of the $\bar{U}$, $\bar{V}$, and $\bar{W}$ displacements are compared between the iFEM and high-fidelity FEM analyses. In these figures, the iFEM contours correspond to the iFEM analysis that uses the iKLS model ($n^e = 6$) with

36×2 strain rosettes in total. The percent difference between the iFEM and FEM for the maximum values of the $\bar{U}$ displacement is only 3.9%. Similar accuracy is evidenced for the maximum values of others displacement, with the percent difference of 3.6% for the $\bar{V}$ displacement, and 4.1% for the $\bar{W}$ displacement. Both the iFEM and direct FEM contours are graphically indistinguishable in the figures. These results demonstrate the superior bending predictions of iKLS element, especially considering the low-fidelity mesh used in the iFEM analysis.

5.7 Conclusion

This chapter presented an isogeometric Kirchhoff–Love inverse-shell element, iKLS, which couples the NURBS-based IGA with the iFEM, for shape-sensing analyses of complex (curved) thin plate and shell structures that are instrumented with randomly distributed sensors. The membrane and bending capability of the iKLS element was demonstrated by carrying out several numerical simulations including Scordelis–Lo roof, pinched hemisphere, and partly clamped hyperbolic paraboloid. In the analysis of these problems, experimentally measured strains are represented by strain results obtained from a high-fidelity solution using an in-house finite element code. Several types of discretization strategies are examined and comparisons of iFEM and direct FEM displacement solutions are provided. As a result, the membrane robustness and the bending efficiency of iKLS element has been justified even using the low-fidelity discretization with few strain sensors. The effects of sensor locations, number of sensors, and the iFEM discretization of the geometry on solution accuracy are pondered. It has been demonstrated that the iKLS element has the advantage of simply modelling the curved shell structures as a results of its NURBS-based nature. Moreover, it has been confirmed that even if a very coarse mesh (with a low number of strain sensors) is used in the iFEM analysis, the iKLS element provides superior displacement solutions. This is because the polynomial degree of the NURBS basis function can be increased without changing the location of knots. This feature can be exploited to obtain more accurate shape-sensing results for different type of elements that will be developed based on the proposed isogeometric iFEM methodology in the future.

Chapter 6

An Improved iFEM Formulation based on RZT

6.1 Introduction

The aim of this chapter is to describe an enhanced iFEM formulation for performing accurate shape and stress sensing of multilayered composite/sandwich plates and flat shells. The improved iFEM formulation is developed based on a weighted-least-squares functional that uses the complete set of strain measures consistent with RZT. These strain measures involve membrane strain measures, bending curvatures, zigzag strain measures, and full (first and second) transverse-shear strain measures of the RZT. A robust and computationally efficient three-node triangular inverse-shell element, i3-RZT, is developed on the basis of the present iFEM methodology. The main benefit of this new element is that it is applicable for the analysis of thin, moderately thick, and complex shell structures manufactured using composite materials. In the remainder of this chapter, the theoretical foundation of the current formulation and its quantitative assessment are detailed. First of all, the background and motivation of the formulation is well-established in Section 6.2. Secondly, in Section 6.3, the mathematical foundation of the current iFEM methodology is introduced to the reader. Thirdly, the i3-RZT element formulation is described in

Section 6.4, while the predictive capabilities of the i3-RZT element are validated solving various benchmark problems that involves laminates with different laminate stacking sequences, i.e., uniaxial, cross-ply, and angle-ply (Section 6.5). Additionally, in Section 6.5, the practical applicability of present iFEM methodology to more complex composite/sandwich structures is demonstrated by analyzing a wedge structure with a hole near one of the clamped ends. Finally, several conclusions emphasizing the benefits of the RZT-based improved iFEM methodology are highlighted in Section 6.6. The research study presented in this chapter is given in Kefal, Tessler, et al. (2016) which contributes the following novelties to the literature for the first time: (1) an enhanced iFEM methodology based on RZT, and (2) a three-node triangular inverse-shell element based on RZT.

6.2 Background and Motivation

Over the last several decades, composite and sandwich material systems have been substantially used as primary structures in many different engineering applications, such as civil and military aircrafts, launch vehicles, wind turbine blades, and marine structures (Herrmann et al., 2005; Berggree et al., 2007; Lolive et al., 2005). Such composite materials are appealing because they have superior tensile strength and resistance to compression (as a result of its fibrous nature), lighter weight, higher operating temperatures, greater stiffness, and higher reliability. Although composite structures offer numerous advantages, their load carrying capabilities can diminish due to various types of failures, such as delamination (Zou et al., 2000), fibre/matrix cracking (McCartney, 1987), and face/core debonding (Vaddakke and Carlsson, 2004), leading to severe reduction in the strength and integrity of the composite structures. Detecting these kinds of damages is not easy during the inspection process of the composite structures (Bray and McBride, 1992). Therefore, it is necessary to monitor the on-site structural performance of composite and sandwich structures utilizing an SHM system. Moreover, shape sensing is a vital technology for the design of composite smart structures such as a morphing wing (Yin et al., 2009) because these smart structures require real-time reconstruction of the deformations to provide feedback for their actuation and control systems. Hence, a powerful shape sensing algorithm is necessary for the development of novel smart structures made of composite materials. Furthermore, since most of the composite and sandwich structures are built up layer by layer, their nature is very suitable to embed optical-fiber networks (e.g., FBG sensors) within the structure during their manufacturing process. In this manner, a large amount of strain data can be easily collected in operational conditions of the composite structures. As an example, Lee et al. (2003) embedded FBG sensors inside a subscale composite wing to measure dynamic strains of the wing during real-time wind tunnel testing. Then, Dawood et al. (2007) achieved significant technological improvements to embed FBG sensors within composite and sandwich structures during their manufacturing process.

Most of iFEM-based shape sensing algorithms adopted the FSDT to describe kinematics relations of plate/shell structure (vid. Section 2.3). Although generally regarded as an accurate theory, FSDT may lead to somewhat inadequate predictions when applied to relatively thick composite and sandwich structures. For such structures, an accurate and robust formulation is required that can take into account the discrete nature of fiber- and resin-rich layers of individual plies as well as the variation of stiffness and strength properties of the core. Tessler et al. (2009, 2010) developed such a formulation and called it the “refined zigzag theory (RZT)”. Recently, Cerracchio et al. (2013, 2015b) improved the original iFEM formulation (Tessler and Spangler, 2003, 2005) by adding the kinematic assumptions of the RZT. This recent formulation was proposed for shape and stress sensing of composite and sandwich structures possessing a high degree of anisotropy and heterogeneity. Although their formulation performed well for sandwich plates, the proposed variational statement does not involve contributions of average (first) transverse-shear strain measures and accommodates only the second transverse-shear strain measures of RZT in addition to the membrane, bending, and zigzag contributions. Moreover, they have only developed a three-node inverse-plate element, called iRZT3, which limits the application of the RZT-based iFEM methodology to plate structures. Furthermore, the authors utilized a least-squares functional without the weighting coefficients, thus iRZT3 element cannot take into account the problems that involve relatively few strain gauges (i.e., sparse in situ strain data). In what follows, an enhanced iFEM formulation is introduced to address the aforementioned shortcomings of the RZT-based iFEM formulation (Cerracchio et al., 2013, 2015b). Also, the i3-RZT inverse-shell element is developed based on the improved iFEM formulation, which ultimately aims to perform accurate shape and stress sensing of multilayered composite and sandwich shell structures.

6.3 The Enhanced iFEM Formulation for Composite Plate and Shell Structures

This section aims to present an enhanced iFEM formulation that uses a weighted-least-squares functional and takes into account a complete set of strain measures fully consistent with RZT. First of all, the description of the inverse problem is given in Section 6.3.1. Then, in Section 6.3.2, the kinematic relations of the RZT are briefly studied and the strain field is appropriately rewritten in order to define the strain measures to be used in the weighted-least-squares functional. After that, in Section 6.3.3, the computation of in situ section strains is described by introducing a computational tool that can be used to obtain the continuous form of the in situ section strains and to calculate experimental transverse-shear strain measures. Finally, the variational statement of the present iFEM methodology is established for both discrete and continuous forms of the in situ section strains in Section 6.3.4.

6.3.1 The inverse problem

Consider a plate (or laminate) with thickness of $2h$ that is consisted of N perfectly bonded orthotropic layers (or laminae) as depicted in Figure 6.1. The laminate is oriented with respect to an orthogonal Cartesian coordinate system (x_1, x_2, z) where the symbol $z \in [-h, +h]$ identifies the through-the-thickness coordinate with $z = 0$ referring to as the reference plane (or mid-plane) of the plate. In addition, the symbols $(x_1, x_2) \in A$ represent the in-plane coordinates, where A denotes the area of the mid-plane (refer to Figure 6.1). In this chapter, if not otherwise specified, the superscript (k) is used to indicate the k-th lamina, whereas the subscript (k) defines the interface between the k-th and (k+1)-th laminae. As shown in Figure 6.1 (b), the k-th lamina thickness is therefore defined in the range $z \in [z_{(k-1)}, z_{(k)}]$ $(k = 1 - N)$. The laminate is constrained against the rigid body motion and subjected to external loads including the planar and through-the-thickness direction components (q and T).

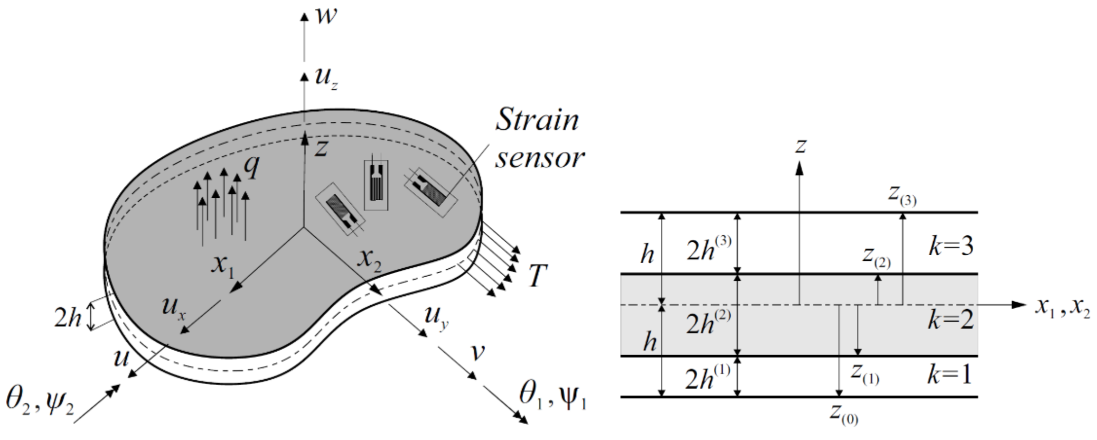

(a) (b)

Figure 6.1 (a) RZT-based iFEM plate notation; (b) Layer notation for a three-layer laminate.

As depicted in Figure 6.1, the strain sensors are mounted at discrete locations on top and bottom surfaces of the laminate and also embedded inside the laminate (e.g, *j*-th interface located at $z_{(j)}$), supplying real-time strain measurements. Herein the inverse problem is shape and stress sensing of the presented laminate, which will be solved by an enhanced iFEM methodology that incorporates the kinematics of RZT and utilizes only the in-situ discrete surface strains and boundary restraints for the solution.

6.3.2 Kinematic relations

According to RZT (Tessler et al., 2010), the orthogonal components of the displacement vector, corresponding to material points of the laminate (refer to Figure 6.1), can be expressed as

$$u_1^{(k)}(x_1,x_2,z) \equiv u(x_1,x_2) + z\,\theta_1(x_1,x_2) + \phi_1^{(k)}(z)\,\psi_1(x_1,x_2) \tag{6.1}$$

$$u_2^{(k)}(x_1,x_2,z) \equiv v(x_1,x_2) + z\,\theta_2(x_1,x_2) + \phi_2^{(k)}(z)\,\psi_2(x_1,x_2) \tag{6.2}$$

$$u_z(x_1,x_2,z) \equiv w(x_1,x_2) \tag{6.3}$$

where the in-plane displacement components $u_\alpha^{(k)} \equiv u_\alpha^{(k)}(x_1,x_2,z)$ $(\alpha = 1,2)$ contain constant, linear, and zigzag variations through-the-thickness coordinate. The zigzag variations are C^0-continuous functions with discontinuous thickness-direction derivatives along the lamina interfaces. In Equation (6.3), the transverse displacement

$u_z \equiv u_z(x_1, x_2, z)$ is assumed to be constant through the thickness and is independent of constitutive properties of the *k*-th lamina; hence, the superscript (*k*) does not appear in its definition and the function $w \equiv w(x_1, x_2)$ represents the transverse deflection of the laminate.

In Equations (6.1-2), the mid-plane translations along x_1 and x_2 directions are denoted by the functions $u \equiv u(x_1, x_2)$ and $v \equiv v(x_1, x_2)$, respectively. Moreover, bending rotations around the positive x_2 and negative x_1 directions are represented as $\theta_1 \equiv \theta_1(x_1, x_2)$ and $\theta_2 \equiv \theta_2(x_1, x_2)$, respectively. Furthermore, the functions $\phi_1^{(k)} \equiv \phi_1^{(k)}(z)$ and $\phi_2^{(k)} \equiv \phi_2^{(k)}(z)$ denote through-the-thickness piecewise-linear zigzag functions associated with heterogeneous plates. Finally, the functions $\psi_1 \equiv \psi_1(x_1, x_2)$ and $\psi_2 \equiv \psi_2(x_1, x_2)$ represent the spatial amplitudes of the zigzag displacements, and they are the unknowns in the analysis together with the other five kinematic variables. These kinematic variables can be expressed by a compact vector form as

$$\mathbf{u} = \begin{bmatrix} u & v & w & \theta_1 & \theta_2 & \psi_1 & \psi_2 \end{bmatrix}^T \tag{6.4}$$

Following the approach in proposed in (Tessler et al., 2010), the zigzag functions $\phi_\alpha^{(k)}$ $(\alpha = 1, 2)$ can be defined as

$$\phi_1^{(k)} \equiv \frac{1}{2}(1 - \xi^{(k)}) u_{(k-1)} + \frac{1}{2}(1 + \xi^{(k)}) u_{(k)} \tag{6.5}$$

$$\phi_2^{(k)} \equiv \frac{1}{2}(1 - \xi^{(k)}) v_{(k-1)} + \frac{1}{2}(1 + \xi^{(k)}) v_{(k)} \tag{6.6}$$

with

$$\xi^{(k)} = \left[\frac{z - z_{(k-1)}}{h^{(k)}} - 1 \right] \in [-1, +1] \quad (k = 1 - N) \tag{6.7}$$

where the first lamina beginning at $z_{(0)} = -h$, the last (*N*-th) lamina ending at $z_{(N)} = +h$, and the *k*-th lamina ending at $z_{(k)} = z_{(k-1)} + 2h^{(k)}$ where $2h^{(k)}$ denotes the thickness of the *k*-th lamina. Evaluating Equations (6.5-6) at the lamina interfaces gives rise to the definitions of the interfacial displacements

$$
\begin{aligned}
&u_{(k-1)} = \phi_1^{(k)}(\xi^{(k)} = -1), \quad u_{(k)} = \phi_1^{(k)}(\xi^{(k)} = +1) \\
&v_{(k-1)} = \phi_2^{(k)}(\xi^{(k)} = -1), \quad v_{(k)} = \phi_2^{(k)}(\xi^{(k)} = +1) \quad (k = 1 - N)
\end{aligned}
\tag{6.8}
$$

where the interfacial displacements at the bottom and top plate surfaces vanish identically; that is,

$$
u_{(0)} = u_{(N)} = v_{(0)} = v_{(N)} = 0 \tag{6.9}
$$

According to Tessler et al. (2010), the $u_{(k)}$ and $v_{(k)}$ interfacial values of the zigzag functions are expressed in terms of piecewise constant slope functions $\beta_\alpha^{(k)}$ $(\alpha = 1, 2; k = 1 - N)$ as

$$
\begin{Bmatrix} u_{(k)} \\ v_{(k)} \end{Bmatrix} = 2h^{(k)} \begin{Bmatrix} \beta_1^{(k)} \\ \beta_2^{(k)} \end{Bmatrix} + \begin{Bmatrix} u_{(k-1)} \\ v_{(k-1)} \end{Bmatrix} \quad (k = 1 - N) \tag{6.10}
$$

where the $\beta_\alpha^{(k)}$ $(\alpha = 1, 2)$ slope of the zigzag functions, namely derivatives of zigzag functions with respect to the through-the-thickness coordinate z, can be explicitly defined for the *k*-th layer as

$$
\begin{Bmatrix} \beta_1^{(k)} \\ \beta_2^{(k)} \end{Bmatrix} = \begin{Bmatrix} G_1 / Q_{11}^{(k)} - 1 \\ G_2 / Q_{22}^{(k)} - 1 \end{Bmatrix} \quad (k = 1 - N) \tag{6.11}
$$

with

$$
\begin{Bmatrix} G_1 \\ G_2 \end{Bmatrix} = \begin{Bmatrix} \left(\dfrac{1}{h} \displaystyle\sum_{i=1}^{N} \dfrac{h^{(i)}}{Q_{11}^{(i)}} \right)^{-1} \\ \left(\dfrac{1}{h} \displaystyle\sum_{i=1}^{N} \dfrac{h^{(i)}}{Q_{22}^{(i)}} \right)^{-1} \end{Bmatrix} \tag{6.12}
$$

where G_1 and G_2 are the weighted-average transverse shear stiffness coefficients of their respective lamina-level coefficients, $Q_{11}^{(k)}$ and $Q_{22}^{(k)}$ $(k = 1 - N)$.

According to the strain-displacement relationship of the linear elasticity theory, the in-plane strain components can be defined as

$$
\varepsilon_{11}^{(k)} = u_{1,1}^{(k)} = e_1 + z\,\kappa_4 + \mu_7^{(k)} \tag{6.13}
$$

$$
\varepsilon_{22}^{(k)} = u_{2,2}^{(k)} = e_2 + z\,\kappa_5 + \mu_8^{(k)} \tag{6.14}
$$

$$\gamma_{12}^{(k)} = u_{1,2}^{(k)} + u_{2,1}^{(k)} = e_3 + z\,\kappa_6 + \mu_9^{(k)} \tag{6.15}$$

where, henceforth, $(\bullet)_{,\alpha} \equiv \frac{\partial(\bullet)}{\partial x_\alpha}$ denotes a partial derivative with respect to in-plane coordinate x_α $(\alpha = 1,2)$. In Equations (6.13-15), the symbols e_α $(\alpha = 1-3)$, κ_α $(\alpha = 4-6)$, and $\mu_\alpha^{(k)}$ $(\alpha = 7-9)$ denote the membrane strain measures, bending curvatures, and zigzag strain measures. The explicit forms of these terms can be defined in terms of the compact form of kinematic variables $\mathbf{u}$ as

$$\mathbf{e}(\mathbf{u}) \equiv \begin{Bmatrix} e_1 \\ e_2 \\ e_3 \end{Bmatrix} = \begin{Bmatrix} u_{,1} \\ v_{,2} \\ u_{,2} + v_{,1} \end{Bmatrix} \tag{6.16}$$

$$\boldsymbol{\kappa}(\mathbf{u}) \equiv \begin{Bmatrix} \kappa_4 \\ \kappa_5 \\ \kappa_6 \end{Bmatrix} = \begin{Bmatrix} \theta_{1,1} \\ \theta_{2,2} \\ \theta_{1,2} + \theta_{2,1} \end{Bmatrix} \tag{6.17}$$

$$\boldsymbol{\mu}^{(k)}(\mathbf{u}) \equiv \begin{Bmatrix} \mu_7^{(k)} \\ \mu_8^{(k)} \\ \mu_9^{(k)} \end{Bmatrix} = \begin{Bmatrix} \phi_1^{(k)} \mu_7 \\ \phi_2^{(k)} \mu_8 \\ \phi_1^{(k)} \mu_9 + \phi_2^{(k)} \mu_{10} \end{Bmatrix} \tag{6.18}$$

with

$$\begin{bmatrix} \mu_7 & \mu_8 & \mu_9 & \mu_{10} \end{bmatrix} = \begin{bmatrix} \psi_{1,1} & \psi_{2,2} & \psi_{1,2} & \psi_{2,1} \end{bmatrix} \tag{6.19}$$

where μ_α $(\alpha = 7-10)$ represents the zigzag curvatures. In order to define the zigzag strain measures $\boldsymbol{\mu}^{(k)}(\mathbf{u})$, the zigzag functions $\phi_\alpha^{(k)}$ $(\alpha = 1,2)$ and the zigzag curvatures μ_α $(\alpha = 7-10)$ are coupled in Equation (6.19).

The transverse-shear strain components can be defined as

$$\gamma_{1z}^{(k)} = u_{1,z}^{(k)} + u_{z,1} = (1 + \beta_1^{(k)})\gamma_{10} - \beta_1^{(k)}\eta_{12} \tag{6.20}$$

$$\gamma_{2z}^{(k)} = u_{2,z}^{(k)} + u_{z,2} = (1 + \beta_2^{(k)})\gamma_{11} - \beta_2^{(k)}\eta_{13} \tag{6.21}$$

where $(\bullet)_{,z} \equiv \frac{\partial(\bullet)}{\partial z}$ denotes a partial derivative with respect to through-the-thickness coordinate z. In Equations (6.20-21), the symbols γ_α $(\alpha = 10,11)$ and η_α $(\alpha = 12,13)$ denote the average (first) and second transverse-shear strain measures of the RZT, respectively. The explicit form of these terms can be described in terms of the kinematic variables $\mathbf{u}$ as

$$\boldsymbol{\gamma}(\mathbf{u}) \equiv \begin{Bmatrix} \gamma_{10} \\ \gamma_{11} \end{Bmatrix} = \begin{Bmatrix} w_{,1} + \theta_1 \\ w_{,2} + \theta_2 \end{Bmatrix} \tag{6.22}$$

$$\boldsymbol{\eta}(\mathbf{u}) \equiv \begin{Bmatrix} \eta_{12} \\ \eta_{13} \end{Bmatrix} = \begin{Bmatrix} \gamma_{10} - \psi_1 \\ \gamma_{11} - \psi_2 \end{Bmatrix} \tag{6.23}$$

Integrating Equations (6.20-21) across the laminate thickness and normalizing the result by the total laminate thickness reveal that

$$\begin{Bmatrix} \gamma_{10} \\ \gamma_{11} \end{Bmatrix} = \frac{1}{2h} \int_{-h}^{h} \begin{Bmatrix} \gamma_{1z}^{(k)} \\ \gamma_{2z}^{(k)} \end{Bmatrix} dz \tag{6.24}$$

Thus, the first transverse-shear strain measures $\gamma_\alpha \ (\alpha = 10{,}11)$ of the RZT coincides with the shear angles of FSDT. This indicates that the zigzag rotations $\psi_\alpha \ (\alpha = 1,2)$ has no contribution to the average transverse-shear strains.

6.3.3 Computation of experimental section strains

The computation of the in situ section strains is vital for performing an accurate RZT-based iFEM analysis. Conventional strain rosettes and embedded FBG sensors can be used to collect a large amount of on-board strain data. To compute in situ section strains, as depicted in Figure 6.2, at least three different in situ strain rosettes $(\boldsymbol{\varepsilon}_i^+, \boldsymbol{\varepsilon}_i^-, \boldsymbol{\varepsilon}_i^j)$ must be placed along the thickness direction of each particular location $(\mathbf{x}_i, z)$ $(i = 1 - n)$ where $\mathbf{x}_i \equiv (x_1, x_2)_i$ and $z \in [\text{-}h, +h]$ are located within the laminate. The exact locations of these sensors and their surface strain measurements (readings) are defined as

$$\boldsymbol{\varepsilon}_i^+(\mathbf{x}_i, z_i = +h) = [\varepsilon_{11}^+ \quad \varepsilon_{22}^+ \quad \gamma_{12}^+]_i \tag{6.25}$$

$$\boldsymbol{\varepsilon}_i^-(\mathbf{x}_i, z_i = -h) = [\varepsilon_{11}^- \quad \varepsilon_{22}^- \quad \gamma_{12}^-]_i \tag{6.26}$$

$$\boldsymbol{\varepsilon}_i^j(\mathbf{x}_i, z_i = z_{(j)}) = [\varepsilon_{11}^j \quad \varepsilon_{22}^j \quad \gamma_{12}^j]_i \tag{6.27}$$

where the surface strain readings with the superscripts '+', '–', and '*j*' refer to as the strain rosettes located on the top surface, bottom surface and *j*-th interface of the laminate, respectively. In Equations (6.25-27), normal strain measurements (along x_1 and x_2 directions) and shear strain measurement (in x_1x_2 plane) are identified by subscripts (11), (22), and (12), respectively.

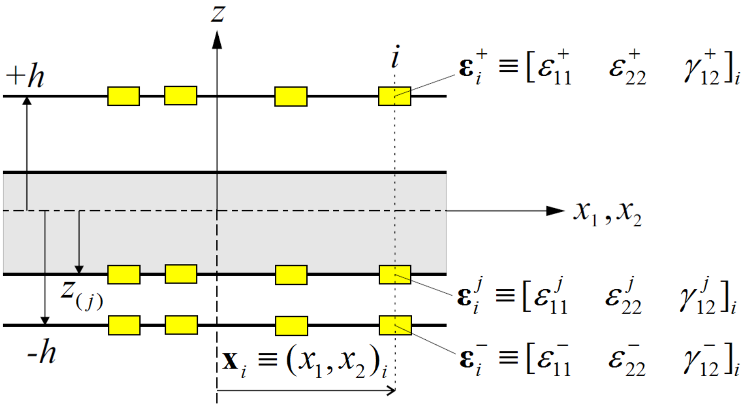

Figure 6.2 Strain rosettes and experimental surface strain measurements.

The zigzag contributions to the in-plane strains vanish at the top and bottom surfaces. Therefore, experimentally measured membrane strains and bending curvatures can be determined using the same relations of the original iFEM plate formulation (Tessler and Spangler, 2003, 2005). These in situ membrane strains $\mathbf{E}_i$ and bending curvatures $\mathbf{K}_i$ can be computed at a particular discrete location $\mathbf{x}_i$ as

$$\mathbf{E}_i \equiv \begin{Bmatrix} \mathrm{E}_1 \\ \mathrm{E}_2 \\ \mathrm{E}_3 \end{Bmatrix}_i = \frac{1}{2} \begin{Bmatrix} \varepsilon_{11}^+ + \varepsilon_{11}^- \\ \varepsilon_{22}^+ + \varepsilon_{22}^- \\ \gamma_{12}^+ + \gamma_{12}^- \end{Bmatrix}_i \quad (i = 1 - n) \tag{6.28}$$

$$\mathbf{K}_i \equiv \begin{Bmatrix} \mathrm{K}_4 \\ \mathrm{K}_5 \\ \mathrm{K}_6 \end{Bmatrix}_i = \frac{1}{2h} \begin{Bmatrix} \varepsilon_{11}^+ - \varepsilon_{11}^- \\ \varepsilon_{22}^+ - \varepsilon_{22}^- \\ \gamma_{12}^+ - \gamma_{12}^- \end{Bmatrix}_i \quad (i = 1 - n) \tag{6.29}$$

where in situ section strains, $\mathbf{E}_i$ and $\mathbf{K}_i$, correspond to their analytic counterparts, $\mathbf{e}(\mathbf{u})$ and $\boldsymbol{\kappa}(\mathbf{u})$, given by Equations (6.16-17), respectively. Substituting *j*-th interface strain readings $(\varepsilon_{11}^j,\, \varepsilon_{22}^j,\, \gamma_{12}^j)_i$ and in situ section strains $\mathbf{E}_i$ and $\mathbf{K}_i$ into Equations (6.13-15), the in situ zigzag strain measures $\mathbf{M}_i^j$ can be computed at a particular discrete location $(\mathbf{x}_i, z_i = z_{(j)})$ as (Cerracchio et al., 2013, 2015b)

$$\mathbf{M}_i^j \equiv \begin{Bmatrix} \mathrm{M}_7^j \\ \mathrm{M}_8^j \\ \mathrm{M}_9^j \end{Bmatrix}_i = \begin{Bmatrix} \varepsilon_{11}^j - \mathrm{E}_1 - z_{(j)}\,\mathrm{K}_4 \\ \varepsilon_{22}^j - \mathrm{E}_2 - z_{(j)}\,\mathrm{K}_5 \\ \gamma_{12}^j - \mathrm{E}_3 - z_{(j)}\,\mathrm{K}_6 \end{Bmatrix}_i \quad (i = 1 - n) \tag{6.30}$$

The in situ section strains $\mathbf{M}_i^j$ are evaluated at the *j*-th interface only; therefore, their analytic counterpart $\boldsymbol{\mu}^{(k)}(\mathbf{u})$ given by Eq. (6.18) must also be computed at exactly the same locations $(\mathbf{x}_i, z_i = z_{(j)})$. Moreover, the in situ transverse-shear strain measures can be represented by a compact vector form as

$$\mathbf{G}_i = \left[\Gamma_{10} \quad \Gamma_{11} \quad \mathrm{H}_{12} \quad \mathrm{H}_{13}\right]_i \; (i = 1 - n) \tag{6.31}$$

where $\Gamma_{\alpha i}$ $(\alpha = 10, 11)$ and $\mathrm{H}_{\alpha i}$ $(\alpha = 12, 13)$ denote discrete first and second transverse-shear strain measures that correspond to their analytic counterparts, $\boldsymbol{\gamma}(\mathbf{u})$ and $\boldsymbol{\eta}(\mathbf{u})$, given by Equations (6.22-23), respectively. In Equations (6.28-31), the uppercase Greek letters are used to indicate the existence of experimental error in the strain measurements.

The surface strain readings obtained from the in situ strain rosettes $(\boldsymbol{\varepsilon}_i^+, \boldsymbol{\varepsilon}_i^-, \boldsymbol{\varepsilon}_i^j)$ cannot be used straightaway to compute the $\mathbf{G}_i$. However, deformation of thin shells exhibits a much smaller transverse-shear strains than in-plane strains. Therefore, the iFEM analysis of thin shells can be safely performed by omitting the $\mathbf{G}_i$ contributions. Instead, in deformation of thick shells, a considerable amount of the transverse deflection is caused by transverse-shear stresses, hence it is necessary to compute the $\mathbf{G}_i$ for obtaining accurate deformed shapes of the shell.

As explained earlier in Section 3.2.3, a priori SEA analysis (Tessler et al., 1998, 1999) can be utilized to smooth the discrete in situ strain measures $\mathbf{E}_i$, $\mathbf{K}_i$, and $\mathbf{M}_i^j$. In this regards, the nine independent section strain measures, $\mathbf{E}$, $\mathbf{K}$, and $\mathbf{M}^j$, can be obtained as C^1-continuous polynomial functions (i.e., having C^0-continuous first-order derivatives) that are defined everywhere in the mid-plane of the laminate. Note that, hereafter, the '*i*' subscript is removed to differentiate these continuous quantities from the discrete ones. The main advantage of the SEA analysis is that it enables the first-order derivatives of in situ membrane strains, bending curvatures, and zigzag curvatures to be accurately computed and subsequently used to obtain the in situ transverse shear strain measures, $\mathbf{G}$. The method involves accurate solution of four equilibrium equations which contain the transverse-shear stress resultants of the RZT. In order to solve these four equilibrium equations, the continuous form of the in situ zigzag curvatures, M_α $(\alpha = 7-10)$,. That correspond to their analytic counterparts, μ_α $(\alpha = 7-10)$, given by Eq. (6.19), has to be well-defined. The continuous form of M_α $(\alpha = 7,8)$ can be simply obtained utilizing the continuous form of zigzag strain measures, M_α^j $(\alpha = 7,8)$, as

$$\begin{bmatrix}\mathrm{M}_7 & \mathrm{M}_8\end{bmatrix} = \begin{bmatrix}\dfrac{\mathrm{M}_7^j}{\phi_1^{(k)}(z_{(j)})} & \dfrac{\mathrm{M}_8^j}{\phi_2^{(k)}(z_{(j)})}\end{bmatrix} \tag{6.32}$$

where $\phi_\alpha^{(k)}(z_{(j)})$ $(\alpha = 1,2)$ represents the zigzag function evaluated at the *j*-th interface, $(z_i = z_{(j)})$. On the other hand, as only three strain rosettes are located through the thickness of each discrete location, $\mathbf{x}_i$, neither the discrete form, $\mathrm{M}_{\alpha i}$ $(\alpha = 9,10)$, nor the continuous form, M_α $(\alpha = 9,10)$, of the remaining zigzag curvatures can be directly computed from the experimentally measured surface strains. However, a highly accurate estimate of $\mathrm{M}_{\alpha i}$ $(\alpha = 9,10)$ can be made through a preliminary iFEM analysis using the continuous in situ strain measures ($\mathbf{E}$, $\mathbf{K}$, $\mathbf{M}^j$) and omitting the contributions of the transverse-shear strain measures, $\mathbf{G}$. This preliminary iFEM analysis can provide promising solutions for bending and zigzag rotations even for thick laminates. This analysis, nevertheless, may not provide an accurate enough solution for the deflection. Therefore, the aim to perform a preliminary iFEM analysis is to compute only $\mathrm{M}_{\alpha i}$ $(\alpha = 9,10)$. Then, these discrete quantities can be mapped on the smooth functions and the C^1-continuous quantities; i.e., M_α $(\alpha = 9,10)$, can be obtained by performing an additional SEA analysis. The final step to obtain the transverse-shear strain measures, $\mathbf{G}$, is to solve the four equilibrium equations by utilizing the first order derivatives of $\mathbf{E}$, $\mathbf{K}$, and M_α $(\alpha = 7-10)$. The overall outcome of this computational procedure will provide the continuous form of all experimental section strains, e.g., $\boldsymbol{\varepsilon} = \begin{bmatrix} \mathbf{E} & \mathbf{K} & \mathbf{M}^j & \mathbf{G} \end{bmatrix}$. All the steps followed within the described computational tool are schematically detailed in Figure 6.3.

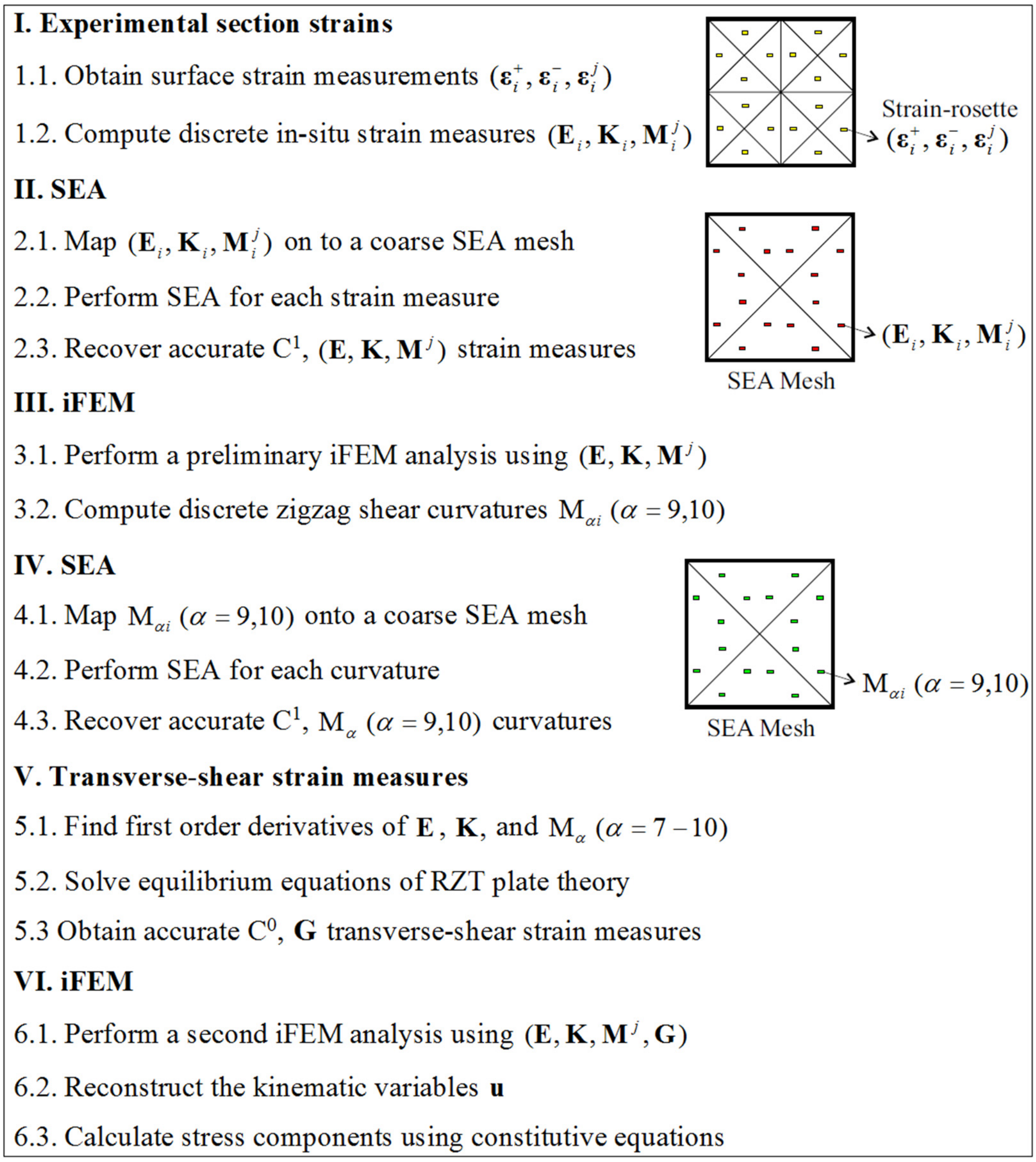

I. Experimental section strains

1.1. Obtain surface strain measurements $(\boldsymbol{\varepsilon}_i^+, \boldsymbol{\varepsilon}_i^-, \boldsymbol{\varepsilon}_i^j)$

1.2. Compute discrete in-situ strain measures $(\mathbf{E}_i, \mathbf{K}_i, \mathbf{M}_i^j)$

II. SEA

2.1. Map $(\mathbf{E}_i, \mathbf{K}_i, \mathbf{M}_i^j)$ on to a coarse SEA mesh

2.2. Perform SEA for each strain measure

2.3. Recover accurate C^1, $(\mathbf{E}, \mathbf{K}, \mathbf{M}^j)$ strain measures

III. iFEM

3.1. Perform a preliminary iFEM analysis using $(\mathbf{E}, \mathbf{K}, \mathbf{M}^j)$

3.2. Compute discrete zigzag shear curvatures $\mathrm{M}_{\alpha i}$ $(\alpha = 9,10)$

IV. SEA

4.1. Map $\mathrm{M}_{\alpha i}$ $(\alpha = 9,10)$ onto a coarse SEA mesh

4.2. Perform SEA for each curvature

4.3. Recover accurate C^1, M_α $(\alpha = 9,10)$ curvatures

V. Transverse-shear strain measures

5.1. Find first order derivatives of $\mathbf{E}$, $\mathbf{K}$, and M_α $(\alpha = 7-10)$

5.2. Solve equilibrium equations of RZT plate theory

5.3 Obtain accurate C^0, $\mathbf{G}$ transverse-shear strain measures

VI. iFEM

6.1. Perform a second iFEM analysis using $(\mathbf{E}, \mathbf{K}, \mathbf{M}^j, \mathbf{G})$

6.2. Reconstruct the kinematic variables $\mathbf{u}$

6.3. Calculate stress components using constitutive equations

Figure 6.3 The iFEM computational tool to calculate all in situ section strains.

6.3.4 The weighted-least-squares functional

Accounting for the membrane, bending, zigzag, and transverse-shear deformations of the RZT and adopting the iFEM methodology (Tessler et al., 2011) as general basis, a weighted-least-squares functional, $\Phi(\mathbf{u})$, can be defined as

$$\Phi(\mathbf{u}) = \sum_{\alpha=1}^{13} w_\alpha \, \varphi_\alpha \tag{6.33}$$

where w_α $(\alpha = 1-13)$ are positive valued weighting coefficients associated with the individual section strains. The significance of their usage for an iFEM discretization in which relatively few elements have in situ strain measurements was previously discussed (vid. Section 3.2.4). Besides, in Equation (6.33), the functional φ_α $(\alpha = 1-13)$ is the least-squares functional of in situ section strains ($\boldsymbol{\varepsilon}$ or $\boldsymbol{\varepsilon}_i$) and kinematic variables $\mathbf{u}$. For the direct input of discrete section strains, $\boldsymbol{\varepsilon}_i$, the least-squares functional becomes $\varphi_\alpha = \varphi_\alpha(\mathbf{u}, \boldsymbol{\varepsilon}_i)$ $(\alpha = 1-13)$ and can be defined by the normalized Euclidean norms given as

$$\varphi_\alpha \equiv \frac{1}{n} \sum_{i=1}^{n} \left[e_\alpha(\mathbf{u})_i - \mathrm{E}_{\alpha i} \right]^2 \quad (\alpha = 1,2,3) \tag{6.34}$$

$$\varphi_\alpha \equiv \frac{(2h)^2}{n} \sum_{i=1}^{n} \left[\kappa_\alpha(\mathbf{u})_i - \mathrm{K}_{\alpha i} \right]^2 \quad (\alpha = 4,5,6) \tag{6.35}$$

$$\varphi_\alpha \equiv \frac{1}{n} \sum_{i=1}^{n} \left[\mu_\alpha^{(k)}(\mathbf{u})_i - \mathrm{M}_{\alpha i}^{j} \right]^2 \quad (\alpha = 7,8,9) \tag{6.36}$$

$$\varphi_\alpha \equiv \frac{1}{n} \sum_{i=1}^{n} \left[\gamma_\alpha(\mathbf{u})_i - \Gamma_{\alpha i} \right]^2 \quad (\alpha = 10,11) \tag{6.37}$$

$$\varphi_\alpha \equiv \frac{1}{n} \sum_{i=1}^{n} \left[\eta_\alpha(\mathbf{u})_i - \mathrm{H}_{\alpha i} \right]^2 \quad (\alpha = 12,13) \tag{6.38}$$

where $1 < k < N$ and $j = k$ or $(k-1)$. Instead, if the computational tool (as described in previous section) is used to perform SEA analysis such that the continuous experimental strain measures, $\boldsymbol{\varepsilon}$, become available for iFEM analysis, the least-squares functional becomes $\varphi_\alpha = \varphi_\alpha(\mathbf{u}, \boldsymbol{\varepsilon})$ $(\alpha = 1-13)$ and can be expressed in terms of the dimensionless L_2 squared norms given as

$$\varphi_\alpha \equiv \frac{1}{A} \int_A \left[e_\alpha(\mathbf{u}) - \mathrm{E}_\alpha \right]^2 dA \quad (\alpha = 1,2,3) \tag{6.39}$$

$$\varphi_\alpha \equiv \frac{(2h)^2}{A} \int_A \left[\kappa_\alpha(\mathbf{u}) - \mathrm{K}_\alpha \right]^2 dA \quad (\alpha = 4,5,6) \tag{6.40}$$

$$\varphi_\alpha \equiv \frac{1}{A}\int_A \left[\mu_\alpha^{(k)}(\mathbf{u}) - \mathrm{M}_\alpha^j\right]^2 dA \;\; (\alpha = 7,8,9) \tag{6.41}$$

$$\varphi_\alpha \equiv \frac{1}{A}\int_A \left[\gamma_\alpha(\mathbf{u}) - \Gamma_\alpha\right]^2 dA \;\; (\alpha = 10,11) \tag{6.42}$$

$$\varphi_\alpha \equiv \frac{1}{A}\int_A \left[\eta_\alpha(\mathbf{u}) - \mathrm{H}_\alpha\right]^2 dA \;\; (\alpha = 12,13) \tag{6.43}$$

Furthermore, in the case of a missing in situ strain component, Equations (6.34-38) or (6.39-43) take on the reduced form defined by the L_2 squared norms

$$\varphi_\alpha \equiv \frac{1}{A}\int_A \left[e_\alpha(\mathbf{u})\right]^2 dA \quad (\mathrm{w}_\alpha = \lambda),\; (\alpha = 1,2,3) \tag{6.44}$$

$$\varphi_\alpha \equiv \frac{(2h)^2}{A}\int_A \left[\kappa_\alpha(\mathbf{u})\right]^2 dA \quad (\mathrm{w}_\alpha = \lambda),\; (\alpha = 4,5,6) \tag{6.45}$$

$$\varphi_\alpha \equiv \frac{1}{A}\int_A \left[\mu_\alpha^{(k)}(\mathbf{u})\right]^2 dA \;\; (\mathrm{w}_\alpha = \lambda),\; (\alpha = 7,8,9) \tag{6.46}$$

$$\varphi_\alpha \equiv \frac{1}{A}\int_A \left[\gamma_\alpha(\mathbf{u})\right]^2 dA \quad (\mathrm{w}_\alpha = \lambda),\; (\alpha = 10,11) \tag{6.47}$$

$$\varphi_\alpha \equiv \frac{1}{A}\int_A \left[\eta_\alpha(\mathbf{u})\right]^2 dA \quad (\mathrm{w}_\alpha = \lambda),\; (\alpha = 12,13) \tag{6.48}$$

where the corresponding weighting constant is set as a small number, e.g., $\lambda = 10^{-5}$.

6.4 A Three-Node Triangular Inverse-Shell Element Formulation based on RZT

A three-node triangular inverse-shell element, named “i3-RZT”, is developed on the basis of an improved iFEM algorithm. The inverse-element formulation is derived using the Tessler-Dong interdependent interpolation concept (Tessler and Dong, 1981; Tessler, 2000). The key concept originates from the RZT beam-frame formulation, from which constraint equations are devised and imposed to each edge of an unconstrained triangular element. The unconstrained element is a six-node triangular element with seven displacement DOF on the corner nodes and three displacement

DOF on the mid-side nodes. After the application of relevant constant shear edge constraint conditions, the displacement DOF on the mid-nodes are condensed out into the corner nodes. Finally, the i3-RZT inverse-element has nine displacement DOF per node (only corner nodes) including drilling rotations and artificial zigzag rotations, as shown in Figure 6.4. Due to the inclusion of drilling rotations, the i3-RZT element has two beneficial aspects: (1) Singular solutions can be simply avoided when modelling complex shell structures; and (2) the i3-RZT element has less tendency toward shear locking for membrane problems. Furthermore, it is much easier to implement the i3-RZT element than the unconstrained element because each single node has the same number of displacement DOF.

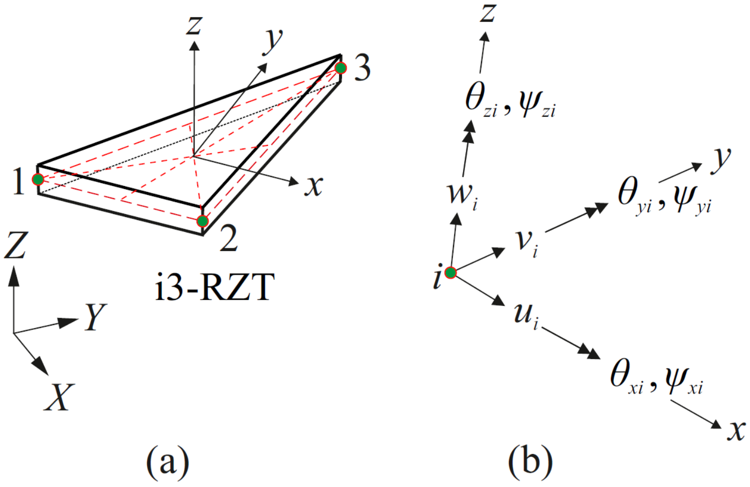

Figure 6.4 (a) Three-node triangular inverse-shell element, i3-RZT, depicted within global (*X, Y, Z*) and local (*x, y, z*) frames of reference; (b) Nodal degrees-of-freedom corresponding to local (element) coordinates (*x, y, z*).

An orthogonal coordinate system (x, y, z) with its origin $(0,0,0)$ located at the centroid of the mid-plane triangle is defined as an element (local) coordinate system. In the following formulation, these local coordinates (x, y, z) are related with the laminate (plate) coordinates (x_1, x_2, z) used to define the kinematic relations of RZT in Section 6.3.2. Thus, the coordinates $(x, y) \equiv (x_1, x_2)$ are the in-plane coordinates and $z \in [-h, +h]$ defines the thickness coordinate. With the element nodes referred to the global coordinates (X, Y, Z), suitable transformation matrices $\mathbf{T}^e$ defining the local-to-global transformations are readily established in accordance with standard finite element procedures to assemble element matrices into a global system of equations. For instance, the following Equations (6.49-58) defines the relevant transformations. The coordinates of element nodes referred to the global coordinate system (X, Y, Z) are given as

$$\mathbf{X}_i = \begin{bmatrix} X_i & Y_i & Z_i \end{bmatrix}^T (i = 1-3) \tag{6.49}$$

Firstly, unit vector along local *x*-axis, $\mathbf{l}$, can be defined as a unit vector pointing out from node-1 to node-2, that is

$$\mathbf{l} = \frac{\mathbf{X}_2 - \mathbf{X}_1}{\left\| \mathbf{X}_2 - \mathbf{X}_1 \right\|} \tag{6.50}$$

Secondly, a unit vector pointing out from node-1 to node-3 can be defined as

$$\mathbf{a} = \frac{\mathbf{X}_3 - \mathbf{X}_1}{\left\| \mathbf{X}_3 - \mathbf{X}_1 \right\|} \tag{6.51}$$

Then, the cross product of these vectors $\mathbf{l}$ and $\mathbf{A}$ can establish a unit normal vector to the mid-plane triangle, $\mathbf{n}$, can be defined by

$$\mathbf{n} = \mathbf{l} \times \mathbf{A} \tag{6.52}$$

Finally, the unit vector along local *y*-axis, $\mathbf{p}$, can readily be computed from the cross product of the vectors $\mathbf{n}$ and $\mathbf{l}$ as

$$\mathbf{p} = \mathbf{n} \times \mathbf{l} \tag{6.53}$$

Each edge length d_i of the mid-plane triangle and global coordinates of each edge's mid-point $\mathbf{c}_i$ can be calculated as

$$\left.\begin{aligned} d_i &= \left\| \mathbf{X}_j - \mathbf{X}_i \right\| \\ \mathbf{c}_i &= \frac{\mathbf{X}_j + \mathbf{X}_i}{2} \end{aligned}\right\} (i = 1, 2, 3; j = 2, 3, 1) \tag{6.54}$$

Then, global coordinates of centroid of the mid-plane triangle can be defined as

$$\mathbf{C} = \frac{\mathbf{c}_1 d_1 + \mathbf{c}_2 d_2 + \mathbf{c}_3 d_3}{d_1 + d_2 + d_3} \tag{6.55}$$

Using Equations (6.49-50), (6.53), and (6.55), local coordinates of the i3-RZT element nodes can be determined as

$$\left.\begin{array}{l} x_i = (\mathbf{X}_i - \mathbf{C}) \cdot \mathbf{l} \\ y_i = (\mathbf{X}_i - \mathbf{C}) \cdot \mathbf{p} \end{array}\right\} (i = 1 - 3) \tag{6.56}$$

With the unit vectors $\mathbf{l}$, $\mathbf{p}$, and $\mathbf{n}$, the transformation matrix, $\mathbf{T}^e$, can be defined as

$$\mathbf{T}^e = \begin{bmatrix} \mathbf{T} & 0 & 0 & 0 & 0 & 0 & 0 & 0 & 0 \\ 0 & \mathbf{T} & 0 & 0 & 0 & 0 & 0 & 0 & 0 \\ 0 & 0 & \mathbf{T} & 0 & 0 & 0 & 0 & 0 & 0 \\ 0 & 0 & 0 & \mathbf{T} & 0 & 0 & 0 & 0 & 0 \\ 0 & 0 & 0 & 0 & \mathbf{T} & 0 & 0 & 0 & 0 \\ 0 & 0 & 0 & 0 & 0 & \mathbf{T} & 0 & 0 & 0 \\ 0 & 0 & 0 & 0 & 0 & 0 & \mathbf{T} & 0 & 0 \\ 0 & 0 & 0 & 0 & 0 & 0 & 0 & \mathbf{T} & 0 \\ 0 & 0 & 0 & 0 & 0 & 0 & 0 & 0 & \mathbf{T} \end{bmatrix} \tag{6.57}$$

with

$$\mathbf{T} = \begin{bmatrix} \mathbf{l}^T & \mathbf{p}^T & \mathbf{n}^T \end{bmatrix}^T \tag{6.58}$$

where $\mathbf{T}$ is the stress transformation matrix from the local to the global coordinate system.

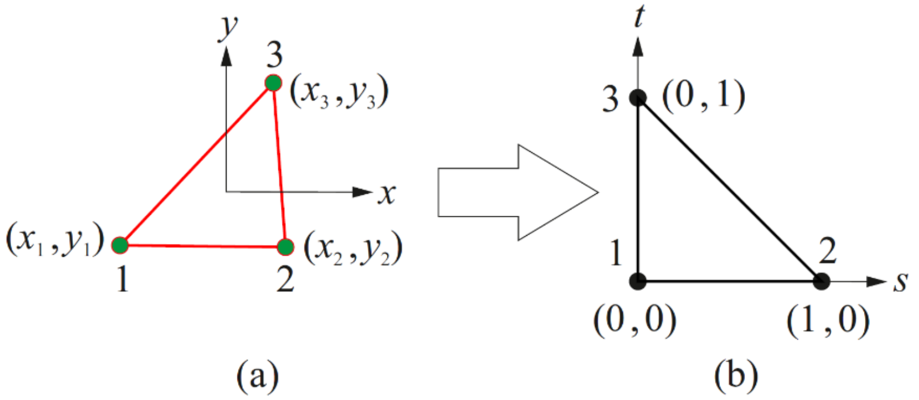

Figure 6.5 (a) Mid-plane (*x*, *y*)-reference surface and nodal coordinates of i3-RZT element; (b) Parent element in isoparametric coordinates.

The (x, y) reference plane of the i3-RZT element can be uniquely defined in terms of bilinear mapping functions as

$$x(s,t) = (1 - s - t)\, x_1 + s\, x_2 + t\, x_3 \tag{6.59}$$

$$y(s,t) = (1 - s - t)\, y_1 + s\, y_2 + t\, y_3 \tag{6.60}$$

where s and t are dimensionless isoparametric coordinates and (x_i, y_i) $(i = 1 - 3)$ are the local nodal coordinates of the element, as illustrated in Figure 6.5. This definition is necessary for numerical Gauss integration of any functional on the surface of the element, A^e.

The nodal DOF, consisting of positive x translations u_i, positive y translations v_i, and positive counter clockwise drilling rotations θ_{zi}, define the u and v mid-plane membrane displacements by

$$u = \sum_{i=1}^{3} (N_i\, u_i + L_i\, \theta_{zi}) \tag{6.61}$$

$$v = \sum_{i=1}^{3} (N_i\, v_i + M_i\, \theta_{zi}) \tag{6.62}$$

where N_i is the linear area-parametric coordinates of the triangle and the interpolation functions L_i and M_i are the anisoparametric shape functions that define the interaction between the hierarchical drilling rotation DOF and the membrane displacements of the element.

Besides, the transverse deflection w, two bending rotations θ_α $(\alpha = 1,2)$, and two zigzag rotations ψ_α $(\alpha = 1,2)$ are defined by the nodal DOF of positive z translation w_i and positive counter clockwise rotations around the x- and y- axes, θ_{xi}, ψ_{xi} and θ_{yi}, ψ_{yi}. These kinematic variables are interpolated as

$$w = \sum_{i=1}^{3} [N_i w_i - L_i(\theta_{xi} - \psi_{xi}) - M_i(\theta_{yi} - \psi_{yi})] \tag{6.63}$$

$$\theta_1 = \sum_{i=1}^{3} N_i \theta_{yi} \tag{6.64}$$

$$\theta_2 = -\sum_{i=1}^{3} N_i \theta_{xi} \tag{6.65}$$

$$\psi_1 = \sum_{i=1}^{3} N_i \psi_{yi} \tag{6.66}$$

$$\psi_2 = -\sum_{i=1}^{3} N_i \psi_{xi} \tag{6.67}$$

where area-parametric coordinates, N_i, interpolates bending and zigzag rotations and the anisoparametric shape functions, L_i and M_i, combine z translation, bending, and zigzag rotation DOF altogether in the interpolation of the transverse deflection, w. In fact, these shape functions were originally developed by Tessler and Hughes (1985) for a three-node plate element, MIN3 (Mindlin-type, three-nodes), and were used by many authors e.g., Versino et al. (2013), Cerracchio et al. (2013, 2015b). The explicit forms can be defined as

$$\left.\begin{aligned} N_i &= \frac{b_i x + a_i y + c_i}{2A_e} \\ M_i &= \frac{N_i}{2}(a_k N_j - a_j N_k) \\ L_i &= \frac{N_i}{2}(b_k N_j - b_j N_k) \end{aligned}\right\} (i = 1,2,3;\ j = 2,3,1;\ k = 3,1,2) \tag{6.68}$$

with

$$\left.\begin{aligned} a_i &= x_k - x_j \\ b_i &= y_j - y_k \\ c_i &= x_j y_k - x_k y_j \end{aligned}\right\} (i = 1,2,3;\ j = 2,3,1;\ k = 3,1,2) \tag{6.69}$$

Taking the relevant partial derivatives of Equations (6.61-67), then substituting these derivatives into Equations (6.16-18) and (6.22-23), gives rise to explicit definitions of membrane strain measures, bending curvatures, zigzag strain measures, and first and second transverse-shear strain measures in terms of the element nodal displacement vector, $\mathbf{u}^e$, as

$$\mathbf{e}(\mathbf{u}^e) = \begin{bmatrix} \mathbf{B}_1\mathbf{u}^e & \mathbf{B}_2\mathbf{u}^e & \mathbf{B}_3\mathbf{u}^e \end{bmatrix}^T \tag{6.70}$$

$$\boldsymbol{\kappa}(\mathbf{u}^e) = \begin{bmatrix} \mathbf{B}_4\mathbf{u}^e & \mathbf{B}_5\mathbf{u}^e & \mathbf{B}_6\mathbf{u}^e \end{bmatrix}^T \tag{6.71}$$

$$\boldsymbol{\mu}^{(k)}(\mathbf{u}^e) = \begin{bmatrix} \phi_1^{(k)}\mathbf{B}_7\mathbf{u}^e & \phi_2^{(k)}\mathbf{B}_8\mathbf{u}^e & \mathbf{H}_\phi^{(k)}\mathbf{B}_9\mathbf{u}^e \end{bmatrix}^T \tag{6.72}$$

$$\boldsymbol{\gamma}(\mathbf{u}^e) = \begin{bmatrix} \mathbf{B}_{10}\mathbf{u}^e & \mathbf{B}_{11}\mathbf{u}^e \end{bmatrix}^T \tag{6.73}$$

$$\boldsymbol{\eta}(\mathbf{u}^e) = \begin{bmatrix} \mathbf{B}_{12}\mathbf{u}^e & \mathbf{B}_{13}\mathbf{u}^e \end{bmatrix}^T \tag{6.74}$$

with

$$\mathbf{H}_\phi^{(k)} = [\phi_1^{(k)} \quad \phi_2^{(k)}]^T \tag{6.75}$$

$$\mathbf{u}^e = \begin{bmatrix} \mathbf{u}_1^e & \mathbf{u}_2^e & \mathbf{u}_3^e \end{bmatrix}^T \tag{6.76}$$

$$\mathbf{u}_i^e = \begin{bmatrix} u_i & v_i & w_i & \theta_{xi} & \theta_{yi} & \theta_{zi} & \psi_{xi} & \psi_{yi} & \psi_{zi} \end{bmatrix}^T \quad (i = 1-3) \tag{6.77}$$

and where the matrices $\mathbf{B}_\alpha$ $(\alpha = 1-13)$ contain derivatives of the shape functions and are can be expressed as

$$\mathbf{B}_\alpha = \begin{bmatrix} \mathbf{B}_\alpha^1 & \mathbf{B}_\alpha^2 & \mathbf{B}_\alpha^3 \end{bmatrix} \quad (\alpha = 1-13) \tag{6.78}$$

with

$$\left.\begin{aligned} \mathbf{B}_1^i &= \begin{bmatrix} N_{i,x} & 0 & 0 & 0 & 0 & L_{i,x} & 0 & 0 & 0 \end{bmatrix} \\ \mathbf{B}_2^i &= \begin{bmatrix} 0 & N_{i,y} & 0 & 0 & 0 & M_{i,y} & 0 & 0 & 0 \end{bmatrix} \\ \mathbf{B}_3^i &= \begin{bmatrix} N_{i,y} & N_{i,x} & 0 & 0 & 0 & L_{i,y}+M_{i,x} & 0 & 0 & 0 \end{bmatrix} \end{aligned}\right\} (i = 1-3) \tag{6.79}$$

$$\left.\begin{aligned} \mathbf{B}_4^i &= \begin{bmatrix} 0 & 0 & 0 & 0 & N_{i,x} & 0 & 0 & 0 & 0 \end{bmatrix} \\ \mathbf{B}_5^i &= \begin{bmatrix} 0 & 0 & 0 & -N_{i,y} & 0 & 0 & 0 & 0 & 0 \end{bmatrix} \\ \mathbf{B}_6^i &= \begin{bmatrix} 0 & 0 & 0 & -N_{i,x} & N_{i,y} & 0 & 0 & 0 & 0 \end{bmatrix} \end{aligned}\right\} (i = 1-3) \tag{6.80}$$

$$\left.\begin{aligned} \mathbf{B}_7^i &= \begin{bmatrix} 0 & 0 & 0 & 0 & 0 & 0 & 0 & N_{i,x} & 0 \end{bmatrix} \\ \mathbf{B}_8^i &= \begin{bmatrix} 0 & 0 & 0 & 0 & 0 & 0 & -N_{i,y} & 0 & 0 \end{bmatrix} \end{aligned}\right\} (i = 1-3) \tag{6.81}$$

$$\mathbf{B}_9^i = \begin{bmatrix} 0 & 0 & 0 & 0 & 0 & 0 & 0 & N_{i,y} & 0 \\ 0 & 0 & 0 & 0 & 0 & 0 & -N_{i,x} & 0 & 0 \end{bmatrix} \quad (i = 1-3) \tag{6.82}$$

$$\left.\begin{aligned}\mathbf{B}_{10}^{i}&=\begin{bmatrix}0 & 0 & N_{i,x} & -L_{i,x} & (N_i-M_{i,x}) & 0 & L_{i,x} & M_{i,x} & 0\end{bmatrix}\\ \mathbf{B}_{11}^{i}&=\begin{bmatrix}0 & 0 & N_{i,y} & -(L_{i,y}+N_i) & -M_{i,y} & 0 & L_{i,y} & M_{i,y} & 0\end{bmatrix}\end{aligned}\right\}(i=1-3) \tag{6.83}$$

$$\left.\begin{aligned}\mathbf{B}_{12}^{i}&=\begin{bmatrix}0 & 0 & N_{i,x} & -L_{i,x} & (N_i-M_{i,x}) & 0 & L_{i,x} & (M_{i,x}-N_i) & 0\end{bmatrix}\\ \mathbf{B}_{13}^{i}&=\begin{bmatrix}0 & 0 & N_{i,y} & -(L_{i,y}+N_i) & -M_{i,y} & 0 & (L_{i,y}+N_i) & M_{i,y} & 0\end{bmatrix}\end{aligned}\right\}(i=1-3) \tag{6.84}$$

where, $(\bullet)_{,x} \equiv \frac{\partial(\bullet)}{\partial x}$ and $(\bullet)_{,y} \equiv \frac{\partial(\bullet)}{\partial y}$ denote the partial derivative with respect to in-plane coordinates x and y, respectively.

Firstly, the continuous section strains $\boldsymbol{\varepsilon}$ can be obtained using the computational tool described in Section 6.3.3. Secondly, the analytic section strains can be calculated as given by Equations (6.70-74). Thirdly, substituting these experimental and analytical section strains into the weighted-least-squares functional, given by Equations (6.33) and (6.39-43), give rise to

$$\Phi_e(\mathbf{u}^e)=\sum_{\alpha=1}^{13} w_\alpha \, \varphi_\alpha(\mathbf{u}^e,\boldsymbol{\varepsilon}) \tag{6.85}$$

where the functional $\Phi_e(\mathbf{u}^e)$ is defined for an individual i3-RZT element. Finally, minimizing this functional, $\Phi_e(\mathbf{u}^e)$, with respect to the nodal displacement DOF, $\mathbf{u}^e$, reveals that

$$\frac{\partial\Phi_e(\mathbf{u}^e)}{\partial\mathbf{u}^e}=\boldsymbol{\Gamma}^e\mathbf{u}^e-\boldsymbol{\varepsilon}^e=0 \;\Rightarrow\; \boldsymbol{\Gamma}^e\mathbf{u}^e=\boldsymbol{\varepsilon}^e \tag{6.86}$$

where $\boldsymbol{\Gamma}^e$ is the element left-hand-side matrix; $\boldsymbol{\varepsilon}^e$ is the element right-hand-side vector, which is a function of the measured strain values; and $\mathbf{u}^e$ is the nodal displacement vector of the element.

The $\boldsymbol{\Gamma}^e$ matrix combines the contribution of every analytic section strain component and its corresponding weighting constant w_α $(\alpha=1-13)$ and is given by

$$\boldsymbol{\Gamma}^e=\sum_{\alpha=1}^{13} w_\alpha \, \mathbf{k}_\alpha^e \tag{6.87}$$

where $\mathbf{k}_\alpha^e$ $(\alpha=1-13)$ matrices denote the contribution of each analytic section strain component and can be explicitly written in terms of the $\mathbf{B}_\alpha$ $(\alpha=1-13)$ matrices as

$$\mathbf{k}_{\alpha}^{e} = \frac{1}{A_e}\int_{A_e} \mathbf{B}_{\alpha}^{T}\,\mathbf{B}_{\alpha}\,dx\,dy \quad (\alpha = 1-3, 10-13) \tag{6.88}$$

$$\mathbf{k}_{\alpha}^{e} = \frac{(2h)^2}{A_e}\int_{A_e} \mathbf{B}_{\alpha}^{T}\,\mathbf{B}_{\alpha}\,dx\,dy \quad (\alpha = 4-6) \tag{6.89}$$

$$\mathbf{k}_{7}^{e} = \frac{(\phi_1^{(k)})^2}{A_e}\int_{A_e} \mathbf{B}_{7}^{T}\,\mathbf{B}_{7}\,dx\,dy \tag{6.90}$$

$$\mathbf{k}_{8}^{e} = \frac{(\phi_2^{(k)})^2}{A_e}\int_{A_e} \mathbf{B}_{8}^{T}\,\mathbf{B}_{8}\,dx\,dy \tag{6.91}$$

$$\mathbf{k}_{9}^{e} = \frac{1}{A_e}\int_{A_e} \mathbf{B}_{9}^{T}\left(\mathbf{H}_{\phi}^{(k)}\right)^{T}\mathbf{H}_{\phi}\,\mathbf{B}_{9}\,dx\,dy \tag{6.92}$$

The $\boldsymbol{\varepsilon}^{e}$ vector is a function of the experimentally measured section-strain values, and is given by

$$\boldsymbol{\varepsilon}^{e} = \sum_{\alpha=1}^{13} w_{\alpha}\,\mathbf{f}_{\alpha}^{e} \tag{6.93}$$

where $\mathbf{f}_{\alpha}^{e}$ $(\alpha = 1-13)$ vectors denote the contribution of each experimental section strain component and can be explicitly written in terms of the continuous section strains $\boldsymbol{\varepsilon}$ and the $\mathbf{B}_{\alpha}$ $(\alpha = 1-13)$ matrices as

$$\mathbf{f}_{\alpha}^{e} = \frac{1}{A_e}\int_{A_e} \mathbf{B}_{\alpha}^{T}\,\mathrm{E}_{\alpha}\,dx\,dy \quad (\alpha = 1-3) \tag{6.94}$$

$$\mathbf{f}_{\alpha}^{e} = \frac{(2h)^2}{A_e}\int_{A_e} \mathbf{B}_{\alpha}^{T}\,\mathrm{K}_{\alpha}\,dx\,dy \quad (\alpha = 4-6) \tag{6.95}$$

$$\mathbf{f}_{7}^{e} = \frac{(\phi_1^{(k)})^2}{A_e}\int_{A_e} \mathbf{B}_{7}^{T}\,\mathrm{M}_{7}^{j}\,dx\,dy \tag{6.96}$$

$$\mathbf{f}_{8}^{e} = \frac{(\phi_2^{(k)})^2}{A_e}\int_{A_e} \mathbf{B}_{8}^{T}\,\mathrm{M}_{8}^{j}\,dx\,dy \tag{6.97}$$

$$\mathbf{f}_{9}^{e} = \frac{1}{A_e}\int_{A_e} \mathbf{B}_{9}^{T}\left(\mathbf{H}_{\phi}^{(k)}\right)^{T}\mathrm{M}_{9}^{j}\,dx\,dy \tag{6.98}$$

$$\mathbf{f}_\alpha^e = \frac{1}{A_e} \int_{A_e} \mathbf{B}_\alpha^T \Gamma_\alpha \, dx\, dy \quad (\alpha = 10,11) \tag{6.99}$$

$$\mathbf{f}_\alpha^e = \frac{1}{A_e} \int_{A_e} \mathbf{B}_\alpha^T \mathrm{H}_\alpha \, dx\, dy \quad (\alpha = 12,13) \tag{6.100}$$

After the left-hand-side matrix, $\mathbf{\Gamma}^e$ is constructed using the Equations (6.87-92), the element equation, $\mathbf{\Gamma}^e \mathbf{u}^e = \boldsymbol{\varepsilon}^e$, has the following form

$$\begin{bmatrix} \mathbf{\Gamma}_U & \mathbf{0} \\ \mathbf{0} & \mathbf{0} \end{bmatrix} \begin{bmatrix} \mathbf{U} \\ \boldsymbol{\psi}_z \end{bmatrix} = \begin{bmatrix} \mathbf{f}_U \\ \mathbf{0} \end{bmatrix} \tag{6.101}$$

with

$$\boldsymbol{\psi}_z = \begin{bmatrix} \psi_{z1} & \psi_{z2} & \psi_{z3} \end{bmatrix}^T \tag{6.102}$$

An artificial contribution matrix $\mathbf{\Gamma}_\psi$ that corresponds to the artificial zigzag amplitudes $\boldsymbol{\psi}_z$ can be constructed as follows

$$\mathbf{\Gamma}_\psi = \begin{bmatrix} k_{\psi z}^1 & 0 & 0 \\ 0 & k_{\psi z}^2 & 0 \\ 0 & 0 & k_{\psi z}^3 \end{bmatrix} \tag{6.103}$$

with

$$k_{\psi z}^i = \lambda \times \min(k_{\psi x}^i, k_{\psi y}^i) \quad (i = 1,2,3) \tag{6.104}$$

where the constant λ is a small number, e.g., $\lambda = 10^{-5}$, and the coefficients $k_{\psi x}^i, k_{\psi y}^i$ $(i = 1,2,3)$ are diagonal terms of the $\mathbf{\Gamma}_U$ matrix that correspond to the zigzag amplitudes DOF, (ψ_{xi}, ψ_{yi}) $(i = 1-3)$. To avoid singular solutions, $\mathbf{\Gamma}_\psi$ must be added to the $\mathbf{\Gamma}^e$ matrix, and the element equations defined in Equation (6.101) can be rewritten in the following final form as

$$\begin{bmatrix} \mathbf{\Gamma}_U & \mathbf{0} \\ \mathbf{0} & \mathbf{\Gamma}_\psi \end{bmatrix} \begin{bmatrix} \mathbf{U} \\ \boldsymbol{\psi}_z \end{bmatrix} = \begin{bmatrix} \mathbf{f}_U \\ \mathbf{0} \end{bmatrix} \tag{6.105}$$

Using the local matrix equations (i.e., Equation 6.105), the global linear equation system of the discretized structure can simply be constructed revisiting the steps described in Section 3.3 (refer to Equations 3.81-84). Then, the resulting system of equations, given by Equation (3.85), can be obtained by applying problem-specific constraint boundary conditions, and then subsequently solved to acquire real-time deformed shape of the entire structure. By using the evaluated displacement values, strains and displacements throughout the structure can be obtained. Furthermore, the constitutive relationship between stress and strain (i.e., the generalized Hooke's law for the *k*-th orthotropic lamina) will allow determination of stress distribution everywhere within the laminate. Finally, these stress distributions can be utilized with a suitable failure criterion for composite materials, allowing the damage detection as part of the SHM process.

6.5 Numerical Examples

A simply supported rectangular plate (laminate) with three different lamina stacking sequences (uniaxial, cross-ply and angle-ply) has been originally analyzed by Tessler et al. (2010) based on the analytical solution of the RZT plate theory. The authors obtained superior displacement and stress results in comparison to other solutions such as 3D elasticity theory (Pagano, 1969), FSDT, and the theory of Di Sciuva (1984). In Section 6.5.1, this problem is revisited to validate the accuracy of the RZT-based improved iFEM formulation. Following the validation case, the applicability of the present iFEM formulation to more complex composite/sandwich structures is demonstrated by analyzing a wedge structure with a hole near one of the clamped ends (refer to Section 6.5.2). The detailed distributions of the displacements and stresses are examined for both example problems.

6.5.1 Simply supported rectangular laminates

As depicted in Figure 6.6, the plate has a length of $\mathrm{a} = 1\ \mathrm{m}$, height of $\mathrm{b} = 1\ \mathrm{m}$, and uniform thickness $2\mathrm{h} = 0.2\ \mathrm{m}$. The plate is subjected to a sinusoidal varying transverse pressure, $q(\mathrm{X},\mathrm{Y}) = q_0 \sin(\pi \mathrm{X}/\mathrm{a}) \sin(\pi \mathrm{Y}/\mathrm{b})$, where the pressure magnitude is $q_0 = -1\ \mathrm{MPa}$. As presented in Figure 6, the kinematic variables are defined as follows: $\mathrm{U}, \mathrm{V}, \text{and } \mathrm{W}$ represent the translations along the coordinate directions $\mathrm{X}, \mathrm{Y}, \text{and } \mathrm{Z}$, respectively; $\theta_\mathrm{X}, \theta_\mathrm{Y}$ and $\psi_\mathrm{X}, \psi_\mathrm{Y}$ represent bending and zigzag rotations around the positive X and Y directions, respectively.

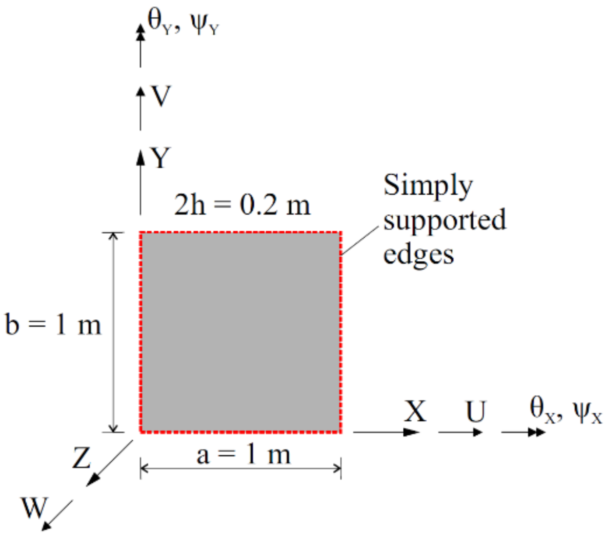

Figure 6.6 Simply supported plate subjected to sinusoidal varying pressure.

The four edges of the plate are simply supported and the following kinematic boundary conditions satisfy the simply supported boundary condition of the plate: For cross-ply and uniaxial laminates, the kinematic boundary conditions along $X = 0$ and $X = a$ are

$$V = W = \theta_X = \psi_X = 0 \tag{6.106}$$

and along $Y = 0$ and $Y = b$ are

$$U = W = \theta_Y = \psi_Y = 0 \tag{6.107}$$

For angle-ply laminates, the kinematic boundary conditions along $X = 0$ and $X = a$ are

$$U = W = \theta_X = \psi_X = 0 \tag{6.108}$$

and along $Y = 0$ and $Y = b$ are

$$V = W = \theta_Y = \psi_Y = 0 \tag{6.109}$$

Three different laminates (I, II, III) are considered for representing relatively thick laminated composite and sandwich plates with a span-to-thickness ratio of $a/2h = b/2h = 5$. Laminate I is a two-layer, cross-ply carbon-epoxy laminate. Laminate II is a three-layer sandwich laminate with uniaxial carbon-epoxy face sheets and a thick, closed cell polyvinyl chloride (PVC) core, where PVC is represented as an isotropic material. Laminate III is a five-layer, angle-ply sandwich laminate with carbon-epoxy face sheets and a thick PVC core. The mechanical material properties and the stacking sequences of the laminates are listed in Tables 6.1-2, respectively.

Table 6.1 Mechanical properties of orthotropic and isotropic materials.

Lamina material		Young's modulus [GPa]	Poisson's ratio	Shear modulus [GPa]
C	Carbon-epoxy unidirectional composite	$E_1^{(k)} = 157.9$ $E_2^{(k)} = 9.584$ $E_3^{(k)} = 9.584$	$\upsilon_{12}^{(k)} = 0.32$ $\upsilon_{13}^{(k)} = 0.32$ $\upsilon_{23}^{(k)} = 0.49$	$G_{12}^{(k)} = 5.930$ $G_{13}^{(k)} = 5.930$ $G_{23}^{(k)} = 3.227$
P	PVC core	$E^{(k)} = 0.104$	$\upsilon^{(k)} = 0.3$	$G^{(k)} = 0.04$

Table 6.2 Laminate stacking sequences (in the positive Z direction).

Laminate		Normalized lamina thickness, $\mathrm{h}^{(k)} / \mathrm{h}$	Lamina materials	Lamina orientation [°]
I	Cross-ply composite	(0.5/0.5)	(C/C)	(0/90)
II	Uniaxial sandwich	(0.1/0.8/0.1)	(C/P/C)	(0/0/0)
III	Angle-ply sandwich	(0.05/0.05/0.8/0.05/0.05)	(C/C/P/C/C)	(30/-45/0/45/-30)

To establish an accurate reference solution, a convergence study was performed using direct RZT-based FEM analyses utilizing an in-house FEM code. The most refined mesh consisted of 10000 uniformly distributed triangular elements that possessed 35707 DOF. For each laminate (I, II, III), comparisons of the normalized central deflection are listed in Table 6.3, where the normalization factor of $10^2 D_{11} / q_0 \mathrm{a}^4$ is used with D_{11} denoting the bending stiffness coefficient. These results demonstrate that the high-fidelity RZT-based FEM analyses predict plate displacements that are comparably accurate to those of the RZT analytical solutions (Tessler et al., 2010). Therefore, the high-fidelity FEM deflections and rotations are used to compute the simulated strain-sensor strains. For each laminate (I, II, III), maximum deflection $\mathrm{W}_{\mathrm{max}}^{\mathrm{FEM}}$, von Mises stress $\sigma_{\mathrm{v,\,max}}^{\mathrm{FEM}}$, bending rotations $\theta_{\mathrm{X,\,max}}^{\mathrm{FEM}}$ and $\theta_{\mathrm{Y,\,max}}^{\mathrm{FEM}}$, and zigzag rotations $\psi_{\mathrm{X,\,max}}^{\mathrm{FEM}}$ and $\psi_{\mathrm{Y,\,max}}^{\mathrm{FEM}}$ obtained from the high-fidelity FEM solutions (reference) are listed in Tables 6.4-5, respectively. To assess the accuracy of the displacement, rotation, and stress responses, it would be convenient to use these reference values as normalization factors.

Table 6.3 Normalized central deflection, $\overline{\mathrm{w}} = (10^2 D_{11} / q_0 \mathrm{a}^4)\,\mathrm{W}(0.5\mathrm{a}, 0.5\mathrm{b})$.

Laminate	Normalization Factor ($10^2 D_{11} / q_0 \mathrm{a}^4$)	RZT Analytic ($\overline{\mathrm{w}}$) (Tessler et al., 2010)	FEM ($\overline{\mathrm{w}}$)
I	5617.72	1.219	1.219
II	5173.04	29.785	29.775
III	2448.38	14.105	14.101

Table 6.4: Maximum deflections and von Mises stresses of the plate.

Laminate	$\mathrm{W}_{\mathrm{max}}^{\mathrm{FEM}}$ [m]	$\sigma_{\mathrm{v,\,max}}^{\mathrm{FEM}}$ [Pa]
I	-2.169×10^{-4}	1.306×10^{7}
II	-5.756×10^{-3}	1.397×10^{6}
III	-5.759×10^{-3}	2.587×10^{7}

Table 6.5 Maximum bending and zigzag rotations of the plate

Laminate	$\theta_{\mathrm{X,\,max}}^{\mathrm{FEM}}$ [rad]	$\theta_{\mathrm{Y,\,max}}^{\mathrm{FEM}}$ [rad]	$\psi_{\mathrm{X,\,max}}^{\mathrm{FEM}}$ [rad]	$\psi_{\mathrm{Y,\,max}}^{\mathrm{FEM}}$ [rad]
I	5.128×10^{-4}	5.128×10^{-4}	5.520×10^{-5}	5.520×10^{-5}
II	4.009×10^{-3}	1.913×10^{-3}	1.415×10^{-2}	1.607×10^{-2}
III	2.732×10^{-3}	1.571×10^{-3}	1.538×10^{-2}	1.652×10^{-2}

In the present iFEM analysis, the strain rosettes are regularly distributed, and each strain rosette configuration pertains to a discretization with the same number of element subdivisions along the plate edges, n^e. Through the thickness coordinate, three strain rosettes are located at the centroid of each element; one on the top surface, one on the bottom surface, and one on the nearest interface to the bottom surface of the laminate. In Figure 6.7, an example of a strain rosette configuration for discretization, $n^e = 4$, is demonstrated.

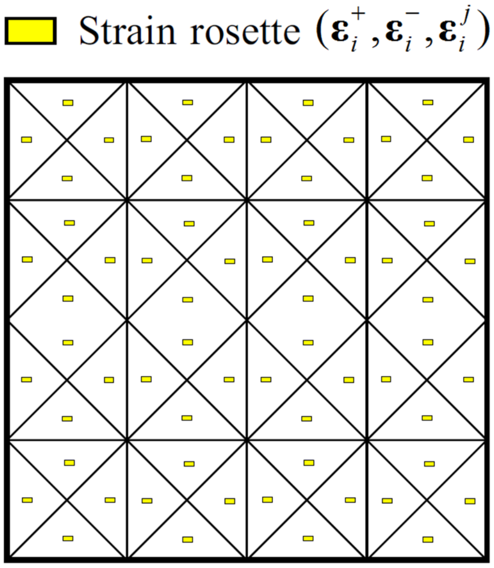

Figure 6.7 Strain rosette configuration of the simply supported plate for discretization $n^e = 4$

Utilizing the computational tool described in Section 6.3.3, the continuous in situ strain measures ($\mathbf{E}$, $\mathbf{K}$, $\mathbf{M}^j$, and $\mathbf{G}$) are calculated for each laminate. Therefore, the continuous form of section strains $\boldsymbol{\varepsilon}$ is used in the following RZT-based iFEM analyses. The weighting constants associated with the membrane, bending, and zigzag strain measures are adjusted as $w_\alpha = 1 \; (\alpha = 1-9)$, whereas the weighting constants corresponding to the transverse-shear strain measures are set to a small value as $w_\alpha = 10^{-8} \; (\alpha = 10-13)$. As a consequence of this adjustment, the minimization of the weighted-least-squares functional will enforce the match between the membrane, bending and zigzag strain measures, and their measured values much more than the condition of small-valued transverse-shear strain measures. The analytical expressions of both bending curvatures and transverse-shear strain measures involve quantities related to bending rotations. Also, the analytical expressions of both zigzag and transverse-shear strain measures involve quantities related to zigzag rotations. As a result of the above stated adjustment of the weighting constants, the bending curvatures and zigzag strain measures will contribute to reconstruction of the bending and zigzag rotations much more than the small-valued transverse-shear strain measures will. Furthermore, the small weighting coefficient will not affect the accuracy of the deflection reconstruction because the only strain measure that involves the quantities related to the deflection is transverse-shear strain measures. Hence, the deflection will accurately be reconstructed based on the match between transverse-shear strain measures and their experimental values.

For each laminate (I, II, III), the deflections, bending and zigzag rotations, and von Mises stresses obtained from both iFEM and FEM analyses are normalized by absolute values of the FEM solutions listed in Tables 6.4-5. These normalized expressions are given as follows

$$\bar{\chi} = \chi / \left|\chi_{\max}^{\mathrm{FEM}}\right| \quad (\chi = W, \theta_X, \theta_Y, \psi_X, \psi_Y, \sigma_v) \tag{6.110}$$

In Tables 6.6-9, the percent difference between iFEM and FEM predictions for the maximum values of the normalized expressions given in Equation (6.110) are listed versus the number of element subdivisions n^e for each laminate (I, II, III), respectively.

Table 6.6 Percent difference between the iFEM and FEM predictions for maximum values of the displacements of laminate I.

n^e	Percent difference				
	$\bar{W}$	$\bar{\theta}_X$	$\bar{\theta}_Y$	$\bar{\psi}_X$	$\bar{\psi}_Y$
2	1.7	2.1	2.1	2.1	2.1
4	1.6	0.7	0.7	0.9	0.9
6	0.4	0.2	0.2	0.6	0.6
8	0.2	0.1	0.1	0.3	0.3
10	0.0	0.0	0.0	0.3	0.3

Table 6.7 Percent difference between the iFEM and FEM predictions for maximum values of the displacements of laminate II.

n^e	Percent difference				
	$\bar{W}$	$\bar{\theta}_X$	$\bar{\theta}_Y$	$\bar{\psi}_X$	$\bar{\psi}_Y$
2	1.3	2.3	1.7	1.9	2.1
4	0.8	0.8	0.5	0.7	0.7
6	0.2	0.1	0.2	0.1	0.2
8	0.2	0.1	0.0	0.1	0.1
10	0.1	0.0	0.0	0.1	0.0

Table 6.8 Percent difference between the iFEM and FEM predictions for maximum values of the displacements of laminate III.

n^e	Percent difference				
	$\bar{W}$	$\bar{\theta}_X$	$\bar{\theta}_Y$	$\bar{\psi}_X$	$\bar{\psi}_Y$
2	1.3	2.0	1.5	1.7	1.9
4	0.7	0.8	0.5	0.7	0.7
6	0.1	0.1	0.1	0.0	0.1
8	0.1	0.1	0.1	0.1	0.1
10	0.0	0.1	0.1	0.1	0.0

These results shows that the iFEM predictions for all displacements convergence to the reference solution very quickly, even if only a few strain sensors are used for the shape sensing analysis of each simply supported laminate (I, II, III). For example, the total number of sensors used for strain rosette configuration, $n^e = 2$, is only 48 and none of percent differences corresponding to this configuration exceeds the 2.3% for all laminates (refer to Tables 6.6-9). Remarkably, these results demonstrate that the improved iFEM formulation predicts plate displacements and rotations that are as accurate as those of the reference solutions.

In addition, for each simply supported square laminate (I, II, III), through-the-thickness distributions of the in-plane displacements, normal and transverse-shear stresses are plotted in Figures 6.8-17, respectively, where the following normalization was used

$$\bar{\mathrm{U}}(0,0.5\mathrm{b},\mathrm{Z}) = (10^3 D_{11} / q_0 \mathrm{a}^4)\,\mathrm{U}(0,0.5\mathrm{b},\mathrm{Z}) \tag{6.111}$$

$$\bar{\sigma}_{\mathrm{XX}}(0.55\mathrm{a},0.6\mathrm{b},\mathrm{Z}) = (4\mathrm{h}^2 / q_0 \mathrm{a}^2)\,\sigma_{\mathrm{XX}}(0.55\mathrm{a},0.6\mathrm{b},\mathrm{Z}) \tag{6.112}$$

$$\bar{\tau}_{\mathrm{XZ}}(0.11\mathrm{a},0.2\mathrm{b},\mathrm{Z}) = (20\mathrm{h} / q_0 \mathrm{a}^2)\,\tau_{\mathrm{XZ}}(0.11\mathrm{a},0.2\mathrm{b},\mathrm{Z}) \tag{6.113}$$

In these figures, the legend “iFEM” represents the normalized iFEM solutions, whereas the legend “Reference” represents the normalized high-fidelity FEM solutions. It is important to note, moreover, that the $\bar{\tau}_{\mathrm{XZ}}$ stress results are obtained using Cauchy's 3D equilibrium equations; therefore, the $\bar{\tau}_{\mathrm{XZ}}$ stress distributions are continuous through the thickness of the laminates (refer to Figures 6.8-17).

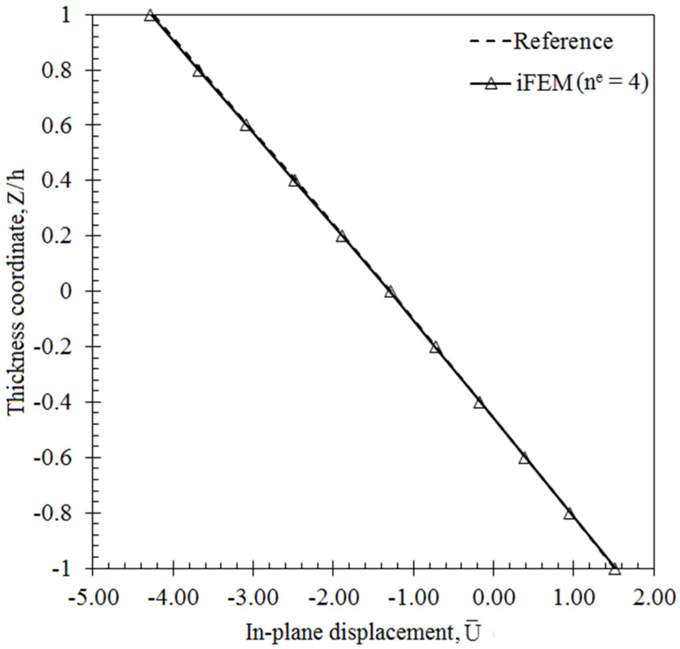

Figure 6.8 In-plane displacement $\bar{\mathrm{U}}(0,0.5\mathrm{b},\mathrm{Z})$ variation through the thickness of laminate I.

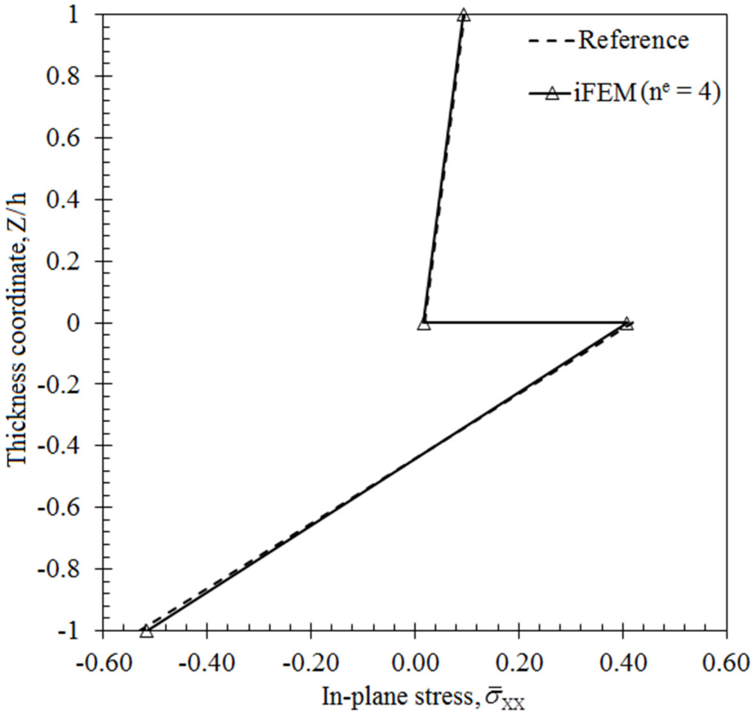

Figure 6.9 In-plane stress $\bar{\sigma}_{XX}(0.55\,a, 0.6\,b, Z)$ variation through the thickness of laminate I.

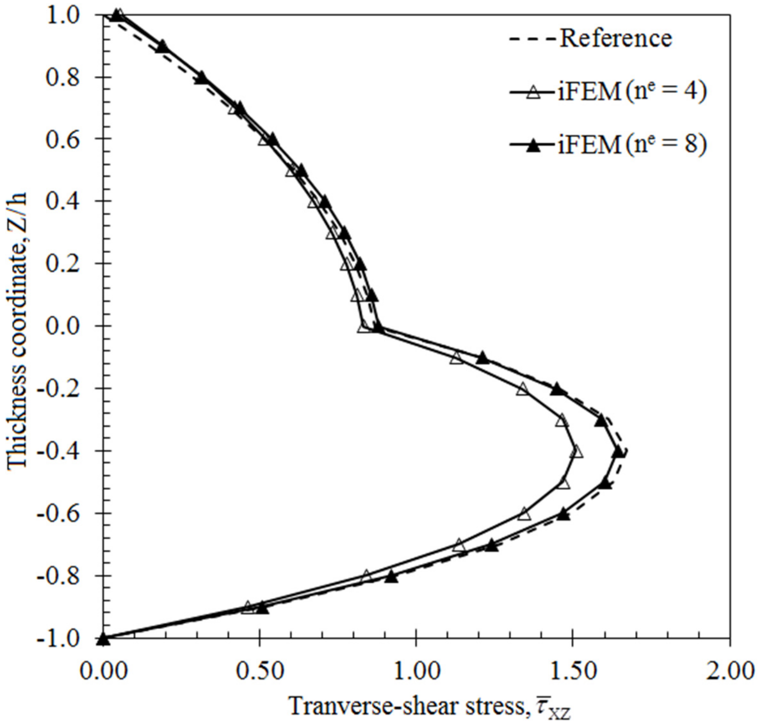

Figure 6.10 Transverse-shear stress $\bar{\tau}_{XZ}(0.11\,a, 0.2\,b, Z)$ variation through the thickness of laminate I.

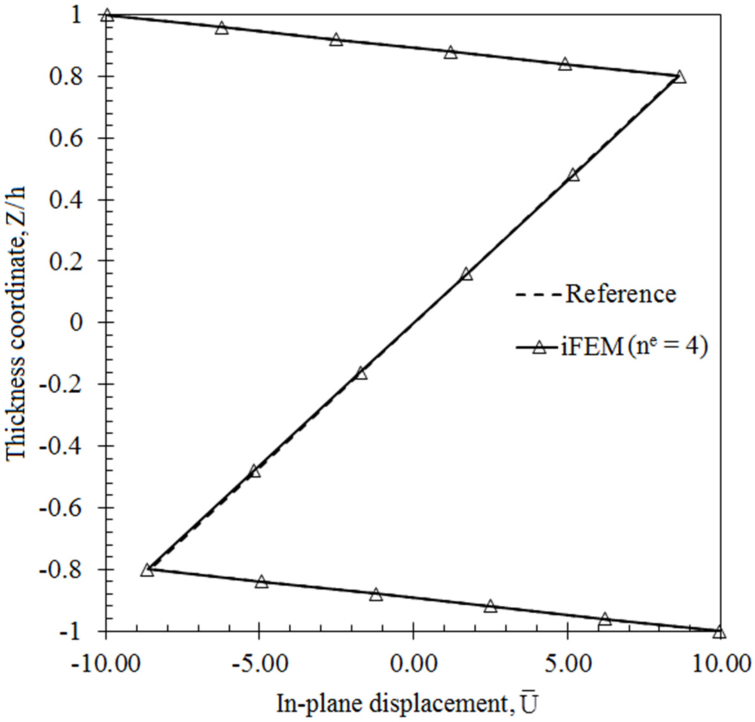

Figure 6.11 In-plane displacement $\bar{U}(0, 0.5\,b, Z)$ variation through the thickness of laminate II.

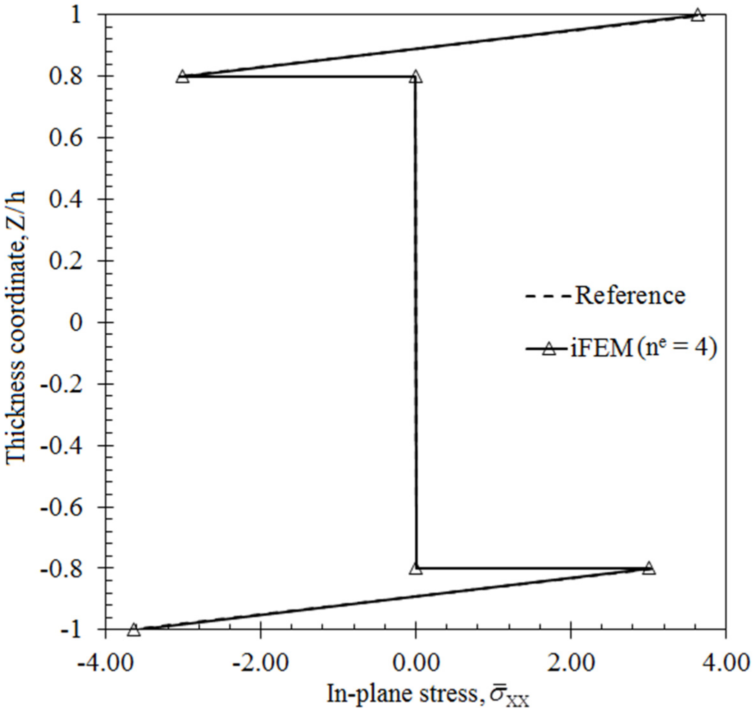

Figure 6.12 In-plane stress $\bar{\sigma}_{XX}(0.55\,a, 0.6\,b, Z)$ variation through the thickness of laminate II.

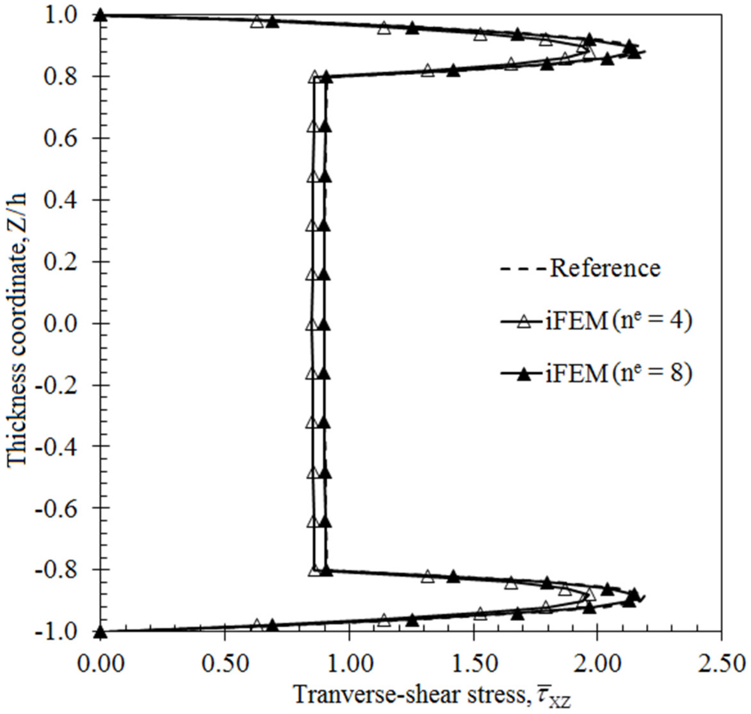

Figure 6.13 Transverse-shear stress $\bar{\tau}_{XZ}(0.11a, 0.2b, Z)$ variation through the thickness of laminate II.

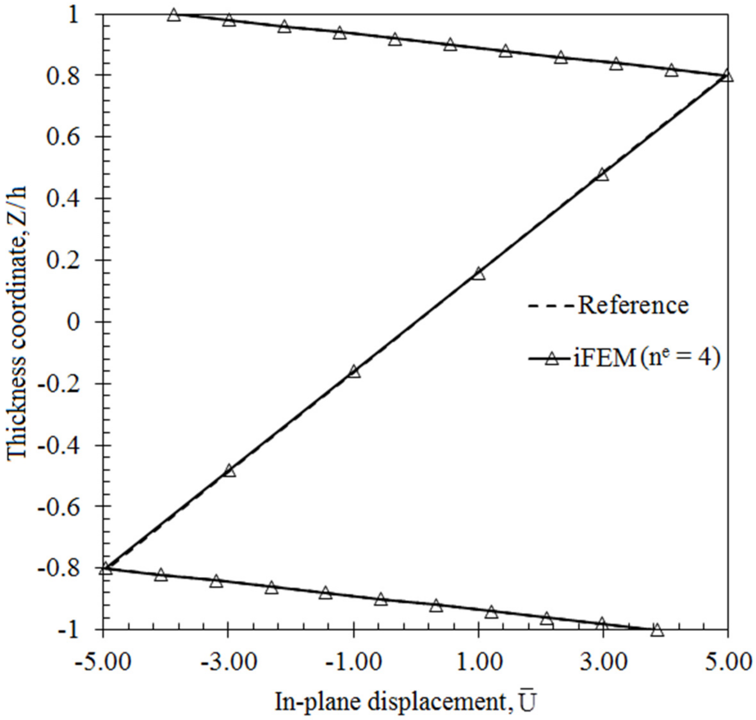

Figure 6.14 In-plane displacement $\bar{U}(0, 0.5b, Z)$ variation through the thickness of laminate III.

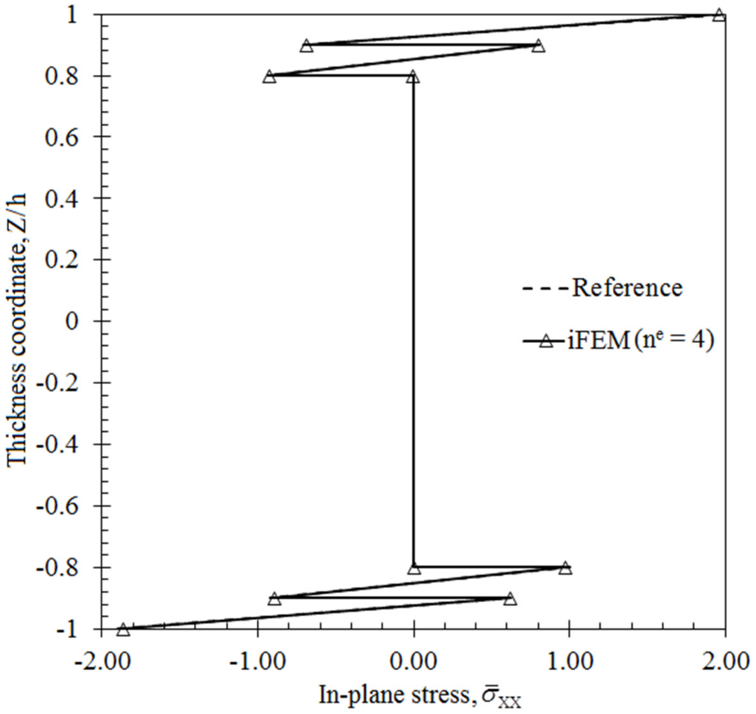

Figure 6.15 In-plane stress $\bar{\sigma}_{XX}(0.55\,a, 0.6\,b, Z)$ variation through the thickness of laminate III.

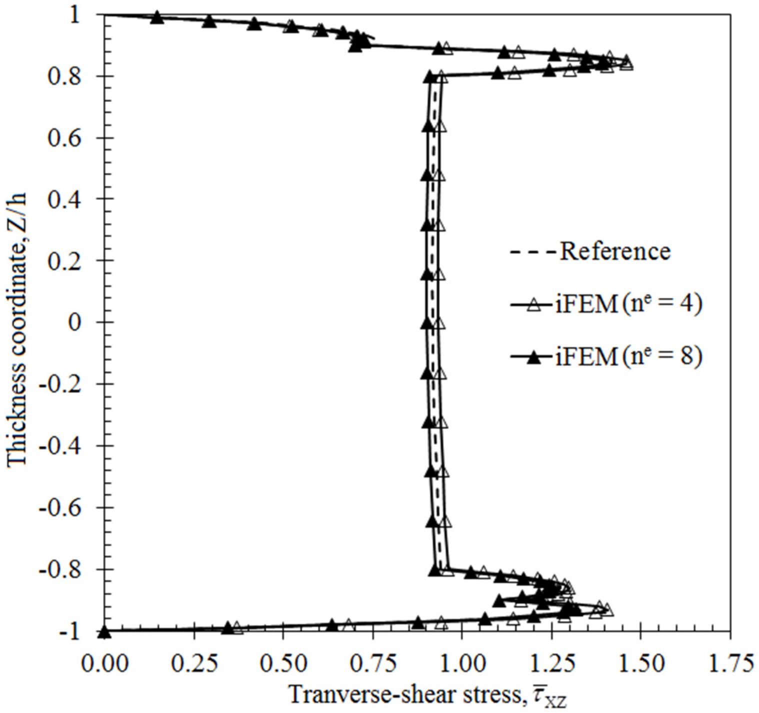

Figure 6.16 Transverse-shear stress $\bar{\tau}_{XZ}(0.11\,a, 0.2\,b, Z)$ through the thickness of laminate III.

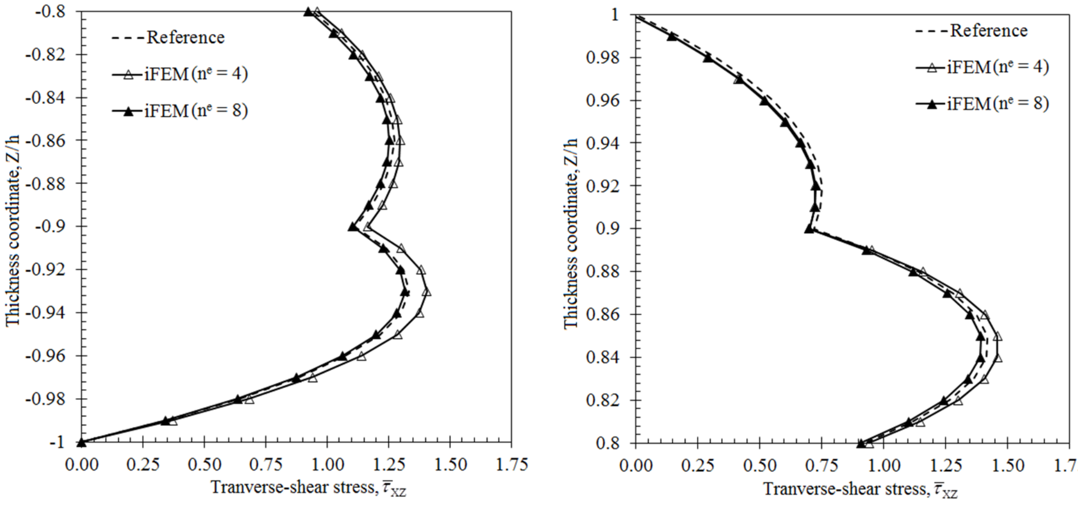

(a) (b)

Figure 6.17 Zoomed view of the Figure 31: (a) Thickness coordinate, $Z/h \in [-0.8, -1]$; (b) Thickness coordinate, $Z/h \in [0.8, 1]$.

In these figures, the $\bar{U}$, $\bar{\sigma}_{XX}$, and $\bar{\tau}_{XZ}$ distributions obtained using improved iFEM formulation are virtually indistinguishable from their corresponding reference solutions. The accuracy of these results demonstrates the superior capability of iFEM formulation for shape and stress sensing of a wide range of lamina stacking sequences (i.e., uniaxial, cross-ply, and angle-ply). Furthermore, these results confirm that the present iFEM formulation is suitable for displacement and stress monitoring of relatively thick laminates ($a/2h = b/2h = 5$) even using a very low number of strain rosettes. For instance, the total number of sensors used for the i3-RZT model, $n^e = 4$, is only 64.

Furthermore, in Figures 6.18-23, contour plots of the $\bar{W}$, $\bar{\theta}_X$, $\bar{\theta}_Y$, $\bar{\psi}_X$, $\bar{\psi}_Y$, and $\bar{\sigma}_v$ variables are compared between iFEM and high-fidelity FEM analyses of laminate III, respectively. Note that, only contour plots of the laminate III (i.e., the most complex laminate in comparison to others) is included herein for conciseness of this chapter. However, the contour plots pertaining to laminates I and II can be found in Kefal, Tessler, et al. (2016). The percent difference between iFEM and FEM predictions for the maximum $\bar{W}$ displacement is only 0.7% as depicted in Figure 6.18.

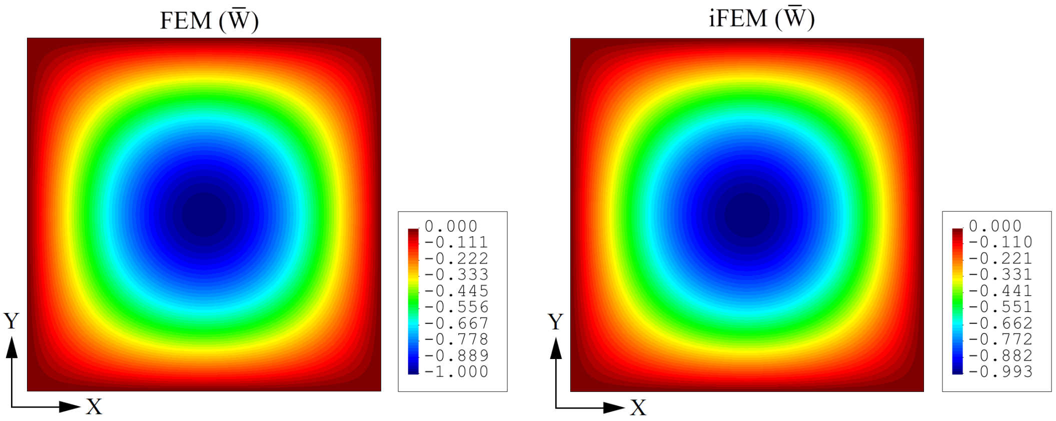

Figure 6.18 Contour plots of $\overline{W}$ displacement for laminate III: Comparison between high-fidelity FEM and iFEM ($n^e = 4$) analyses.

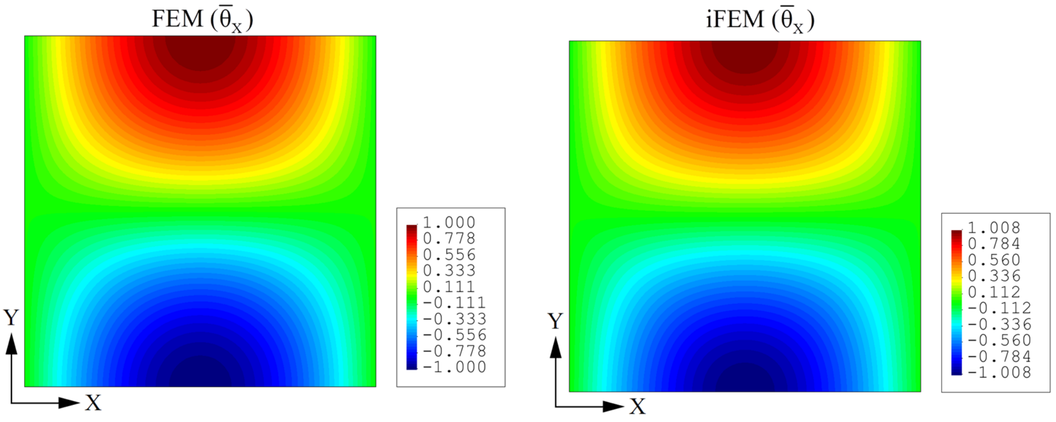

Figure 6.19 Contour plots of $\overline{\theta}_X$ bending rotation for laminate III: Comparison between high-fidelity FEM and iFEM ($n^e = 4$) analyses.

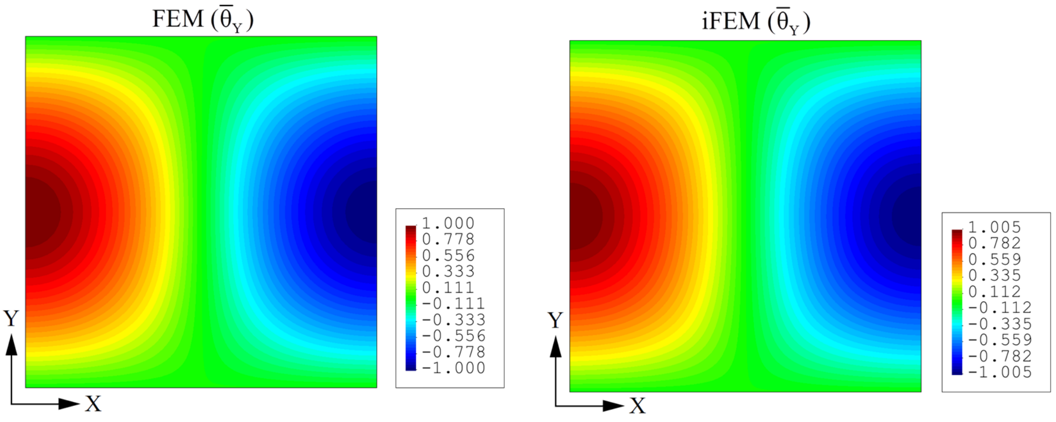

Figure 6.20 Contour plots of $\overline{\theta}_Y$ bending rotation for laminate III: Comparison between high-fidelity FEM and iFEM ($n^e = 4$) analyses.

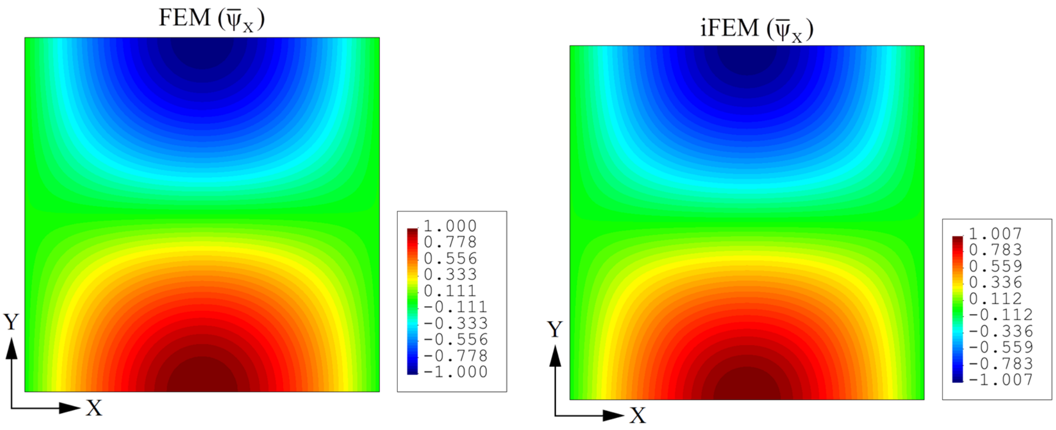
FEM ($\overline{\psi}_X$)

iFEM ($\overline{\psi}_X$)

Figure 6.21 Contour plots of $\overline{\psi}_X$ zigzag rotation for laminate III: Comparison between high-fidelity FEM and iFEM ($n^e = 4$) analyses.

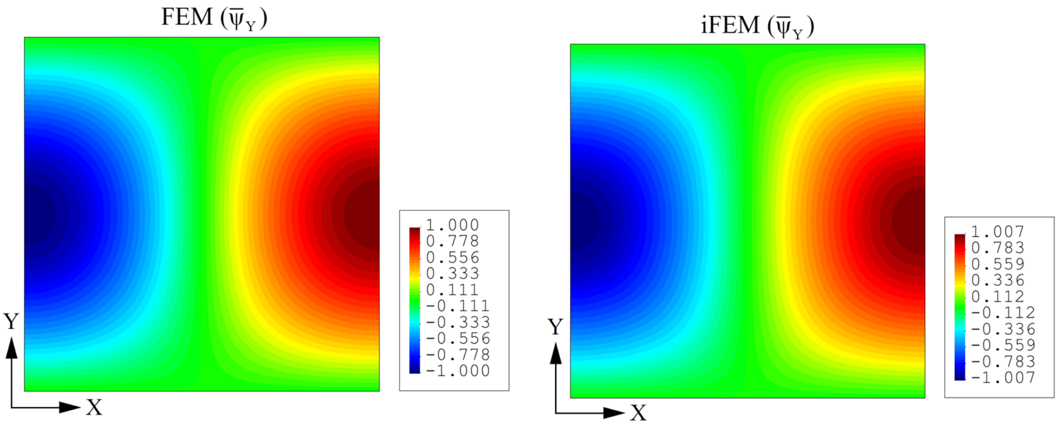
FEM ($\overline{\psi}_Y$)

iFEM ($\overline{\psi}_Y$)

Figure 6.22 Contour plots of $\overline{\psi}_Y$ zigzag rotation for laminate III: Comparison between high-fidelity FEM and iFEM ($n^e = 4$) analyses.

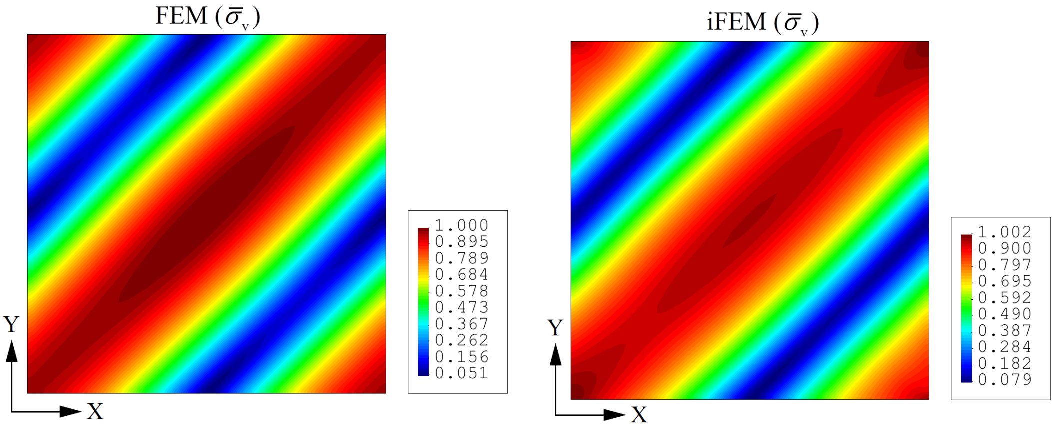
FEM ($\overline{\sigma}_v$)

iFEM ($\overline{\sigma}_v$)

Figure 6.23 Contour plots of $\overline{\sigma}_v$ von Mises stress at thickness coordinate $Z / h = -1$ of laminate III: Comparison between high-fidelity FEM and iFEM ($n^e = 4$) analyses.

Similar accuracy is obtained for the maximum bending and zigzag rotations, $\overline{\theta}_X$, $\overline{\theta}_Y$ and $\overline{\psi}_X$, $\overline{\psi}_Y$, with a percent difference less than 0.8% and 0.7%, respectively (refer to Figures 6.19-22). Besides, as depicted in Figure 6.23, iFEM and FEM predictions differ from each other by only 0.2% for the maximum $\overline{\sigma}_v$ stress. As can be seen from all these figures, both iFEM and FEM contours are graphically indistinguishable. These results altogether confirm the superior bending predictions of the new i3-RZT element, especially considering the low number of strain sensors, $n^e = 4$, used in iFEM analysis.

6.5.2 A wedge structure with a hole

A wedge structure with a hole near one of the clamped ends is analyzed to demonstrate the applicability of the improved iFEM formulation to more complex engineering structures. As depicted in Figure 6.24, the wedge structure has overall length of $L_1 = 6\text{ m}$, width of $L_2 = 2\text{ m}$, and uniform thickness of $2h = 0.2\text{ m}$. The wedge structure is composed of panels A and B, each of which has an element group coordinate system, i.e., $(X_\alpha, Y_\alpha, Z_\alpha)$ $(\alpha\text{=A, B})$.

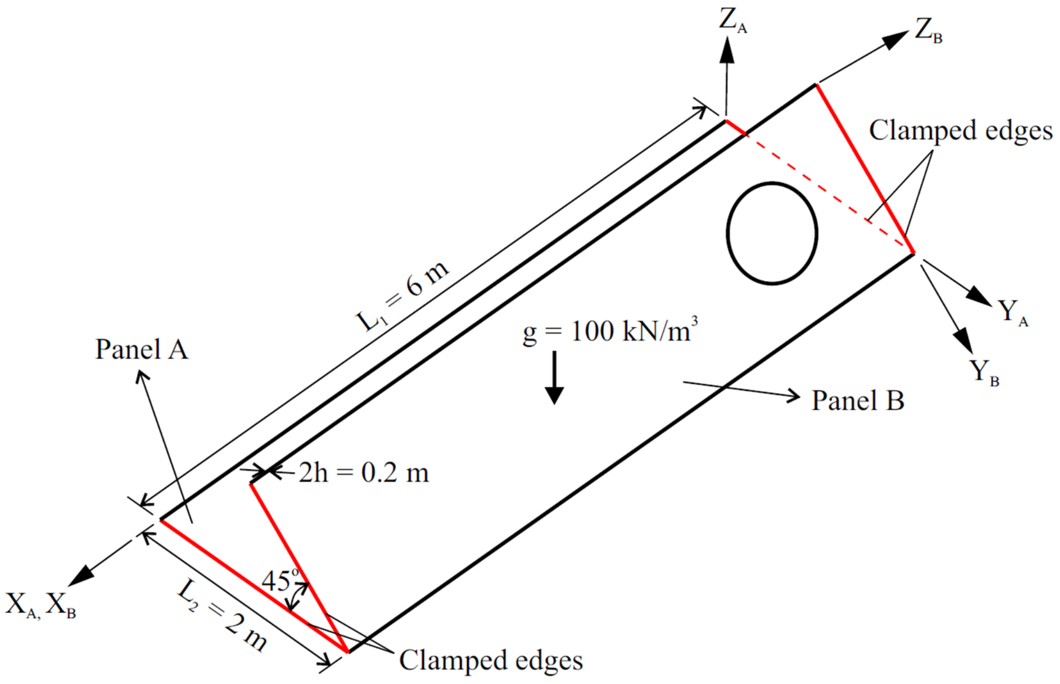

Figure 6.24 Isometric view of the wedge structure.

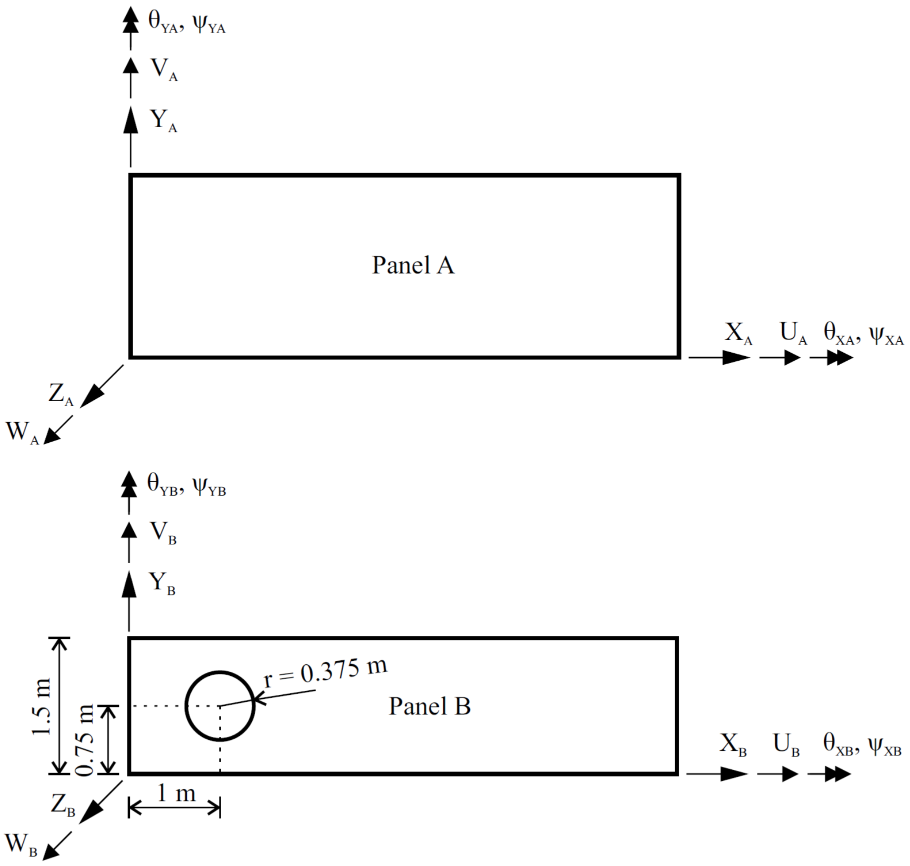

Figure 6.25 Panels A and B, group coordinate systems, and kinematic variables.

As presented Figure 6.25, the kinematic variables $(\mathrm{U}_\alpha, \mathrm{V}_\alpha, \mathrm{W}_\alpha)$ $(\alpha = \mathrm{A, B})$ represent the translations along the positive coordinate $(\mathrm{X}_\alpha, \mathrm{Y}_\alpha, \mathrm{Z}_\alpha)$ $(\alpha\text{=A, B})$ directions, respectively, whereas the kinematic variables $(\theta_{\mathrm{X}\alpha}, \theta_{\mathrm{Y}\alpha})$ $(\alpha = \mathrm{A, B})$ and $(\psi_{\mathrm{X}\alpha}, \psi_{\mathrm{Y}\alpha})$ $(\alpha = \mathrm{A, B})$ denote bending and zigzag rotations around the positive $(\mathrm{X}_\alpha, \mathrm{Y}_\alpha)$ $(\alpha\text{=A, B})$ directions, respectively. Both ends of the wedge are clamped, and the clamped boundary conditions along $\mathrm{X_A} = \mathrm{X_B} = 0\ \mathrm{m}$ and $\mathrm{X_A} = \mathrm{X_B} = 6\ \mathrm{m}$ are specified as

$$\mathrm{U}_\alpha = \mathrm{V}_\alpha = \mathrm{W}_\alpha = \theta_{\beta\alpha} = \psi_{\beta\alpha} = 0 \quad (\alpha = \mathrm{A, B};\ \beta = \mathrm{X, Y}) \tag{6.114}$$

A body force of $\mathrm{g} = 100\ \mathrm{kN/m^3}$ is applied to the wedge structure along the negative $\mathrm{Z_A}$ direction as shown in Figure 6.24. A five-layer, cross-ply sandwich laminate with carbon-epoxy face sheets and a thick PVC core is considered to represent moderately thin sandwich plates with a span-to-thickness ratio of $L_1/2h = 30$. The stacking sequences of the wedge laminate are listed in Table 6.9.

Table 6.9 Laminate stacking sequence of the wedge structure (in the positive Z_A and Z_B directions).

Wedge Laminate	Normalized lamina thickness, $h^{(k)}/h$	Lamina materials	Lamina orientation [°]
Cross-ply sandwich	(0.05/0.05/0.8/0.05/0.05)	(C/C/P/C/C)	(0/90/0/90/0)

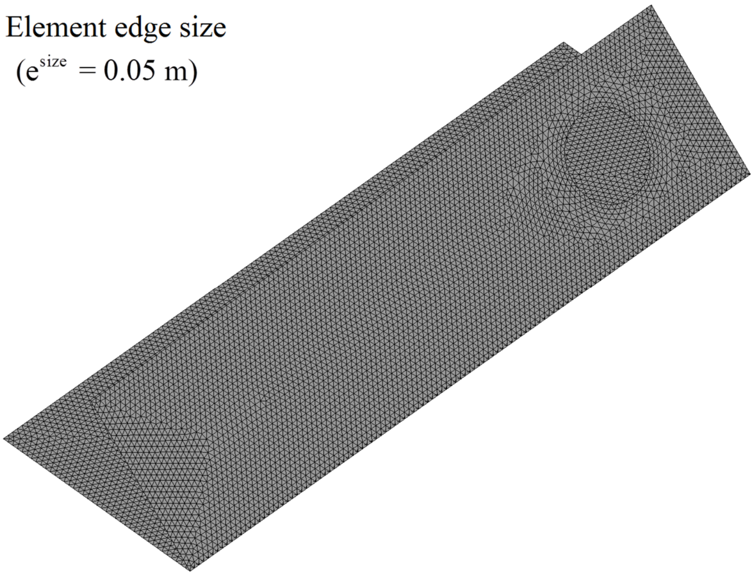

Figure 6.26 Discretization of the wedge structure using 18802 elements.

An RZT-based FEM convergence study was performed to establish an accurate reference solution for this problem. As depicted in Figure 6.26, the highest fidelity FEM mesh consisted of 18802 randomly distributed triangular elements with an edge size of $e^{size} = 0.05$ m and 86535 DOF. The FEM deflections and rotations are used to compute the simulated strain-sensor strains. For panels A and B, the maximum displacements, von Mises stresses, bending and zigzag rotations obtained from FEM analysis are listed in Tables 6.10-11, respectively. To assess the accuracy of the displacement, rotation, and stress responses, it would be convenient to use these reference values as normalization factors.

Table 6.10 Maximum displacements and von Mises stresses of the wedge panels.

α	$U_{\alpha,\max}^{FEM}$ [m]	$V_{\alpha,\max}^{FEM}$ [m]	$W_{\alpha,\max}^{FEM}$ [m]	$\sigma_{v\alpha,\max}^{FEM}$ [Pa]
A	-4.353×10^{-5}	-2.059×10^{-4}	-1.389×10^{-2}	9.874×10^{7}
B	1.101×10^{-4}	8.601×10^{-4}	-1.031×10^{-2}	9.238×10^{7}

Table 6.11 Maximum bending and zigzag rotations of the wedge panels.

α	$\theta_{X\alpha,\max}^{FEM}$ [rad]	$\theta_{Y\alpha,\max}^{FEM}$ [rad]	$\psi_{X\alpha,\max}^{FEM}$ [rad]	$\psi_{Y\alpha,\max}^{FEM}$ [rad]
A	6.119×10^{-3}	1.243×10^{-3}	-1.350×10^{-3}	-7.128×10^{-3}
B	6.084×10^{-3}	1.120×10^{-3}	-2.117×10^{-3}	5.314×10^{-3}

Five different iFEM analyses of the wedge structure were performed using five different networks of strain rosettes. Each iFEM analysis refers to a case study number; e.g., the first analysis is called “iFEM (Case I)” and the third analysis is called “iFEM (Case III).” Through the thickness coordinate, three strain rosettes are located at the centroid of each element for all iFEM cases; one on the top surface, one on the bottom surface, and one on the nearest interface to the bottom surface of the laminate. In contrast to example presented in Section 6.5.1, the discrete strain measures were not smoothed a priori and they were directly used as input in iFEM (Cases I-V). Using the absolute values of the reference solutions listed in Tables 6.10-11, the displacements, bending and zigzag rotations, and von Mises stresses obtained from both iFEM and FEM analyses are normalized as

$$\bar{\chi}_{\alpha} = \chi_{\alpha} \,/\, \left|\chi_{\alpha,\max}^{FEM}\right| \quad (\chi = U, V, W, \theta_X, \theta_Y, \psi_X, \psi_Y, \sigma_v) \tag{6.115}$$

where $\alpha = A$ is for panel A and $\alpha = B$ is for panel B.

In iFEM (Case I), the i3-RZT discretization is identical to high-fidelity mesh used in the FEM analysis. As presented in Figure 6.27, the i3-RZT model has 18802 uniformly distributed triangular elements, each of which has three strain rosettes $(\boldsymbol{\varepsilon}_i^{+}, \boldsymbol{\varepsilon}_i^{-}, \boldsymbol{\varepsilon}_i^{j})$. In iFEM (Case II), the top-surface, bottom-surface, and *j*-th interface strain rosettes are removed from 13678 i3-RZT elements, and the resulting i3-RZT mesh has only 5124×3 strain rosettes as shown in Figure 6.28. A coarser i3-RZT discretization is used in the last three case studies, iFEM (Cases III-V). As depicted in Figure 6.29, the coarser i3-RZT discretization consisted of 4644 randomly distributed triangular elements with an edge size of $e^{\text{size}} = 0.1\ \text{m}$ and 21861 DOF.

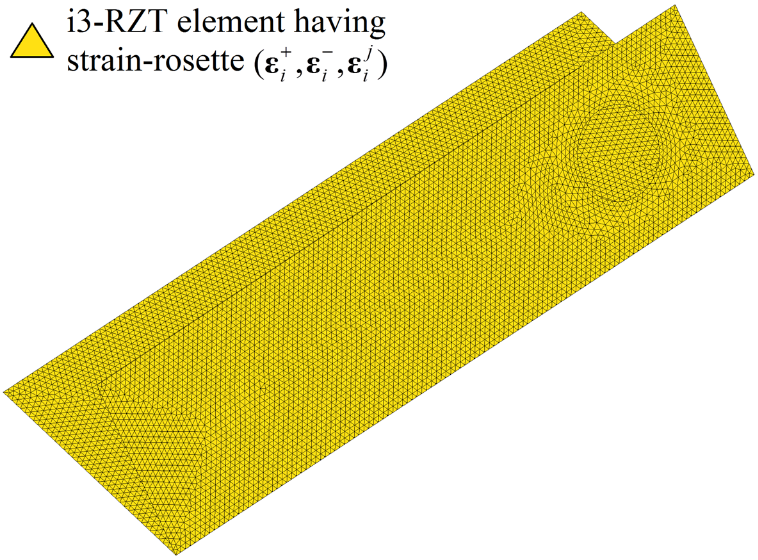

Figure 6.27 The i3-RZT model used in iFEM (Case I).

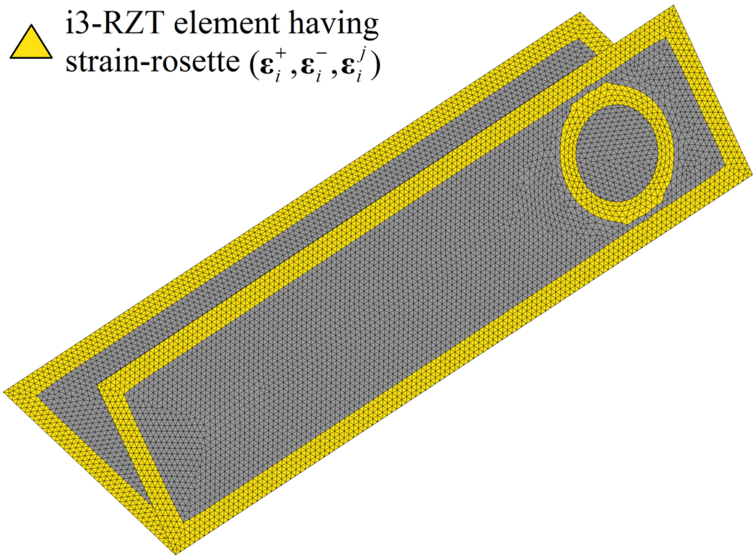

Figure 6.28 The i3-RZT model used in iFEM (Case II).

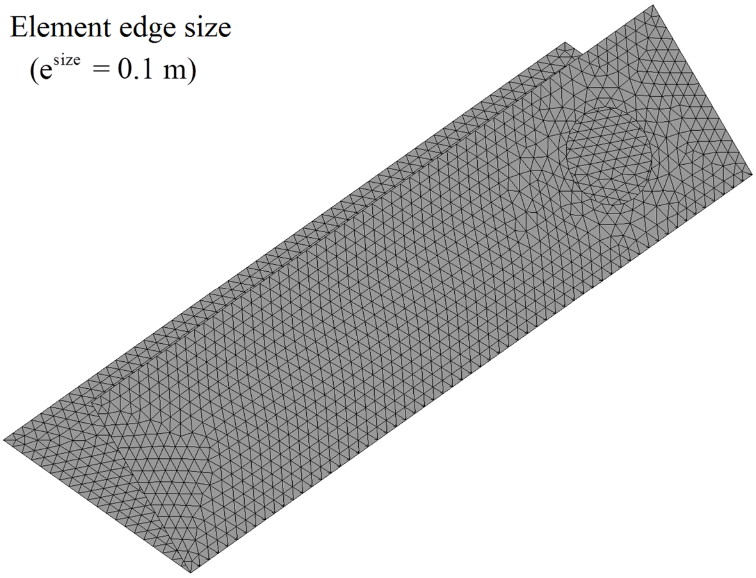

Figure 6.29 Discretization of the wedge structure using 4644 elements.

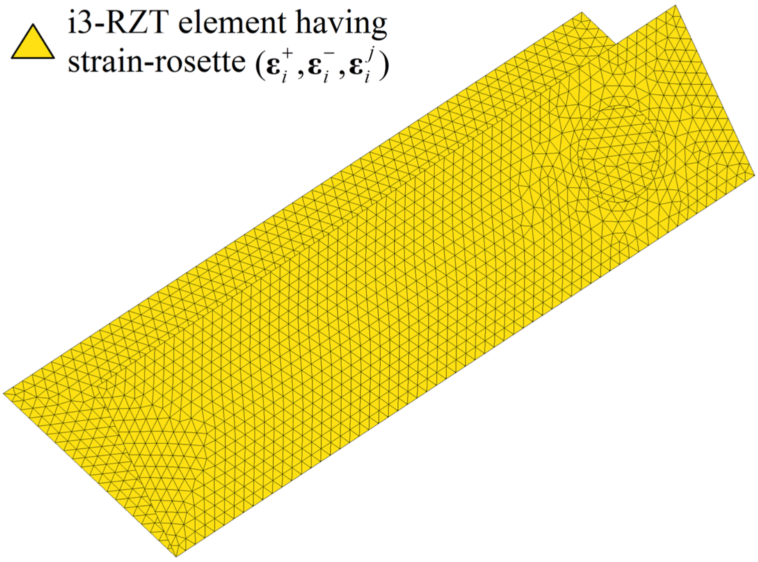

Figure 6.30 The i3-RZT model used in iFEM (Case III).

In iFEM (Case III), as presented in Figure 6.30, the i3-RZT model has 4644 inverse-elements each of which has three strain rosettes $(\boldsymbol{\varepsilon}_i^+,\boldsymbol{\varepsilon}_i^-,\boldsymbol{\varepsilon}_i^j)$. In iFEM (Case IV), the top-surface, bottom-surface, and *j*-th interface strain rosettes are removed from 2839 i3-RZT elements, and the resulting i3-RZT mesh has only 1825×3 strain rosettes (refer to Figure 6.31). In iFEM (Case V), as shown in Figure 6.32, the i3-RZT model has only 1288 inverse-elements installed with three strain rosettes $(\boldsymbol{\varepsilon}_i^+,\boldsymbol{\varepsilon}_i^-,\boldsymbol{\varepsilon}_i^j)$, and the remaining 3376 i3-RZT elements has no in situ strain components. For an i3-RZT element that has no in situ strain components, the corresponding weighting coefficients are set to 10^{-5}. Moreover, the weighting constants corresponding to the transverse-shear strain measures are set to a small value as $w_\alpha = 10^{-8}$ $(\alpha = 10,11)$ and $w_\alpha = 10^{-6}$ $(\alpha = 12,13)$ for iFEM (Cases I-V).

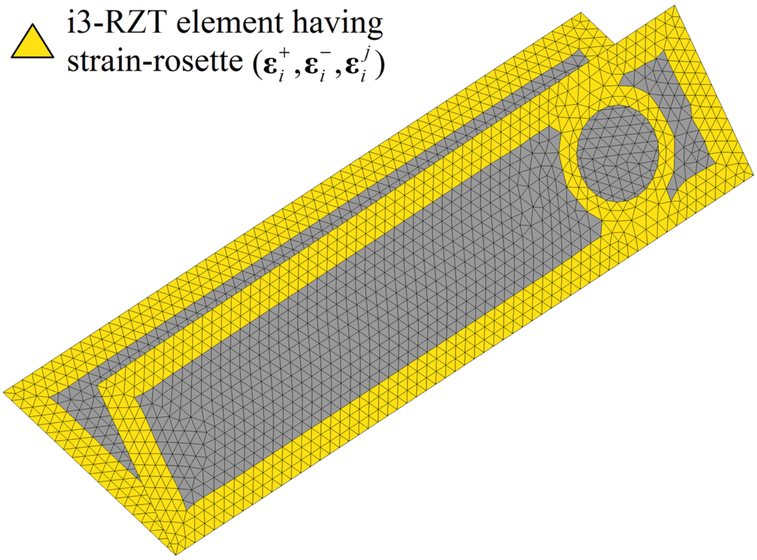

Figure 6.31 The i3-RZT model used in iFEM (Case IV).

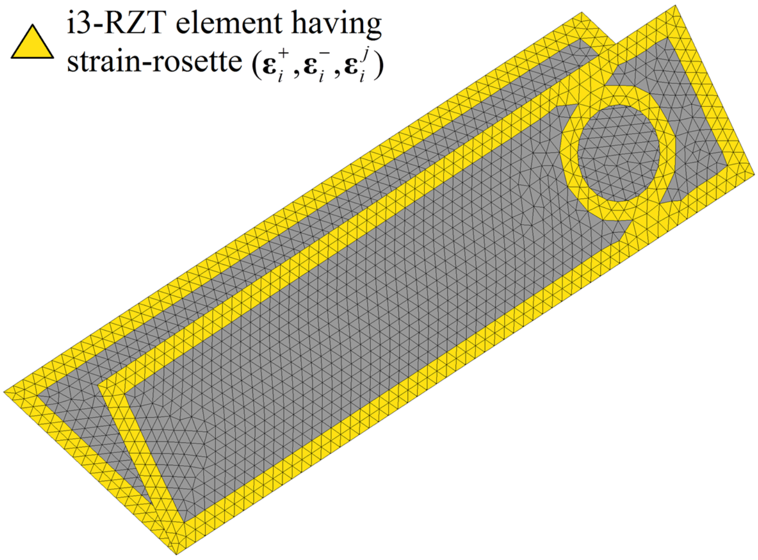

Figure 6.32 The i3-RZT model used in iFEM (Case V).

The percent difference between iFEM (Cases I-V) and FEM predictions for the maximum values of normalized expressions given in Equation (6.115) are listed for panels A and B in Tables 6.12-13, respectively. As can be seen from these tables, iFEM (Case I) and FEM predictions are almost the same for all the variables. These results clearly demonstrate the superior accuracy of the iFEM/i3-RZT solutions when a high-fidelity i3-RZT model in which all elements have in situ strain measurements is used. The percent differences between iFEM (Case II) and FEM estimates for all of the variables are less than 4% and 2% for panels A and B, respectively. These results confirm the superior membrane-bending coupled predictions of the i3-RZT element, especially considering a high-fidelity i3-RZT model in which relatively few elements have in situ strain measurements. The percent differences between iFEM (Case III) and FEM predictions for displacement and rotation variables are not more than 5.6% and 10.8% for panel A and 1.1% and 5.9% for panel B, respectively. These results demonstrate the high accuracy of the iFEM/i3-RZT capability for shape sensing even when relatively coarse discretization is used. Moreover, iFEM (Case III) solutions for von Mises stresses differ from the FEM solutions by approximately 14% for panel A and 15.5% for panel B. Even though these results might be acceptable for some practical applications, they clearly demonstrate that iFEM/i3-RZT formulation needs a higher fidelity mesh to compute high strain gradients to obtain improved stresses.

Table 6.12 Percent difference between the iFEM (Cases I-V) and FEM predictions for maximum values of the variables (panel A).

Case	Percent difference							
	$\bar{U}_A$	$\bar{V}_A$	$\bar{W}_A$	$\bar{\theta}_{XA}$	$\bar{\theta}_{YA}$	$\bar{\psi}_{XA}$	$\bar{\psi}_{YA}$	$\bar{\sigma}_{vA}$
I	0.0	0.0	0.0	0.0	0.0	0.1	0.0	0.2
II	0.1	0.0	0.0	1.1	3.7	2.8	0.0	0.2
III	5.6	0.8	1.0	0.8	0.8	10.8	1.7	14.0
IV	12.4	22.5	2.3	9.0	3.3	7.6	3.8	14.6
V	18.1	52.2	3.8	19.4	7.7	3.2	4.7	14.5

As can be seen from Table 6.10, the maximum deflections, $W_{\alpha,\max}^{FEM}$ $(\alpha = A, B)$, are much greater than the maximum in-plane displacements and/or rotations, thus the deformed shape (total deformation) of the wedge structure is mainly caused by the deflections. Hence, the accuracy of monitoring the deflections $\bar{W}_A$ and $\bar{W}_B$ is crucial for monitoring total deformation.

Table 6.13 Percent difference between the iFEM (Cases I-V) and FEM predictions for maximum values of the variables (panel B).

Case	Percent difference							
	$\bar{U}_B$	$\bar{V}_B$	$\bar{W}_B$	$\bar{\theta}_{XB}$	$\bar{\theta}_{YB}$	$\bar{\psi}_{XB}$	$\bar{\psi}_{YB}$	$\bar{\sigma}_{vB}$
I	0.0	0.0	0.0	0.0	0.0	0.0	0.0	0.2
II	0.2	0.3	0.0	1.1	0.1	1.7	0.0	0.2
III	1.1	0.7	1.1	0.8	5.9	5.7	2.4	15.5
IV	3.6	0.3	2.0	9.1	8.5	6.4	5.0	15.5
V	5.1	2.5	4.9	19.5	21.5	8.5	5.8	15.5

The percent differences between iFEM (Case IV) and FEM estimates for $\bar{W}_A$ and $\bar{W}_B$ are only 2.3% and 2.0%, whereas iFEM (Case V) predictions for $\bar{W}_A$ and $\bar{W}_B$ differ from the FEM predictions by only 3.8% and 4.9%, respectively. These results demonstrate that iFEM predictions remain sufficiently accurate even considering a coarse i3-RZT model with the missing strain rosette data in many elements. Besides, these results remarkably prove the superior capability of the i3-RZT element for shape sensing, even though the percent differences between iFEM (Cases IV-V) for in-plane displacement and rotations are relatively higher. Furthermore, the percent differences between iFEM (Cases IV-V) and FEM predictions for von Mises stresses are not more than 14.6% and 15.5% for panels A and B, respectively. These percent differences are very similar to the corresponding percent differences obtained for iFEM (Case III). Hence, these results prove that an i3-RZT model in which few elements have strain rosettes can predict similar maximum stresses in comparison to an i3-RZT model in which all elements have strain rosettes.

In addition to the percent difference results, contour plots for the normalized expressions given in Equation (6.115) are compared between iFEM (Case IV) and high-fidelity FEM analyses in Figures 6.33-40. Note that, only contour plots of the iFEM (Case IV), i.e., one of the most challenging case study in comparison to others, is included herein for conciseness of this chapter. However, the contour plots pertaining to iFEM (Cases I-III and V) can be found in Kefal, Tessler, et al. (2016). In Figures 6.35-37 and 6.39-40, contour plots for iFEM (Case IV) are graphically almost identical to those of FEM. Moreover, the remaining contour plots for iFEM (Cases IV) are generally in good agreement with the contour plots of FEM (refer to Figures 6.33, 6.34, and 6.38). The iFEM predictions remain sufficiently accurate even with the missing strain rosette data in many elements. Thus, these results demonstrates the superior predictive capability and practical applicability of the enhanced iFEM formulation for shape and stress sensing of complex composite/sandwich structures exhibiting complicated deformed shapes.

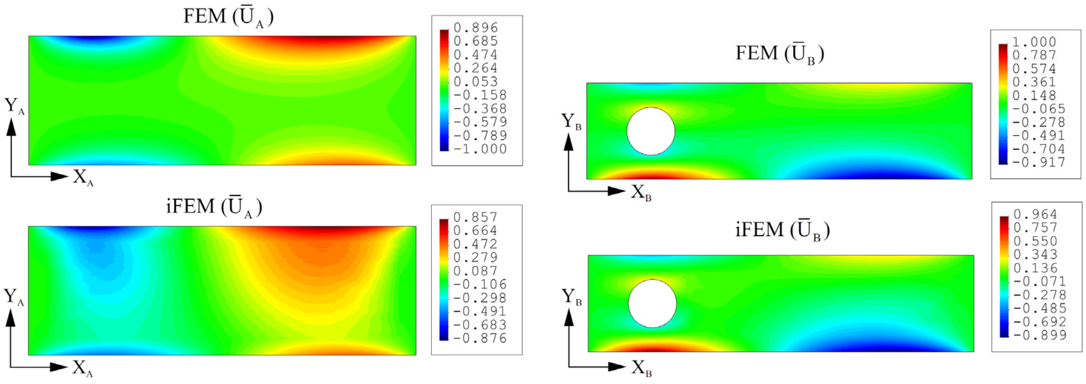

Figure 6.33 Contour plots of $\bar{U}_A$ and $\bar{U}_B$ displacements of the wedge panels A and B: Comparison between high-fidelity FEM and iFEM (Case IV) analyses.

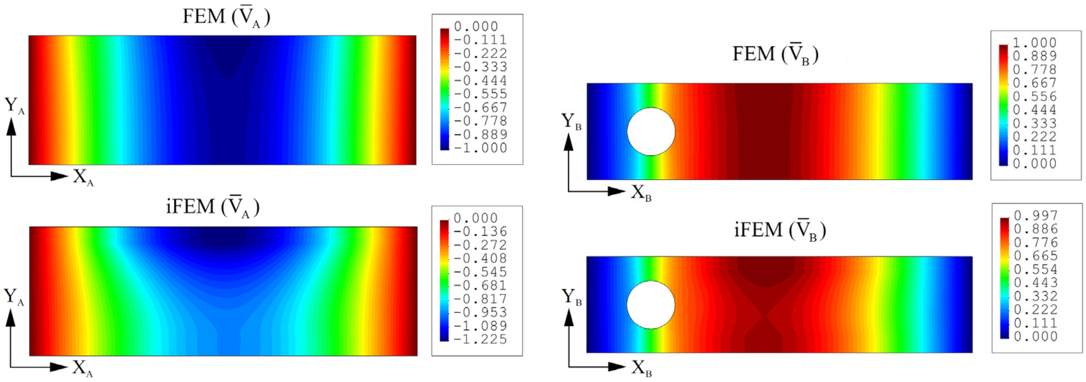

Figure 6.34 Contour plots of $\bar{V}_A$ and $\bar{V}_B$ displacements of the wedge panels A and B: Comparison between high-fidelity FEM and iFEM (Case IV) analyses.

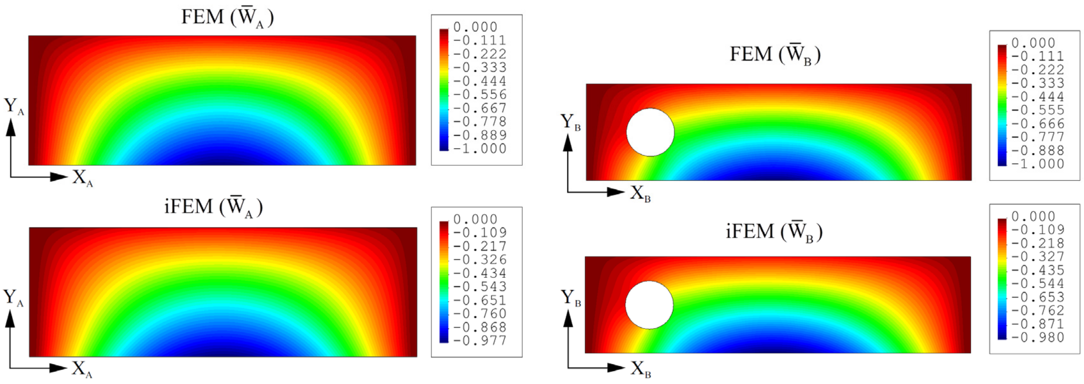

Figure 6.35 Contour plots of $\bar{W}_A$ and $\bar{W}_B$ displacements of the wedge panels A and B: Comparison between high-fidelity FEM and iFEM (Case IV) analyses.

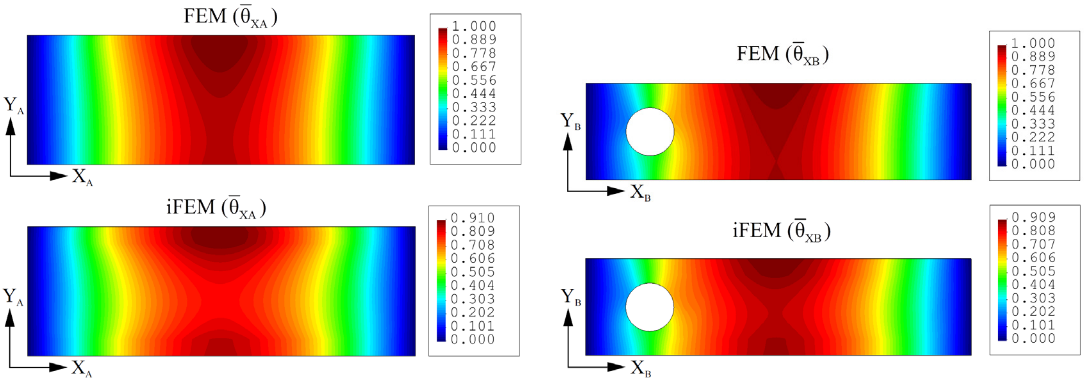

Figure 6.36 Contour plots of $\bar{\theta}_{XA}$ and $\bar{\theta}_{XB}$ bending rotations of the wedge panels A and B: Comparison between high-fidelity FEM and iFEM (Case IV) analyses.

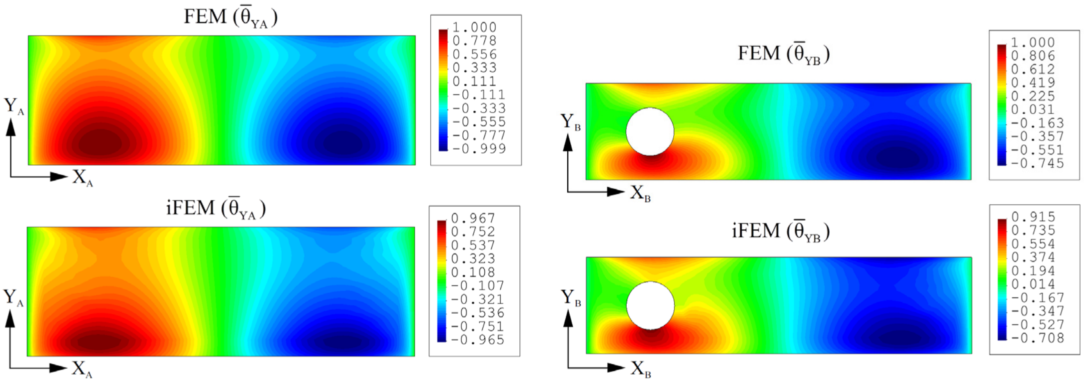

Figure 6.37 Contour plots of $\bar{\theta}_{YA}$ and $\bar{\theta}_{YB}$ bending rotations of the wedge panels A and B: Comparison between high-fidelity FEM and iFEM (Case IV) analyses.

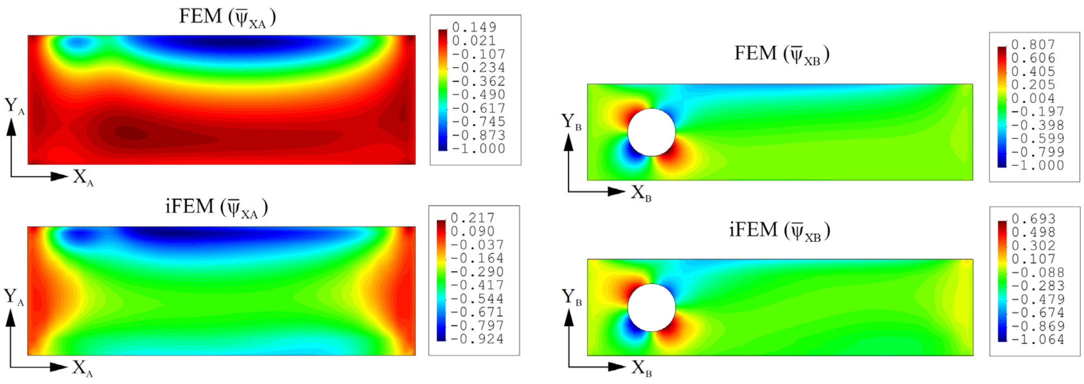

Figure 6.38 Contour plots of $\overline{\psi}_{XA}$ and $\overline{\psi}_{XB}$ zigzag rotations of the wedge panels A and B: Comparison between high-fidelity FEM and iFEM (Case IV) analyses.

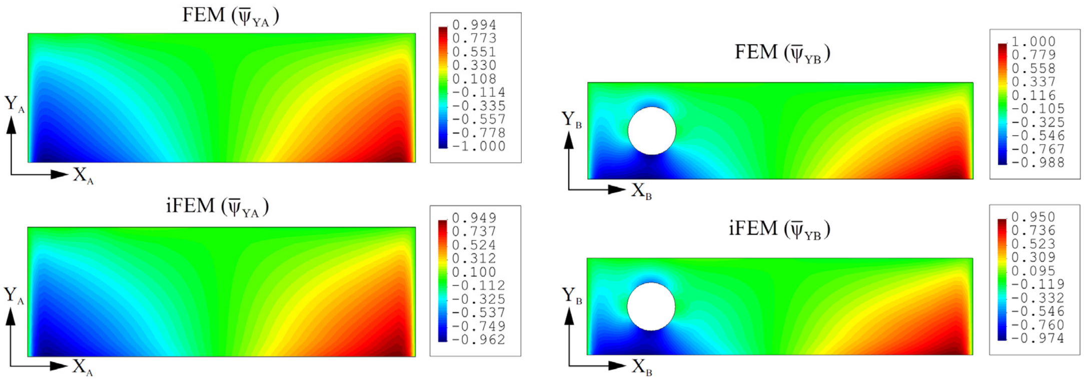

Figure 6.39 Contour plots of $\overline{\psi}_{YA}$ and $\overline{\psi}_{YB}$ zigzag rotations of the wedge panels A and B: Comparison between high-fidelity FEM and iFEM (Case IV) analyses.

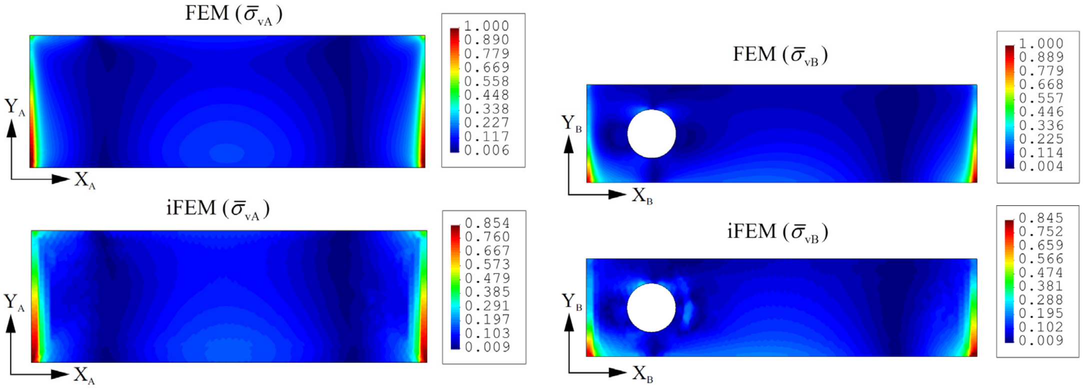

Figure 6.40 Contour plots of $\bar{\sigma}_{vA}$ and $\bar{\sigma}_{vB}$ von Mises stresses at thickness coordinates $Z_A / h = -1$ and $Z_B / h = 1$ of wedge panels A and B, respectively: Comparison between high-fidelity FEM and iFEM (Case IV) analyses.

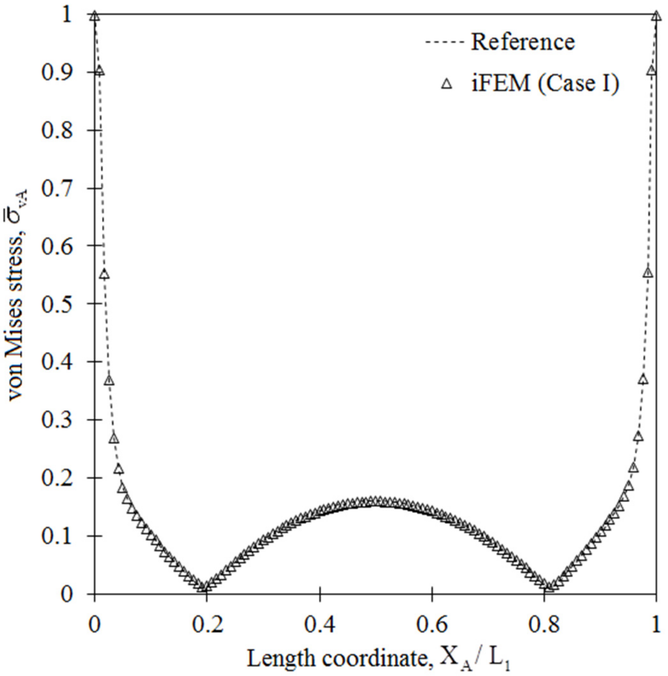

Figure 6.41 The von Mises stress $\bar{\sigma}_{vA}$ variation along length L_1 of panel A: Comparison between high-fidelity FEM and iFEM (Case I) analyses.

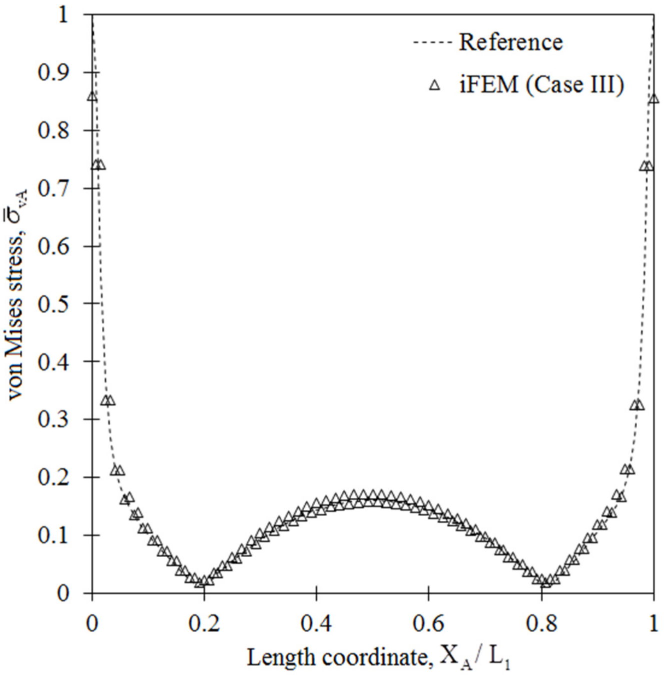

Figure 6.42 The von Mises stress $\bar{\sigma}_{vA}$ variation along length L_1 of panel A: Comparison between high-fidelity FEM and iFEM (Case III) analyses.

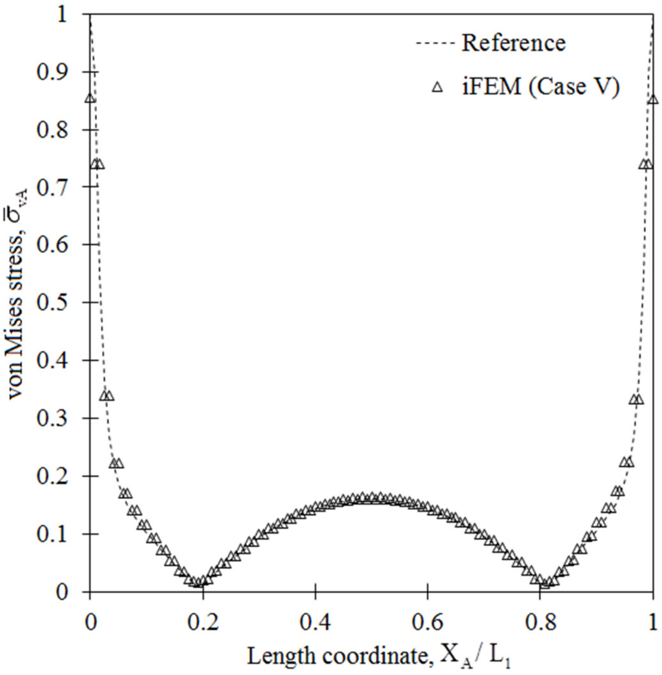

Figure 6.43 The von Mises stress $\bar{\sigma}_{vA}$ variation along length L_1 of panel A: Comparison between high-fidelity FEM and iFEM (Case V) analyses.

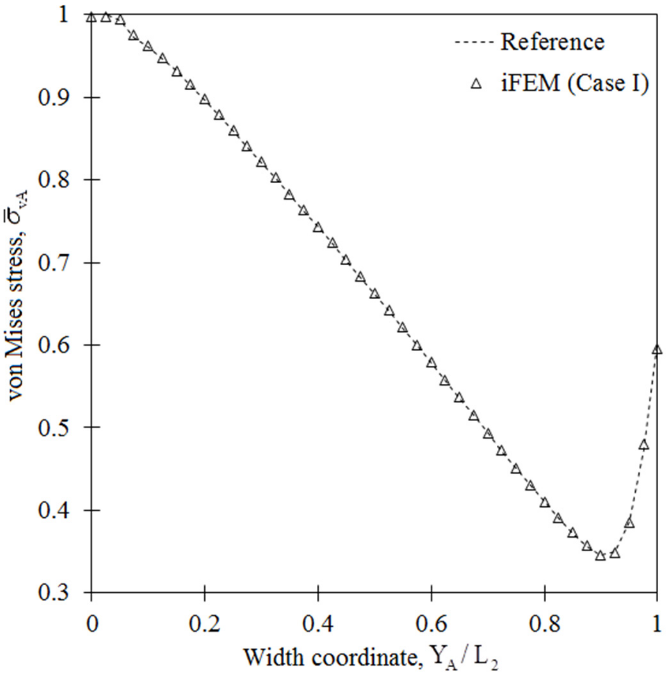

Figure 6.44 The von Mises stress $\bar{\sigma}_{vA}$ variation along width L_2 of panel A: Comparison between high-fidelity FEM and iFEM (Case I) analyses.

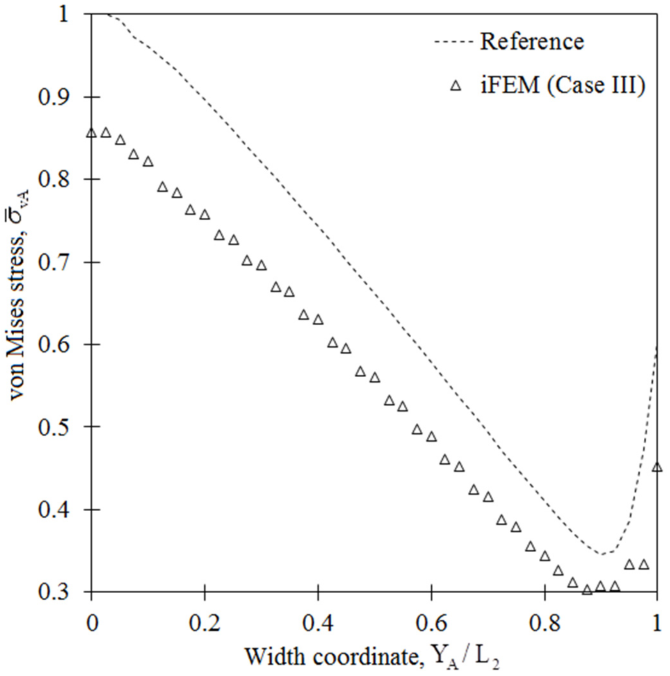

Figure 6.45 The von Mises stress $\bar{\sigma}_{vA}$ variation along width L_2 of panel A: Comparison between high-fidelity FEM and iFEM (Case III) analyses.

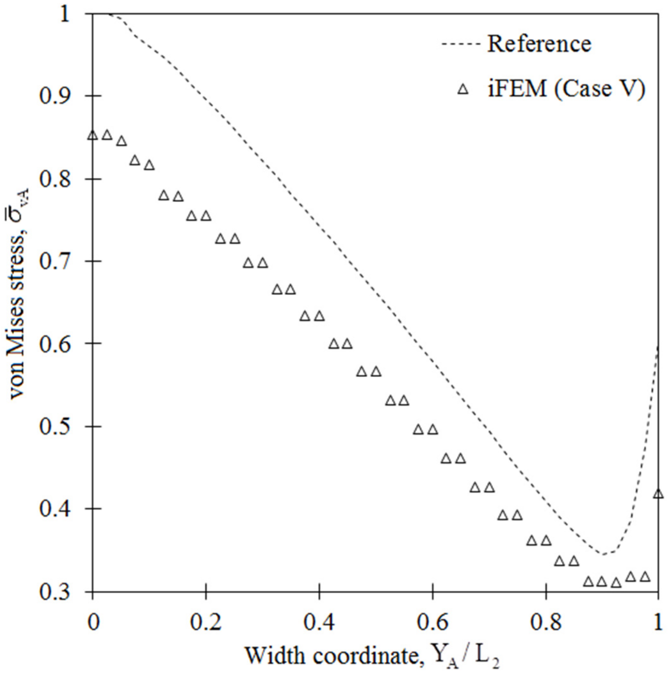

Figure 6.46 The von Mises stress $\bar{\sigma}_{vA}$ variation along width L_2 of panel A: Comparison between high-fidelity FEM and iFEM (Case V) analyses.

Furthermore, in Figures 6.41-46, variation of von Mises stress $\bar{\sigma}_{\mathrm{vA}}$ along L_1 and L_2 is compared between iFEM (Cases I, III, and V) and reference FEM solutions, respectively. These results prove the following three observations: (1) the improved iFEM formulation predicts von Mises stresses that are comparably accurate to those of the reference solutions, (2) the i3-RZT element formulation requires higher fidelity discretization to calculate high strain gradients to obtain improved stresses, and finally (3) an i3-RZT model with relatively very sparse measured strain data can predict von Mises stresses that are as accurate as those obtained using an i3-RZT model in which all elements have strain-sensor data.

6.6 Conclusion

An improved iFEM formulation is presented to solve the inverse problem of shape and stress sensing of multilayered composite and sandwich plates/shells that have randomly distributed strain sensors. The plate/shell kinematics are described using RZT plate theory. The formulation is based on minimization of a weighted-least-squares functional that accounts for the complete set of strain measures consistent with RZT plate theory. Based on the present iFEM methodology, laminated composite and sandwich plate/shell structures that involve relatively few strain gauges can be analyzed by utilizing weighting constants. One advantage of the present iFEM methodology is that it can be used for the analysis of thin and moderately thick plate and shell structures because the variational principle accommodates for full transverse-shear deformation of the RZT plate theory. Moreover, the formulation is suitable for C^0-continuous discretization, enabling the development of robust inverse-shell elements for performing shape and stress sensing of complex engineering structures. A new three-node triangular inverse-shell element (i3-RZT) was developed based on the improved iFEM formulation. The i3-RZT element kinematic field accommodates quadratic interpolation functions that permit a robust drilling DOF implementation that has the advantage of avoiding singular solutions when modeling complex shell structures. The formulation is free from the membrane and shear-locking phenomena. Several numerical studies were performed and demonstrated the computational efficiency, high accuracy, and robustness of i3-RZT discretization with respect to the membrane, bending, and membrane-bending coupled structural responses. The practical utility of iFEM/i3-RZT technology for application to engineering structures has been assessed using relatively low- and high-fidelity discretization strategies. The effects of sensor locations and number of sensors were also explored. It was demonstrated that even in the presence of relatively sparse strain data, sufficiently accurate reconstruction of deformed structural shapes and stresses can be achieved. Finally, the presented iFEM/i3-RZT technology can be readily implemented in any general-purpose finite element software (e.g., ABAQUS, ANSYS), serving a highly desirable and viable computational tool for real-time structural health monitoring of laminated-composite and sandwich structures, such as high-performance aerospace vehicles.

Chapter 7

General Conclusion

7.1 Achievements against the Objectives

As is obvious in the Chapter 1, the ultimate goal of this PhD thesis was to produce non-conventional and superior iFEM frameworks that can be used as guidelines for SHM of general engineering structures and marine structures in particular. The list below summarizes the main achievements of this work, which are in line with the research objectives:

1. A novel four-node quadrilateral inverse-shell element (iQS4) was developed on the basis of an iFEM weighted-least-square functional. The iQS4 element was intended to solve shape-sensing problems composed of thin and moderately thick plate or shell structures with randomly distributed strain sensors. The element kinematic field interpolated using quadratic shape functions permit robust drilling DOF implementation and serve the advantage of avoiding singular solutions when modelling complex shell structures. It was demonstrated that the formulation is also robust with respect to the membrane- and shear-locking phenomena. Finally, it was proven that even in the presence of the relatively sparse strain data subject to experimental noise, sufficiently accurate reconstructions of the deformed structural shapes can be achieved.

2. Displacement and stress monitoring of three different marine structures, i.e., (1) a longitudinally and transversely stiffened plate, (2) a long barge with a typical chemical tanker cross-section, and (3) the parallel mid-body of a Panamax container ship, was achieved by using iFEM/iQS4 methodology. In order to represent realistic structural responses by these marine structures, in-house hydrodynamic and FEM software was utilized to simulate the in situ strain-sensor strains. Using relatively low-fidelity iQS4 discretization, the optimum strain sensor locations were determined and demonstrated for each marine structure. Overall, the practical utility and robustness of the iFEM/iQS4 technology was confirmed for application to marine structures.
3. An isogeometric Kirchhoff–Love inverse-shell element (iKLS) was developed by coupling the isogeometric analysis with the iFEM methodology, leading to the creation of a novel isogeometric iFEM formulation. The iKLS element was aimed at performing shape-sensing analysis of complex (curved) thin shell structures instrumented with several strain sensors. The element kinematic field was defined in convected curvilinear coordinates and interpolated by high-order continuous $(C^p, p > 0)$ NURBS basis functions which were also used to create the geometry. It was demonstrated that the iKLS element has the advantage of simply modelling the curved shell structures as a result of its NURBS-based nature. Finally, the superior membrane and bending capability of the iKLS element was justified even when using low-fidelity discretization with few strain rosettes.
4. An improved iFEM formulation was developed based on a weighted-least-squares variational principle that uses the complete set of strain measures consistent with RZT. In addition, a robust and computationally efficient three-node inverse-shell element, i3-RZT, was implemented based upon the improved iFEM formulation. The i3-RZT element was intended to perform shape- and stress-sensing analysis of multilayered composite and sandwich plates/shells with randomly distributed strain sensors. It was demonstrated that the i3-RZT formulation is free from the membrane- and shear-locking phenomena and can predict very accurate through-the-thickness distributions of in-plane displacements, normal stresses, and transverse-shear stresses. Overall, it was confirmed that even in the presence of

relatively sparse strain data, sufficiently accurate reconstructions of deformed structural shapes and stresses can be achieved by using i3-RZT models.

7.2 Novelty and Contribution to the Field

Shape- and stress-sensing capabilities are well-recognized as an enabling technology for SHM systems. Although many researchers have proposed various types of shape-sensing algorithms (vid. Section 2.2), due to their inherent limitations, the algorithms were not general enough to perform displacement and stress monitoring of large-scale structures such as marine structures. Moreover, several class societies, the IMO, and many researchers have found hull structural monitoring was to be significant enough to study; thus, various SHM systems have been proposed for marine structures (vid. Section 2.3). However, none of these systems can monitor three-dimensional full-field displacements and stresses of a marine vessel. In fact, they only monitor several points on the weather deck amidships. The study described in Chapter 3 demonstrates that the iFEM/iQS4 methodology can overcome these limitations and is a general tool for the shape and stress sensing of large-scale structures. The literature was lacking such a framework, whose formulation can now be found in Kefal, Oterkus, et al. (2016), which further expands the library of existing iFEM-based inverse elements by implementing a four-node inverse-shell element for the first time in the literature. Although various types of iFEM formulations and inverse elements have been developed on the basis of different beam, plate, and shell theories, the numerical and experimental applications of these formulations on engineering structures have been limited to the SHM of aerospace vehicles (vid. Section 2.4). The study described in Chapter 4 demonstrates the application of the iFEM/iQS4 methodology to the shape and stress sensing of various types of marine structures. The literature was lacking such a novel application, which can now be found in the series of works conducted by Kefal and Oterkus (2015, 2016a, 2016b).

The CAD industry nowadays offer many efficient computer software applications for fast evaluation and refinement of NURBS. Isogeometric analysis or IGA (Hughes et al., 2005) bridged the gap between CAD and engineering analysis by employing NURBS to describe the geometry of the computational domain in the analysis framework. IGA serves a number of beneficial aspects and has thus received a considerable amount of attention in recent years in many fields of computational mechanics (vid. Section 5.2). For an accurate iFEM analysis of any structure, especially of curved structures, exact representation of the actual structural geometry is vital. Moreover, a smoother geometry requires more refined mesh generation with the existing flat inverse-shell elements, e.g., iQS4 (vid. Chapter 3) and iMIN3 (Tessler and Spangler, 2004). This may lead to a large number of strain sensors installed on-board a structure, thus resulting in expensive shape-sensing analysis for a complex/curved geometry. Furthermore, the shape functions of these flat shell elements are generally limited to only C^0-continuity for the displacement field. The study described in Chapter 5 demonstrates that an isogeometric iFEM formulation (i.e., iKLS element) can overcome the limitations mentioned above and further expand the horizons of the iFEM methodology to employ novel isogeometric inverse elements. The literature was lacking such a framework, whose formulation can now be found in Kefal and Oterkus (2017) and can be used for shape-sensing analysis of curved thin shells instrumented with several strain sensors.

Over the last few decades, the usage of composite and sandwich material systems as primary structures has dramatically increased in various engineering applications. Hence, a powerful shape-sensing algorithm is necessary for ensuring the safety and structural integrity of these structures. In fact, Cerracchio et al. (2013, 2015b) developed a novel RZT-based iFEM methodology for such composite structures. Although their formulation performed well for sandwich plates, the proposed variational statement was lacking the precise contribution of full transverse-shear strain measures. Moreover, the application of their RZT-based iFEM methodology was only limited to composite plate structures, since they only presented an inverse-plate element formulation (i.e., iRZT3). Furthermore, the authors did not introduce the weighting coefficients in the least-squares functional; thus, the iRZT3 element cannot take into account the problems involving sparse in situ strain data. The study described in Chapter 6 demonstrated that (1) an enhanced iFEM formulation and (2) the i3-RZT inverse-shell element can address the aforementioned shortcomings. The literature was lacking such a framework, whose formulation can now be found in Kefal, Tessler, et al. (2016); ultimately, the aim is to perform accurate shape and stress sensing of multilayered composite and sandwich plate and shell structures.

7.3 Gaps and Future Studies

Despite the realistic performance of the novel iFEM frameworks developed in this work, experimentally measured strains are simulated using high-fidelity FEM analysis. Instead, real experimental measurements can be coupled with the presented iFEM frameworks to reproduce and investigate their performance further in a laboratory environment.

Concerning the iFEM/iQS4 models developed for the marine structure applications in Chapter 4, the numerical framework could be extended by modelling other types of marine structures, such as bulk carriers, offshore platforms, and wind turbines.

Concerning the isogeometric iFEM methodology presented in Chapter 5, further investigations can allow the development of other types of isogeometric inverse elements, such as isogeometric inverse-beam, -plate, -shell, and -solid elements.

Concerning the improved RZT-based iFEM methodology demonstrated in Chapter 6, future studies can be developed by implementing the presented framework utilizing a four-node inverse-shell element.

7.4 Research Outputs

The following section provides all of the author's research outputs, which are directly related to the iFEM research study presented in this thesis. These outputs include the journal papers, conference papers/presentations, technical reports, and research collaborations that have already been published or submitted and are still in preparation stage.

7.4.1 Journal papers

Kefal, A., and Oterkus, E. (2016). Displacement and stress monitoring of a chemical tanker based on inverse finite element method. *Ocean Engineering*, **112**: 33-46.

Kefal, A., and Oterkus, E. (2016). Displacement and stress monitoring of a Panamax containership using inverse finite element method. *Ocean Engineering*, **119**: 16-29.

Kefal, A., Oterkus, E., Tessler, A., and Spangler, J.L. (2016). A quadrilateral inverse-shell element with drilling degrees of freedom for shape sensing and structural health monitoring. *Engineering Science and Technology, an International Journal*, **19**: 1299-1313.

Kefal, A., Tessler, A., and Oterkus, E. (2016). An enhanced inverse finite element method for displacement and stress monitoring of multilayered composite and sandwich structures. Submitted to *Composite Structures*.

Kefal, A., and Oterkus, E. (2016). An isogeometric Kirchhoff-Love inverse-shell element for shape sensing of curved thin shells. In preparation for *Computer Methods in Applied Mechanics and Engineering*.

Kefal, A., Bungamayang, J., and Oterkus, E. (2016). Shape sensing of a Capsize bulk carrier using fiber-optic cables and iFEM methodology. In preparation for *Ocean Engineering*.

7.4.2 Conference papers/presentations

Kefal, A., and Oterkus, E. (2015). Structural health monitoring of marine structures by using inverse finite element method. In C. Guedes Soares and R.A. Shenoi (Eds.), *Analysis and Design of Marine Structures V*, pp. 341-349, Taylor and Francis Group, London.

Kefal, A., Hizir, O., and Oterkus, E. (2015). A smart system to determine sensor locations for structural health monitoring of ship structures. *Proceedings of 9th International Workshop on Ship and Marine Hydrodynamics*. Glasgow, Scotland.

Kefal, A., and Oterkus, E. (2016). Shape- and stress-sensing of a container ship by using inverse finite element method. *Proceedings of the Royal Institution of Naval Architects International Conference on Smart Ship Technology*. London, England.

Kefal, A., and Oterkus, E. (2017). Shape sensing of aerospace structures by coupling of isogeometric analysis and inverse finite element method. *Proceedings of the 58th AIAA/ASCE/AHS/ASC Structures, Structural Dynamics, and Materials Conference*. Grapevine, TX.

Kefal, A., and Oterkus, E. (2017). Shape and stress sensing of offshore structures by using inverse finite element method. Submitted to *the 6th International Conference on Marine Structures*. Lisbon, Portugal.

7.4.3 Reports

Kefal, A., Tessler, A. and Oterkus, E. (2016). Development of an improved inverse finite element method for shape and stress sensing of laminated composite and sandwich plates and shells. Submitted as *NASA Technical Paper*.

7.4.4 Research collaborations

This research has contributed, and continues to contribute, to the research collaboration between the NASA Langley Research Center in Hampton, VA, USA and the University of Strathclyde, concerning the applications of the iFEM/i3-RZT methodology (vid. Chapter 6) in aerospace vehicles.

7.5 Final Remarks

The formulations developed and the results obtained in this study support the state-of-the-art methodology, i.e., the inverse finite element method (iFEM), due to its revolutionary mathematical formulation, which enables the development of superior shape sensing tools. To sum up, the iFEM frameworks produced as part of this PhD thesis can therefore be helpful for shape sensing and SHM of general engineering structures, especially of marine structures.

References

American Bureau of Shipping (1995). *Guide for Hull Condition Monitoring Systems*.

American Bureau of Shipping (2015). *Guide for Hull Condition Monitoring Systems*.

Allman, D.J. (1988). A quadrilateral finite element including vertex rotations for plane elasticity analysis. *International Journal for Numerical Methods in Engineering*, **26**(3): 717-730.

Andersson, S., Haller, K., Hellbratt, S.E., and Hedberg, C. (2011). Damage monitoring of ship FRP during exposure to explosion impacts. *Proceedings of 18th International Conference on Composite Materials*. Jeju Island, Korea.

Bathe, K.J., Iosilevich, A., and Chapelle, D. (2000). An evaluation of the MITC shell elements. *Computers and Structures*, **75**(1): 1-30.

Bazilevs, Y., Calo, V.M., Hughes, T.J.R., and Zhang, Y. (2008). Isogeometric fluid-structure interaction: theory, algorithms, and computations. *Computational Mechanics*, **43**(1): 3-37.

Belytschko, T., Stolarski, H., Liu, W.K., Carpenter, N., and Ong, J.S. (1985). Stress projection for membrane and shear locking in shell finite elements. *Computer Methods in Applied Mechanics and Engineering*, **51**(1): 221-258.

Benson, D.J., Bazilevs, Y., Hsu, M.C., and Hughes, T.J.R. (2010). Isogeometric shell analysis: the Reissner–Mindlin shell. *Computer Methods in Applied Mechanics and Engineering*, **199**(5): 276-289.

Berggreen, C., Branner, K., Jensen, J.F., and Schultz, J.P. (2007). Application and analysis of sandwich elements in the primary structure of large wind turbine blades. *Journal of Sandwich Structures and Materials*, **9**(6): 525-552.

Bogert, P.B., Haugse, E.D., and Gehrki, R.E. (2003). Structural shape identification from experimental strains using a modal transformation technique. *Proceedings of 44th AIAA/ASME/ASCE/AHS Structures, Structural Dynamics and Materials Conference*. Norfolk, VA.

Bray, D.E., and McBride, D. (1992). *Nondestructive Testing Techniques*. John Wiley and Sons, New York.

Chapelle, D., and Bathe, K.J. (1998). Fundamental considerations for the finite element analysis of shell structures. *Computers and Structures*, **66**(1): 19-36.

Cerracchio, P., Gherlone, M., Mattone, M., Di Sciuva, M., and Tessler, A. (2010). Shape sensing of three-dimensional frame structures using the inverse finite element method. *Proceedings of 5th European Workshop on Structural Health Monitoring*. Sorrento, Italy.

Cerracchio, P., Gherlone, M., Di Sciuva, M., and Tessler, A. (2013). Shape and stress sensing of multilayered composite and sandwich structures using an inverse finite element method. *Proceedings of V International Conference on Computational Methods for Coupled Problems in Science and Engineering*. Ibiza, Spain.

Cerracchio, P., Gherlone, M., and Tessler, A. (2015a). Real-time displacement monitoring of a composite stiffened panel subjected to mechanical and thermal loads. *Meccanica*, **50**(10): 2487-2496.

Cerracchio, P., Gherlone, M., Di Sciuva, M., and Tessler, A. (2015b). A novel approach for displacement and stress monitoring of sandwich structures based on the inverse finite element method. *Composite Structures*, **127**: 69-76.

Chierichetti, M. (2014). Load and response identification for a nonlinear flexible structure subject to harmonic loads. *Journal of Computational and Nonlinear Dynamics*, **9**(1): 011009.

Cook, R.D. (1994). Four-node ‘flat’ shell element: drilling degrees of freedom, membrane-bending coupling, warped geometry, and behaviour. *Computers and Structures*, **50**(4): 549-555.

Cottrell, J.A., Hughes, T.J.R., and Bazilevs, Y. (2009). *Isogeometric Analysis: Toward Integration of CAD and FEA*. John Wiley and Sons, England.

Cox, M.G. (1972). The numerical evaluation of B-splines. *IMA Journal of Applied Mathematics*, **10**(2): 134-149.

Davis, M.A., Kersey, A.D., Sirkis, J., and Friebele, E.J. (1996). Shape and vibration mode sensing using a fiber optic Bragg grating array. *Smart Materials and Structures*, **5**(6): 759-765.

Dawood, T.A., Shenoi, R.A., and Sahin, M. (2007). A procedure to embed fibre Bragg grating strain sensors into GFRP sandwich structures. *Composites Part A: Applied Science and Manufacturing*, **38**(1): 217-226.

De Boor, C. (1972). On calculating with B-splines. *Journal of Approximation Theory*, **6**(1): 50-62.

De Mooij, C., Martinez, M.J., and Benedictus, R. (2016). Sensor fusion for shape sensing: theory and numerical results. *Proceedings of 27th International Conference on Adaptive Structures and Technologies*. Lake George, New York.

Derkevorkian, A., Masri, S.F., Alvarenga, J., Boussalis, H., Bakalyar, J., and Richards, W.L. (2013). Strain-based deformation shape-estimation algorithm for control and monitoring applications. *AIAA Journal*, **51**(9): 2231-2240.

Det Norske Veritas (1997). Hull monitoring system. *DNV Rules for Classification of Ships*, Part 6, Chapter 11.

Det Norske Veritas (2011). Hull monitoring systems. *DNV Rules for Classification of Ships/High Speed, Light Craft and Naval Surface Craft*, Part 6, Chapter 11.

Di Sciuva, M. (1984). A refinement of the transverse shear deformation theory for multilayered orthotropic plates. *L'aerotecnica Missili e Spazio*, **62**: 84–92.

Dokkum, K.V. (2003). *Ship Knowledge, a Modern Encyclopedia*. Dokmar, Netherlands.

Echter, R., Oesterle, B., and Bischoff, M. (2013). A hierarchic family of isogeometric shell finite elements. *Computer Methods in Applied Mechanics and Engineering*, **254**:170–180.

Foss, G.C., and Haugse E.D. (1995). Using modal test results to develop strain to displacement transformations. *Proceedings of the 13th International Modal Analysis Conference*, pp. 112-118. Nashville, TN.

Frei, W. (2013). *Meshing Example 1: Wheel Rim* (Image). Retrieved from https://www.comsol.com/blogs/meshing-your-geometry-various-element-types/.

Gherlone, M., Cerracchio, P., Mattone, M., Di Sciuva, M., and Tessler, A. (2011a). Beam shape sensing using inverse finite element method: theory and experimental validation. *Proceeding of 8th International Workshop on Structural Health Monitoring*. Stanford, CA.

Gherlone, M., Cerracchio, P., Mattone, M., Di Sciuva, M., and Tessler, A. (2011b). Dynamic shape reconstruction of three-dimensional frame structures using the inverse finite element method. *NASA/TP-2011-217315*.

Gherlone, M., Cerracchio, P., Mattone, M., Di Sciuva, M., and Tessler, A. (2012). Shape sensing of 3D frame structures using an inverse finite element method. *International Journal of Solids and Structures*, **49**(22): 3100-3112.

Gherlone, M., Cerracchio, P., Mattone, M., Di Sciuva, M., and Tessler, A. (2014). An inverse finite element method for beam shape sensing: theoretical framework and experimental validation. *Smart Materials and Structures*, **23**(4), 045027.

Glaser, R., Caccese, V., and Shahinpoor, M. (2012). Shape monitoring of a beam structure from measured strain or curvature. *Experimental Mechanics*, **52**(6): 591-606.

Glisic, B., and Inaudi, D. (2007). *Fibre Optic Methods for Structural Health Monitoring*. John Wiley and Sons, England.

Hageman, R., Aalbetrs, P., Shaik, M., and Van den Boom, H. (2013). Development of an advisory hull fatigue monitoring system. *Proceedings of SNAME Annual Meeting and Expo and Ship Production Symposium*. Bellevue, WA.

Herrmann, A.S., Zahlen, P.C., and Zuardy, I. (2005). Sandwich structures technology in commercial aviation. In O.T. Thomsen et al. (Eds.), *Sandwich Structures 7: Advancing with Sandwich Structures and Materials*, pp. 13-26. Springer, Netherlands.

Hughes, T.J.R., Cottrell, J.A., and Bazilevs, Y. (2005). Isogeometric analysis: CAD, finite elements, NURBS, exact geometry and mesh refinement. *Computer Methods in Applied Mechanics and Engineering*, **194**(39): 4135-4195.

Ibrahimbegovic, A., Taylor, R.L., and Wilson, E.L. (1990). A robust quadrilateral membrane finite element with drilling degrees of freedom. *International Journal for Numerical Methods in Engineering*, **30**(3): 445-457.

Jones, R.T., Bellemore, D.G., Berkoff, T.A., Sirkis, J.S., Davis, M.A., Putnam, M.A., and Kersey, A.D. (1998). Determination of cantilever plate shapes using wavelength division multiplexed fiber Bragg grating sensors and a least-squares strain-fitting algorithm. *Smart Materials and Structures*, **7**(2): 178-188.

Kageyama, K., Kimpara, I., Suzuki, T., Ohsawa, I., Murayama, H., and Ito, K. (1998). Smart marine structures: an approach to the monitoring of ship structures with fiber-optic sensors. *Smart Materials and Structures*, **7**(4): 472-478.

Kang, L.H., Kim, D.K., and Han, J.H. (2007). Estimation of dynamic structural displacements using fiber Bragg grating strain sensors. *Journal of Sound and Vibration*, **305**(3): 534-542.

Kefal, A., and Oterkus, E. (2015). Structural health monitoring of marine structures by using inverse finite element method. In C. Guedes Soares and R.A. Shenoi (Eds.), *Analysis and Design of Marine Structures V*, pp. 341-349, Taylor and Francis Group, London.

Kefal, A., Hizir, O., and Oterkus, E. (2015). A smart system to determine sensor locations for structural health monitoring of ship structures. *Proceedings of 9th International Workshop on Ship and Marine Hydrodynamics*. Glasgow, Scotland.

Kefal, A., and Oterkus, E. (2016a). Displacement and stress monitoring of a chemical tanker based on inverse finite element method. *Ocean Engineering*, **112**: 33-46.

Kefal, A., and Oterkus, E. (2016b). Displacement and stress monitoring of a Panamax containership using inverse finite element method. *Ocean Engineering*, **119**: 16-29.

Kefal, A., Oterkus, E., Tessler, A., and Spangler, J.L. (2016). A quadrilateral inverse-shell element with drilling degrees of freedom for shape sensing and structural health monitoring. *Engineering Science and Technology, an International Journal*, **19**: 1299-1313.

Kefal, A., Tessler, A. and Oterkus, E. (2016). Development of an improved inverse finite element method for shape and stress sensing of laminated composite and sandwich plates and shells. Submitted as *NASA Technical Paper*.

Kefal, A., and Oterkus, E. (2017). Shape sensing of aerospace structures by coupling of isogeometric analysis and inverse finite element method. *Proceedings of the 58th AIAA/ASCE/AHS/ASC Structures, Structural Dynamics, and Materials Conference*. Grapevine, TX.

Kim, N.S., and Cho, N.S. (2004). Estimating deflection of a simple beam model using fiber optic Bragg-grating sensors. *Experimental Mechanics*, **44**(4): 433-439.

Kim, H.I., Kang, L.H., and Han, J.H. (2011). Shape estimation with distributed fiber Bragg grating sensors for rotating structures. *Smart Materials and Structures*, **20**(3): 035011.

Kirchhoff, G.R. (1850). Über das gleichgewicht und die bewegung einer elastischen scheibe. *Journal Für Reine Angewandte Mathematik*, **40**: 51–58.

Ko, W.L., Richards, W.L., and Fleischer, V.T. (2009). Applications of Ko displacement theory to the deformed shape predictions of the doubly-tapered Ikhana Wing. *NASA/TP-2009-214652*.

Lancaster, P., and Salkauskas, K. (1986). *Curve and Surface Fitting: An Introduction*. Academic Press, London.

Lee, J.R., Ryu, C.Y., Koo, B.Y., Kang, S.G., Hong, C.S., and Kim, C.G. (2003). In-flight health monitoring of a subscale wing using a fiber Bragg grating sensor system. *Smart Materials and Structures*, **12**(1): 147-155.

Li, C.J., and Ulsoy, A.G. (1999). High-precision measurement of tool-tip displacement using strain gauges in precision flexible line boring. *Mechanical Systems and Signal Processing*, **13**(4): 531-546.

Liu, P.L., and Lin, H.T. (1996). Direct identification of non-uniform beams using static strains. *International Journal of Solids and Structures*, **33**(19): 2775-2787.

Lloyds Register (2004). *ShipRight Ship Event Analysis*.

Lolive, E., Casari, P., and Davies, P. (2005). Loading rate effects on foam cores for marine sandwich structures. In O.T. Thomsen et al. (Eds.), *Sandwich structures 7: Advancing with Sandwich Structures and Materials*, pp. 895-903. Springer, Netherlands.

Love, A. (1888). On the small vibrations and deformations of thin elastic shells. *Philosophical Transactions of the Royal Society A: Mathematical, Physical and Engineering Sciences*, **179**: 491-546.

MacNeal, R., and Harder, R. (1985). A proposed standard set of problems to test finite element accuracy. *Finite Elements in Analysis and Design*, **1**: 3–20.

Majewska, K., Mieloszyk, M., Ostachowicz, W., and Król, A. (2014). Experimental method of strain/stress measurements on tall sailing ships using Fibre Bragg Grating sensors. *Applied Ocean Research*, **47**: 270-283.

Maniatty, A.M., and Zabaras, N.J. (1989). Method for solving inverse elastoviscoplastic problems. *Journal of Engineering Mechanics*, **115**(10): 2216-2231

Maniatty, A.M., and Zabaras, N.J. (1994). Investigation of regularization parameters and error estimating in inverse elasticity problems. *International Journal for Numerical Methods in Engineering*, **37**(6): 1039-1052.

Maniatty, A.M., Zabaras, N.J., and Stelson, K. (1989). Finite element analysis of some inverse elasticity problems. *Journal of Engineering Mechanics*, **115**(6): 1303-1317.

McCartney, L.N. (1987). Mechanics of matrix cracking in brittle-matrix fibre-reinforced composites. *Proceedings of the Royal Society of London A: Mathematical, Physical and Engineering Sciences*, **409**(1837): 329-350.

Mindlin, R.D. (1951). Influence of rotatory inertia and shear deformation on flexural motions of isotropic elasticplates. *Journal of Applied Mechanics (American Society of Mechanical Engineers: ASME)*, **18**: 31–38.

Morley, L.S.D., and Morris, A.J. (1978). Conflict between finite elements and shell theory. *Royal Aircraft Establishment Report*. London, England.

Murawski, L., Ostachowicz, W., Opoka, S., Mieloszyk, M., and Majewska, K. (2012). Practical application of monitoring system based on optical sensors for marine constructions. *Key Engineering Materials*, **518**: 261-270.

Newman, J.N. (1985). Algorithms for the free-surface Green function. *Journal of Engineering Mathematics*, **19**(1): 57-67.

Nichols, J.M., Fackler, P.L., Pacifici, K., Murphy, K.D., and Nichols, J.D. (2014). Reducing fatigue damage for ships in transit through structured decision making. *Marine Structures*, **38**: 18-43.

Nishio, M., Mizutani, T., Takeda, N. (2010). Structural shape reconstruction with consideration of the reliability of distributed strain data from a Brillouin-scattering-based optical fiber sensor. *Smart Materials and Structures*, **19**(3): 035011.

Noblesse, F. (1982). The Green function in the theory of radiation and diffraction of regular water waves by a body. *Journal of Engineering Mathematics*, **16**(2): 137-169.

Paczkowski, K., and Riggs, H.R. (2007). An inverse finite element strategy to recover full-field, large displacements from strain measurements. *Proceedings of the 26th International Conference on Offshore Mechanics and Arctic Engineering*. San Diego, CA.

Pagano, N.J. (1969). Exact Solutions for Composite Laminates in Cylindrical Bending. *Journal of Composite Materials*, **3**(3): 398-411.

Phelps, B., and Morris, B. (2013). Review of hull structural monitoring systems for navy ships. *DSTO-TR-2818*.

Piegl, L., and Tiller, W. (1997). *The NURBS Book*, **2nd edn**. Springer-Verlag, Berlin.

Pisoni, A.C., Santolini, C., Hauf, D.E., and Dubowsky, S. (1995). Displacements in a vibrating body by strain gauge measurements. *Proceedings of the 13th International Modal Analysis Conference*, pp. 119-125. Nashville, TN.

Quach, C.C., Vazquez, S.L., Tessler, A., Moore, J.P., Cooper, E.G., and Spangler, J.L. (2005). Structural anomaly detection using fiber optic sensors and inverse finite element method. *Proceedings of AIAA Guidance, Navigation, and Control Conference and Exhibit*. San Francisco, California.

Rapp, S., Kang, L.H., Han, J.H., Mueller, U.C., and Baier, H. (2009). Displacement field estimation for a two-dimensional structure using fibre Bragg grating sensors. *Smart Materials and Structures*, **18**(2): 025006.

Reissner, E. (1945). The effect of transverse shear deformation on the bending of elastic plates. *Journal of Applied Mechanics (American Society of Mechanical Engineers: ASME)*, **12**: 69–77.

Rogers, D.F. (2001). *An Introduction to NURBS: With Historical Perspective*. Academic Press, San Diego, CA.

Schnur, D.S., and Zabaras, N. (1990). Finite element solution of two-dimensional inverse elastic problems using spatial smoothing. *International Journal for Numerical Methods in Engineering*, **30**(1): 57-75.

Scordelis, A.C., and Lo, K.S. (1969). Computer analysis of cylindrical shells. *Journal of the American Concrete Institute*, **61**: 539-561.

Shkarayev, S., Krashantisa, R., and Tessler, A. (2001). An inverse interpolation method utilizing in-flight strain measurements for determining loads and structural response of aerospace vehicles. *Proceedings of 3rd International Workshop on Structural Health Monitoring*. Stanford, CA.

Shkarayev, S., Raman, A., and Tessler, A. (2002). Computational and experimental validation enabling a viable in-flight structural health monitoring technology. *Proceedings of 1st European Workshop on Structural Health Monitoring*. Paris, France.

Sielski, R.A. (2012). Ship structural health monitoring research at the Office of Naval Research. *Journal of the Minerals, Metals and Materials Society*, **64**(7): 823-827.

Stoesz, C.W. (2013). *Method for Analyzing Strain Data*. US 8,515,675 B2.

Tarantola, A. (1987). *Inverse Problem Theory: Methods for Data Fitting and Model Parameters Estimation*. Elsevier, New York.

Taus, M. F. (2015). *Isogeometric Analysis for Boundary Integral Equations* (Doctoral dissertation). The University of Texas at Austin.

Temizer, I., Wriggers, P., and Hughes, T.J.R. (2011). Contact treatment in isogeometric analysis with NURBS. *Computer Methods in Applied Mechanics and Engineering*, **200**(9): 1100-1112.

Tessler, A., and Dong, S.B. (1981). On a hierarchy of conforming Timoshenko beam elements. *Computers and Structures*, **14**(3): 335-344.

Tessler, A., and Hughes, T.J.R. (1983). An improved treatment of transverse shear in the Mindlin-type four-node quadrilateral element. *Computer Methods in Applied Mechanics and Engineering*, **39**(3): 311-335.

Tessler, A., and Hughes, T.J.R. (1985). A three-node Mindlin plate element with improved transverse shear. *Computer Methods in Applied Mechanics and Engineering*, **50**(1): 71-101.

Tessler, A., Riggs, H.R., Freese, C.E., and Cook, G.M. (1998). An improved variational method for finite element stress recovery and a posteriori error estimation. *Computer Methods in Applied Mechanics and Engineering*, **155**(1): 15-30.

Tessler, A., Riggs, H.R., and Dambach, M. (1999). A novel four-node quadrilateral smoothing element for stress enhancement and error estimation. *International Journal for Numerical Methods in Engineering*, **44**(10): 1527-1541.

Tessler, A. (2000). Comparison of interdependent interpolations for membrane and bending kinematics in shear-deformable shell elements. *Proceedings of International Conference on Computational Engineering and Sciences*. Los Angeles, CA.

Tessler, A., and Spangler, J.L. (2003). A variational principal for reconstruction of elastic deformation of shear deformable plates and shells. *NASA TM-2003-212445*.

Tessler, A., and Spangler, J.L. (2004). Inverse FEM for full-field reconstruction of elastic deformations in shear deformable plates and shells. *Proceedings of 2nd European Workshop on Structural Health Monitoring*. Munich, Germany.

Tessler, A., and Spangler, J.L. (2005). A least-squares variational method for full-field reconstruction of elastic deformations in shear-deformable plates and shells. *Computer Methods in Applied Mechanics and Engineering*, **194**(2): 327-339.

Tessler, A. (2007). Structural analysis methods for structural health management of future aerospace vehicles. *Key Engineering Materials*, **347**: 57-66.

Tessler, A., Di Sciuva, M., and Gherlone, M. (2009). A refined zigzag beam theory for composite and sandwich beams. *Journal of Composite Materials*, **43**: 1051-1081.

Tessler, A., Di Sciuva, M., and Gherlone, M. (2010). A consistent refinement of first-order shear deformation theory for laminated composite and sandwich plates using improved zigzag kinematics. *Journal of Mechanics of Materials and Structures*, **5**(2): 341-367.

Tessler, A., Spangler, J.L., Gherlone, M., Mattone, M., and Di Sciuva, M. (2011). Real-time characterization of aerospace structures using onboard strain measurement technologies and inverse finite element method. *Proceedings of the 8th International Workshop on Structural Health Monitoring*. Stanford, CA.

Tessler, A., Spangler, J.L., Gherlone M., Mattone M., and Di Sciuva, M. (2012). Deformed shape and stress reconstruction in plate and shell structures undergoing large displacements: application of inverse finite element method using fiber bragg grating strains. *10th World Congress on Computational Mechanics*, Sao Paulo, Brazil. Retrieved from https://ifem.larc.nasa.gov/publications/2012-WCCM-Brazil-Tessler.pdf.

Tikhonov, A.N., and Arsenin, V.Y. (1977). *Solutions of Ill-Posed Problems*. Winston and Sons, Washington, DC.

Timoshenko, S., and Goodier, J.N. (1951). *Theory of Elasticity*. McGraw-Hill Book Company, New York.

Todd, M.D., and Vohra, S.T. (1999). Shear deformation correction to transverse shape reconstruction from distributed strain measurements. *Journal of Sound and Vibration*, **225**(3): 581-594.

Torkildsen, H.E., Grovlen, A., Skaugen, A., Wang, G., Jensen, A.E., Pran, K., and Sagvolden, G. (2005). Development and applications of full-scale ship hull health monitoring systems for the Royal Norwegian Navy. *Proceedings of Recent Developments in Non-Intrusive Measurement Technology for Military Application on Model- and Full-Scale Vehicles*, pp. 1-14. Neuilly-sur-Seine, France.

Vadakke, V., and Carlsson, L.A. (2004). Experimental investigation of compression failure of sandwich specimens with face/core debond. *Composites Part B: Engineering*, **35**(6): 583-590.

Van der Cammen, J.J. (2008). *Fatigue Prediction and Response Monitoring on a FPSO* (Doctoral dissertation). Delft University of Technology, TU Delft.

Van der Horst, M.P., Kaminski, M.L., and Puik, E. (2013). Methods for sensing and monitoring fatigue cracks and their applicability for marine structures. *Proceedings of the 23rd International Offshore and Polar Engineering Conference*. International Society of Offshore and Polar Engineers. Anchorage, Alaska.

Vazquez, S.L., Tessler, A., Quach, C.C., Cooper, E.G., Parks, J., and Spangler J.L. (2005). Structural health monitoring using high-density fiber optic strain sensor and inverse finite element methods. *NASA TM-2005-213761*.

Versino, D., Gherlone, M., Mattone, M., Di Sciuva, M., and Tessler, A. (2013). C^0 triangular elements based on the Refined Zigzag Theory for multilayer composite and sandwich plates. *Composites Part B: Engineering*, **44**(1): 218-230.

Wall, W.A., Frenzel, M.A., and Cyron, C. (2008). Isogeometric structural shape optimization. *Computer Methods in Applied Mechanics and Engineering*, **197**(33): 2976-2988.

Wang, G., Pran, K., Sagvolden, G., Havsgard, G.B., Jensen, A.E., Johnson, G.A., and Vohra, S.T. (2001). Ship hull structure monitoring using fibre optic sensors. *Smart Materials and Structures*, **10**(3): 472-478.

Wehausen, J.V., and Laitone, E.V. (1960). Surface waves. In S. Flugge and C. Truesdell (Eds.), *Encyclopedia of Physics*, **9**: 446-778. Springer-Verlag, Berlin.

Wu, M., and Hermundstad, O.A. (2002). Time-domain simulation of wave-induced nonlinear motions and loads and its applications in ship design. *Marine Structures*, **15**(6): 561–597.

Yin, W., Fu, T., Liu, J., and Leng, J. (2009). Structural shape sensing for variable camber wing using FBG sensors. *Proceedings of the International Society for Optical Engineering*, **7292**: 72921H.

Zhu, B., and Frangopol, D.M. (2013). Incorporation of structural health monitoring data on load effects in the reliability and redundancy assessment of ship cross-sections using Bayesian updating. *Structural Health Monitoring*, **12**(4): 377-392.

Zou, Y., Tong, L.P.S.G., and Steven, G.P. (2000). Vibration-based model-dependent damage (delamination) identification and health monitoring for composite structures—a review. *Journal of Sound and Vibration*, **230**(2): 357-378.